9-17-2013 12:00 AM

Nanostructured Tin-Based Anodes for Lithium Ion Batteries with X-Ray Absorption Fine Structure Studies

Dongniu Wang
The University of Western Ontario

Supervisor
Xueliang(Andy) Sun
The University of Western Ontario

Graduate Program in Mechanical and Materials Engineering
A thesis submitted in partial fulfillment of the requirements for the degree in Doctor of Philosophy

Recommended Citation

Wang, Dongniu, "Nanostructured Tin-Based Anodes for Lithium Ion Batteries with X-Ray Absorption Fine Structure Studies" (2013). *Electronic Thesis and Dissertation Repository*. 1625.
https://ir.lib.uwo.ca/etd/1625

NANOSTRUCTURED TIN-BASED ANODES FOR LITHIUM ION BATTERIES WITH X-RAY ABSORPTION FINE STRUCTURE STUDIES

(Thesis format: Integrated Article)

by

Dongniu Wang

Graduate Program in Mechanical and Materials Engineering

A thesis submitted in partial fulfillment
of the requirements for the degree of
Doctor of Philosophy

The School of Graduate and Postdoctoral Studies
The University of Western Ontario
London, Ontario, Canada

Abstract

The practical applications of lithium ion batteries are highly dependent on the choice of electrodes, where boosting the materials innovations to design and achieve high capacity, excellent cycling performance, rate capability, low-cost and safe electrode materials provide the best solution. Based on this, tin-based anodes have gained great attention due to its high theoretical capacity, low cost and nontoxic nature to environment. Nevertheless, it undergoes significant volume variation (259%) during the operation of the battery, leading to pulverization and significant capacity fade. Thus, the practical application of tin-based anodes is still quite challenging. This thesis tackles issues related to tin-based anodes. It is demonstrated that designing hierarchical nanostructured tin and tin-based carbon composites particular tin-based graphene composites are the most effective routes to achieve excellent electrochemical properties.

In this thesis, we reported the rational design and fabrication of nanostructured tin-based anodes which began with the synthesis of relevant electrode materials as well as evaluation of their electrochemical performance. Further, synchrotron based X-ray absorption spectroscopy was conducted to unveil the electronic structure of these composites for better understanding of the mechanism behind the performance. Various strategies of material design have been used. These include:

(i) SnO_2 nanowires on conducting substrates are successfully obtained using hydrothermal process. The electronic structure and the optical properties study revealed the different crystallinity and surface/defect states related luminescence. **(ii)** Further we extend the research to fabricate the hierarchical tin-based graphene composites such as graphene-SnO_2 nanoparticles and SnO_2 nanowire/graphene/carbon composites using hydrothermal method. The hierarchical nanocomposites exhibit better performance in both high and stable capacity benefitting from the buffering effect of carbonaceous materials as well as high capacity of tin dioxide. **(iii)** In addition, Sn@C-graphene was obtained using chemical vapor deposition method. The core-shelled Sn@C nanoparticles are well embedded in graphene matrix with superior electrochemical performances. **(iv)** Refer to Sn@C nanowires on metallic substrates obtained by the same route, the high cyclic capability is achieved benefitting from the one dimensional core-shell structure. (**v**) Most interestingly, through surface coating of Al_2O_3 on SnO_2 electrodes via atomic layer deposition, we found that the well defined and optimized Al_2O_3 layer could relieve mechanical degradation and form an artificial SEI layer, leading to improved electrochemical performances compared with bare SnO_2 electrodes. The element specific X-ray absorption spectra uniquely characterize the Sn, C and O specified edge of target samples, providing the information of the cystallinity and surface/defect states, revealing the strong chemical bonding and interactions between Sn or SnO_2 with graphene or carbon layer, allowing for better understanding of the performance. The study in this thesis demonstrates nanostructured tin-based anodes can be alternative high performance anodes in the next generation lithium ion batteries.

Keywords

Nanomaterials, X-ray absorption fine structure, X-ray excited optical luminescence, Tin oxide, Graphene, Core-shell structures, Anodes, Nanocomposites, Lithium ion batteries, Atomic layer deposition, Hierarchical structures, Sandwiched structures, Capacities, Rate capabilities, Surface/defect States.

Co-Authorship Statement

Chapter Three:

The experimental work, reference review and paper writing was performed by Dongniu Wang under the guidance of Dr Xueliang Sun and Dr Tsun Kong Sham. Jinli Yang-discussed the results, helped to do characterization and draw 3D scheme and revised paper; Xifei Li-contribute to the final version and useful discussions; Jiajun Wang-discussed paper organizations; Ruying Li-helped to do characterizations; Mei Cai-made revision and recommendations.

Chapter Four:

Dongniu Wang designed and performed experiments, collected and analyzed data, and wrote the paper under the guidance of Dr Xueliang Sun and Dr Tsun Kong Sham. Xifei Li-contribute to the final version and useful discussions on LIB performances; Jiajun Wang-discussed paper style and organizations; Jinli Yang- draw 3D scheme and revised paper; Dongsheng Geng-synthesized graphene nanosheets; Ruying Li-helped to do TEM characterizations; Mei Cai-made revision and recommendations.

Chapter Five:

The experimental and theorectical work was peformed by Dongniu Wang under the guidance of Dr Xueliang Sun and Dr Tsun Kong Sham. Jinli Yang-discussed the results, helped to do characterization and draw 3D scheme and revised paper; Xifei Li-contribute to the final version and useful discussions on LIB performances; Dongsheng Geng-synthesized graphene nanosheets; Ruying Li-helped to do TEM characterizations; Mei Cai-made revision and recommendations.

Chapter Six:

Dongniu Wang designed and did experiments, collected and analyzed data, and wrote the paper under the guidance of Dr Xueliang Sun and Dr Tsun Kong Sham. Xifei Li- contribute to the final version and useful discussions on LIB performances; Jinli Yang-discussed the results, helped to do characterization and draw 3D scheme and revised paper; Jiajun Wang-made useful discussions on organizations; Dongsheng Geng- synthesized graphene nanosheets; Ruying Li-helped to do TEM characterizations; Mei Cai-made revision and recommendations.

Chapter Seven:

The experimental deign, operation and theoretical work was performed by Dongniu Wang under the guidance of Dr Xueliang Sun and Dr Tsun Kong Sham. Jinli Yang-helped to optimized experimental results, useful discussions, contributed to final version; Jian Wang and Zhiqiang Wang- conducted STXM experiments and analyzed results; Jigang Zhou-useful comments and helpful analysis on data; Xifei Li-contribute to the final version; Ruying Li-helped to do TEM characterizations; Mei Cai-made revision and recommendations.

Chapter Eight:

Dongniu Wang designed and conducted experiments, performed characterization, collected and analyzed data, and wrote the paper under the guidance of Dr Xueliang Sun and Dr Tsun Kong Sham. Jinli Yang- fruitful discussions, helped to do characterization and draw 3D scheme and revised paper; Jian Liu- conducted ALD coating and useful discussions; Xifei Li-contribute to the final version and LIB data; Ruying Li- helped to do TEM characterizations; Mei Cai-made revision and recommendations.

DEDICATION

To my wife-Jinli

I dedicate the thesis to my wife. She is so special and important beyond any description. I am what I am today because of her in my life. With her, I have everything.

Hearts filled with feelings
White head never separated

Acknowledgments

This thesis is the summary of my most Ph.D. research work. It was conducted in Dr. Sun's Nanomaterials and Energy group and in Dr Sham's group at Western University, London, Ontario, Canada.

First of all, I would like to express my deep gratitude to my supervisors: Dr. Xueliang (Andy) Sun and Dr Tsun Kong Sham during my four years of graduate study. I really appreciate that they offer me the chance study in their groups learning about lithium ion batteries and synchrotron technology. Your serious attitude and great enthusiasm to science always motivate and inspire me. Your dedication for scientific research, broad-based and focused knowledge as well as patience helped me learning in various fields. I am grateful for the chances and opportunities you provided to get exposure to versatile experimental and synchrotron facilities, master and gain experience on various techniques. I really appreciate your financial support and guidance.

I am grateful to Mrs. Ruying (Kathy) Li and Dr. Yun-Mui Yiu. Kathy arranged everything perfect in our lab and made our lab a wonderful workplace; especially she helped me a lot on the TEM experiment and take cares of our lives. Mui provided solid support for data simulation; I really appreciate that Mui cooked delicious food for me and my wife through these four years.

I would like to sincerely thank my advisory committee members Dr. Jun Yang and Dr. Liying Jiang two professors in MME in Western. They provided very valuable advices to my studies in every stage. Also, particularly I would also like to thank my examiners of my thesis defense Dr. Xiaoyu Cui and Dr. Yang Song for their careful examination, insightful suggestions and comments.

Next I would like to give thanks to my group members: Dr. Xifei Li, Dr. Yongji Tang, Dr. Niancai Cheng, Dr. Mohammad Norouzi Banis, Jinli Yang, Yongliang Li, Jian Liu, Yuhai Hu, Biwei Xiao, Biqiong Wang, Xia Li, Andrew Lushington, and Dr Hossein Yadegari in Andy's group as well as Dr Zhiqiang Wang, Mr. Xiaoxuan Guo, Mr. Fuyan Zhao, Mr. AnKang Zhao, Ms. Olga Lobacheva, Ms. Dong Zhao, Mr Jun Li in Sham's group. I really appreciate the generous help from them and helpful discussions. Also, I would like to give my thanks to previous group members, they are: Dr. Yong Zhang, Dr. Jiajun Wang, Dr.

Liang Li, Dr. Gaixia Zhang, Dr. Shuhui Sun, Dr. Dongsheng Geng, Dr. Xiangbo (Henry) Meng, Dr. Mihnea Ioan Ionescu, Dr. Yu Zhong, Harmid Norouzi Banis, Dr. Ying Chen, Dr. Hao Liu, Dr. Yougui Chen, Dr. Jigang Zhou, Dr. Songlan Yang, Dr. Matthew J. Ward, Dr. Lijia Liu, Dr. Michael W. Murphy and Dr. J.Y. (Peter) Ko. Thanks for the help and wish you all a bright future.

I deeply appreciate to Dr. Mei Cai (group manager in General Motors) and Dr. Guoxian Liang (director in Clariant Inc.), for the funding support. It is a valuable experience to cooperate with companies for challenging but meaningful projects.

Technical support is greatly appreciated from the following people: Beamline scientists Dr. Yongfeng Hu, Dr. Qunfeng Xiao, Dr. Lucia Zuin, Dr. Xiaoyu Cui, Mr. Chris Ryan, Dr. Tom Regier and Mr. David Chevier from Canadian Light Source; Dr. Robert A. Gordon from Advanced Photon Source; Mr. Fred Pearson and Mrs. Carman from McMaster University.

The four year Ph. D graduate study in Western is the first time I go aboard and start my new life. I would like to thank the support and encouragement from my family. I would also like to give my special thanks to Leo and Eva, without them, my life wouldn't be so nice here.

I am grateful to the Natural Sciences and Engineering Research Council of Canada (NSERC), General Motors of Canada, Canada Research Chair (CRC) Program for Andy Sun and T. K. Sham, Canada Foundation for Innovation (CFI), Ontario Early Researcher Award, Ontario Innovation Trust and the University of Western Ontario for funding.

Last but not least, I am grateful to everyone who has helped me in one way or another.

Dongniu Wang

Table of Contents

Abstract ii

Co-Authorship Statement iv

Table of Contents ix

List of Figures xiv

List of Appendices xxi

List of Abbreviations xxii

Chapter 1 1

1 Introduction 1

1.1 Lithium-ion Batteries 1

1.1.1 Principles of Lithium-ion Batteries 1

1.1.2 Developments and Challenges of Lithium-ion Batteries 4

1.1.3 Nanostructured Tin-Based Anodes 5

1.2 Synchrotron Radiation for Anodes in Lithium-ion Batteries 15

1.2.1 Overview of Synchrotron Radiation 15

1.2.2 Intercalation/Deintercalation based Anodes 17

1.2.3 Alloying/Dealloying based Anodes 22

1.2.4 Conversion reaction based Anodes 27

1.3 Objectives and Scope of the thesis 32

1.4 References 34

Chapter 2 41

2 Experimental, Characterization and Electrochemical Measurements 41

2.1 Experimental Method 41

2.1.1 Synthesis of SnO_2 Nanowires on Different Substrates via Hydrothermal Route 41

2.1.2 Synthesis of SnO_2 and SnO_2/Graphene via Microwave-Assisted Hydrothermal Method 42

2.1.3 Synthesis of Sn@C-Graphene via Chemical Vapor Deposition (CVD) Route 43

2.1.4 Syntheisis of Sn@C Nanocables on Metallic Foil Substrates via CVD Route 44

2.1.5 Synthesis of Al_2O_3 Coated SnO_2 via Atomic Layer Deposition (ALD) Method 45

2.2 Characterizations 46

2.2.1 Structural Characterizations (SEM, TEM, XRD, EDX, XPS, RAMAN). 46

2.2.2 X-ray Absorption Fine Structure 47

2.2.3 X-ray Excited Optical Luminescence 51

2.3 Electrochemical Measurements 53

2.3.1 Cyclic voltammetry (CV) and charge-discharge profiles 53

2.3.2 Cyclic and Rate Performances 53

2.4 References 53

Chapter 3 55

3 Observation of Surface/Defect States of SnO_2 Nanowires on Different Substrates from X-ray Excited Optical Luminescence 55

3.1 Introduction 56

3.2 Experimental Section 58

3.2.1 Synthesis SnO_2 NWs on different substrates. 58

3.2.2 Characterization 58

3.3 Results and Discussion 59

3.3.1 Morphology and Structures 59

3.3.2 Morphology Evolution 60

3.3.3 Electronic and Optical Properties (XANES and XEOL) 62

3.4 Conclusions 66

3.5 Acknowledgements 67

3.6 References 67

3.7 Supporting Information 70

Chapter 4 71

4 Defect-Rich Crystalline SnO_2 Immobilized on Graphene Nanosheets with Enhanced Cycle Performance for Li Ion Batteries 71

4.1 Introduction 72

4.2 Experimental Section 74

4.2.1 SnO_2/Graphene Synthesis 74

4.2.2 Characterization 74

4.2.3 Electrochemical Measurement 75

4.3 Results and Discussion 75

4.4 Conclusions 86

4.5 Acknowledgements 87

4.6 References 87

4.7 Supporting Information 90

Chapter 5 93

5 Layer by Layer Assembly of Sandwiched Graphene/SnO_2 Nanorod/Carbon Nanostructures with Ultrahigh Lithium Ion Storage Properties 93

5.1 Introduction 94

5.2 Experimental 96

5.2.1 Synthesis of Graphene, SnO_2 nanoparticle/Graphene and SnO_2 nanorod/Graphene 96

5.2.2 Synthesis of carbon coated SnO_2 nanorod Graphene 96

5.2.3 Characterization 96

5.2.4 Electrochemical Measurement 97

5.3 Results and Discussion 97

5.4 Conclusions 109

5.5 Acknowledgements 110

5.6 References 110

5.7 Supporting Information 115

Chapter 6 119

6 Hierarchical nanostructured core–shell Sn@C nanoparticles embedded in graphene nanosheets: spectroscopic view and their application in lithium ion batteries 119

6.1 Introduction 120

6.2 Experimental 121

6.2.1 Sn@C-GNs synthesis 121

6.2.2 Characterization 122

6.2.3 Electrochemical Measurement 122

6.3 Results and Discussion 123

6.4 Conclusions 136

6.5 Acknowledgements 136

6.6 References 137

6.7 Supporting Information 140

Chapter 7 142

7 Engineering of co-axial carbon sheath tin core nanowires with chemical vapor deposition and its improved lithium storage capability 142

7.1 Introduction 143

7.2 Experimental 144

7.2.1 Synthesis of Sn@C-Cu and Sn@C-SS composites 144

7.2.2 Characterization 144

7.2.3 Electrochemical Measurement 144

7.3 Results and Discussion 145

7.4 Conclusions 154

7.5 Acknowledgements 154

7.6 References 155

7.7 Supporting information 157

Chapter 8 160

8 Aluminum Oxide Surface Coating on Various Sized Tin Dioxide Anodes with Enhanced Electrochemical Performances 160

8.1 Introduction 161

8.2 Experimental 162

8.2.1 Synthesis of SnO_2 nanoparticles 162

8.2.2 Synthesis of ALD-Al_2O_3 coated SnO_2 electrodes 163

8.2.3 Characterization 163

8.2.4 Electrochemical Measurement 164

8.3 Results and Discussion 164

8.4 Conclusions 174

8.5 Acknowledgements 174

8.6 References 175

8.7 Supporting Information 178

Chapter 9 183

9 Conclusions and Future Perspectives 183

9.1 Conclusions 183

9.2 Future Work 186

9.3 References 188

Appendices 189

Curriculum Vitae 193

List of Figures

Figure 1.1 Comparison of the different battery technologies in terms of volumetric and gravimetric energy density [8]. 2

Figure 1.2 Schematic overview of charging and discharging of a Li-ion battery [12]. 3

Figure 1.3 Electrodes for LIB in the view of potential and capacity [9]. 5

Figure 1.4 Model of lithium insertion into a loosely packed small particle size Sn matrix. Even 100% volume expansion of individual particles doesn't crack the electrode [20]. 6

Figure 1.5 Capacity vs. cycle number for nanometer-scale Sn/Li cell and lager particle Sn /Li cell [21]. 7

Figure 1.6 Scheme of the nanowires as a promising anode materials [22] 8

Figure 1.7 (a) SEM of the SnO_2 Nanowires and (b) its cyclic performance in the first 15 cycles [28]. 10

Figure 1.8 SEM image of SnO_2 mesoscale tubes [33]. 11

Figure 1.9 (a-d) TEM images of SnO_2 nanowires obtained using hard template [34]. 11

Figure 1.10 (a) Schematic diagram of as-obtained carbon-coated SnO_2 nanorod array; (b) carbon coating on SnO_2 nanorod; (c) overview of the SnO_2 nanorod on substrate [37]. 12

Figure 1.11 Cycle performances the Cu_6Sn_5 and tin powder [38]. 13

Figure 1.12 SEM image of SnO_2/GNS and its cycle performance (a) compared with bare SnO_2 nanoparticle (a), graphite (b) and graphene (c) [42] 14

Figure 1.13 Scheme layout of the Canadian light source (CLS) [48]. 16

Figure 1.14 a) Li 1s IXS intensity for several materials; b) C 1s IXS intensity for HOPG, chemical lithiated LiC_6 and electrochemically prepared LiC_6 [52]. 19

Figure 1.15 (a) Synchrotron XRD measurements at the stages of discharged to 1.25 V vs Li/Li$^+$ (brown curve), discharged to 0.9 V (red), followed by charged to 2.5 V (black). Inset: pre-edge feature in the Ti K-edge XANES. T_2O_3 spectrum (blue) is shown for reference. b) Charge/discharge voltage profile of a TiO_2NT-$LiNi_{0.5}Mn_{1.5}O_4$ battery at ambient temperature cycled a rate of C/15 [61] 20

Figure 1.16 X-ray scattering data from an in situ lithiated graphene sample [64]. 22

Figure 1.17 a) Voltage profiles and (b) CV curves the Si/NiTi alloy for the several selected cycles. (c) Ex situ synchrotron XRD results of the Si/NiTi alloy at selected potential [68]. . 24

Figure 1.18 STXM chemical maps from individual SnO_2-CNTs: (a) surface oxygen-containing functional groups on O-CNTs (representative of oxidized CNTs), the grey scale is proportional to the extent of surface oxidation (1 represents the intensity prior to SnO_2 coating, intensity greater than 1 shows the effect of oxidation); (b) quantitative chemical map of SnO_2 , the vertical grey scale represents the thickness in nm; (c) the colored composite map for relevant components (red: O-CNT, green:SnO_2). The component maps are rescaled individually in each color channel. Three white dashed boxes labelled 1 to 3 are selected regions of interest for XANES comparison [76]. 25

Figure 1.19 Pair distribution function profile of (a) SiO, milled-$Sn_{30}Co_{30}C_{40}$, SPEX OAC, and UHEM OAC; (b) Sn, Si/Sn, SiO, and SiO/Sn; and (c) annealed OAC [78]................... 26

Figure 1.20 Schematic view of the mechanisms occurring at the surface of the silicon nanoparticles; Formation of the SEI at the beginning of discharge; Formation of the Li−Si alloy upon further discharge, together with Li_2O and Li_xSiO_y interfacial phases [80]........... 27

Figure 1.21 The normalized Mn K-edge XANES spectra: (a) the C/MnO electrode, (b) the MnO electrode with different lithiated states. Black line: initial electrode, red line: discharging to 0 V, olive line: charging to 3 V. The inset shows the detail of the pre-edge of the C/MnO and the MnO electrode with different lithiated states [83]. 29

Figure 1.22 X-ray fluorescence compositional maps for Cu Kα and Mn Kα of an in situ $Sr_2MnO_2Cu_{3.5}S_3$/Li cell at different stages of discharge (a) and charge (b) [89]................... 30

Figure 1.23 (a) Voltage curve at the first discharge state versus metallic Li counter electrode. (b) XRD data (stars correspond to simulated patterns of lithiated rock salt iron oxide. (c) XANES spectra and (d) EXAFS data measured at eight points depicted in the voltage profile shown in (a). The Fourier transforms of k3-weighted Fe EXAFS data were plotted in (d) [92]. 31

Figure 2.1 Synthetic drawing of the preparation of SnO_2 NWs on substrates [1] 41

Figure 2.2 Illustration of (a) microwave-assisted hydrothermal system and (b) synthesis process of SnO_2/graphene nanocomposites [3] 43

Figure 2.3 Scheme for CVD set up to grow Sn@C-GNs composites [4] 44

Figure 2.4 Experimental set up for ALD device 46

Figure 2.5 Scheme representing the photoelectron wave produced by a free atom and a diatomic system upon X-ray absorption and the corresponding XANES spectrum [8]. 48

Figure 2.6 Detection modes in X-ray absorption spectroscopy 49

Figure 2.7 Sn K edge XAFS of SnO_2 50

Figure 2.8 Layout of SGM beamline [9]. 51

Figure 2.9 Emission channel specificity of XEOL, illustrating the conversion of X-ray energy into optical emission- X-rays in, optical photons out process 52

Figure 3.1 Scheme of synthetic drawing of the preparation of SnO_2 NWs on substrates 59

Figure 3.2 SEM images of SnO_2 NWs growing on different substrates: Stainless steel (a) top view; (b) side view; Copper as substrate (c) top view; (d) side view. 59

Figure 3.3 (a) morphology evolution of SnO_2 NWs on SS at different reaction time; (b) schematic SnO_2 NWs growth mechanism. 61

Figure 3.4 XRD patterns of as prepared SnO_2 NWs grown on SS and copper substrates 62

Figure 3.5 O K-edge and Sn $M_{5,4}$ edge XANES spectra of SnO_2 NWs grown on SS (a) Sn $M_{5,4}$ edge and (b) O K-edge, on Copper (c) Sn $M_{5,4}$ edge and (d) O K-edge. 64

Figure 3.6 XEOL of SnO_2 NWs on different substrates: a, b) SS; c, d) copper. 66

Figure 4.1 Illustration of (a) microwave-assisted hydrothermal system and (b) synthesis process of SnO_2/graphene nanocomposites. 73

Figure 4.2 Characterization of graphene and as- prepared SnO_2/graphene nanocomposites: a) XRD spectra b) Raman spectra 77

Figure 4.3 SEM images of (a) GNSs and (b) SnO_2/Graphene nanocomposites; (c) TEM image and (d) HRTEM image of SnO_2/Graphene nanocomposites. The inset in panel (d) is SAED patterns. 78

Figure 4.4 XANES region of the XAS spectra of the SnO_2/graphene composites: 80

Figure 4.5 (a) Carbon K edge XANES spectra of the SnO_2/graphene composites and graphene. The inset indicates the energy shift (b) Schematic of the interaction between GNSs and nanoparticles 82

Figure 4.6 Electrochemical performance of SnO_2/graphene composites: (a) Cyclic Voltammetry (CV). (b) First two Charge-discharge profiles. (c) Cycle performance plots of bare graphene, SnO_2 and SnO_2/graphene composites at 60mA g^{-1}, inserted TEM image shows the morphology of nanocomposites electrodes after cycling. (d) Rate performance and inset shows size distribution of nanoparticles in composites after cycling. 83

Figure 4.7 Electrochemical impedance spectra of (a) SnO_2 and (b) SnO_2/GNSs, inset: the equivalent circuit to fit the EIS. 86

Figure 5.1 Illustration of the synthesis processes of G/SnO_2 NR/C nanocomposites: firstly, in-situ hydrolysis of Sn salts and immobilization of SnO_2 nanoparticles on graphene; secondly, SnO_2 nanoparticles seed-assisted hydrothermal process to get SnO_2 NR grafted on graphene; finally, nano-carbon coating on G/SnO_2 NR hierarchical structures by hydrothermal carbonization of glucose. 98

Figure 5.2 SEM image of G/SnO_2 NR nanocomposites (a) shows high density of SnO_2 NR on graphene and HRTEM image of G/SnO_2 NR hybrids (c) shows no obvious carbon layer; (b) SEM image and (d), (e) TEM images of G/SnO_2 NR/C nanocomposites, where arrows indicate the outmost carbon layer; (f) XRD patterns of G/SnO_2 NR and G/SnO_2 NR/C hybrids.......... 101

Figure 5.3 (a) C K edge XANES spectra of graphene, G/SnO_2 NP, G/SnO_2 NR and G/SnO_2 NR/C composites (the inset is the magnified region which shows gradually red shift of the π^*); (b) O K edge XANES spectra of G/SnO_2 NP, G/SnO_2 NR and G/SnO_2 NR/C composites.......... 103

Figure 5.4 (a) Charge-discharge profiles of G/SnO_2 NR/C composites (inset shows the related charge-discharge capacities value versus cycle numbers); (b) Cycle performance plots of G/SnO_2 NR (0.1 C) and G/SnO_2 NR/C (0.1C and 1C) hybrids in the voltage window of 0.01-3.00 V; (c) Rate performances of G/SnO_2 NR and G/SnO_2 NR/C nanocomposites; (d) Nyquist plots of G/SnO_2 NR and G/SnO_2 NR/C nanocomposites at specified cycles, inset: the magnified curves show different diameters of semicircles. Note 1C= 1000 mA g^{-1}........... 106

Figure 5.5 HRTEM images of nanocomposites after cycling: (a) and (b) G/SnO_2 NR after 50 cycles discharge/charge at 0.1C; (c) and (d) G/SnO_2 NR/C after 350 cycles discharge/charge at 1C, where the inset shows the Fast Fourier Transform (FFT) electron diffraction pattern taken from the red circled particles; (e) Schematic representation showing that sandwiched structure prevents isolation of SnO_2 NR during cycling.......... 108

Figure 6.1 Schematic sketch for the Sn@C-GNs composites growth procedures............... 123

Figure 6.2 XRD patterns of GNs, Sn@C and Sn@C-GNs composites.............................. 124

Figure 6.3 SEM images of (a) Sn@C composites and (b) Sn@C-GNs nanocomposites (insets show the relevant low magnification images); (c), (d) TEM images and (e), (f) HRTEM images of Sn@C-GNs nanocomposites at red rectangular region e (tin core) and f (carbon shell); (g) SAED patterns and (h) EDS patterns of Sn@C-GNs nanocomposites............... 127

Figure 6.4 (a) TEY spectrum of Sn L_3 edge for Sn@C-GNs, Sn and SnO_2 nanoparticles. Carbon K-edge XANEs for Sn@C-GNs and GNs: (b) TEY spectrum, (c) Magnified TEY spectrum and (d) FLY spectrum. 131

Figure 6.5 (a) XANES spectrum of Sn K edge and (b) Fourier-transformed (FT) magnitudes of Sn K edge k^3-weighted EXAFS spectra for Sn@C-GNs, SnO_2 nanoparticles and Sn foil. (c) The schematic representation of chemical bonding and lattice compression in Sn@C-GNs composites.. 132

Figure 6.6 (a) Cyclic voltammogram (CV) and (b) First two Charge-discharge profiles of Sn@C-GNs composites (c) Cycle performance plots of bare graphene, Sn@C composites and Sn@C-GNs nanocomposites at 75 mA g^{-1}. (d) Rate performance of Sn@C-GNs and Sn@C composites. 135

Figure 7.1 XRD patterns of (a) Sn@C-Cu and (b) Sn@C-SS composites. 145

Figure 7.2 SEM images of (a) Sn@C-Cu and (b) Sn@C-SS nanocomposites; (c) TEM images of (c) Sn@C-Cu and (d) Sn@C-SS nanocomposites; 147

Figure 7.3 HRTEM images of the carbon shell from (a) Sn@C-Cu and (b) Sn@C-SS nanocomposites; SAED patterns of (c) Sn@C-Cu and (d) Sn@C-SS nanocomposites....... 148

Figure 7.4 STXM chemical maps of Sn@C-Cu: (a) Composite map at 292 eV, the red square region shows the picked region of interest; (b) Composite map for relevant components from the average of the stacked images; (c) chemical map of carbon; (d) chemical map of Cu from the Cu-Sn alloys. 149

Figure 7.5 Transmission XANES of the core and the shell regions of a single nanowire (in Figure 7.4) at (a) carbon K-edge and (b) copper L_3-edge recorded in TEY mode. 150

Figure 7.6 First two Charge-discharge profiles of (a) Sn@C-Cu and (b) Sn@C-SS nanocomposites; Cyclic Voltammetry of (c) Sn@C-Cu and (d) Sn@C-SS nanocomposites;. 151

Figure 7.7 (a) Cycle performance plots of bare Sn, Sn@C-Cu and Sn@C-SS composites at 50 mA g^{-1}; (b) Rate performances of Sn@C-Cu and Sn@C-SS composites. 152

Figure 7.8 TEM images of (a) Sn@C-Cu and (b) Sn@C-SS composites after cycling. 153

Figure 7.9 Electrochemical impedance spectra (EIS) of Sn@C-Cu and Sn@C-SS nanocomposites 154

Figure 8.1 (a) XRD spectrum of different sized SnO_2: (i) SnO_2-A; (ii) 20-SnO_2-A; (iii) SnO_2-B; (iv) 20-SnO_2-B; (v) SnO_2-C; (vi) 20-SnO_2-C; (b) Al K edge XANES of 20-SnO_2-C and standard Al_2O_3. 165

Figure 8.2 TEM images of SnO_2 (inset show HRTEM images of single particles) and Al_2O_3 coated SnO_2 samples: (a) SnO_2-A;(b) SnO_2-B; (c) SnO_2-C; (d) 2-SnO_2-C; (e) 5-SnO_2-C; (f) 20-SnO_2-C. 167

Figure 8.3 (a, c, e) Cycling performances (at 50 mA/g) and (b, d, f) rate performances (at 50 mA/g to 1000 mA/g) of Al_2O_3 coated and no coated SnO_2 samples: (a, b) SnO_2-A series; (c, d) SnO_2-B series; (e, f) SnO_2-C series 170

Figure 8.4 TEM images of (a) SnO_2-A and (b) 2-SnO_2-A after 60 cycles at 50 mA g-1. (c) SnO_2-C and (d) 20-SnO_2-C after 60 cycles at 50 mA g-1. (e) Schematic representation showing that SEI formation on pure SnO_2 and Al_2O_3 coated SnO_2 upon cycling 172

Figure 8.5 (a) XANES spectrum of Sn K edge and (b) Fourier-transformed (FT) magnitudes of Sn K edge k^3-weighted EXAFS (Extended X-ray absorption fine structure) spectra for 2 cycle ALD coated and bare SnO_2 electrodes before and after cycling. 174

List of Appendices

Appendix A Copyright release from ACS Publications 190

Appendix B Copyright release from ACS Publications 191

Appendix C Permission from Royal Society of Chemistry (RSC) for published article 192

List of Abbreviations

2D: two dimensional

3D: three dimensional

A

ALD: atomic layer deposition

APS: Advanced Photon Source

B

BE: binding energy

C

CB: carbon black

CCD: charge-coupled device

CLS: canadian light source

CNTs: carbon nanotubes

CV: cyclic voltammetry

CVD: chemical vapor deposition

D

DMC: dimethyl carbonate

DOS: density of states

E

EC: ethylene carbonate

EVs: electrical vehicles

EDS: energy dispersive X-ray spectroscopy

EDX: energy dispersive X-ray spectroscopy

EXAFS: extended X-ray absorption fine structure

EIS: electrochemical impedance spectroscopy

F

FESEM: field emission scanning electron microscope

FFT: fast Fourier transforms

FLY: fluorescence yield

FTIR: Fourier transform infrared spectroscopy

G

GNS: graphene nanosheets

H

HAADF: high angle annular dark field

HEVs: hybrid electrical vehicles

HRTEM: high resolution transmission electron microscopy

I

IR: infrared

IXS: inelastic x-ray scattering spectroscopy

L

LIB: lithium ion battery

M

MOCVD: metal-organic chemical vapor deposition

MWCNTs: multiwalled caron nanotubes

MWHM: microwave-assisted hydrothermal system

N

N-CNTs: nitrogen-doped carbon nanotubes

NMP: N-methylpyrrolidinone

NPs: nanoparticles

NWs: nanowires

NRs: nanorods

P

PLD: pulse-laser-deposition

PLY: photoluminescence yield

PNC/XSD: X-ray Science Division partnered with the Pacific Northwest Consortium

PVDF: polyvinylidene fluoride

S

SAED: selected area electron diffraction

SEI: solid electrolyte interface

SEM: scanning electron microscopy

SGM: Spherical Grating Monochromator

SR: synchrontron-radiation

SS: stainless steel

STEM: scanning transmission electron microscopy

STXM: scanning transmission X-ray microscopy

SWCNTs: single-walled carbon nanotubes

SXRMB: Soft X-ray Microcharacterization

T

TEM: transmission electron microscope

TEY: total electron yield

TGA: thermogravimetric analysis

TMA: Trimethylaluminum

U

UV: ultraviolet

V

VLS: vapor–liquid–solid process

VS: vapor–solid process

X

XAFS: X-ray absorption fine structure

XANES: X-ray absorption near edge structure

XAS: X-ray absorption spectroscopy

XEOL: X-ray excited optical luminescence

XPS: X-ray photoelectron spectrometer

XRD: X-ray diffraction

XSD: X-ray Science Division

Chapter 1

1 Introduction

1.1 Lithium-ion Batteries

1.1.1 Principles of Lithium-ion Batteries

It is essential to pursue and develop novel, safe, low-cost and environmental benign energy storage system to keep pace with the progress of modern society and accompanying ecological issues. Batteries which were first invented by Alessandro Volta in 1800 are composed by a pack of interconnected electrochemical cell (in series or in parallel) that could liberate chemical energy into electricity with specified voltage and capacity [1,2]. However, batteries are not regarded as a real energy storage system until the emergence and development of secondary (or rechargeable) batteries, where electrons could be stored in a chemical manner through a charge current and released as electrical energy through a discharge current upon chemical reactions in an opposite direction.

After decades of evolution for various generations of batteries, lithium ion batteries (LIB) have been witnessed its great success in portable electronic devices since commercialization in 1991 by Sony Company, Japan [3]. It is composed by cathodes ($LiCoO_2$), anodes (Graphite) and separator (polypropylene) immersed in non-aqueous electrolyte (such as ethylene carbonate and dimethyl carbonate) with concentrated lithium salt (such as $LiPF_6$) [4-8]. LIB as a member of rechargeable batteries, is superior compared with many other successful recyclable batteries systems such as lead acid, nickel-cadmium, and nickel-metal hydride in the view of the energy density (per volume or per mass) as shown in Figure 1.1 [9]. Besides, it has many other advantages including no memory effect, light weight, long cycle life, high working voltage and almost no loss of charge when not in use. Benefiting from these advantages, it has been widely applied in portable electrical devices such as mobile telephones, ipads, personal laptops, video external cameras and so on, accounting for more than 63% worldwide sale in portable devices fields [9-11].

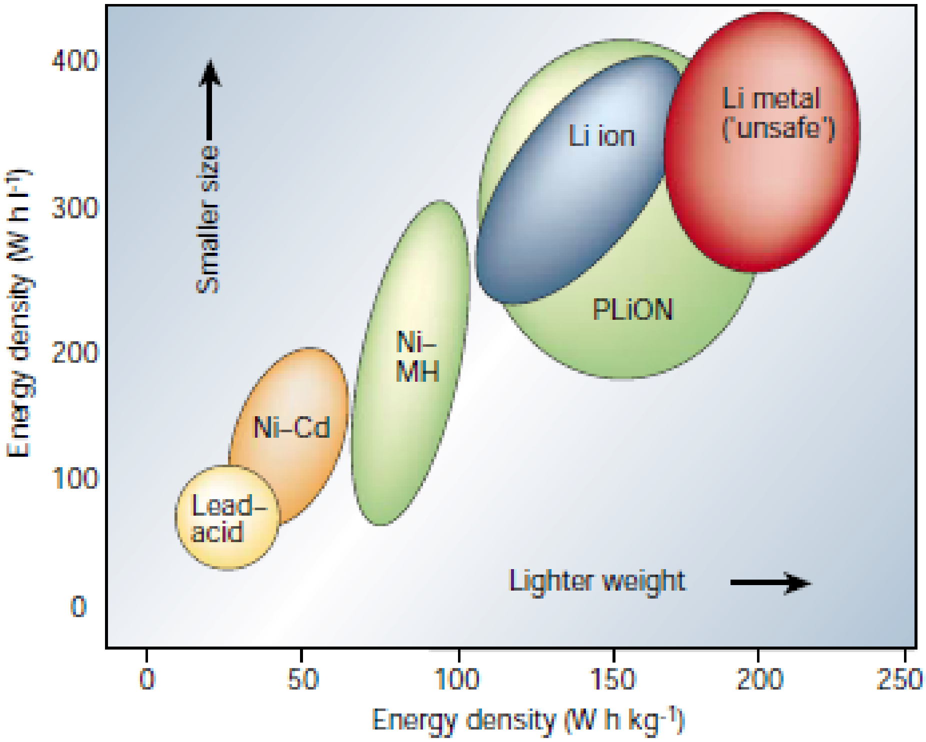

Figure 1.1 Comparison of the different battery technologies in terms of volumetric and gravimetric energy density [8].

The principle of LIB is basically storing and delivering energy charging and discharging processes, where electrons travel external circuit while lithium ions diffuses inside between anode and cathode through electrolyte. Taking the widely communalized $LiCoO_2$/C (graphite) system for example, during the charging process, Li^+ will be extracted from the $LiCoO_2$ by electrochemical oxidation and then pass through the separator to reach and intercalated into C (graphite) through the electrolyte. Simultaneously, electrons would be provided by the externally supply from cathode to anode, where electrical energy is stored in the form of chemical energy. In the discharging process, the lithium ions would transferred in the opposite direction from anode to cathode, while electrons continuously generated at the anode part through chemical redox reaction would also transport in the same direction externally to provide energy for the load. A scheme representing the basic principles of LIB during operation is shown in Figure 1.2 [12].

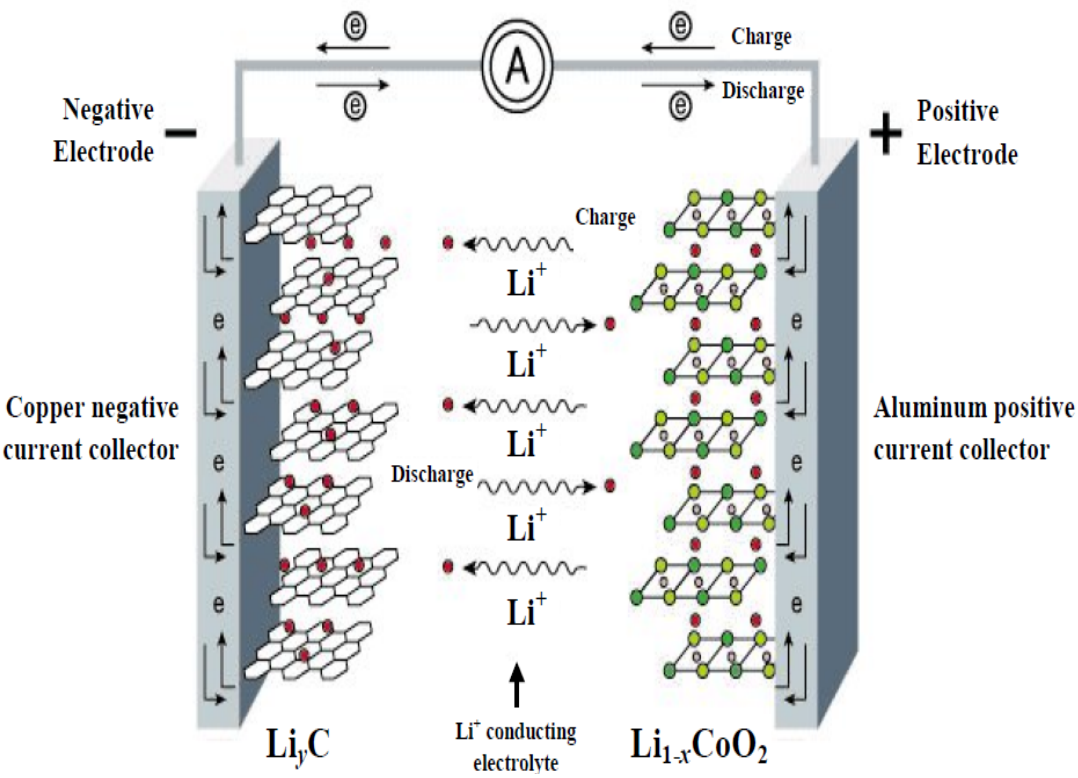

Figure 1.2 Schematic overview of charging and discharging of a Li-ion battery [12].

The performances of battery such as electrical energy are defined by several important parameters including capacity, current rate, cyclic capabilities, power and energy densities. Capacity is defined as the amount of charge stored or released during charging or discharging process with units of mAh and specific capacity is calculated per mass or per surface area. Energy density is decided by the voltage multiplied with capacity, thus the higher voltage and/or capacity, the higher energy density is achieved. Current rate or widely accepted C-rate is terminated as follows: xC rate equals an electrode achieves its fully charged/discharged state in 1/x hours. For example, 2C means that batteries are operating with 0.5 h to reach fully discharging/charging state. Power density is highly corresponding to rate performance of cell since it describes the energy delivery speed with a unit of W/kg. Cyclic capabilities or cyclability measures the stability of the battery versus cycles (noting one charging/discharging process is called one electrochemistry cycle), reflecting the stability of the capacity for the battery. The performance of a full cell is relied on performances of cathodes and anodes as well as other components’ mass.

1.1.2 Developments and Challenges of Lithium-ion Batteries

Recently, with the increasing social concerns about the environmental pollution and the depletion of fossil fuels, more and more attention are focusing on LIB which are regarded as a promising clean energy system. Extensive efforts have been focused on overcoming the limitation of commercialization of lithium ion batteries on large scale applications such as electrical vehicles (EV), hybrid electrical vehicles (HEV), electrical grids and so on, which could replace or complement the internal combustion engine relying on conversional fossil fuels. The key problems are cost, safety, cycle life and more importantly the energy density. To satisfy the need for EV, a battery pack should proved an energy density around 25-45 kWh, which is more than twice of that of the currently levels for LIBs [13]. As discussed above, the key factors to improve the capacity for battery depend on the capacities and operating voltage of the selected anodes and cathodes. The higher capacities of electrodes and bigger voltage differences (potential of cathode minus anode), the higher energy densities are obtained. Figure 1.3 illustrates the summary for voltage versus capacity for positive and negative electrode materials presently. Different fro cathode, the working voltage and more significantly, the capacities for different anodes show big range (e.g. from over 4000 mA h g^{-1} for Si [14] to less than 200 mA h g^{-1} for $Li_4Ti_5O_{12}$ [15]). Thus, one avenue to achieve next generation high performance LIB focuses on the exploitation of anodes.

Besides the well known graphite, only one alternative anode have been successfully been commercialized namely the Sn-Co-C developed also by Sony in 2005. A higher and stable reversible capacity of 350 to 450 mAh g^{-1} could be obtained for this electrode. However, various anode materials in Figure 1.3 [9] have been continuously studied recent years to pursue electrodes with high energy densities and they could be generally divided into three groups based on the reaction mechanism with lithium which will be discussed in detail later in this chapter.

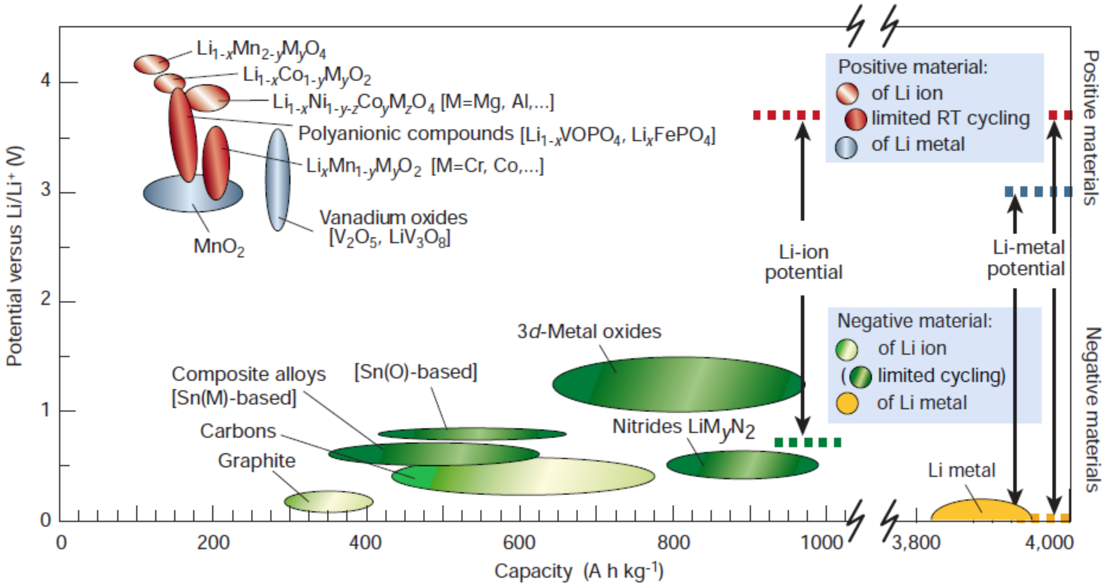

Figure 1.3 Electrodes for LIB in the view of potential and capacity [9].

1.1.3 Nanostructured Tin-Based Anodes

Since the commercial carbon (graphite) anode delivers a limited specific capacity of 372 mAh g^{-1}, much research attempts have been applied on exploring substitutes with high energy densities. Tin based anodes have been intensively studied as promising alternatives owing to their high specific capacities (e.g., Sn: 992mA h g^{-1} [16], SnO_2: 781 mA h g^{-1} [17, 18], SnO: 876mA hg^{-1} [19], etc.) while the capacity of conventional graphite is only 372 mA h g^{-1}. In the cycling process, Li-Sn alloy will form and decompose upon charging/discharging process repeatedly and the reactions can be indicated into the following equation 1 (Eq. 1):

$$Sn + 4.4e^- + 4.4Li^+ \leftrightarrow Li_{4.4}Sn \quad (Eq. 1)$$

From the above equation, it can be seen that per mol tin can alloy 4.4 mol Li at most upon cycling while for commercialized graphite, six carbon can intercalate only one Li. Based on this, the capacity of tin-based anodes are generally two times higher than that of graphite [19].

However, also due to the large amount of alloyed lithium ions, the lithium driven volume swings is huge, where a large specific volume change inevitably occurs in the host matrix of Sn upon cycling, leading to serious pulverization and re-aggregation of the active materials and the loss of electrical conductivity with the current collector. As a result, tin based anodes show very poor cycle performance which hampers its industrial application.

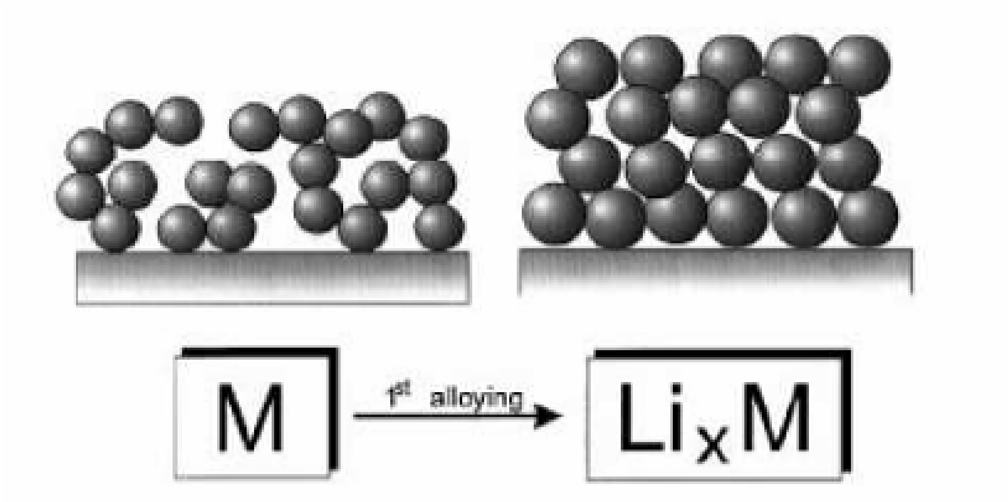

Figure 1.4 Model of lithium insertion into a loosely packed small particle size Sn matrix. Even 100% volume expansion of individual particles doesn't crack the electrode [20].

Generally, there are two avenues to solve or alleviate the volume variation problems. One route is designing nanostructured tin-based anodes benefiting from progresses and advantages with rapid development of nanotechnology. As shown in Figure 1.4 [20], for nanosized materials with high voids due to low tap density, after lithiation, a volume increase of over 100% of each particle does not cause the collapse of the whole electrode since the absolute changes in dimensions are still small and thus the integrity of electrodes could still be maintained. Besides, there are more advantages associated with the fabrication of anodes in nanoscale for LIB [10] including: 1) better accommodation of the stress and strain during lithium alloying/dealloying to improve mechanical stability of electrode; (ii) catalyze or facilitate new reactions which are limited in bulk materials; (iii) high surface to volume ratio for nanosized materials will increase contact area with electrolyte, favouring high electrons and charge transfer; (iv) shortened path ways for electrons and ions in at least one dimensions to obtain higher conductivity than bulk materials.

Decreasing size to enhance the electrochemical performance has been intensively studied. Choi prepared [21] the nanosized tin particles and compared the charge–discharge cycling performances of nanosized Sn electrodes with microsized Sn particles and it is proved that the nanosized Sn powder exhibits better lithium storage capability, as shown in Figure 1.5.

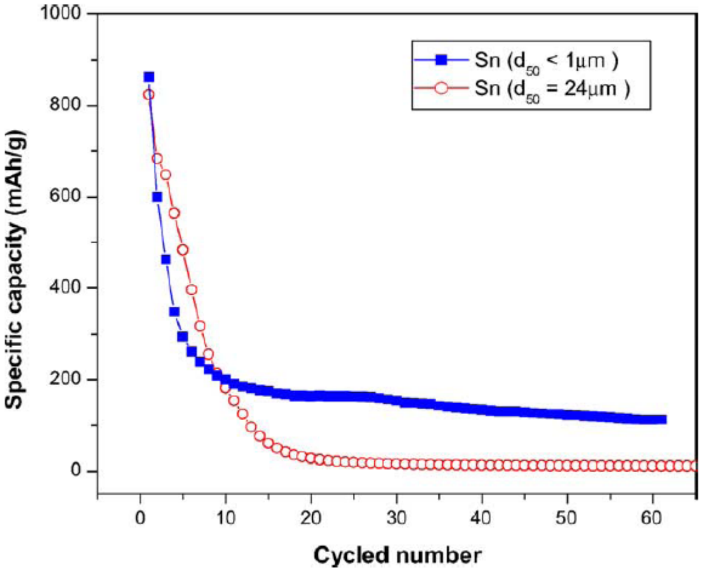

Figure 1.5 Capacity vs. cycle number for nanometer-scale Sn/Li cell and lager particle Sn /Li cell [21].

Recent study brought the concept of successful design of nanowires acting as favourable nanostructures (Figure 1.6) [22]. In comparison with other nanostructures such as thin film and nanoparticles, nanowires have several advantages: nanowires still maintains short diffusion length due to the small diameter and more over, it could provide a facile strain relaxation along a well defined orientation due to the anisotropic geometrical nature, rather than the irregular expansion happened in films and particles. Furthter, the interval spaces between neighboring nanowires could inhibit the agglomeration and facilitate the diffusion and percolation of electrolyte into the inner region. In contrast, films and particles tend to pulverize during cycling, leading to poor transportation of electrons and then failure of the electrode.

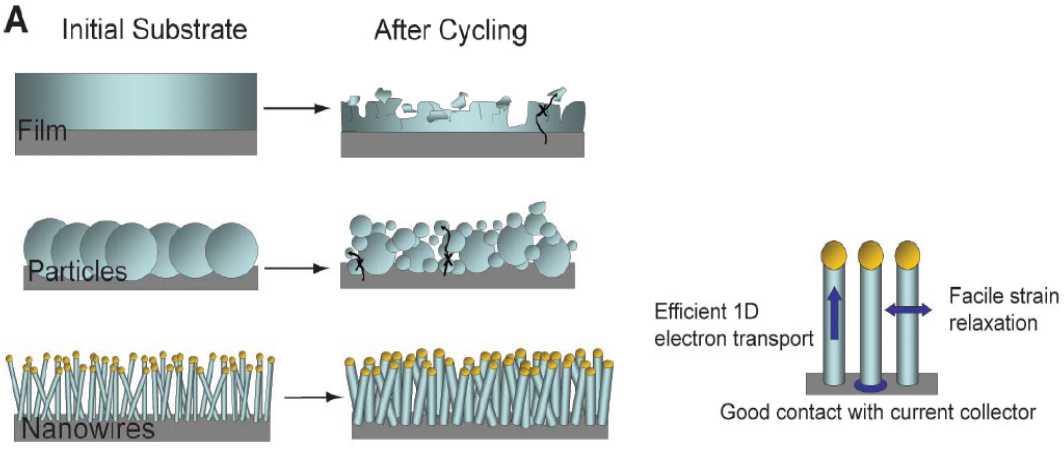

Figure 1.6 Scheme of the nanowires as a promising anode materials [22].

Another avenue is to introduce other inert metals or carbonaceous materials to form intermetallic alloys and/or composites instead of pure tin anodes. In this strategy, the ideal matrixes could confine the volume change of tin through a so-called “cushion effect. At certain discharging/charging states, Li-Sn alloys will form or decompose to introduce big volume variation, whereas the other metals are less active or even inactive (such as inert metal of Cu, Ni, Co), or highly mechanically flexible (such as carbonaceous materials), which will function as a “matrix” buffering the volume alternations of the whole electrodes. An optimized matrix should satisfy the following needs: 1) the well dispersed or combined between reactant and matrix; (ii) matrix should be ionic and electronic conductive to allow its effective transportation. Combining the advantages of nanomaterials, the active materials should also be sufficiently small. Thus, designing a nanostructured composite is demonstrated as most effective strategies so far. For the carbon matrix, extensive researches have been focused on designing carbon-tin composites and many fruitful results have been realized [23-26]. In the following, more details of the synthesis methods for tin-based nanostructures especially one dimenaisonal nanowires and tin based carbon composites will be provided with examples.

According to the synthesis environment, synthesis strategies can be mainly divided into two categories: vapor phase growth and liquid (solution) phase growth. Nanowires are easily obtained via the well-developed vapor phase technique based on the chemical reaction between metal vapor and oxygen gas. The synthesis mechanisms are the vapor–liquid–solid process (VLS) and vapor–solid process (VS) [27]. On the other hand, solution-phase growth methods provide more flexible synthesis process and an alternative to achieve lower cost. For vapor phase growth, it can be further divided into: direct thermal evaporation method; chemical vapor deposition; pulse-laser-deposition (PLD); metal-organic chemical vapor deposition (MOCVD). For solution phase growth, it can be divided into hard template method and template-free methods. Various templates such as anodic aluminum oxide, molecular sieves, and polymer membranes have been employed. Combining with electrochemical deposition and sol-gel deposition, and then removing the template, it is easier to get the one dimensional structure. For template free methods, it can be further divided into sonochemistry, hydrothermal and surfactant methods.

Massive SnO_2 nanowires were successfully fabricated by thermal evaporation of metallic tin-based on the metal catalyst (usually gold) assisted VLS growth route. Ying [28] synthesized the SnO_2 nanowires applying the VLS method and investigated its LIB performances. The nanowires have a length up to few micros with a quadrate cross section size of 50 nm as shown in Figure 1.7. Although the cycle is only extended to 15 cycles, the capacity fading is greatly reduced, demonstrated that nanowires are a promising anode material for Li-ion battery applications. Similarly, other groups also synthesized the one dimension SnO_2 naowires using modified VLS method including self catalyzed route [29], Ag-Sn precursors [30] and desired electrochemical performances than that of bulk or nanoparticles is realized. Moreover, Ko et al. [31] successfully grew SnO_2 nanowires arrays rooted on stainless steel, which can serve as a current collector directly without the using of binder and conductive carbon. As demonstrated from the excellent electrochemical results, this novel fabrication design guaranteed excellent rate capabilities because of reduced of inner impedance and stable cycling since the electrons can be transferred quickly from the active redox sites to the conductive substrate along a highway rather than a random walk in disordered nanocrystals.

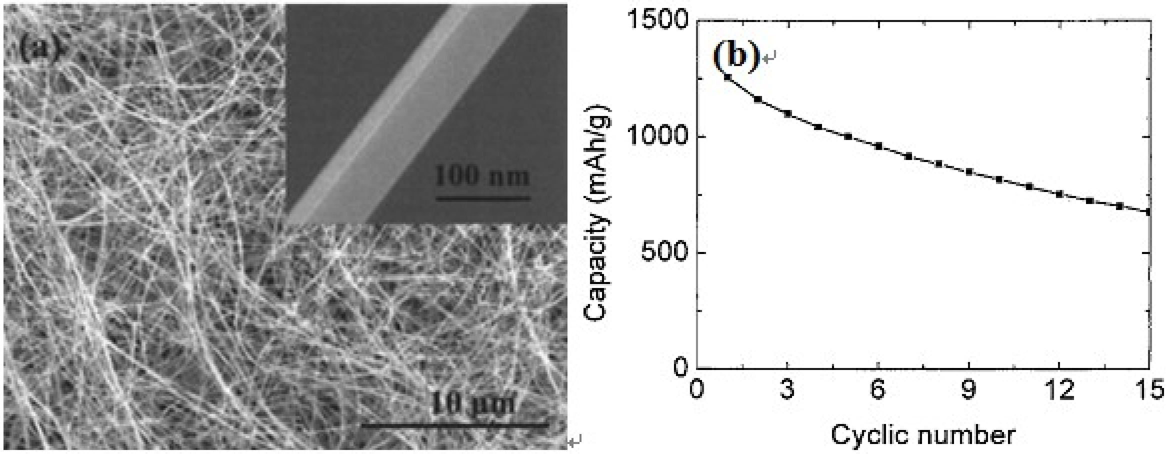

Figure 1.7 (a) SEM of the SnO_2 Nanowires and (b) its cyclic performance in the first 15 cycles [28].

Using periodic structured hard template such as anodic aluminum oxide, molecular sieves, and polymer membranescould also aid to form one dimensional nanostructure. Filling these pores through electrodeposition and sol–gel deposition methods and then removing these templates aggressively could form high-order nanostructures. Since it is easy to manipulate the neighboring channels distance and choose various diameters for these nanochannels, it is convenient to get the desired surface to volume ratio for tin-based nanostructures. Lai et al. applying polycarbonate as template to deposit SnO_2 nanoparticles and then dissolve polycarbonate membrane using dichloromethane to get nanotube [32]. Shu-Lei Chou [33] et al. has synthesized SnO_2 meso-scale tubes and microbowls using electrodeposition method under ambient conditions. The self-bubbling O_2 would function both as template and the oxidant for achieving SnO_2 tube structures. Figure 1.8 shows the SEM image of the as-obtained meso-scale tubes. More interestingly, the electrochemical result illustrated that the meso-scale tubes have higher discharge capacity and rate capability. Beside the electrodepostion, sol-gel method is also widely applied for hard template to get nanowire structure. With the help of KIT-6 and SBA-15 SiO_2, Kim [34] et al. obtained mesoporous 1D SnO_2 materials for lithium batteries. The nanowire has ordered structure with a length over 3 mm and diameter of only 6 nm as shown in Figure 1.9. The electrochemical properties of mesoporous SnO_2 showed excellent capacity retention which is partially due to the high diffusion rate for lithium ions since mesopores are immersed in electrolyte thoroughly.

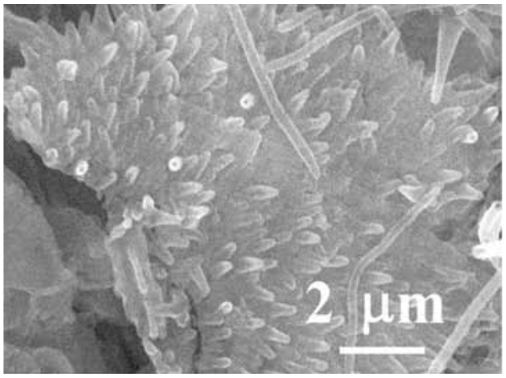

Figure 1.8 SEM image of SnO_2 mesoscale tubes [33].

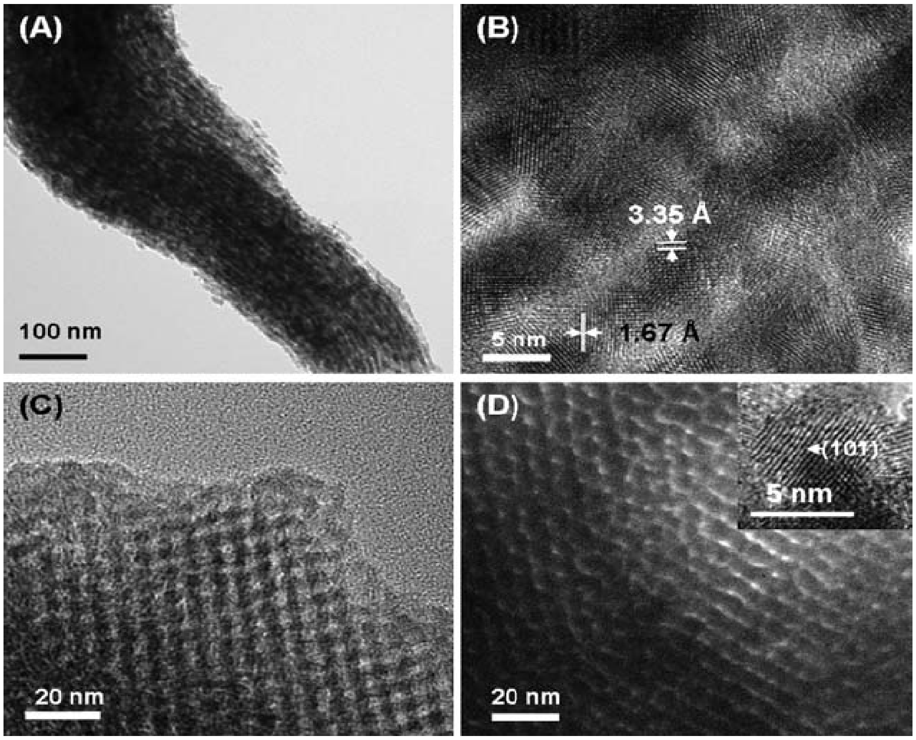

Figure 1.9 (a-d) TEM images of SnO_2 nanowires obtained using hard template [34].

Hydrothermal method is effective for creating novel nano-architectures or hierarchical nanostructures. Shi Song-Lin [35] et al. has synthesized SnO_2 nanorods with a length around 150 nm and diameter around 10 nm through a hydrothermal oven. The as-prepared SnO_2 nanord exhibit higher initial discharge capacity of 1778 mAh/g than the theoretical value of the bulk SnO_2 (1494 mAh/g). The capacity fading is greatly suppressed at the initial 15 cycles. Similar to VLS process, the current collector supported SnO_2 nanorod could also be obtained by immersing substrates in the vessels beforehand. Liu et al. [36] synthesized the SnO_2 nanorod on Ti substrates and superior electrochemical performances are achieved. As shown in Figure 1.10, Ji et al. [37] directly deposit SnO_2 nanorod on substrate and they further applied carbon coating outside the nanorod. The SnO_2 nanorod posses a sharp tip around 100 nm and a length of 400 nm and a carbon coating of 6 nm. The carbon coated SnO_2 nanorods exhibit even higher rate capability due to the high conductive and flexible carbon layer.

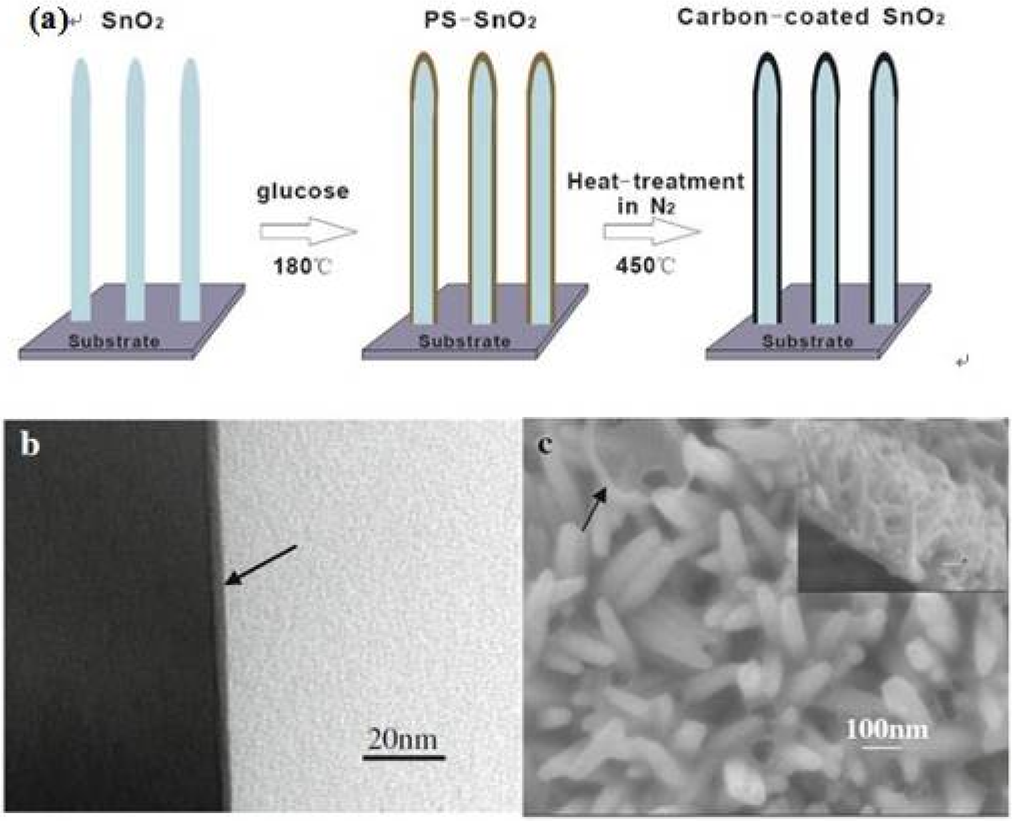

Figure 1.10 (a) Schematic diagram of as-obtained carbon-coated SnO_2 nanorod array; (b) carbon coating on SnO_2 nanorod; (c) overview of the SnO_2 nanorod on substrate [37].

Refer to another group for synthesizing tin-based nanostructures in inert matrix such as carbonaceous materials or metal, various approaches are also applied. A. Finke prepared the intermetallic Cu–Sn alloys films by electro-deposition and evaluated the cycling performances of Cu-Sn alloys compared with pure Sn. As shown in Figure 1.11, it is found that after 20 cycles, the remaining capacity is approximately four times greater than that of pure Sn powder electrode, indicating the advantage of copper-rich Sn alloys [38]. Similar effect is also observed for Ni-Sn alloys prepared by Dong et al. using H_2 reduction CVD processes and also the solution method [39], the optimized Ni to Sn ratio is determined as Ni_3Sn_2.

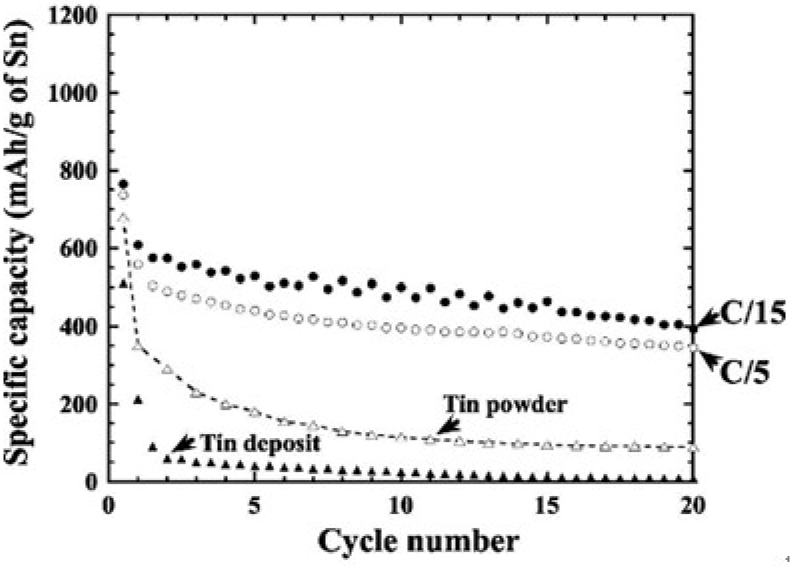

Figure 1.11 Cycle performances the Cu_6Sn_5 and tin powder [38].

Recently, nanocarbon materials have attracted more attention, since it could only buffer the volume change, but also act as the active materials to contribute to the whole capacity. Especially CNTs and the new group member of graphene, because CNTs or graphene has many excellent properties such as high electronic conductivity, chemical tolerance, high surface to volume ratio, a broad electrochemical voltage window and mechanical flexibility which could buffer the volume variation of tin-based electrodes. Thus, many reported results have been focusing on utilizing CNTs or Graphene to synthesize composites for desired high performance anodes. Wen et al. [40] has deposited mesoporous tin dioxide (SnO_2) on the surface of multiwalled carbon nanotubes (MWCNTs) through hydrothermal method. The MWCNTs has uniform distribution of SnO_2 nanoparticles and stable LIB performances which is attributed to the buffering effect from carbon matrix. Wang et al. [41] also fabricated SnO_2/MWCNTs composites using a wet chemical method and by controlling the PH value and reaction time of the solution, SnO_2 layer with various thicknesses could be achieved. A variety of tin-based graphene composites are also proposed. Paek et al. [42] synthesized the graphene nanosheets/SnO_2 composites. The graphene are obtained using modified Hummer's method to get graphene oxide first and then using hydrazine hydrate to reduce it to graphene. Further, a wet chemical method is applied to synthesize SnO_2 graphene composites. As shown in Figure 1.12, the lines and spherical ones stand for graphene layers and SnO_2 nanoparticles, respectively, indicating the well-combined composites are obtained. The comparison of its cycle performance with pure graphene, graphite and SnO_2 illustrate that the SnO_2/graphene composites has the high and stable lithium storage capabilities, benefitting from the 3-dimentionally delaminated flexible structure. The successful of this design for high LIB performance of graphene supported SnO_2 nanoparticles is further confirmed by Yao [43] and Lian [44] et al, where they performed in situ chemical synthesis to reduce graphene oxide, then deposit the SnO_2 and applied hydrothermal route using a "gas–liquid interfacial synthesis" to obtain the composites with improved electrochemical performances.

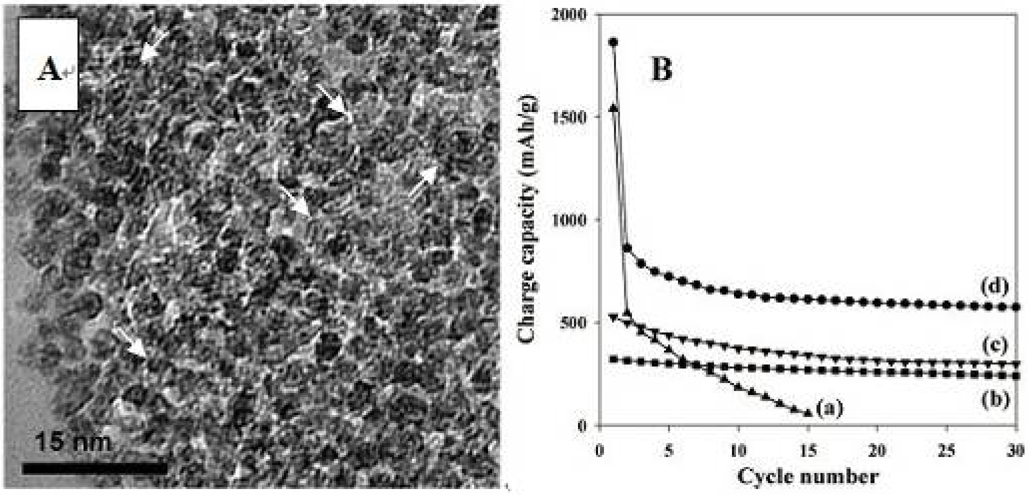

Figure 1.12 SEM image of SnO_2/GNS and its cycle performance (a) compared with bare SnO_2 nanoparticle (a), graphite (b) and graphene (c) [42].

1.2 Synchrotron Radiation for Anodes in Lithium-ion Batteries

1.2.1 Overview of Synchrotron Radiation

The development and perfection of the experimental technique and theory for synchrotron facilities is in progress from the middle of last century till today. It is regarded as a powerful photon tool and a high bright light source which is at least six orders of magnitude higher than that of X-ray tube [45]. After the pioneer work at Tantalus [46] which was among the first operational synchrotron radiation source for photon research and later Sayer et al. [47] who made the acceptable theory for the Extended X-ray Absorption Fine Structure (EXAFS), many synchrotron facilities have been built around the world. Upon the developing of instrumentation, there have been three generations of synchrotron facilities. The parasitic first generation synchrotron light sources are relied on the accelerators for high energy physics. With the sole purpose of synchrotron radiation, second generation synchrotron facilities with storage rings emerged quickly and facilities such as KEK (Japan), BESSY I (Germany), NSLS (US) and Aladdin (US) came into service in the nineteen eighties. The third generation light sources produce light with many orders of magnitude brighter compared with the second one, with the aid of the state of the art insertion devices such as undulators and wigglers, which generating light through undulating the electrons by linear packed alternating magnetic fields. The size of synchrotron facilities could be huge, for example, Spring-8 located in Japan has a circumference of 1436 m and Advanced Photo Source in USA is 1104 m in circumference. In advanced photon source (APS), the electrons generated by a cathode that is heated to about 1000 ^{o}C will be accelerated to a speed close to the light via linear accelerator, and then be injected into the booster to further gain more speed, followed by travelling at the storage ring with the trajectory altered by magnets. Then, the tangential direction of the big rings emits the synchrotron radiation and the energy loss with be replenished by the radio-frequency (RF) cavity. Each beamline will direct the beam from storage ring using mirrors, slits and monochromators for various energy range demand and application at the end station. Figure 1.13 [48] shows the scheme layout of third generation synchrotron facility in Canadian Light Source (CLS). The energy for electrons could reach 2.9 GeV, generating beam with ultrahigh brightness.

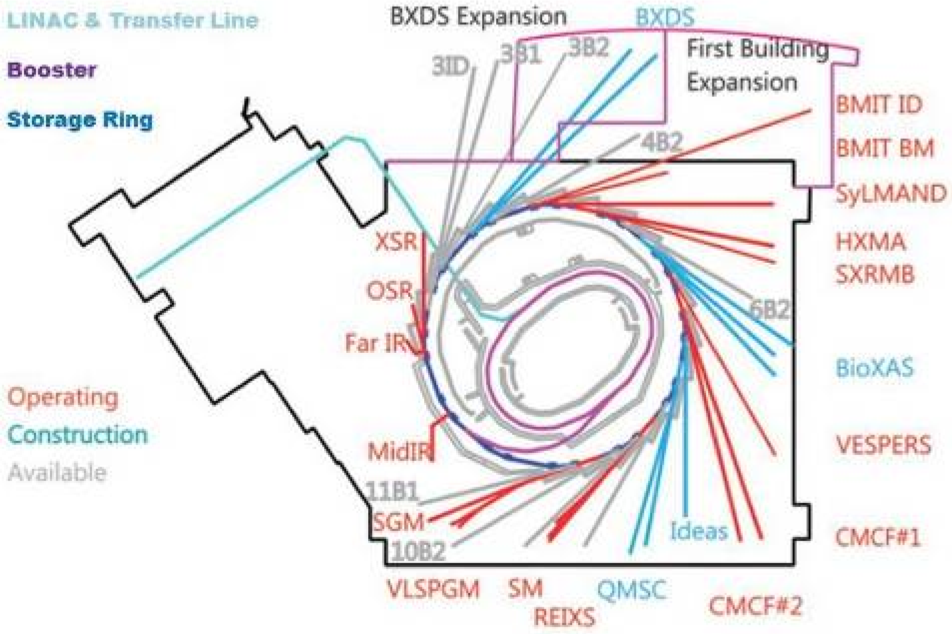

Figure 1.13 Scheme layout of the Canadian light source (CLS) [48].

Beside the high brightness, synchrotron radiation has the following advantages including inherent collimation, time structure, polarization and high tunability which cover the energy range from sub-electronvolt up to the megaelectronvolt and the wavelength is from the infrared (IR) radiation to hard X-ray region. Since the source could satisfy the demand for various excitation energies at all elemental edges, it has been widely applied to different fields from materials to life science and so on.

Returning to the LIB field, scientists have applied many techniques to study and explain the reaction mechanism behind the different performances in different battery system. However, conventional techniques are generally hard to track or exploit the mechanism and information of the lithium reaction as well as the intermediate and final products. For example, the lab based X-ray diffraction using (XRD) on electrodes after cycling, which exhibit overlapped and complex diffraction peaks with serious noise background in composite system coming from the original active anodes, binder, conductor and solid electrolyte interface (SEI). Depending on the development and design of sampling technique, Fourier transform infrared spectroscopy (FTIR) has the probing depth from several nanometers to microns but low element selectivity. Applying the X-ray photoemission spectroscopy (XPS) could precisely reveal the chemical environment of the specific elements of interest; however, it has limited depth of 0.5 nm to 5 nm [49]. The sputtering with Ar could help to yield the information below surface of targets with the destroying of the original structure and morphology of the materials. Besides, it also faces serious charging problems.

Contrastively, synchrotron radiation related techniques such as X-ray Absorption Fine Structure (XAFS) could be an ideal method for studies of electrochemical systems. It is an elemental and chemical specific tool which could be used as fingerprint to identify the phase composition of electrodes, the formed SEI [5, 6, 8, 10, 50] upon interaction which is more pronounced for anodes with electrolyte during cycling. It is highly sensitive to local chemical environment including unoccupied electronic states, oxidation states, hybridization, neighboring atoms and local symmetry. Thus the valence alternation and further reaction mechanism of electrodes with lithium could be concluded. It could also unveil the bonding and charge transfer between each component in composites systems, more interestingly, unique behavior and phenomena in nanostructure systems compared with bulk materials. It could be applied to dilute, amorphous, liquid, gases and other versatile systems while maintaining high resolution and high accuracy due to the highly focused beam with high energy resolution, demonstrating its wide compatibility for in-situ and ex-situ study. Up to now, lots of groups have reported the success of synchrotron radiation technique on the study of LIBs and the relevant research is becoming more and more intensively. The purpose of this report is to summarize the recent progresses of synchrotron radiation studies on anodes of LIBs based on three different reaction mechanisms prior to work conducted in this thesis.

1.2.2 Intercalation/Deintercalation based Anodes

This mechanism is based on intercalation of electrode with lithium in charging process while deintercalation of lithium out of lattice for electrode in discharging process. They are generally two typed anodes under this mechanism. Lithium intercalates into two dimensional layered structures such as graphite or three dimensional lattices such as

TiO_2. The general mechanism for this category is that the lithium will be inserted in and extracted from the empty sites for host anode. After fully lithium intercalation (charged state) and deintercalation (discharged state), there is no destroy to the original crystal structure except minor lattice variation. Synchrotron radiation could help to monitor the lithiation and delithiation process. In another hand, the SEI on commercial graphitic carbon which formed from decomposition of electrolyte could reduce the capacity and life time of the battery functioning as a key factor to control the safety. It will also cause great irreversible capacity loss on graphite anode thus understanding the SEI is necessary. Synchrotron radiation technique could unveil the information about SEI which have complex composition and low crystallinity (most are amorphous products) to improve the electrochemical behavior of anodes.

Although commercialized graphite has been widely applied in real packed batteries, the continuous debate about whether the charge transfer between the Li and the graphite host and detailed proof is rare. To overcome this, Schulke [51] for the first time compared the LiC_6 with the pristine graphite and observed the displacement and broadening of the first peak in the x-ray nonresonant inelastic x-ray scattering (IXS) spectrum. The 2 eV shift of the "metal" σ state of LiC_6 to lower energies is deducted compared with the σ-type interlayer state of graphite. Similarly Balasubramanian [52] et al. also performed the IXS experiment on LiC_6 samples prepared by both chemical and electrochemical methods. They found direct evidence of a 2 eV chemical shift in the Li 1s spectrum towards high energy of LiC_6 compared to Li metal. Similarly, for C 1s, a shift to lower energy is tracked for LiC_6 than pure graphite, illustrating that IXS could be used as sensitive tool for monitoring lithium intercaltion/deintercalation into graphite, as shown in Figure 1.14, Augustsson et al. [49] also tracked the energy shift at the C Kedge for the LiC_6 in different electrolyte.

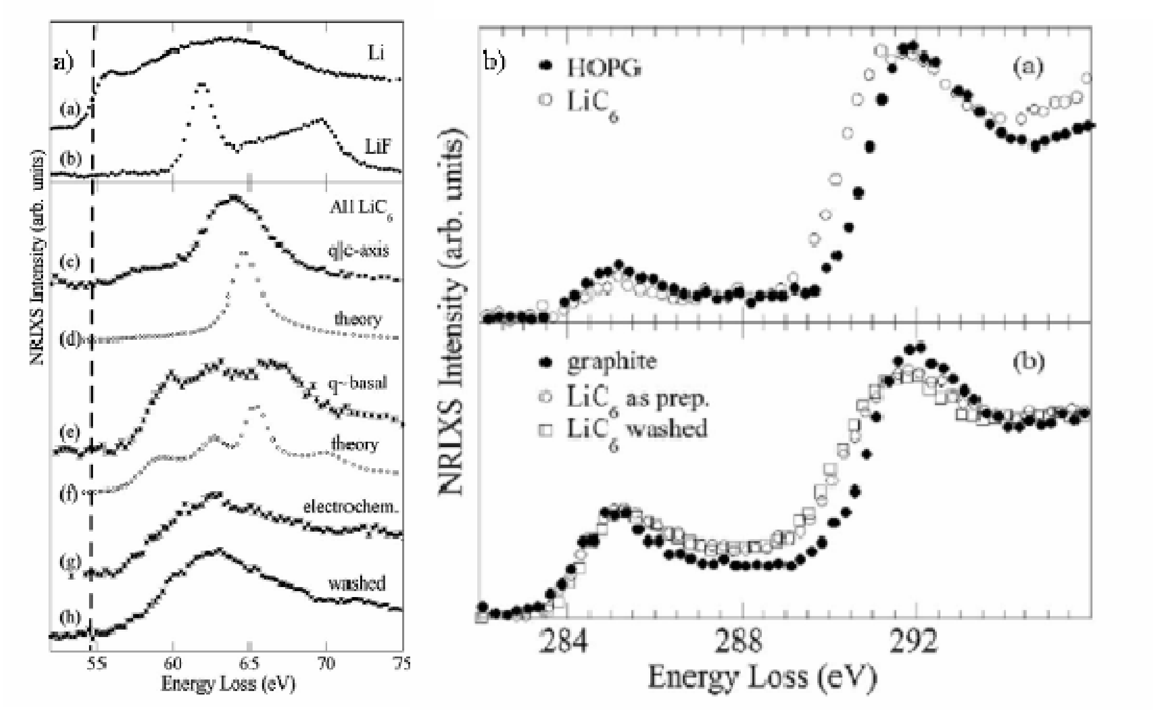

Figure 1.14 a) Li 1s IXS intensity for several materials; b) C 1s IXS intensity for HOPG, chemical lithiated LiC_6 and electrochemically prepared LiC_6 [52].

Refer to another group of TiO_2, the lithiation process could also be tracked by performing synchrotron radiation at Ti edge. Henningsson [53] prepared the nanoporous anatase TiO_2 and they perform the x-ray absorption spectroscopy (XAS) to study the electronic structure of the electrodes. They demonstrated that core level (Ti 2p) and valence level spectra exhibit reduced Ti^{3+} in Li_xTiO_2. Further experiment [54] performed at the O 1s XAS illustrates the shift of binding energy (BE) and charge transfer to lithium. Wagemaker et al. [55] designed a new cell to characterize the rutile and anatase TiO_2 using XANES, beside the valence variation concluded from the energy shift from the spectrum, the comparison between rutile and anatase TiO_2 further demonstrated that the fully intercalation is realized for anatase TiO_2 while only 0.6 mol Li could be intercalated in to rutile TiO_2, forming a $Li_{0.6}TiO_2$ phase. Lafont [56] also applied in-situ XAS to confirm the fully lithiation and phase transformation in anatase TiO_2. Refer to TiO_2-B, which have high capacity in the family of TiO_2 anodes, Okumura et al. [57] performed the XANES and EXAFS at the Ti and O edge, it is proved that the the electronic structure of TiO_2 is rather a a charge-transfer-type or an intermediate between the charge-transfer and Mott–Hubbard regimes. They also claimed the inflection point around 0.5 for x in $LixTiO_2$, beyond that point; it will lead to dramatic increment of the atomic distance and distortion to the TiO_6 octahedral. Further study on nanosized effect of TiO_2-B nanowires [58] with XAS indicated that band energy of surface of TiO_2-B was lower than that of the bulk, which favors the high rate capability.

Ra et al. [59] synthesized the ramsdellite-type $Li_2Ti_3O_7$ and $LiTi_2O_4$ [60] and using XAS and extended X-ray absorption fine structure (EXAFS) to unveil the information of electronic and local structural changes upon lithiation. The energy shifts and the changes reveal the oxidation variation of Ti valence and the EXAFS data indicate the slight local structural distortions around Ti ions. Xiong et al. [61] recently synthesized the amorphous TiO_2 nanotubes, it is interested that they found an electrochemically driven transformation from amorphous to face-centered-cubic crystalline phase as convinced by synchrotron XRD, as shown in figure 1.15. The so called self-improved anode shows superior stability over 600 cycles and exhibits high specific energy.

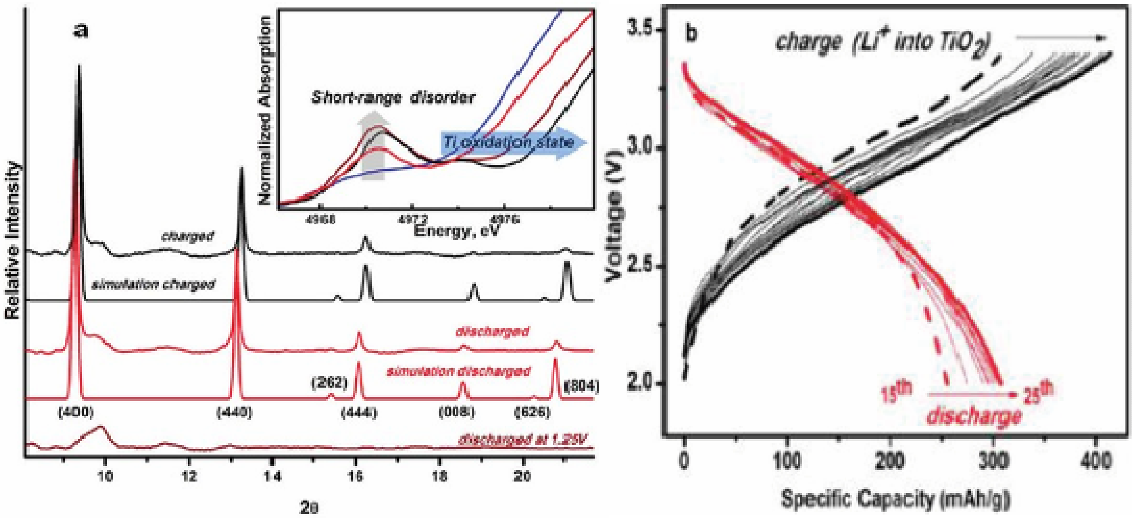

Figure 1.15 (a) Synchrotron XRD measurements at the stages of discharged to 1.25 V vs Li/Li$^+$ (brown curve), discharged to 0.9 V (red), followed by charged to 2.5 V (black). Inset: pre-edge feature in the Ti K-edge XANES. T_2O_3 spectrum (blue) is shown for reference. b) Charge/discharge voltage profile of a TiO_2NT-$LiNi_{0.5}Mn_{1.5}O_4$ battery at ambient temperature cycled a rate of C/15 [61].

Defining the composition of the SEI film related to graphitic carbon is usually hard due to the complex components and low crystallization. To have better understanding of SEI which has direct relation to the battery performances, synchrotron radiation technique was applied. Herstedt et al. [62] synthesized the jet-milled graphite, and characterized them using SR photoelectron spectroscopy, they found the SEI is composed of LiF, Li_xPFy and organic SEI layer. They also found the disordered surface structure during cycling. Malmgren et al. [63] claimed a depth gradient in the SEI layer in the graphite electrode using same technique. Augustsson et al. [49] applied the XAS and X-ray emission spectroscopy (XES) at C 1s edge and they found the existence of lithium oxylate, lithium succinate and lithium methoxide in the SEI layer of graphite. Recently, Chattopadhyay et al. [64] applied the in situ synchrotron X-ray scattering to examine the SEI layer on graphene, where the LiF with texture was demonstrated grow parallel to the graphene sheets, as shown in Figure 1.16. They also confirmed the similar composition of organic compounds in SEI layer to graphite based electrodes. These studies will assist to model and engineer the SEI formed on anode electrodes for high electrochemical performances.

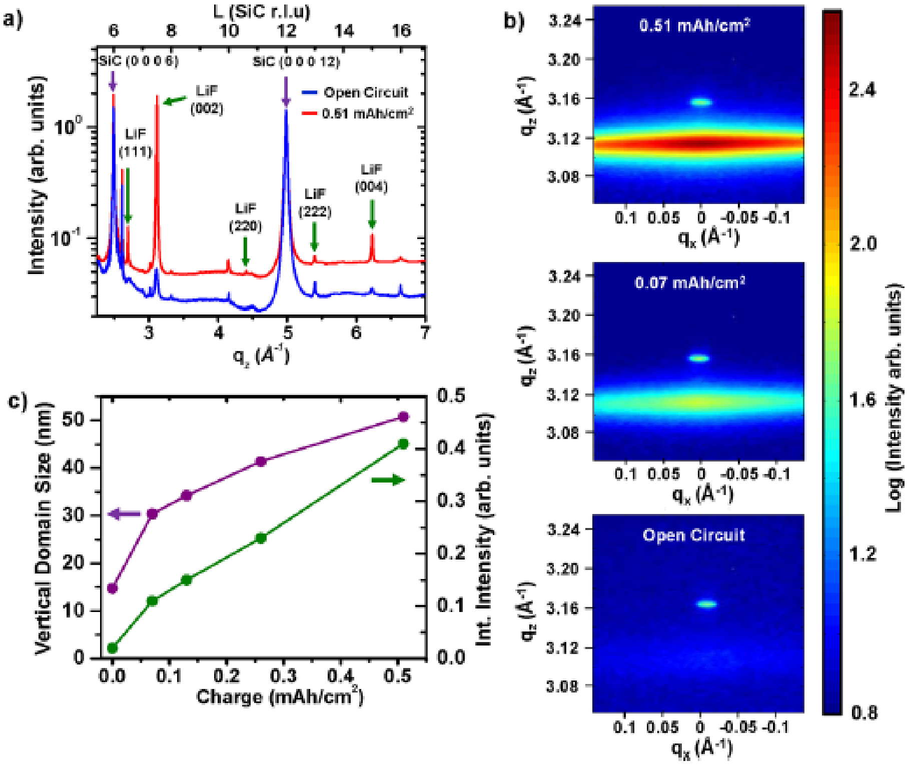

Figure 1.16 X-ray scattering data from an in situ lithiated graphene sample [64].

1.2.3 Alloying/Dealloying based Anodes

Another group of anodes is reacted with lithium based on alloying and dealloying processes. These anodes will storage lithium during cycling when the potential lower than 1 V. The anodes include Si, Ge, Sn, Pb, Bi, Sb, As, P [65] as well as the related metal oxides such as GeO_2, SnO and SnO_2 [66]. Compared with the first category of intercalated compounds (graphite or TiO_2), these anodes have higher lithium storage capabilities due to larger amount of lithium involved in the charging/discharging processes. However, upon cycling, it experiences significant lithium-driven volume changes in the unit cell volume, more than 300% in some cases, which deteriorates the long-term Li storage stability caused by the pulverization of active anodes and loss of electrical contact between active materials and the current collector. To overcome this issue, fabricating nanosized electrodes and hybridized with inert matrix such as carbon and other low active metals are demonstrated as the most effective routes. For this group of anodes, Synchrotron radiation (SR) technique could not only help us to unveil the reaction mechanism between anodes and lithium to explore the intermediate and final lithiated products. More importantly, refer to the composite system; it offers a direction using spectroscopy to understand the interaction between each component and the synergic effect.

Identification of the intermediate lithiated products would help to further confirm the electrochemical reaction and mechanism between lithium and the targets. Yang et al. identify the LiSi phase using SR-XRD [67]. As illustrated in Figure 1.17, Kim and Sohn et al. [68] performed the synchrotron XRD data on ex-situ cycled Si in Ni-Ti alloys substrate. The phase transition of Si to Li-Si alloys and back to Si was elucidated as $Li_{21}Si_5$. Similarly, Lin et al. [69] identify phase transformation for Cu-Sn film upon cycling. The Li_2Sb phase could also be detected in AlSb anodes using same technique [70]. Isabelle et al. [71] applied XAS to define the reaction mechanism between lithium and $CoSb_3$ electrodes. They claimed the intermediate phase of Li_xCoSb_y and distortion for $CoSb_6$ octahedral units. Winter [72] clarified the mechanism of NiSi alloy with lithium using in-situ synchrotron XRD. The reaction mechanism of Sn_2Fe [73], Sb_2S_3 [74] and AgSn [75] are also revealed using synchrotron radiation XRD.

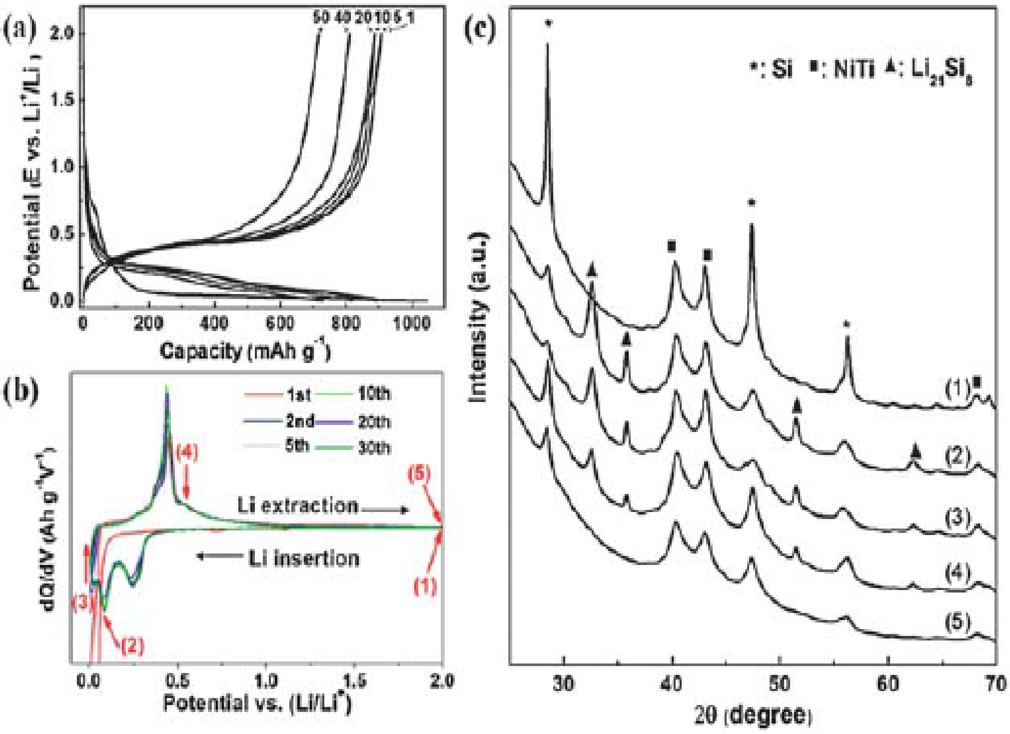

Figure 1.17 a) Voltage profiles and (b) CV curves the Si/NiTi alloy for the several selected cycles. (c) Ex situ synchrotron XRD results of the Si/NiTi alloy at selected potential [68].

Fabricating hybrid nanostructures by embedding active materials into or immobilized onto soft and conductive matrix is an effect route to enhance the cyclability. Employing SR could illustrate the mechanism and interaction between the components thus better examination for the improved electrochemical performances. For Sn@C-Graphene proposed by Zhou et al. [76], synchrotron spectroscopy of XAS confirms chemical bonding and charge transfer exists between SnO_2 and CNTs, resulting charge transfer and intimate chemical bonding. They further conducted Scanning Transmission X-ray Microscopy (STXM) to examine the SnO_2/CNTs at different regions as shown in Figure 1.18, where similar charge transfer and bonding variation between SnO_2 and CNTs are locally monitored and the results matched well with the XAS results [77].

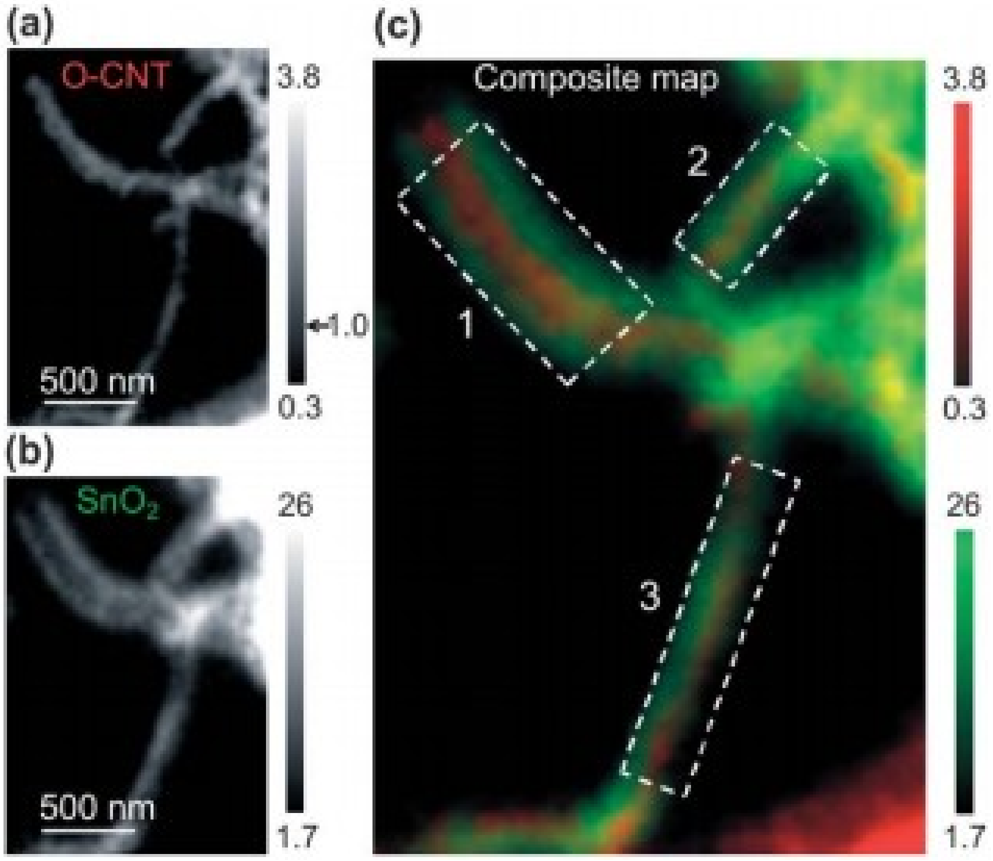

Figure 1.18 STXM chemical maps from individual SnO_2-CNTs: (a) surface oxygen-containing functional groups on O-CNTs (representative of oxidized CNTs), the grey scale is proportional to the extent of surface oxidation (1 represents the intensity prior to SnO_2 coating, intensity greater than 1 shows the effect of oxidation); (b) quantitative chemical map of SnO_2 , the vertical grey scale represents the thickness in nm; (c) the colored composite map for relevant components (red: O-CNT, green:SnO_2). The component maps are rescaled individually in each color channel. Three white dashed boxes labelled 1 to 3 are selected regions of interest for XANES comparison [76].

Amine et al. [78] synthesized of SiO-SnxCoyCz composites using modified ball milling method and then conducted the pair distribution function experiment (Figure 1.19), the local structure further indicated that SiO and SnCoC reacted chemically to form a Si-Sn or Si-C bond rather than bare physical mixture. Park et al. synthesized the Ge-Si thin film and they found the Si-Ge bond and inter-phase areas in the film helped to buffer the volume change in the electrode during cycling as revealed in the XAS spectrum [79]. For Si in Ni-Ti memory alloy, Sohn et al. [68] also found the local structural changes of the Ni–Ti inactive matrix during cycling identified by ex situ-x-ray absorption spectroscopy analyses. For alloyed metal anodes, synchrotron technique could not only identify the phase transformation after lithium alloying and dealloying, but also illustrating the local chemical environment of target elements in composites systems, providing a new direction for revealing mechanism behind its high performances.

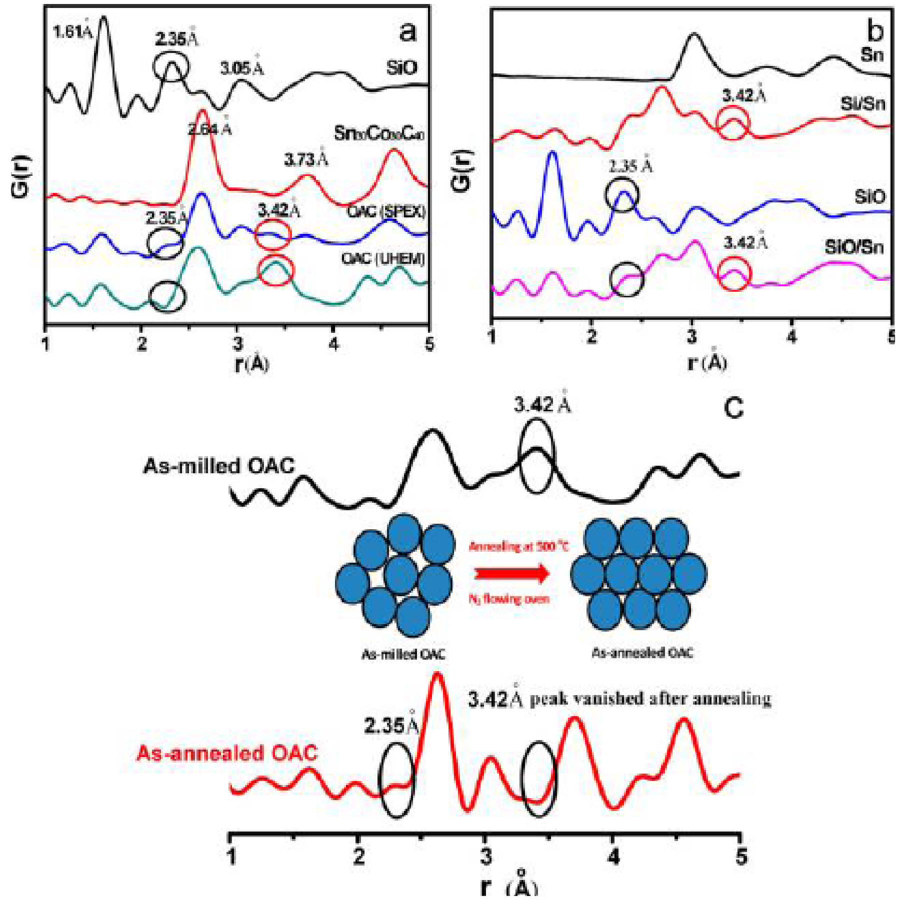

Figure 1.19 Pair distribution function profile of (a) SiO, milled-$Sn_{30}Co_{30}C_{40}$, SPEX OAC, and UHEM OAC; (b) Sn, Si/Sn, SiO, and SiO/Sn; and (c) annealed OAC [78].

Engineering the SEI on alloying/dealloying based anodes is crucial since the nanostuctured anodes have higher amount of SEI due to their high specific surface areas which function as one of the key points for Li-ion battery performance and safety. A recent work reported on SEI film of nano silicon anodes by Kristina revealed different compositions at different stages. At the beginning, the SEI film already formed with composition similar to Sn and Sb based electrodes. Further discharge lead to the formation of Li_2O and LixSiOy, and finally the LiSi alloys, while after full charge, the Li_2O can be removed with no obvious change to the SEI film. A scheme is shown in Figure 1.20 [80].

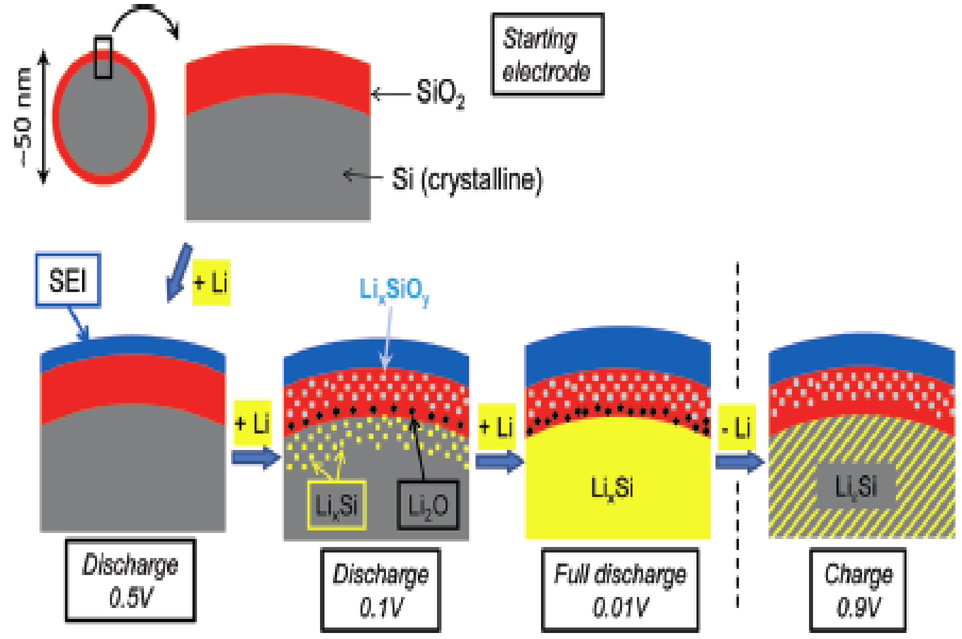

Figure 1.20 Schematic view of the mechanisms occurring at the surface of the silicon nanoparticles; Formation of the SEI at the beginning of discharge; Formation of the Li–Si alloy upon further discharge, together with Li_2O and Li_xSiO_y interfacial phases [80].

1.2.4 Conversion reaction based Anodes

The third group anodes are based on the reaction with lithium ions in the following reactions: $MO + 2Li^+ + 2e^- \longleftrightarrow M + Li_2O$ (M= Mn, Fe, Co, Ni, Cu) [81]

As shown in the above equations, the lithiation and delithiation processes involve the formation/decomposition of Li_2O and oxidation/reduction of metal nanoparticles. It is believed the inert Li_2O could be reduced by the metal catalysts, leading to the recyclable and success for this group of anodes. Since the success of anodes in this category generally deals with nanosized structures and the related catalytic effect, SR could unveil the unclear reaction mechanism in this system and exploit more structure information such as vacancies in nanomaterials to yield fruitful understanding for conversion reaction based anodes.

Upon cycling, conversion reaction based electrodes will endure dramatic structural and chemical changes. Generally, it is hard to distinguish the electrochemical performances caused by the mechanism or original samples' morphologies. Therefore, exploring the reaction mechanism is urgent for exploiting proper high performance anodes considering their high performances. Li et al. reported the synthesis of MnO microspheres for LIBs. With the aid of ex situ XANES and EXAFS study, they found MnO is decomposed to Mn/Li_2O after discharging to 0 V without intermediate phase [82]. Lowe et al. performed the SR XRD and XAS study on the Mn_3O_4 electrode. It is elucidated that the excellent electrochemical features are attributed to specific reactions, including the formation of $LiMn_3O_4$, MnO, metallic Mn, and non-metal-centered reactions as shown in Figure 1.21 [83]. They also demonstrated the necessary for complex conversion reactions in operando characterization to solve electrochemical dependence of reactions in sequence. The Cu_2O film reaction mechanism with lithium is reported by Bijani et al. [84] using XANES and EXAFS, where they claimed the formation of Cu dependent on the thickness of thin film. For FeOx series, Jain et al. [85] studied the hematite behavior upon charging and discharging using XAFS, they found a transformation to a cubic lattice during discharging from the isosbestic points. SR could also be extended to investigate the similar mechanism of metal sulfide or binary metal oxide. Senoh et al applied XANES to explain the reaction mechanism for Al_2S_3, where the surface of Al_2S_3 reacts reversibly during cycling, while the core of Al_2S_3 showed structural irreversibility [86]. They also investigated the gallium sulfide, using XANES and EXAFS, where they found the formation of Li_2S and rebuilding/removing of Ga-S bonds upon cycling [87].

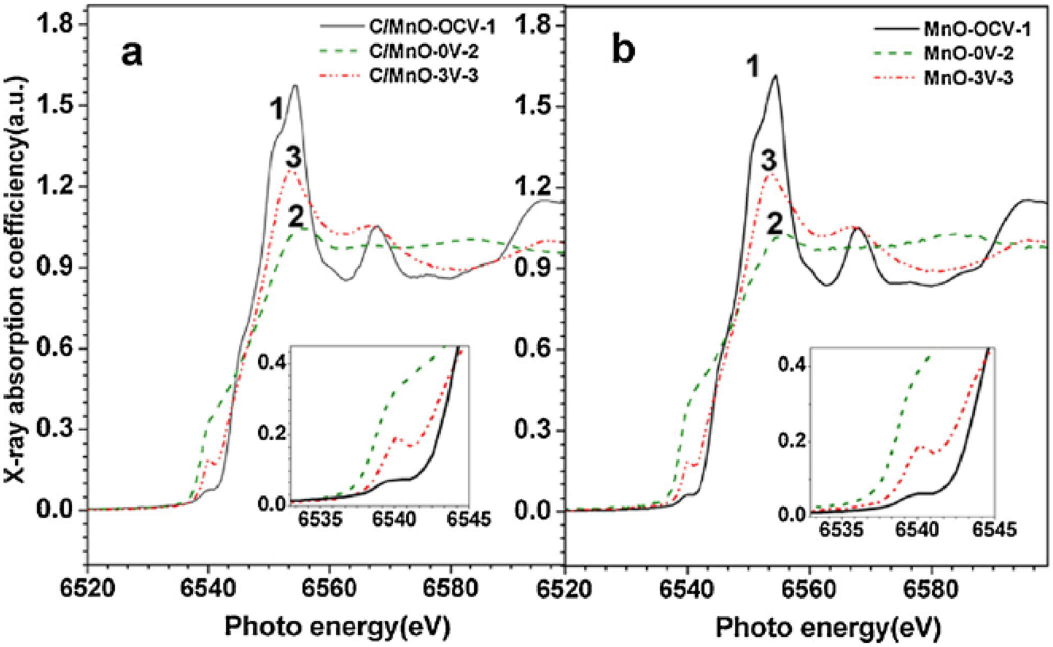

Figure 1.21 The normalized Mn K-edge XANES spectra: (a) the C/MnO electrode, (b) the MnO electrode with different lithiated states. Black line: initial electrode, red line: discharging to 0 V, olive line: charging to 3 V. The inset shows the detail of the pre-edge of the C/MnO and the MnO electrode with different lithiated states [83].

Tarascon et al. [88] studied the $Co_2V_2O_6$ composites, where the valence variation of Co from 2^+ to 0 and 5^+ to 2^+ for V was observed. Grey et al. studied the $Sr_2MnO_2Cu_{3.5}S_3$ compounds by ex situ and in situ Synchrotron X-ray fluorescence imaging coupled with selective micro-X-ray absorption near-edge spectroscopy (XANES) and micro-X-ray diffraction (XRD), it is revealed that Cu metal extrusion happened during conversion, and a segregation between the Cu metal particles and the $Sr_2MnO_2Cu_{3.5-x}LixS_3$ phase starts to be present [89]. The Li insertion/Cu extrusion process is directly observed as shown in Figure 1.22. Based on synchrotron based technique, one can exploit and explain the lithium reaction of conversion-based anodes and image the elemental chemical states upon cycling.

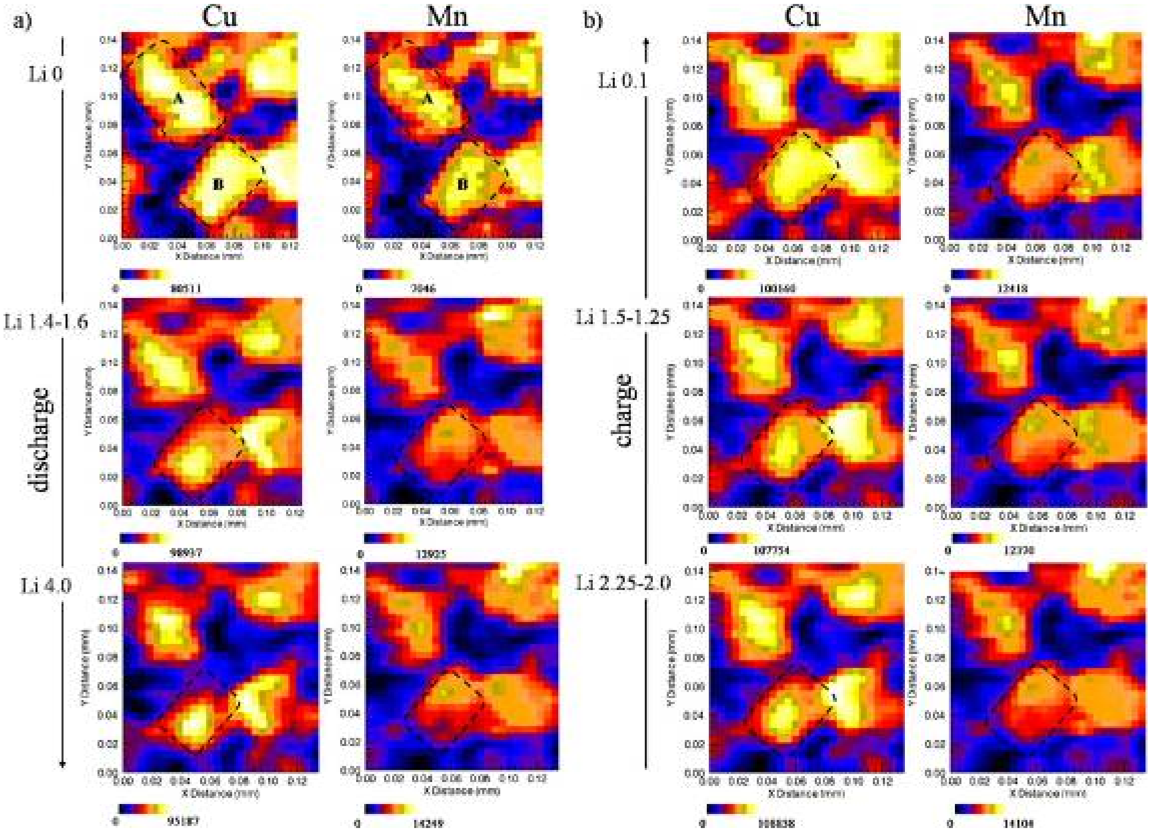

Figure 1.22 X-ray fluorescence compositional maps for Cu Kα and Mn Kα of an in situ $Sr_2MnO_2Cu_{3.5}S_3$/Li cell at different stages of discharge (a) and charge (b) [89].

Due to the small sized conversion anodes, the accompanying defects or cation vacancies are of great importance role for next generation energy storage devices. Jung et al. [90] synthesized the Cu_XO embedded carbon nanofiber composites, applying XANES and EXAFS, they found the CuxO/CNF-800 prepared at intermediate temperature consists of disordered CuO and Cu_2O, where the disordered phase could help to increase the cyclic capability and specific capacity. Chen et al. [91] reported the CoO nano anodes and from XANES and EXAFS data, they conclude the excessive oxygen content in CoO contribute to the origin of the anomalously high capacity. Koo [92] synthesized hollow iron oxide and characterized the oxygen vacancies using XAS and XRD (Figure 1.23). It is proved that the cation vacancies are responsible for the increased capacity in conversion reactions.

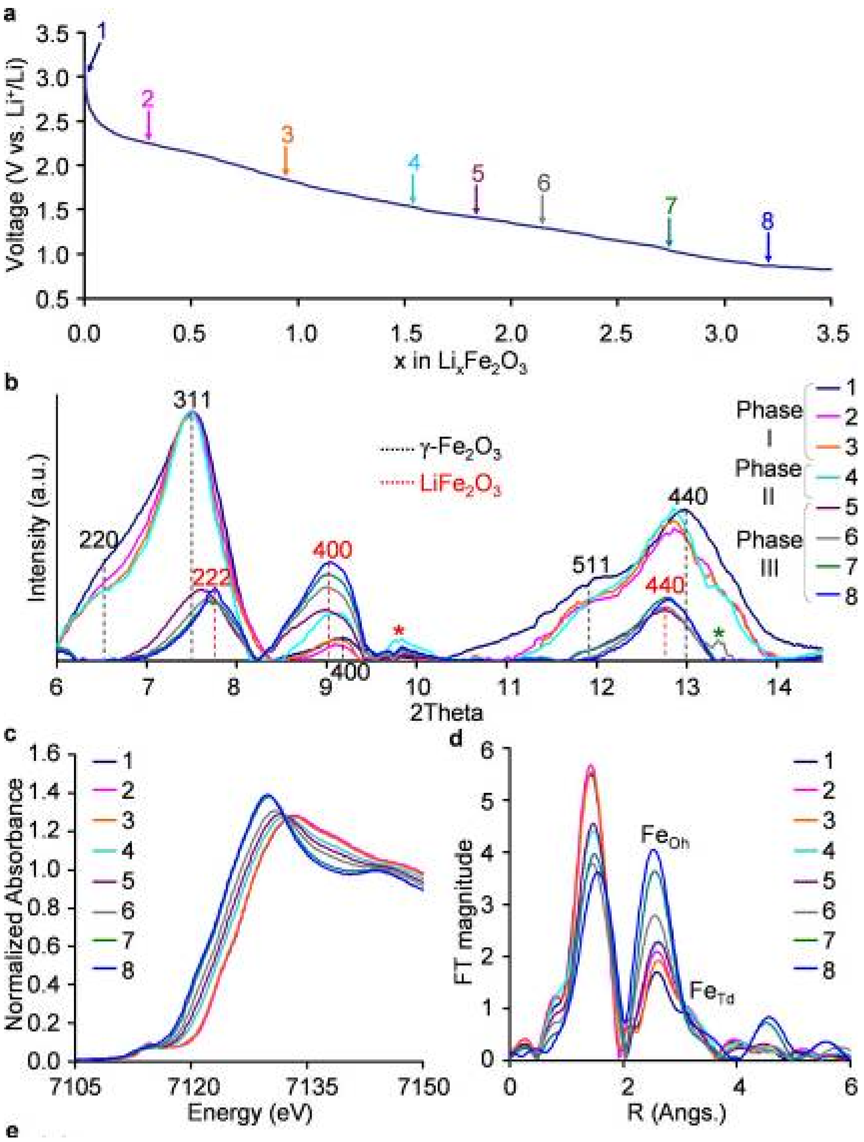

Figure 1.23 (a) Voltage curve at the first discharge state versus metallic Li counter electrode. (b) XRD data (stars correspond to simulated patterns of lithiated rock salt iron oxide. (c) XANES spectra and (d) EXAFS data measured at eight points depicted in the voltage profile shown in (a). The Fourier transforms of k3-weighted Fe EXAFS data were plotted in (d) [92].

Synchrotron technique is widely applied and is proved as powerful technique in study pristine electrodes, composites, SEI and so on, demonstrating its wide adaptability. Combined with synchrotron characterization, detailed mechanism behind the improved electrochemical performances is unveiled according to three typed anodes:

intercalation/deintercalation; alloying/dealloying; conversion based anodes. It is believed that further development both in technique revolution and experiment design will carry forward fruitful advances. The application of SR technique is widely applied but not only limited to LIB fields, it could and already been extended to other systems such as lithium oxygen, metal oxygen, sodium ions batteries and sodium oxygen batteries. Along with the development of instrumentation, SR will play a more and more significant role in energy field.

1.3 Objectives and Scope of the thesis

LIB is a promising energy storage system to be applied in large scale energy devices such as electrical grid, electric vehicles and hybrid electric vehicles to solve the shortage of fossil fuels and environmental concerns. In order to pursuit high performance LIB to satisfy the increasing and urgent demands, the objectives for the thesis are aimed at exploiting high performance nanostructuresd tin-based anodes applied in LIB thus increasing the whole energy densities of batteries. Efforts are devoted to designing and fabricating high performance nanosized tin-based nanostructures including 0D, 1D and 2D nanostructures such as SnO_2 nanoparticles, nanowires and Sn nanoparticles; hierarchical nanocomposites such as sandwiched structures, core-shell structures including SnO_2 nanoparticles on Graphene, carbon coated SnO_2 nanowires on Graphene, core-shelled Sn@C nanoparticles on Graphene and SnO_2@Al_2O_3 nanoparticles. Another effort was also applied to exploit the electronic, chemical states of the interested tin-based nanostructures and also the charge transfer and chemical bonding in nanocomposite Sn anodes using synchrotron based XAFS spectra, providing spectroscopic view combined with extensive other characterizations to unveil the mechanism behind the excellent performances.

This thesis is organized as follows:

Chapter 1 gives the general background introduction for lithium ion batteries including its working principles and applications as well as the challenges. The solution of nanostuctured tin-based anodes is also proposed. Further, the application of synchrotron radiation studies of anodes in lithium-ion batteries is summarized. The objectives and scope for this thesis are presented.

Chapter 2 lists the methodologies. Detailed synthesis routes, characterization techniques including structural characterizations and synchrotron technique as well as electrochemical measurements are introduced.

Chapter 3 describes the synthesis of SnO_2 nanowires directly on two different substrates-stainless steel and copper via a facile hydrothermal method. The growth mechanism is further studied based on morphology revolution at various reaction time. The electronic structure and luminescence properties are illustrated by XANES and XEOL, respectively. It is illustrated that the synthesized SnO_2 nanowries could also be applied as anodes for application in LIB.

Chapter 4 presents SnO_2 nanoparticles/graphene composites fabricated by a one-step microwave-assisted hydrothermal method. XANES reveals the electronic structure of the composites showing the strong interaction between SnO_2 and graphene. The electrochemical results demonstrate that SnO_2/graphene composite is a promising anode material in high-performance lithium ion batteries.

Chapter 5 reports the preparation of sandwiched graphene/SnO_2 nanorod/carbon hierarchical nanocomposites using a seed assisted hydrothermal route and nanocarbon coating. Benefiting from the advanced sandwiched hierarchical structure and the intimate chemical bonding between each layers unveiled by electronic structure study using XANES, the as-prepared nanocomposites exhibit excellent LIB performances.

Chapter 6 depicts the design of the hierarchical carbon encapsulated tin (Sn@C) embedded graphene nanosheets (GNs) composites. Applying chemical vapor deposition (CVD) procedure, the core-shelled nanocomposites are successfully prepared. XANES and EXAFS identified the electronic structure and chemical environment of the composites. The composites exhibit superior cyclic and rate capabilities than current state of art anodes.

Chapter 7 describes a comparative study of two different carbon sheath tin core nanowires obtained on copper and stainless steel, respectively. The phase composition, morphologies, electronic structure and chemical mapping are further illustrated using laboratory structural characterization technique and synchrotron techniques. The obtained core-shell nanowires thus obtained exhibit stable lithium storage capabilities but different storage capacity due to different chemical compositions.

Chapter 8 gives a case study of atomic layer deposition technique applied on various nanosized SnO_2 anodes. A systematic study of the effect of Al_2O_3 coating thickness on electrochemical performances of various sized SnO_2 electrodes has been studied in this chapter. The results show that improved electrochemical performances compared with bare SnO_2 electrodes could be obtained using optimized Al_2O_3 coating.

Chapter 9 summarizes the main conclusions and contributions of the thesis and a description of future work.

1.4 References

[1] Vincent, C. A.; Scrosati, B. Modern Batteries: An Introduction to Electrochemical Power Sources1997: E. Arnold.

[2] Linden, D.; Reddy, T. B. Handbook of batteries2002: McGraw-Hill.

[3] Nagaura, T.; Tozawa, K. Prog. Batteries Sol. Cells, 1990, 9, 209.

[4] Wakihara, M.; Yamamoto, O. Li-Ion Batteries 1998: Wiley-VCH.

[5] Van Schalkwijk, W. A.; Scrosati, B. Advances in Lithium-Ion Batteries 2002: Kluwer Academic/Plenum Publishers.

[6] Nazri, G. A.; Pistoia, G. Lithium Batteries: Science and Technology2003: Kluwer Academic Publishers.

[7] Ozawa, K. Lithium Ion Rechargeable Batteries 2009: Wiley-VCH.

[8] Alifantis, K. E.; Hackney, S. A.; Vasant Kumar, R. High Energy Density Lithium Batteries: Materials, Engineering, Applications 2010: Wiley-VCH.

[9] Tarascon, J. M.; Armand, M. Nature, 2001, 414, 359.

[10] Arico, A. S.; Bruce, P.; Scrosati, B.; Tarascon, J. M.; Van Schalkwijk, W. Nat. Mater, 2005, 4, 366.

[11] Armand, M.; Tarascon, J. M. Nature, 2008, 451, 652.

[12] Huang, C. K.; Sakamoto, J. S.; Wolfenstine, J.; Surampudi, S. J. Electrochem Soc., 2000, 147, 2893.

[13] Zaghib, K.; Dontigny, M.; Guerfi, A.; Charest, P.; Rodrigues, I.; Mauger, A.; Julien, C. M. J. Power Sources, 2011, 196, 3949.

[14] Hatchard, T. D.; Dahn, J. R. J. Electrochem Soc., 2004, 151, A838.

[15] Jung, H. G.; Kim, J.; Scrosati, B.; Sun, Y. K. J. Power Sources, 2011, 196, 7763.

[16] Choi, W.; Lee, J. Y.; Jung, B. H.; Lim, H. S. J. Power Sources, 2004, 136, 154.

[17] Moon, T.; Kim, C.; Hwang, S. T.; Park, B. Electrochem. Solid St., 2006, 9, A408.

[18] Wang, Z. Y.; Chen, G.; Xia, D. G. J. Power Sources, 2008, 184, 432.

[19] Read, J.; Foster, D.; Wolfenstine, J.; Behl, W. J. Power Sources, 2001, 96, 277.

[20] Besenhard, J. O.; Yang, J.; Winter, M. J. Power Sources, 1997, 68, 87.

[21] Choi, W.; Lee, J. Y.; Jung, B. H.; Lim, H. S. J. Power Sources, 2004, 136, 154.

[22] Chan, C. K.; Peng, H. L.; Liu, G.; McIlwrath, K.; Zhang, X. F.; Huggins, R. A.; Cui, Y. Nat. Nanotechnol., 2008, 3, 31.

[23] Lou, X. W.; Li, C. M.; Archer, L. A. Adv. Mater., 2009, 21, 2536.

[24] Lin, Y. S.; Duh, J. G.; Hung, M. H. J. Phys. Chem. C, 2010, 114, 13136.

[25] Noh, M.; Kwon, Y.; Lee, H.; Cho, J.; Kim, Y.; Kim, M. G. Chem. Mater., 2005, 17, 1926.

[26] Yu, Y.; Gu, L.; Zhu, C. B.; van Aken, P. A.; Maier, J. J. Am. Chem. Soc., 2009, 131, 15984.

[27] Ying, Z.; Wan, Q.; Song, Z. T.; Feng, S. L. Nanotechnology, 2004, 15, 1682.

[28] Ying, Z.; Wan, Q.; Cao, H.; Song, Z. T.; Feng, S. L. Appl. Phys, Lett., 2005, 87, 113108.

[29] Park, M. S.; Wang, G. X.; Kang, Y. M.; Wexler, D.; Dou, S. X.; Liu, H. K. Angew. Chem. Int. Edit., 2007, 46, 750.

[30] Ahn, J. H.; Kim, Y. J.; Wang, G. J. Alloy. Compd., 2009, 483, 422.

[31] Ko, Y. D.; Kang, J. G.; Park, J. G.; Lee, S.; Kim, D. W. Nanotechnology, 2009, 20, 455701.

[32] Lai, M.; Lim, J. H.; Mubeen, S.; Rheem, Y.; Mulchandani, A.; Deshusses, M. A.; Myung, N. V. Nanotechnology 2009, 20, 185602.

[33] Chou, S. L.; Wang, J. Z.; Liu, H. K.; Dou, S. X. Electrochem. Commun., 2009, 11, 242.

[34] Kim, H.; Cho, J. J. Mater. Chem., 2008, 18, 771.

[35] Shi, S. L.; Liu, Y. G.; Zhang, J. Y.; Wang, T. H. Chinese Phys. B, 2009, 18, 4564.

[36] Liu, J. P.; Li, Y. Y.; Huang, X. T.; Ding, R. M.; Hu, Y. Y.; Jiang, J.; Liao, L. J. Mater. Chem., 2009, 19, 1859.

[37] Ji, X. X.; Huang, X. T.; Liu, J. P.; Jiang, J.; Li, X.; Ding, R. M.; Hu, Y. Y.; Wu, F.; Li, Q. Nanoscale Res. Lett., 2010, 5, 649.

[38] Finke, A.; Poizot, P.; Guery, C.; Tarascon, J. M. J. Electrochem. Soc., 2005, 152, A2364.

[39] Dong, Q. F.; Wu, C. Z.; Jin, M. G.; Huang, Z. C.; Zheng, M. S.; You, J. K.; Lin, Z. G. Solid State Ionics, 2004, 167, 49.

[40] Wen, Z. H.; Wang, Q.; Zhang, Q.; Li, J. H. Adv. Funct. Mater., 2007, 17, 2772.

[41] Wang, Z. Y.; Chen, G.; Xia, D. G. J. Power Sources, 2008, 184, 432.

[42] Paek, S. M.; Yoo, E.; Honma, I. Nano Lett., 2009, 9, 72.

[43] Yao, J.; Shen, X. P.; Wang, B.; Liu, H. K.; Wang, G. X. Electrochem. Commun., 2009, 11, 1849.

[44] Lian, P. C.; Zhu, X. F.; Liang, S. Z.; Li, Z.; Yang, W. S.; Wang, H. H. Electrochim. Acta., 2011, 56, 4532.

[45] Koch, E. E.; Eastman, D. E.; Farge, Y. Synchrotron radiation-a powerful tool in science1983: North-Holland Publishing Company.

[46] Rowe, E. M.; Mills, F. E. Particle Accelerators, 1973, 4, 211.

[47] Sayers, D.; Stern, E.; Lytle, F. Phys. Rev. Lett., 1971, 27, 1204.

[48] http://www.lightsource.ca/experimental/images/CLS_Experimental_Hall_2011.png

49] Augustsson, A.; Herstedt, M.; Guo, J. H.; Edstrom, K.; Zhuang, G. V.; Ross, P. N.; Rubensson, J. E.; Nordgren, J. Phys. Chem. Chem. Phys., 2004, 6, 4185.

[50] Verma, P.; Maire, P.; Novak, P. Electrochim. Acta., 2010, 55, 6332.

[51] Schulke, W.; Berthold, A.; Kaprolat, A.; Guntherodt, H. Phys. Rev. Lett., 1988, 60, 2217.

[52] Balasubramanian, M.; Johnson, C. S.; Cross, J. O.; Seidler, G. T.; Fister, T. T.; Stern, E. A.; Hamner, C.; Mariager, S. O. Appl. Phys. Lett., 2007, 91, 031904.

[53] Henningsson, A.; Rensmo, H.; Sandell, A.; Siegbahn, H.; Sodergren, S.; Lindstrom, H.; Hagfeldt, A. J. Chem. Phys., 2003, 118, 5607.

[54] Richter, J. H.; Henningsson, A.; Karlsson, P. G.; Andersson, M. P.; Uvdal, P.; Siegbahn, H.; Sandell, A. Phys. Rev. B, 2005, 71, 235418.

[55] Wagemaker, M.; Lutzenkirchen-Hecht, D.; Keil, P.; van Well, A. A.; Frahm. R. Phys. B, 2003, 336, 118.

[56] Lafont, U.; Carta, D.; Mountjoy, G.; Chadwick, A. V.; Kelder, E. M. J. Phys. Chem. C, 2010, 114, 1372.

[57] Okumura, T.; Fukutsuka, T.; Yanagihara, A.; Orikasa, Y.; Arai, H.; Ogumi, Z.; Uchimoto, Y. J. Mater. Chem., 2011, 21, 15369.

[58] Okumura, T.; Fukutsuka, T.; Yanagihara, A.; Orikasa, Y.; Arai, H.; Ogumi, Z.; Uchimoto, Y. Chem. Mater., 2011, 23, 3636.

[59] Ra, W.; Nakayama, M.; Cho, W.; Wakihara, M.; Uchimoto, Y. Phys. Chem. Chem. Phys., 2006, 8, 882.

[60] Ra, W.; Nakayama, M.; Uchimoto, Y.; Wakihara, M. J. Phys. Chem. B, 2005, 109, 1130.

[61] Xiong, H.; Yildirim, H.; Shevchenko, E. V.; Prakapenka, V. B.; Koo, B.; Slater, M. D.; Balasubramanian, M.; Sankaranarayanan, S. K. R. S.; Greeley, J. P.; Tepavcevic, S.; Dimitrijevic, N. M.; Podsiadlo, P.; Johnson, C. S.; Rajh, T. J. Phys. Chem. C, 2012, 116, 3181.

[62] Herstedt, M.; Andersson, A. M.; Rensmo, H.; Siegbahn, H.; Edstrom, K. Electrochim. Acta, 2004, 49, 4939.

[63] Malmgren, S.; Rensmo, H.; Gustafsson, T.; Gorgoi, M.; Edström. K. ECS transactions, 2010, 25, 201.

[64] Chattopadhyay, S.; Lipson, A. L.; Karmel, H. J.; Emery, J. D.; Fister, T. T.; Fenter, P. A.; Hersam, M. C.; Bedzyk, M. J. Chem. Mater., 2012, 24, 3038.

[65] Park, C. M.; Kim, J. H.; Kim, H.; Sohn, H. J. Chem. Soc. Rev., 2010, 39, 3115.

[66] Ning, J. J.; Dai, Q. Q.; Jiang, T.; Men, K. K.; Liu, D. H.; Xiao, N. R.; Li, C. Y.; Li, D. M.; Liu, B. B.; Zou, B.; Zou, G. T.; Yu, W. W. Langmuir, 2009, 25, 1818.

[67] X. Q. Yang, J. McBreen, W. S. Yoon, M. Yoshio, H. Y. Wang, K. Fukuda and T. Umeno, Electrochem. Commun., 2002, 4, 893.

[68] H. Jung, Y. U. Kim, M. S. Sung, Y. Hwa, G. Jeong, G. B. Kim and H. J. Sohn, J. Mater. Chem., 2011, 21, 11213.

[69] Lin, Y. S.; Duh, J. G.; Sheu, H. S. J. Alloy. Compd., 2011, 509, 123.

[70] Stjerndahl, M.; Bryngelsson, H.; Gustafsson, T.; Vaughey, J. T.; Thackeray, M. M.; Edstrom, K. Electrochim. Acta., 2007, 52, 4947.

[71] Devos, I.; Womes, M.; Heilemann, M.; Olivier-Fourcade, J.; Jumas, J.; Tirado, J. L. J. Mater. Chem., 2004, 14, 1759.

[72] Liu, W. R.; Wu, N. L.; Shieh, D. T.; Wu, H. C.; Yang, M. H.; Korepp, C.; Besenhard, J. O.; Winter, M. J. Electrochem. Soc., 2007, 154, A97.

[73] Yoon, S.; Lee, J. M.; Kim, H.; Im, D. M.; Doo, S. G.; Sohn, H. J. Electrochim. Acta, 2009, 54, 2699.

[74] Park, C. M.; Hwa, Y.; Sung, N. E.; Sohn, H. J. J. Mater. Chem., 2010, 20, 1097.

[75] Ronnebro, E.; Yin, J. T.; Kitano, A.; Wada, M.; Tanase, S.; Sakai, T. J. Electrochem. Soc., 2004, 151, A1738.

[76] Zhou, J. G.; Fang, H. T.; Maley, J. M.; Ko, J.Y.P.; Murphy, M.; Chu, Y.; Sammynaiken, R.; Sham, T. K. J. Phys. Chem. C, 2009, 113, 6114.

[77] Zhou, J. G.; Wang, J.; Fang, H. T.; Sham, T. K. J. Mater. Chem., 2011, 21, 5944.

[78] Liu, B.; Abouimrane, A.; Ren, Y.; Balasubramanian, M.; Wang, D. P.; Fang, Z. G. Z.; Amine, K. Chem. Mater., 2012, 24, 4653.

[79] Hwang, C. M.; Park, J. W. J. Power Sources, 2011, 196, 6772.

[80] Philippe, B.; Dedryvere, R.; Allouche, J.; Lindgren, F.; Gorgoi, M.; Rensmo, H.; Gonbeau, D.; Edstrom, K. Chem. Mater., 2012, 24, 1107.

[81] Reddy, M. V.; Subba Rao, G. V.; Chowdari, B. V. R. Chemical Reviews, 2013, dx.doi.org/10.1021/cr3001884

[82] Zhong, K. F.; Zhang, B.; Luo, S. H.; Wen, W.; Li, H.; Huang, X. J.; Chen, L. Q. J. Power Sources, 2011, 196, 6802.

[83] Lowe, M. A.; Gao, J.; Abruna, H. D. J. Mater. Chem. A, 2013, 1, 2094.

[84] Bijani, S.; Gabas, M.; Subias, G.; Garcia, J.; Sanchez, L.; Morales, J.; Martinez, L.; Ramos-Barrado, J. R. J. Mater. Chem., 2011, 21, 5368.

[85] Jain, G.; Balasubramanian, M.; Xu, J. J. Chem. Mater., 2006, 18, 423.

[86] Senoh, H.; Takeuchi, T.; Kageyama, H.; Sakaebe, H.; Yao, M.; Nakanishi, K.; Ohta, T.; Sakai, T.; Yasuda, K. J. Power Sources, 2010, 195, 8327.

[87] Senoh, H.; Kageyama, H.; Takeuchi, T.; Nakanishi, K.; Ohta, T.; Sakaebe, H.; Yao, M.; Sakai, T.; Yasuda, K. J. Power Sources, 2011, 196, 5631.

[88] laruelle, S.; Poizot, P.; Baudrin, E.; Briois, V.; Touboul, M.; Tarascon, J. M. J. Power Sources, 2001, 97-98, 251.

[89] Robert, R.; Zeng, D. L.; Lanzirotti, A.; Adamson, P.; Clarke, S. J.; Grey, C. P. Chem. Mater., 2012, 24, 2684.

[90] Jung, H. R.; Cho, S. J.; Kim, K. N.; Lee, W. J. Electrochim. Acta, 2011, 56, 6722.

[91] Chen, C. H.; Hwang, B. J.; Do, J. S.; Weng, J. H.; Venkateswarlu, M.; Cheng, M. Y.; Santhanam, R.; Ragavendran, K.; Lee, J. F.; Chen, J. M.; Liu, D. G. Electrochem. Commun., 2010, 12, 496.

[92] Koo, B.; Xiong, H.; Slater, M. D.; Prakapenka, V. B.; Baasubramanian, M.; Podsiadlo, P.; Johnson, C. S.; Rajh, T.; Shevchenko, E. V. Nano Lett., 2012, 12, 2429.

Chapter 2

2 Experimental, Characterization and Electrochemical Measurements

2.1 Experimental Method

2.1.1 Synthesis of SnO_2 Nanowires on Different Substrates via Hydrothermal Route

The substrates applied here are copper and stainless steel. In a typical experiment to grow SnO_2 nanowires (SnO2 NWs) on stainless steel (SS 304L), 350.58 mg $SnCl_4 \cdot 5H_2O$ (1 mmol) and 700 mg NaOH (17.5 mmol) were dissolved in a mixture of a 40 mL water/ethanol (1:3) solution. To conduct the synthesis, the alkaline PH value around 12 was needed. After sonication and continuous stirring for about 10 minutes, transparent solution was obtained. Then 10 mL of the solution was transferred to a Telfon-lined autoclave (20 mL), where the substrate, cleaned by acetone beforehand, was laid flat at the bottom of the autoclave. The solution was subsequently heated to 200 ^{o}C at a rate of 5 ^{o}C per minute from room temperature, then maintained for 20 h and then cooled down to room temperature. Once the reaction was completed, the SnO_2 covered substrate was rinsed several times with distilled water and ethanol, followed by final drying at 60 ^{o}C overnight. Similar procedures were used for SnO_2 NWs grow on copper foil. After the alkaline hydrothermal process, both two substrates' surfaces are covered with white-gray products. A schematic representation for the preparation of SnO_2 NWs is given in Figure 2.1 [1].

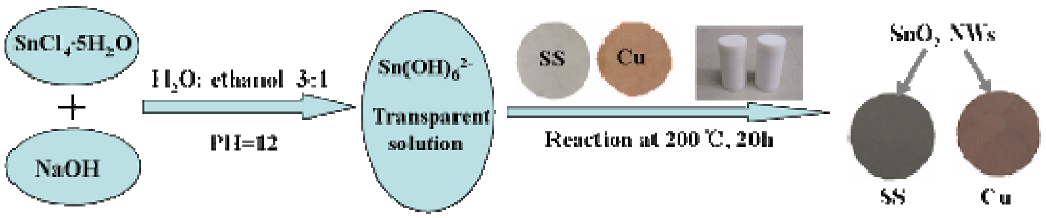

Figure 2.1 Synthetic drawing of the preparation of SnO_2 NWs on substrates [1]

2.1.2 Synthesis of SnO_2 and SnO_2/Graphene via Microwave-Assisted Hydrothermal Method

For the synthesis of SnO_2/Graphene composites, the applied graphene were synthesized using a modified Hummers method followed by the rapid heating of graphene oxide at 1050 ^oC for 30 s under Ar atmosphere [2]. SnO_2/graphene composites were synthesized by a rapid MWHM method. In a typical process, 22.5 mg $SnCl_2 \cdot 2H_2O$ was dissolved in 10 ml water. Then 8.25 mg of the as-prepared GNSs was added in the solution followed by vigorous ultrasonication for 2 h. The resulting black suspension was transferred and sealed in a high pressure Teflon vessel. These vessels were anchored to a rotor which was placed on a turntable in a microwave reaction system (Anton Paar Synthos 3000). The turntable was kept spun to ensure uniform heating during the reaction. The power was set at 1200 W with 8 minutes ramping time to reach 200 ^oC, and maintained at this temperature for 1 h before the system was cooled down to room temperature and the SnO_2/Graphene nanocomposites were collected. The pressure was below 20 bars throughout the synthesis. The as-synthesized product was first washed with ethanol and water several times to remove the Cl^- by centrifugation, and followed by vacuum drying in an oven at 80 ^oC overnight. Pure SnO_2 nanoparticles were prepared under the same parameters except the addition of GNSs. For the synthesis of SnO_2 nanoparticles, the procedures are similar except the addition of graphene nanosheets. A schematic of the synthesis process is depicted in Figure 2.2 [3]. It is shown that the $SnCl_2 \cdot 2H_2O$ will first react with water to hydrolysis and then react witht the residue O_2 in the chamber to form SnO2. After that the product will be collected and washed several times thoroughly with distilled water and ethanol to remove the Cl^-, and then dryied in the oven at 90 ^oC overnight. The collected white SnO_2 nanoparticles are ready for use without further treatment.

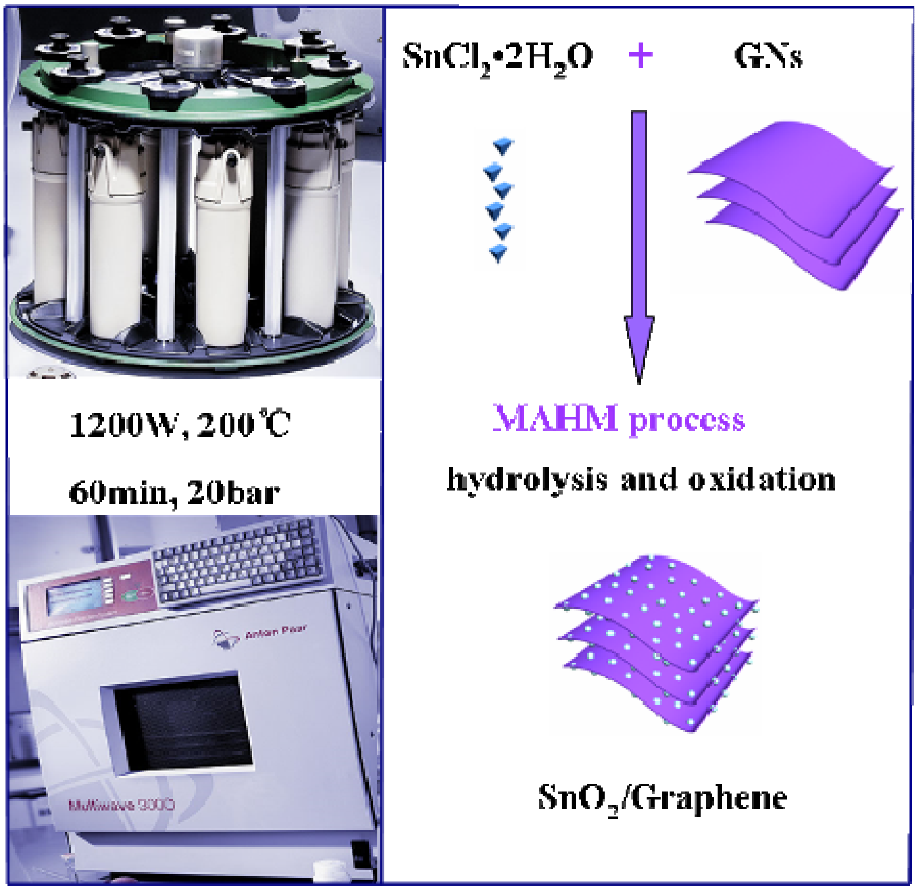

Figure 2.2 Illustration of (a) microwave-assisted hydrothermal system and (b) synthesis process of SnO_2/graphene nanocomposites [3].

2.1.3 Synthesis of Sn@C-Graphene via Chemical Vapor Deposition (CVD) Route

Graphene were prepared applying a modified Hummers method to get graphene oxide first, and then performing the rapid heating of graphene oxide at 1050 °C at Ar atmosphere [2]. After that, the hierarchical Sn@C-Graphene (Sn@C-GNs) nanocomposites are obtained using chemical vapor deposition method, as shown in Figure 2.3. In a typical process of synthesizing Sn@C-GNs composites, the as prepared 80 mg GNs and 400 mg SnO_2 (325mesh, Aldrich) were ultrasonically dispersed into 40 mL ethanol solution for 30 min first. Then the suspension were filtered and dried at 80 °C overnight to collect SnO_2/GNs composites. The as-obtained SnO_2/GNs were put in a tube furnace and heat treated at 800 °C for 30min at 200 sccm gas mixtures (10% ethylene and

90% argon) atmosphere to realize the in-situ formation of Sn@C-GNs composites. After cooling to room temperature with pure Ar, Sn@C-GNs nanostructure was obtained. For Sn@C composites, the procedures are the same except the addition of GNs [4].

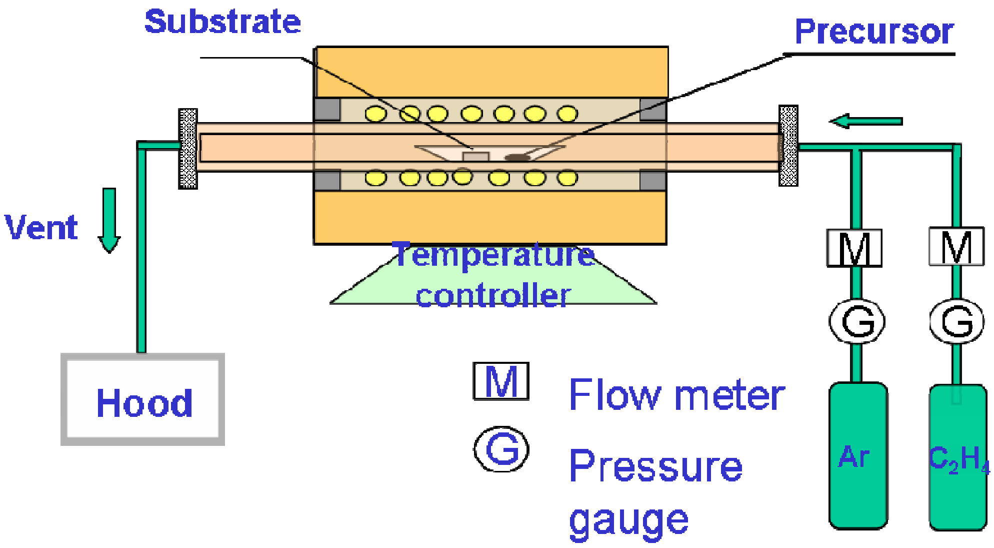

Figure 2.3 Scheme for CVD set up to grow Sn@C-GNs composites [4]

2.1.4 Syntheisis of Sn@C Nanocables on Metallic Foil Substrates via CVD Route

The Sn@C nanocables were prepared following the procedures below: 80 mg SnO_2 nanoparticles (325 mesh, Aldrich) were vigorously sonicated in 20 mL ethanol for 2 h to get an suspension. In the meantime, substrates (copper or stainless steel, 9/16 inch in diameter) were cleaned by acetone and ethanol for several times, and then pressed at 6000 LBs for 3 minutes using hot press devices to get a flat surface. Then the suspension are dropped slowly onto the surface of substrates and baked under 80 ^{o}C in the oven for 5 minutes. The dropping and baking steps are repeated until the surfaces of the substrates are totally covered with a uniform thickness under observation. The as-obtained SnO_2 deposited substrates were transferred to a tube furnace and heat treated at 800 ^{o}C for 1h at gas mixtures (ethylene: argon = 1:9) atmosphere. The Sn@C nanocables were obtained after cooling down to room temperature.

2.1.5 Synthesis of Al_2O_3 Coated SnO_2 via Atomic Layer Deposition (ALD) Method

SnO_2 nanoparticles with three different sizes are prepared first and then made them electrodes followed by ALD coating. At first, different sized SnO_2 nanoparticles are obtained using microwave assisted hydrothermal route followed by heat treament. 2 mmol $SnCl_4$ was dissolved in 10 mL aqueous solution and vigorously stirred for 30 minutes to obtain clear solution. Then the transparent solution was transferred into 20 mL high pressure microwave- assisted Teflon-lined autoclave (Anton Paar Synthos 3000). The solution was subsequently heated to 120 ^{o}C and kept for 20 minutes. After cooling to room temperature, the obtained samples are rinsed with large amount of distilled water and ethanol. Then the as-obtained products were collected after final drying at 100 ^{o}C overnight for use in next step. To get three different sized SnO_2 nanoparticles, the products are annealed in tube furnace at different temperatures for 2h under Ar. Then, the working electrodes are composed of the SnO_2 nanomaterials, conductive carbon black and polyvinylidene fluoride (PVDF) in a weight ratio of 8:1:1. The slurry obtained with N-methylpyrrolidinone (NMP) solvent was uniformly cast on a copper foil and dried at 70 ^{o}C under vacuum overnight. The as-prepared electrodes are ready for ALD coating without further treatment. Finally, ALD-Al_2O_3 was coated directly on SnO_2 electrodes in an ALD reactor (Savannah 100, Cambridge Nanotechnology Inc., USA) using Trimethylaluminum (TMA) as Al precursor and H_2O as the oxidizer. The deposition temperature was set as 100 ^{o}C. Different ALD cycles (2, 5 and 20 cycles) were designed to get different coating layer thickness. The coated electrodes were applied for lithium ion battery testing without further treatment. The ALD device is shown in Figure 2.4.

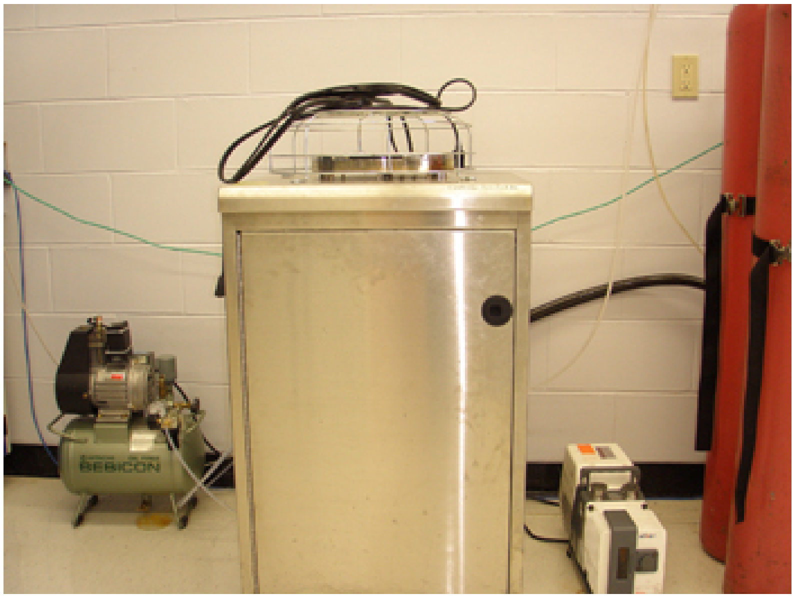

Figure 2.4 Experimental set up for ALD device

2.2 Characterizations

2.2.1 Structural Characterizations (SEM, TEM, XRD, EDX, XPS, RAMAN)

To identify the phase composition, morphology and crystalline of the as-obtained samples, various techniques were applied. Samples in this thesis were characterized by the following structural characterization techniques: X-ray diffraction (XRD, Rigaku RU-200BVH with a Co-Kα source (λ=1.7892 Å)) to determine the crystal's atomic and molecular structure through measurement of angles and intensities of the diffracted beams; field-emission scanning electron spectrometry (FE-SEM, Hitachi 4800S, operation voltage at 5 kV) coupled with dispersive spectroscopy (EDX, operation voltage at 20 kV) to generate the surface topography and composition of the samples using scanned and focused electron beam; transmission electron microscope (TEM, Hitachi H-7000, operated at 100 kV); high-resolution transmission electron microscope (HRTEM, JEOL 2010 FEG microscope, operated at 200 kV) including scanning transmission electron microscopy (STEM), high angle annular dark field (HAADF) to form an image via the interaction of the electrons passed through the specimen; raman micro-spectroscopy (HORIBA Scientific LabRAM HR Raman spectrometer) under ambient condition with an incident laser beam at 532.03 nm to observe vibration rotational and low-frequency modes in the materials; thermogravimetric analysis (TGA; Netzsch) to thermal analysis the physical and chemical properties alternation through measuring the increased temperature versus the mass loss or heat flow; X-ray photoelectron spectroscopy (XPS, Kratos Axis Ultra Al at 14 kV) to quantitatively analysis the elemental composition, oxidation and electronic states at the surface of the materials.

2.2.2 X-ray Absorption Fine Structure

X-ray absorption fine structure (XAFS) characterizes the electronic structure of element of interest via measuring the X-ray absorption coefficieny (μ) across the desired excitation energy range (often across an absorption edge). According to Beer's law, the relation between intensity of incident light (Io), transmitted light I with defined the sample thickness (t) and μ could be interpreted as below:

$$I = Io\, e^{-\mu t} \qquad (Eq\ 2.1)$$

XAFS monitor the modulation of μ and it is composed of two parts: X-ray Absorption Near Edge Structures (XANES) and Extended X-ray Absorption Fine Structures (EXAFS). XANES describes the modulation of the absorption coefficient of an element in a chemical environment in the region of 20 eV below and to ~ 50 eV above the absorption edge. It arises from the dipole excitation of a core electron into previously unoccupied electronic states in the valence region and beyond. Since valence states are chemically sensitive, XANES probes the local chemistry (population and symmetry of unoccupied electronic states, e.g. LUMO in molecules and the conduction band in semiconductors) of the absorbing atom. Using a tunable synchrotron light source, one can probe the local symmetry and occupation (densities of states) of these states including surface and defect states by tracking the absorption coefficient of the element of interest by scanning the photon energy across the absorption edge [5]. EXAFS lies in the region from 50 eV to as much as 1000 eV above the threshold. It mainly comes from the interference of the outgoing and back scattered photoelectron at the absorbing atom via single scattering due to the higher kinetic energy which is back scattered by neighboring atoms with a bond length below 2 to 3 atomic shells [6, 7]. As shown in Figure 2.5 [8], in the free atom model, the core electron of the element is excited to the previously unoccupied electronic states, illustrating a single edge jump with a monotonic decrease. The spectra features can be used as fingerprint and thus is element specific. For the diatomic model, the emitted electrons or photons will be scattered by the neighboring atoms, resulting a modulation (oscillation) of the absorption coefficient. Thus the spectrum could tell us information of the chemical environment.

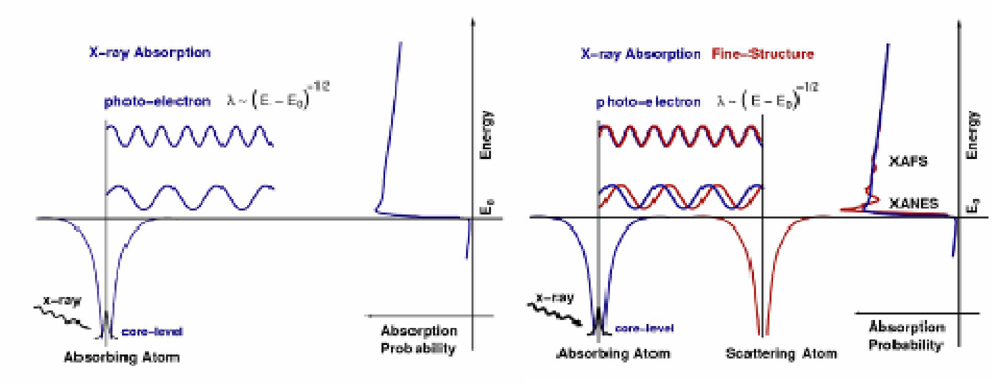

Free Atom model

Diatomic model

Figure 2.5 Scheme representing the photoelectron wave produced by a free atom and a diatomic system upon X-ray absorption and the corresponding XANES spectrum [8].

Once the X-rays from the storage ring is monochromatized and hits the sample, the electromagnetic radiation interacts with the electrons in the atoms via absorption and scattering generating ions, electrons, X-rays, etc as a result of the interaction. The various yields resulting from X –ray absorption are shown in Figure 2.6. In this thesis, we deal mainly with the absorption process. Ionization chambers filled with N_2 were used to collect the signal of incident photon Io and transmitted photon I, and then calculate the absorption coefficiency using Eq 2.1, this is the transmission mode. However, this mode only works on samples that are thin enough and highly uniform. We can collect all the electron yield including Auger, secondary and photo-electrons by recording the sample neutralized current or electron multiplier, which is the total electron yield (TEY) mode. Since electrons have short escape depth, TEY mode is sensitive to the surface and it unveils the information from a region less than 10 nm below the surface. Attention should be paid especially on easily contaminated samples such as air-sensitive samples and the accompanying charging problems happened on low conductive materials. The third mode is called fluorescence yield (FLY), which measures the emitted fluorescence X-rays during the decay process using various detectors including multi-channel plates, silicon drift detector or Ge solid state detectors. Compared with TEY, FLY could detect deeper depth up to micros due to longer attenuation length thus is regarded as bulk sensitive. However, if the sample is thicker than one absorption length, the self absorption is significant, leading to inversion of the obtained spectrum. It should be noted that TEY and FLY modes are based on assumption that the yields are proportional to μ.

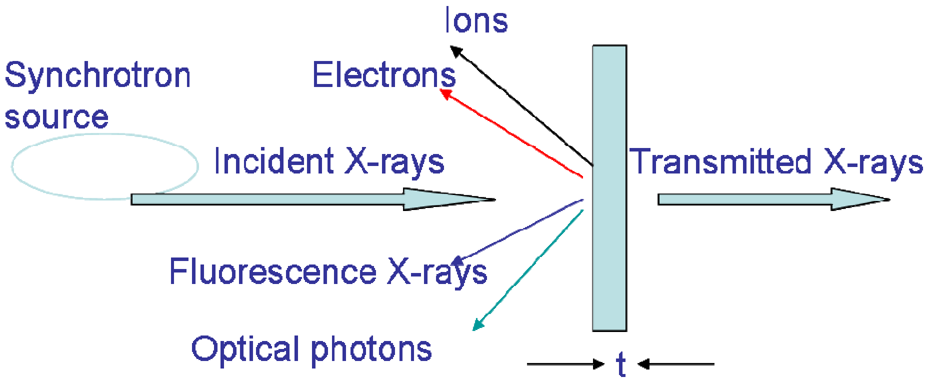

Figure 2.6 Detection modes in X-ray absorption spectroscopy

Figure 2.7 shows an example of Sn K edge XAFS spectrum for SnO_2. It can be divided into two regions: XANES and EXAFS. The pre-edge region in XANES is region where incident photon energy is below the excitation energy for edge transition. Weak features sometimes are seen in the pre-edge regions which are usually dipole forbidden quadruple s-d transitions. These features could sometimes be used to identify the co-ordination and local symmetry. Once the photon energy increases to satisfy the required energy, a sudden rise of absorption will occur (edge jump). The edge jump follows dipole transition roles representing a core electron into bound and quasi-bounded states such as LUMO in molecules, conduction band in semiconductors and states just above the Fermi level in metals. XANES are widely applied to provide the information of local structure and chemical bonding such as oxidation states and hybridization. From EXAFS, which monitors the oscillation in μ beyond the XANES region, the short-medium range structure (bond length, coordination number and Debye Waller factor) can be probed using established Fourier Transform and fitting procedures. In the thesis, the soft X-ray XANES spectra are generally performed on two beamlines: Spherical Grating Monochromator (SGM) beamline and Soft X-ray Microcharacterization Beamline (SXRMB) beamline at the CLS. Hard X-ray XANES and EXAFS data are obtained from the X-ray Science Division (XSD) partnered with the Pacific Northwest Consortium (PNC) at Sector 20 of Advanced Photon Source. Figure 2.8 shows the layout of SGM beamline, it provides an energy range from 250 eV to 2000 eV using dragon-type monochromator and have a resolution higher than 5000 [9].

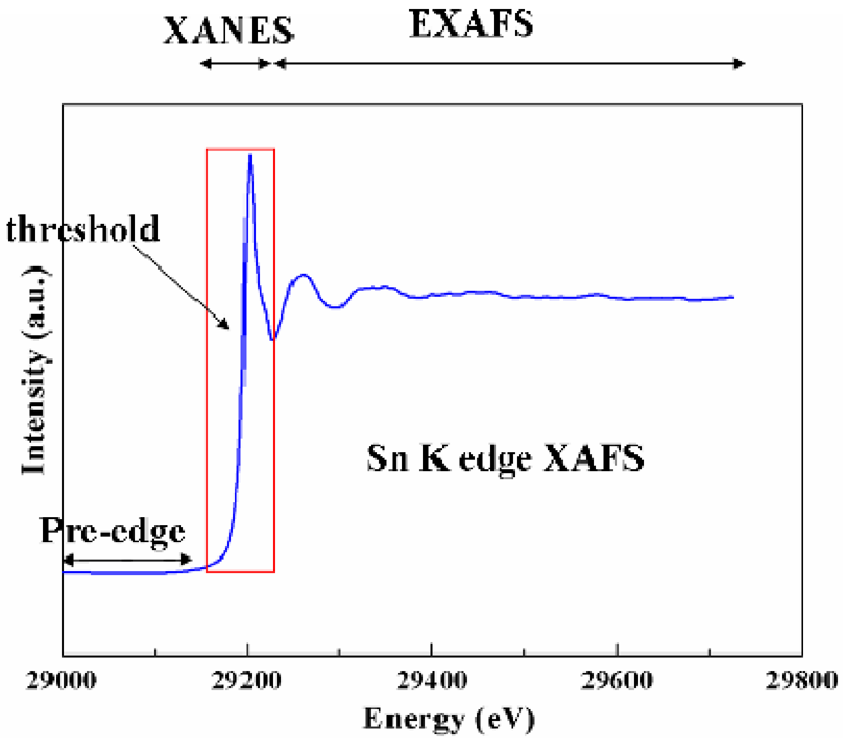

Figure 2.7 Sn K edge XAFS of SnO_2

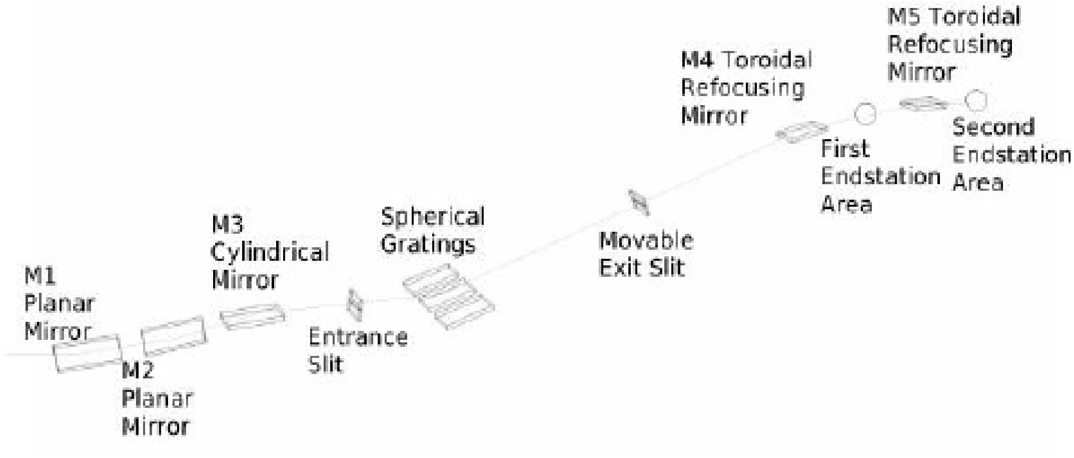

Figure 2.8 Layout of SGM beamline [9].

2.2.3 X-ray Excited Optical Luminescence

The de-excitation processes happen after the core-hole excitation to refill the core-hole. The general processes include non-radiative Auger transitions and radiative X-ray fluorescence, which are both proportional to the absorption coefficienct but competing with each other. Since the total decay is constant, the more Auger yield leads to less fluorescence yield and vice versa. Auger decay contributes dominate transition for low Z element while fluorescence decay mainly accounts for heavy elements. Accompanying the decay process, holes in outer shells and electrons at shallower levers will also be created and excited with the aid of excessive energy. In a semiconductor system, the electron-hole pair which undergoes thermalization results in electrons locating at the bottom of conduction band and holes locating on the valence band. In the next step, the formed electron-hole pair or exciton will recombines and emit energy. X-ray excited optical luminescence (XEOL) illustrates the radiative recombination process with emission of optical photons. XEOL, an X-ray photon in, optical photon out technique, is used to monitor the optical luminescence (UV-visible-Near IR) at selected excitation photon energy, often across the absorption edge; this technique can provide element and site specificity under favorable conditions, one then can determine the origin of the luminescence observation.

Emission channel specificity of XEOL is shown in Figure 2.9. The different excitation channels can be selectively measured at specific excited energy, for example, below and above the absorption edge of an element of interest, thus XEOL is also used as optical XANES to analyze the light emitting material since the variation of absorption coefficiency is in accordance with the variation of the XEOL intensity. XEOL spectrum measures the optical response versus the wavelength at specified excitation energy using a monochromator and a charge-coupled device detector. XEOL could unveil the information of band gap, crystallinity and defects of the materials through investigation of luminescence, providing element and site specificity. In this thesis, the XEOL data are collected at SGM beamline at CLS, recorded with an Ocean Optics, QE65000 spectrometer which is equipped with a dispersive grating and a charge-coupled device (CCD) detector collecting all wavelength (200-900 nm) simultaneously.

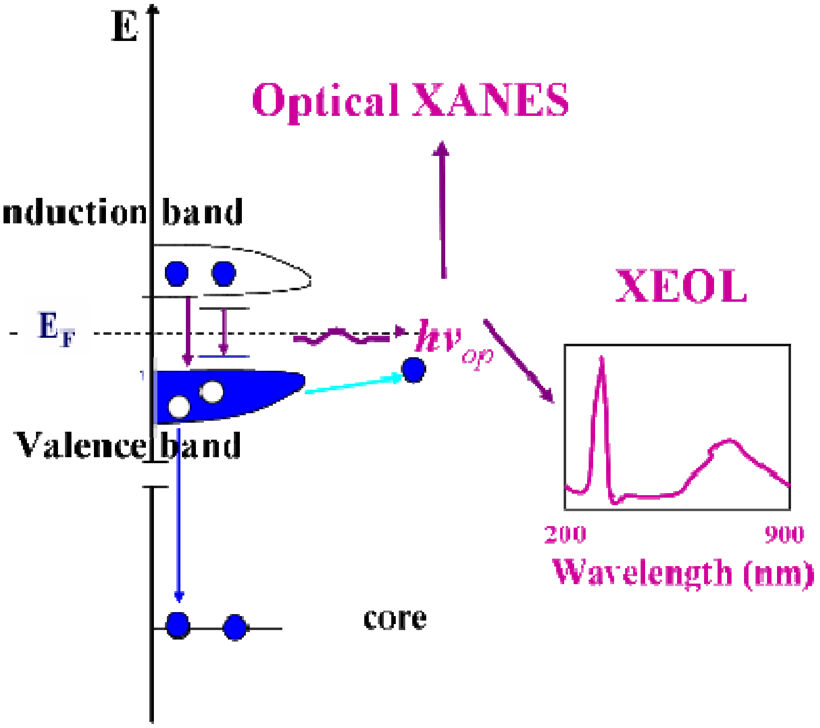

Figure 2.9 Emission channel specificity of XEOL, illustrating the conversion of X-ray energy into optical emission- X-rays in, optical photons out process

2.3 Electrochemical Measurements

2.3.1 Cyclic voltammetry (CV) and charge-discharge profiles

For tin-based anodes synthesized in the thesis, the cyclic voltammetry (CV) measurements are performed on an electrochemical workstation (Potentiostat/Galvanostat/EIS (VMP3)) over the potential range of 0.01–3.0 V (vs. Li^+/Li) at a scanning rate of 0.1 mV s^{-1}. Charge-discharge profiles data are collected on a computer controlled battery tester system (Arbin BT-2000) with a voltage window from 0.01–3.0 V (vs. Li^+/Li) in constant current mode. All the CV and charge-discharge profiles data are collected at room temperature using at least three coin cells with lithium as counter electrode, polypropylene as the separator, 1M $LiPF_6$ in ethylene carbonate (EC) and dimethyl carbonate (DMC) solvent (1:1 volume ratio) as electrolyte.

2.3.2 Cyclic and Rate Performances

All the cyclic and rate performances testing are conducted using a computer controlled battery tester system (Arbin BT-2000) with a voltage window from 0.01–3.0 V (vs. Li^+/Li). For cyclic performances testing, the synthesized anodes are tested under constant and small current densities (generally 0.1C) for 100 cycles at room temperature. For rate performances testing, the electrodes are tested under various current densities (generally from 0.1C stepwise increase to 2 C and reverse back to 0.1 C). The coin cells are assembled using the same procedures mentioned above. To confirm the results, at least six cells were assembled for cycling and rate test.

2.4 References

[1] Wang, D. N.; Yang, J. L.; Li, X. F.; Wang, J. J.; Li, R. Y.; Cai, M.; Sham, T. K.; Sun, X. L. Cryst. Growth Des., 2012, 12, 397.

[2] Hummers, W. S.; Offeman, R. E. J. Am. Chem. Soc., 1958, 80, 1339.

[3] Wang, D. N.; Li, X. F.; Wang, J. J.; Yang, J. L.; Geng, D. S.; Li, R. Y.; Cai, M.; Sham, T. K.; Sun, X. L. J. Phys. Chem. C, 2012, 116, 22149.

[4] Wang, D. N.; Li, X. F.; Yang, J. L.; Wang, J. J.; Geng, D. S.; Li, R. Y.; Cai, M.; Sham, T. K.; Sun, X. L. Phys. Chem. Chem. Phys., 2013, 15, 3535.

[5] Stohr, J. NEXAFS spectroscopy. Springer: 1992; Vol. 25.

[6] Stern, E. A.; Sayers, D. E.; Lytle, F. W. Phys. Rev. B, 1975, 11, 4836.

[7] Rehr, J. J.; Albers, R. C. Rev. Mod. Phys., 2000, 72, 621.

[8] Newville, M. Fundamentals of XAFS; Consortium for Advanced Radiation Source, University of Chicago, Chicago, IL: July, 2004.

[9] Regier, T.; Krochak, J.; Sham, T. K.; Hu, Y. F.; Thompson, J.; Blyth, R. I. R. Nucl Instrum Methods Phys. Res, Sec. A, 2007, 582, 93.

Chapter 3

3 Observation of Surface/Defect States of SnO_2 Nanowires on Different Substrates from X-ray Excited Optical Luminescence

Seminconductor SnO_2 has been widely applied in various fields. With the development of nanotechnology, it is demonstrated that nanosturcutred SnO_2 exhibits better optical, electrical, catalytic and electrochemical properties compared to the bulk counterparts, for example, one dimenasion SnO_2 nanowires exhibit improved LIB performances than bulk SnO2 as shown in the Chapter 1. Among various syntheis method, hydrothermal route is reagared as a facile way to obtain diverse nanostructures, which are highly related to the performances. Therefore, in the beginning of the Ph. D study, we aimed at synthesizing one dimensional tin-based nanostructures using the controllable hydrothermal method and exploit the electronic structures and other basic properties using synchrotron technique, to get a thorough understanding in method and characterization techniques.

In this chapter, SnO_2 nanowires (NWs) have been successfully synthesized on two different substrates (stainless steel (SS) and copper) via a facile hydrothermal process. SnO_2 NWs with varying degrees of crystallinity are obtained on different substrates. The growth mechanisms are also deducted by observing the morphology revolution at various reaction times. Furthermore, the electronic structures and optical properties have been investigated by X-ray absorption near edge structure (XANES) and X-ray excited optical luminescence (XEOL) measurements. The yellow-green luminescence from SnO_2 NWs is originated from the intrinsic surface states. Compared with SnO_2 NWs on copper, a Near Infrared (NIR) luminescence is observed for SnO_2 NWs on SS, which is resulted from poor crystallinity and abundance of defect/surface states.

KEYWORDS: SnO_2, Nanowires, Luminescence, Surface/Defect states

Note: Part of the content in this chapter has been published.

D. Wang, J. Yang, X. Li, J. Wang, R. Li, M. Cai, T. K. Sham, X. Sun Cryst Growth Des, 2012, 12, 397.

3.1 Introduction

Tin dioxide (SnO_2), an n-type semiconductor material with a wide band gap of ~ 3.6 eV (room termperature), has been widely exploited due to its distinct optical and electrical properties. Many advantages such as high optical transparency, electrical conductivity and chemical sensitivity, have made it an attractive material for a wide variety of applications in solar cells [1], field effect transistors[2, 3], catalyst support for fuel cells [4, 5], sensors [6-8] and Li-ion batteries [9-12]. Recently, nanomaterials especially one dimensional SnO_2 nanostructures have been applied in various advanced electric systems owing to superior electrochemical [13, 14], catalytic [4, 5], and optical properties [15, 16] compared with bulk SnO_2.

For the preparation of one dimensional SnO_2 nanostructure on substrates, the methodology can be mainly divided into two categories: vapor phase growth and solution phase growth. The vapor phase technique is well-developed based on reaction between tin vapor and oxygen gas [17-21]. Although high purity and high quality SnO_2 NWs can be synthesized on various substrates, the critical conditions, such as high temperature and catalyst, are also required, not to mention the low yield and high cost which limit its large-scale production. On the other hand, solution-phase growth methods provide a more flexible control and lower cost. To obtain one dimensional SnO_2 structure with controlled diameter and length with solution phase growth, many templates such as anodic aluminum oxide, molecular sieves, and polymer membranes have been used [22, 23]. However, these methods generally require fussy multiple steps and specific templates, which is a time-consuming process with accompanying high cost. For template free methods, organic solvents [24, 25] are generally used, which are deleterious to environment. In addition, removing surfactant after the reaction can also make the synthesis very cumbersome. Recently a one-step hydrothermal process [26-31] was demonstrated to be desirable for the synthesis of SnO_2 NW arrays directly on metallic current collector substrates. Due to the (usually water and ethanol) environment friendly solvent, surfactant free and no need of catalyst, the pure product can be developed by this process. But up to date, despite these findings, there is no report elucidating the growth mechanism of SnO_2 nanowire on a substrate, especially the effect of substrates on the evolution of SnO_2 morphology.

Applying substrate could introduce interface between the products and the substrate. Due to the various types and degrees of strains originated from the lattice mismatch between products and substrates, the crystal growth behavior on different substrates is strongly affected [32, 33], leading to different density of surface or defect state [34, 35]. As previous reported, the surface and defect states play a crucial role on the luminescence [36, 37]. However, the relationship between the density of defect state and luminescence is still unclear.

XANES is a spectroscopic technique that can characterize electronic structures by measuring the X-ray absorption coefficient of an element of interest in the material. XANES arises from the dipole excitation of a core electron into previously unoccupied electronic states in the valence region and beyond. Since valence states are chemically sensitive, XANES probes the local chemistry (population and symmetry of unoccupied electronic states, e.g. LUMO in molecules and the conduction band in semiconductors) of the absorbing atom. Using on a tunable synchrotron light source, one can probe the local symmetry and occupation (densities of states) of these states including surface and defect states by tracking the absorption coefficient of the element of interest by scanning the photon energy across the absorption edge, e.g. Sn $M_{5,4}$ edge and O K-edge in the case of this study. XEOL, an X-ray photon in, optical photon out technique, is used to monitor the optical luminescence (UV-visible-Near IR) at selected excitation photon energy, often across the absorption edge; this technique can provide element and site specificity under favorable conditions, one then can determine the origin of the luminescence observation..

In this report, we choose two typical substrates to grow SnO_2 nanostructures and systematically study the formation mechanism. This study reveals the significant effects of surface or defect state on luminescence using synchrotron light source based XANES and XEOL techniques.

3.2 Experimental Section

3.2.1 Synthesis SnO_2 NWs on different substrates.

In a typical experiment to grow SnO_2 on stainless steel (SS 304L, with chromium oxide on the surface), 350.58 mg $SnCl_4 \cdot 5H_2O$ (1 mmol) and 700 mg NaOH (17.5 mmol) were dissolved in a mixture of a 40 mL water/ethanol (1:3) solution. To conduct the synthesis, the alkaline PH value around 12 was needed. After sonication and continuous stirring for about 10 minutes, transparent solution was obtained. Then 10 mL solution was transferred to a Telfon-lined autoclave (20 mL), where the substrate, cleaned by acetone beforehand with sonication for 10 minutes, was laid flat at the bottom of the autoclave. The solution was subsequently heated to 200 ^{o}C at a rate of 5 ^{o}C per minute from room temperature, then maintained for 20 h and then cooled down to room temperature. Once the reaction was completed, the SnO_2 covered substrate was rinsed several times with distilled water and ethanol, followed by final drying at 60 ^{o}C overnight. Similar procedures were used for SnO_2 NWs grow on copper foil. After the alkaline hydrothermal process, both two substrates' surfaces are covered with white-gray products. A schematic representation for preparation for SnO_2 NWs is given in Figure 3.1.

3.2.2 Characterization

The morphology and phase composition were characterized and analyzed by powder X-ray diffraction (XRD, Rigaku RU-200BVH) with Co Kα radiation (λ= 0.179 nm), field-emission scanning electron microscope (FESEM, Hitachi S-4800, operating at 5 kV) equipped with an energy-dispersive X-ray spectrometer (EDX). The XANES and XEOL experiments were conducted on the undulator Spherical Grating Monochromator (SGM) beamline at the Canadian Light Source (CLS) located at the University of Saskatchewan in Saskatoon. The SGM beamline employs three diffraction gratings to provide a very bright, highly monochromatic photon beam (E/ΔE ~10,000), tunable between 250 and 2000 eV [38]. XEOL was recorded with an Ocean Optics, QE65000 spectrometer which is equipped with a dispersive grating and a CCD detector collecting all wavelength (200 - 900 nm) simultaneously at any given excitation energy.

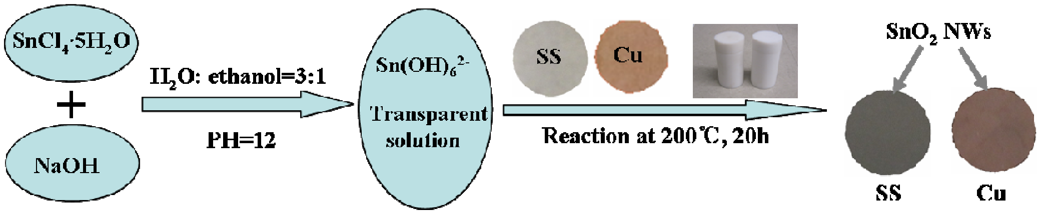

Figure 3.1 Scheme of synthetic drawing of the preparation of SnO_2 NWs on substrates

3.3 Results and Discussion

3.3.1 Morphology and Structures

Figure 3.2a and 3.2b show the typical SEM images, top view and side view respectively, of the as synthesized SnO_2 NWs arrays vertically grown on SS. It can be seen that the NWs were uniformly distributed on the substrate, with a diameter from 100- 150 nm and a length around 500 nm with an octahedral tip. Compared with SnO_2 NWs grown on SS, SnO_2 NWs on copper have similar shape, with the same octahedral structure tip, length and diameter, but are grown in a more random manner as illustrated in Figure 3.2c and 3.2d.

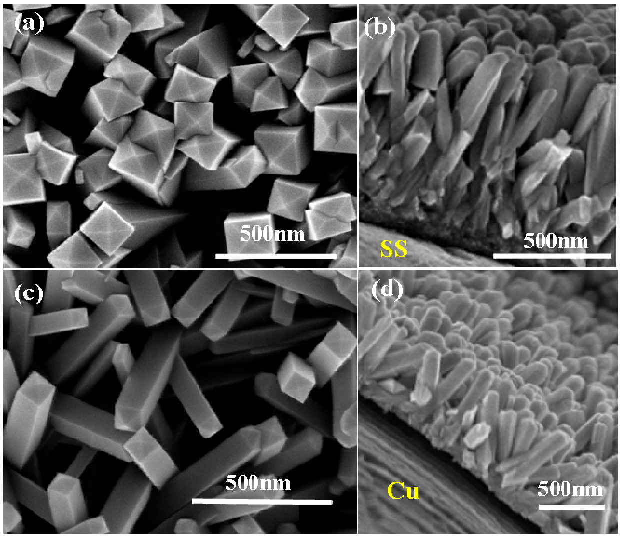

Figure 3.2 SEM images of SnO_2 NWs growing on different substrates: Stainless steel (a) top view; (b) side view; Copper as substrate (c) top view; (d) side view.

3.3.2 Morphology Evolution

To study the growth mechanism, the different reaction time was chosen to investigate the morphology evolution of SnO_2 NWs on SS. Figure 3.3a shows a series of typical morphologies from short reaction time (5h) to aim-reaction time (20h) during hydrothermal synthesis. It can be clearly seen that there exists a morphology transform from initial nuclei of sharp tip (5h), to small aggregates consisting of an irregular needle-like structure (10h), and to NW structure with the octahedral tip (15h), until all precursor transforms to SnO_2 NW arrays (20h). With increase of the reaction time, the density of SnO_2 NWs increases, and finally SnO_2 NWs vertically grow on the substrate after 20h. A similar morphology evolution for SnO_2 NWs on copper foil was also observed in Figure SI 3.1 (see the Supporting Information). Due to different surface roughness, the growth direction to SnO_2 on copper is not as vertical as that of SnO_2 on SS, as one can infer from the initial steps on the copper substrate.

As previous reported [25], the energy barrier between (001) and the other facets were leveled by the excessive thermal energy supplied to the system. The scheme for a proposed possible growth mechanism is presented in Figure 3.3b.The hydrolysis of saturated $Sn(OH)_6^{2-}$ forms the SnO_2 nuclei (see following equations) on the substrates at first; it is worth to mention that the SnO_2 nuclei could not form unless the substrate is present in the solution, that is, substrate could faciliate the formation of SnO_2 nuclei, then due to the hydrothermal condition, the kinetics controls the SnO_2 anisotropic growth to facilitate the [001] direction growth, thus, the SnO_2 NWs arrays are obtained on the metallic substrates. With time, both the diameter and the length of the nanorod increase on the substrate, and the sample on SS is more ordered than copper due to the surface difference (Cu is more susceptible to roughening than SS).

$$Sn^{4+} + 6OH^{-} \longrightarrow Sn(OH)_6^{2-} \qquad (3.1)$$

$$Sn(OH)_6^{2} \longrightarrow SnO_2 + 2H_2O + 2OH^{-} \qquad (3.2)$$

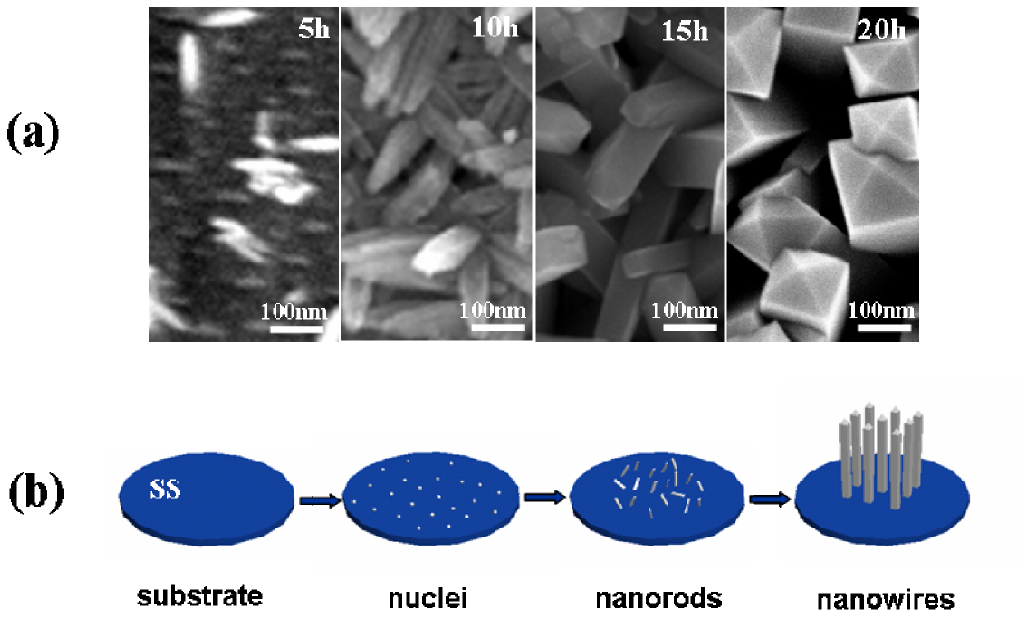

Figure 3.3 (a) morphology evolution of SnO_2 NWs on SS at different reaction time; (b) schematic SnO_2 NWs growth mechanism.

Figure 3.4 compares the XRD patterns of these samples. It can be seen that except the peaks originating from the substrates, all other peaks are arising from SnO_2 rutile structure (JCPDS No. 41-1445). For these samples, the strongest peak corresponds to the (101) plane, demonstrating that individual SnO_2 nanostructures are crystallized along the c-axis. For SnO_2 grown on SS and copper, the ratio of faces between (002) / (101) is higher than those of reference values for crystalline SnO_2 (JCPDS No. 41-1445), indicating that individual SnO_2 nanostructures are crystallized along (001) direction. It is worth to mention that although both samples are crystallized SnO_2, the peaks for SnO_2 grown on SS are not as strong as that on copper, which means that it is less crystalline or richer of surface or defect states. Compared with Huang's work [30, 31], where SnO_2 nanoarrays were fabricated vertically on Ni, Ti, and Fe-Co-Ni substrates without comparing degrees of crystallinity, here, we reveal that different substrates could affect the quality of crystallinity of SnO_2 they supported. Similar as Ghosh's study [32] that the structure of ZnO is affected by different substrates, in this study, SS and copper have significantly different lattice parameters, and the lattice mismatch between SS and SnO_2

is more serious than that between copper and SnO_2, resulting in bigger strain at the interface, which favours the creation of higher disorder SnO_2 crystallites.

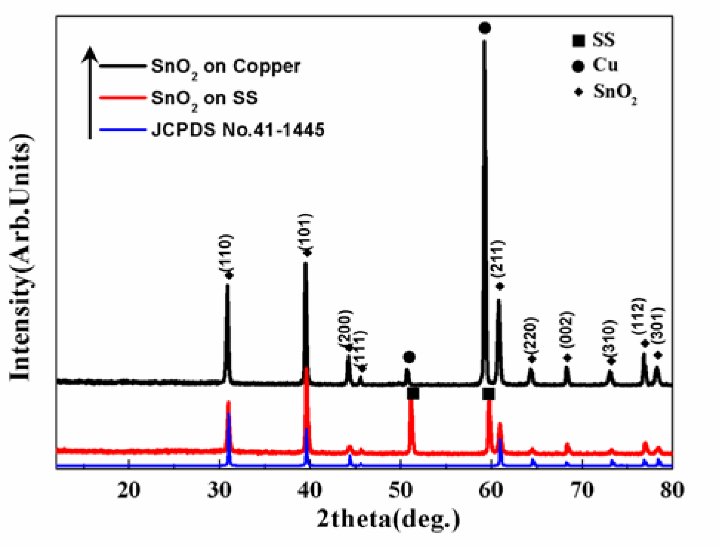

Figure 3.4 XRD patterns of as prepared SnO_2 NWs grown on SS and copper substrates.

3.3.3 Electronic and Optical Properties (XANES and XEOL)

The intriguing surface and defect related optical properties have prompted us to exploit the unusual electronic properties exhibited by SnO_2 nanowires when it is employed on the nano-scale since this behavior is not well understood. In order to better understand the unusual phenomena, we must have a better understanding of the electronic structure of SnO_2 nanostructures. To this end, we have conducted X-ray absorption near edge structure (XANES) and X-ray excited optical luminescence measurement (XEOL) using synchrotron radiation on these SnO_2 nanowires prepared on different substrates to study more about the electronic structure and optical properties of these SnO_2 nanowires.

Figure 3.5 shows the XANES spectra for SnO_2 NWs grown on different substrates measured in Total Electron Yield (TEY), Fluorescence Yield (FLY) and Photoluminescence yield (PLY). In the Sn $M_{5,4}$ edge XANES (Figure 3.5a and 3.5c), two sets of triplets peaks begin at ~ 490 eV and 498 eV, corresponding to $3d_{5/2}$ and $3d_{3/2}$ to 5p transitions, respectively. These features are characteristic of SnO_2 nanostructure (rutile) as reported previously [36]. The Sn $M_{5,4}$ edge tracked by the three yields (TEY, FLY and PLY) are similar, i.e. that all exhibit positive edge jumps. For SnO_2 grown on SS, (Figure 3.5a), the TEY and FLY spectrums show a pre-edge resonance at "486.5eV" (clearly shown in enlarged spectrums inserted) just before the Sn $M_{5,4}$ edge, which has been previously attributed to surface states caused by unsaturated coordination of surface Sn ions due to oxygen vacancies [37]. This observation is confirmed by the very intense third peak of the first triplet (M_5) caused by contribution from the surface state for the M_4 edge underneath. For copper substrate, the surface sensitive TEY and bulk sensitive FLY and optically sensitive PLY of the Sn M edge are also similar. It is noteworthy that there is no pre-edge resonance peak at "486.5eV" before the Sn M-edge for SnO_2 on copper substrate. Meanwhile, the third peak of the first triplet (M_5) is less intense compared to that of SS, indicating the defect/surface states are less abundant for SnO_2 on copper substrates which are in accordance with the XRD results. Further examination of the PLY spectrum in Figure 3.5a, reveals the pre-edge and the very intense third peak of the first triplet (M_5) (arrow pointed) in PLY indicating that the selective excitation of Sn associated with defects has a strong effect on the luminescence yield. For SnO_2 on the copper substrate, at the resonance, the PLY spectrum (Figure 3.5b) shows a less intense peak which is due to the low densities of surface or defect states.

Turning to the O K-edge, it is found that the FLY XANES tracks that of TEY but the PLY does not. In fact the PLY is inverted; this inversion (reduction in quantum yield at the edge) is due to saturation (self-absorption) effect. A simple calculation using the X-ray calculator (http://henke.lbl.gov/optical_constants/atten2.html) shows that for SnO_2, the attenuation length of the incident photon is considerable longer (at least a factor of 3) at the Sn$M_{5,4}$ edge than at the O K-edge. Thus, in a total absorption situation, as is in the case of most soft X-ray absorption measurements of solids, the penetration depth of the photon at the O K-edge is significant shorter than at the Sn $M_{5,4}$ edge. Since the secondary process (attenuation of energetic electrons and fluorescent X-rays describe above) contributes significantly in the energy transfer to the optical de-excitation channel, a reduction in the secondary events will reduce the photoluminescence. Thus the photoelectrons, Auger electron and fluorescence X-rays associated with the O 1s core hole will have a good chance of escaping the surface without contributing to the secondary processes (thermalization of electrons and holes), which in turn contribute to the photoluminescence, resulting in a negative edge jump when the absorption coefficient increases sharply at the edge threshold. In other words, above the O K-edge, the optical photons produced per eV of energy absorbed are less than that just below the edge. The crystallinity could also be deducted from O K-edge spectrums. Closer examination of the O K-edge TEY XANES reveals that the spectral feature for SnO_2 on copper is sharper than SS (as marked by lines and arrows), indicating higher quality crystallites of SnO_2 NWs on copper (less disorder or surface and defects states). This conclusion also proves the point those degrees of crystallinity for SnO_2 are relied on the substrate we mentioned above.

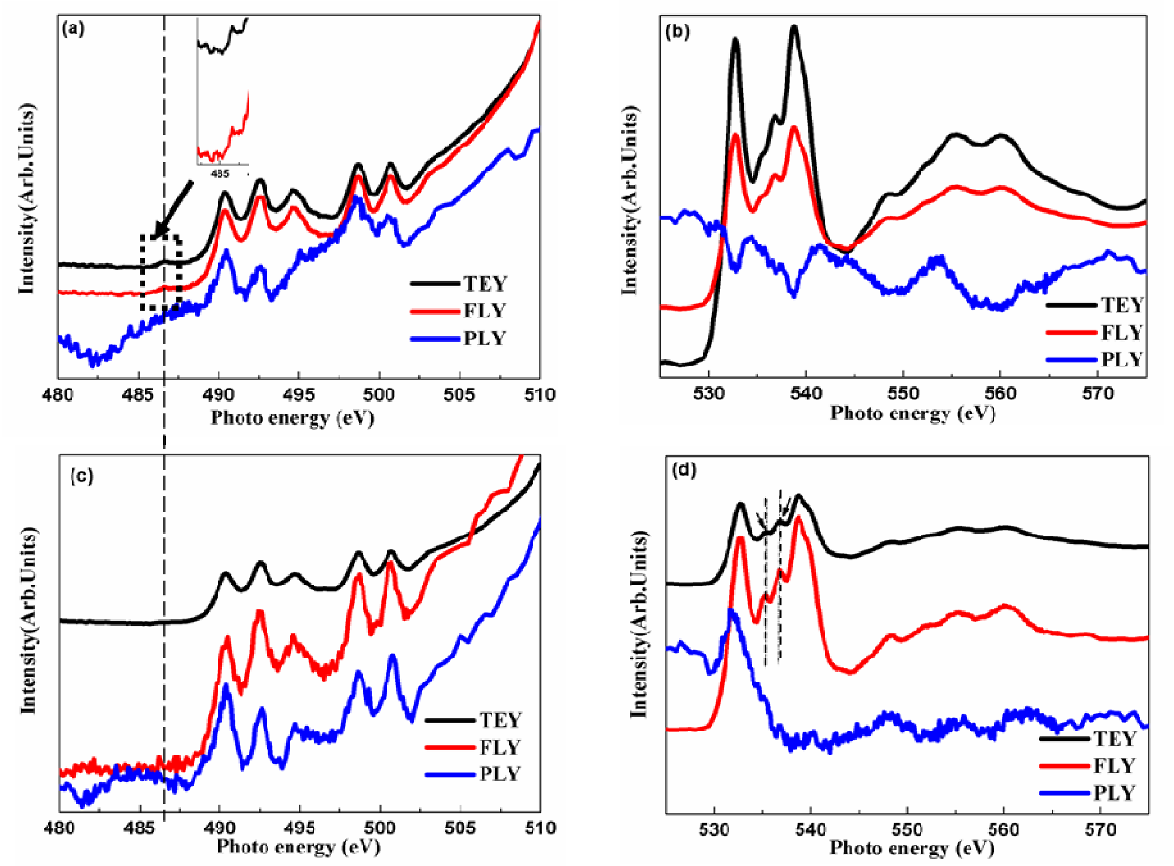

Figure 3.5 O K-edge and Sn $M_{5,4}$ edge XANES spectra of SnO_2 NWs grown on SS (a) Sn $M_{5,4}$ edge and (b) O K-edge, on Copper (c) Sn $M_{5,4}$ edge and (d) O K-edge.

In order to investigate the luminescence properties of SnO_2 NWs with different density of surface or defects states, XEOL was performed at room temperature, as shown in Figure 3.6. Each sample was excited with soft X-ray photons both below and above the threshold of the O K-edge and Sn $M_{5,\,4}$-edge. This is equivalent to the XEOL excited using selected excitation energy in the PLY XANES shown above. All spectra show an intense emission band from 400-900 nm (3.1-1.4 eV), centered on 498nm (yellow-green luminescence) which has been reported in XEOL studies of SnO_2 nanoribbons originating from intrinsic surface states [36, 37]. Very weak emission was observed originating from the band gap of SnO_2 (3.6 eV), which would have resulted in a peak at 344 nm. It has been shown previously that near band-gap emission is quenched by the surface or defect states in the band-gap of SnO_2. A log plot of the XEOL does show a weak band gap feature. For SS, it can be seen in the XEOL spectra that the luminescence intensity increases across the Sn $M_{5,\,4}$-edge but the intensity decreases across the O K-edge as displayed above in the PLY-XANES.

For SnO_2 grown on the SS substrate, which is less crystalline, two distinct features are observed, as compared to the XEOL from crystalline SnO_2 on copper; first, the short wavelength onset exhibits a more pronounced feature at 315 nm (~3.9 eV) as compared to 325 nm (~3.8 eV), indicating that the band gap widens much due to quantum confinement. More importantly, SnO_2 on SS exhibits a near IR peak 780 nm (1.6 eV), resulting from high density of surface or defect states, which is totally absent in SnO_2 on copper (as marked by frame). From the XEOL, together with the PLY data, it can be seen that for SnO_2 on SS when excited at 485 eV and 495 eV (Sn ion associated with defects), the transition from Sn $3d_{5/2}$ to surface or defect states is turned on, and the intensity of luminescence at 780 nm increases markedly compared with those with off-resonance excitations, e.g. at 530 eV, 543.1 eV and 580 eV. This observation indicates that the near IR peak 780 nm (1.6 eV) results from high densities of surface or defect states. Thus, the high density of surface or defect states affects bands of the SnO_2 NWs, then inducing the near IR luminescence. Incidentally, a similar IR band is observed in the rutile structure of TiO_2 nanotube, a somewhat stressed structure [39]. More studies are required to identify the origin of this emission for certainty.

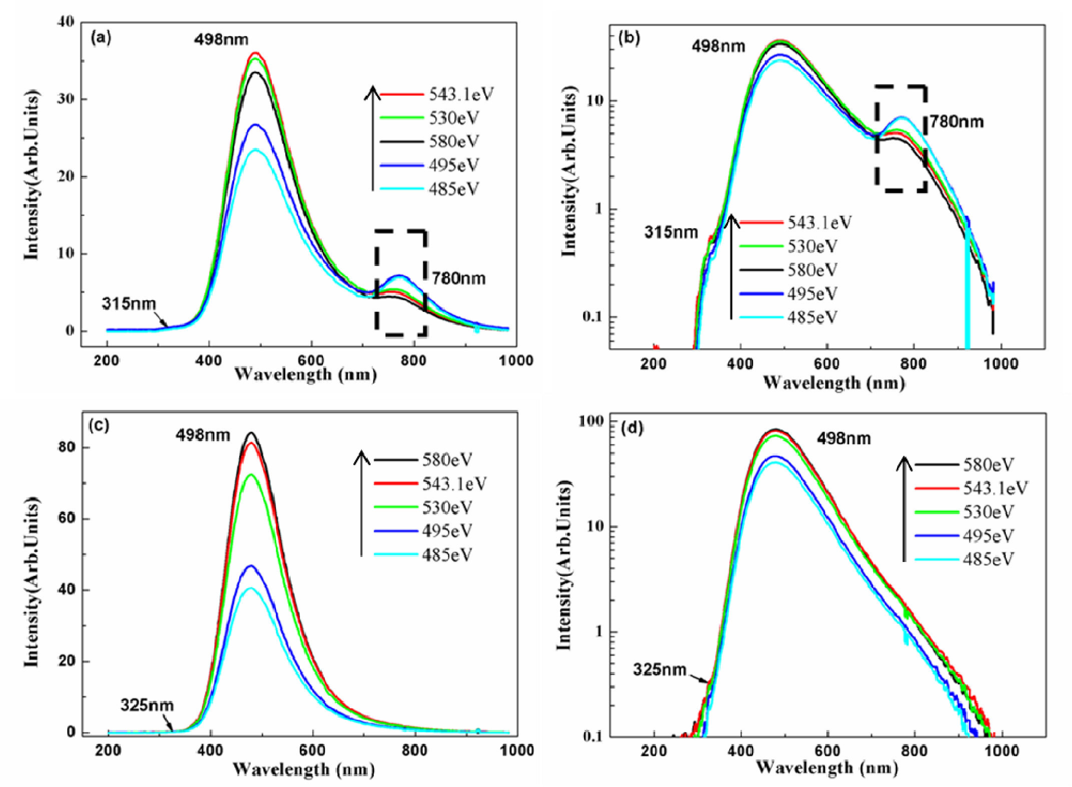

Figure 3.6 XEOL of SnO_2 NWs on different substrates: a, b) SS; c, d) copper.

3.4 Conclusions

In conclusion, vertically aligned SnO_2 NWs arrays are obtained on SS and Copper substrates via hydrothermal route. The NWs have a diameter from 100 to 150nm and a length around 500nm with an octahedral tip. For copper substrate, random oriented SnO_2 NWs was formed after the 20h reaction. Morphology evolution explains the growth mechanism, from initial nuclei to SnO_2 NW arrays. XEOL data shows that both SnO_2 samples exhibit yellow-green luminescence, which originates from the intrinsic surface states. Moreover, SnO_2 NWs on SS have lower quality of crystallites with more defect/surface states than that of copper ones as proved by XRD and XANEs. It is noteworthy mentioning that SnO_2 on SS showed unique near IR luminescence which is attributed to high density of surface or defect states itself. From our measurement, the luminescence is depending on the degree of crystallinility of SnO_2, revealing that the bands of the semiconductor materials are related to density of surface or defect states.

3.5 Acknowledgements

This research was supported by Natural Sciences and Engineering Research Council of Canada (NSERC), General Motors of Canada, Canada Research Chair (CRC), Canada Foundation for Innovation (CFI), Ontario Innovation Trust (OIT) Program and University of Western Ontario. The Canadian Light Source is supported by CFI, NSERC, NRC, CHIR, and the University of Saskatchewan. Assistance from Tom Regier, the SGM beamline scientist is gratefully acknowledged.

3.6 References

[1] Chappel, S.; Chen, S. G.; Zaban, A. *Langmuir* **2002**, *18*, 3336-3342.

[2] Sun, J.; Tang, Q. X. *Nanotechnology* **2009**, *20*, 255202.

[3] Dattoli, E. N.; Wan, Q.; Guo, W.; Chen, Y.; Pan, X.; Lu, W. *Nano Lett.* **2007**, *7*, 2463–2469.

[4] Saha, M.; Li, R.; Cai, M.; Sun, X. *Electrochem. Solid St.* **2007**, *10*, B 130-133.

[5] Saha, M.; Li, R.; Sun, X. *Electrochem. Commun.* **2007**, *9*, 2229-2234.

[6] Wei, B.Y.; Hsu, M. C.; Su, P. G.; Lin, H. M.; Wu, R. J.; Lai, H. J. *Sens. Actuators B* **2004**, *101*, 81-89.

[7] Liu, Y. L.; Yang, H. F.; Yang, Y.; Liu, Z. M.; Shen, G. L.; Yu, R. Q. *Thin Solid Films* **2006**, *497*, 355-360.

[8] Leite, E. R.; Weber, I. T.; Longo, E.; Varela, J. A. *Adv Mater.* **2000**, *12*, 965–968.

[9] Courtney, I. A.; Dahn, J. R. *J. Electrochem. Soc.* **1997**, *144*, 2045-2052.

[10] Kim, D. W.; Hwang, I. S.; Kwon, S. J.; Kang, H. Y.; Park, K. S.; Choi, Y. J.; Choi, K. J.; Park, J. G. *Nano Lett.* **2007**, *7*, 3041-3045.

[11] Wang, Y.; Lee, J. Y. *J. Phys. Chem. B* **2004**, *108*, 17832-17837.

[12] Ying, Z.; Wan, Q.; Cao, H.; Song, Z. T.; Feng, S. L. *Appl. Phys. Lett.* **2005**, *87*, 113108.

[13] Park, M. S.; Wang, G. X.; Kang, Y. M.; Wexler, D.; Dou, S. X.; Liu, H. K. *Angew. Chem. Int. Ed.* **2007**, *46*, 750-753.

[14] Wang, Y.; Zeng, H.C.; Lee, J. Y. *Adv. Mater.* **2006**, *18*, 645-649.

[15] Hu, J. Q.; Bando, Y.; Liu, Q. L.; Golberg, D. *Adv. Funct. Mater.* **2003**, *13*, 493-496.

[16] Fan, W. Q.; Song, S. Y.; Feng, J.; Lei, Y. Q.; Zheng ,G. L.; Zhang, H. J. *J. Phys. Chem.C* **2008**, *112*, 19939-19944.

[17] Lu, J. G.; Chang, P. C. *Mat. Sci. Eng. R.* **2006**, *52*,49-91.

[18] Ying, Z.; Wan, Q. *Nanotechnology* **2004**, *15*, 1682-1684.

[19] Ahn, J. H.; Kim, Y. J.; Wang, G. X. *J. Alloy. Compd.* **2009**, *483*,422-424.

[20] Ko, Y. D.; Kang, J. G. *Nanotechnology* **2009**, *20*, 455701.

[21] Mathur, S.; Barth, S. *Small* **2007**, *3*, 2070-2075.

[22] Zhao, N. H.; Yang, L. C.; Zhang, P.; Wang, G. J.; Wang, B.; Yao, B. D.; Wu, Y. P. *Mater. Lett.* **2010**, *64*, 972-975.

[23] Kim, H.; Cho, J. *J. Mater. Chem.* **2008**, *18*, 771–775.

[24] Wang, Y.; Jiang, X.; Xia, Y. *J. Am. Chem. Soc.* **2003**, *125*, 16176-16177.

[25] Zhang, D.F.; Sun, L.D;. Xu, G.; Yan, C.H. *Phys. Chem. Chem. Phys.* **2006**, *8*, 4874–4880.

[26] Shi, S. L.; Liu, Y. G. *Chinese Physics B* **2009**, *18*, 1674-1056.

[27] Qin, L. P.; Xu, J. Q.; Dong, X. W.; Pan, Q. Y.; Cheng, Z. X.; Xiang, Q.; Li, F. *Nanotechnology* **2008**, *19*, 185705.

[28] Cheng, B.; Russell, J. M.; Shi, W. S.; Zhang, L.; Samulski, E. T. *J. Am. Chem. Soc.* **2004**, *126*, 5972-5973.

[29] Ye, J. F.; Qi, L.M. *J. Mater. Sci. Technol.* **2008**, *24*, 529-540.

[30] Ji, X. X.; Huang, X. T. *Nanoscale Res. Lett.* **2010**, *5*, 649–653.

[31] Liu, J. P.; Li, Y. Y.; Huang, X. T.; Ding, R. M.; Hu, Y. Y.; Jiang, J.; Liao, L. *J. Mater. Chem.* **2009**, *19*, 1859–1864.

[32] Ghosh, R.; Basak, D.; Fujihara, S. *J. Appl. Phys.* **2004**, *96*, 2689.

[33] Schwenzer, B.; Gomm, J. R.; Morse, D.E. *Langmuir* **2006,** *22,* 9829-9831.

[34] Lee, H. Y.; Ko, H. J.; Yao, T. *Appl. Phys. Lett.* **2003**, 82, 523.

[35] Shi, W. S.; Agyeman, O.; Xu, C. N. *J. Appl. Phys.* **2002**, 91, 5640.

[36] Zhou, X. T.; Heigl, F.; Murphy, M. W.; Regier, T.; Coulthard, I.; Blyth, R. I. R.; Sham, T. K. *Appl. Phys. Lett.* **2006**, *89*, 213109.

[37] Zhou, X. T.; Zhou, J. G.; Murphy, M. W.; Ko, J. Y. P.; Heigl, F.; Regier, T.; Blyth, R. I. R.; Sham, T. K. *J. Chem. Phys.* **2008**, *128*, 144703.

[38] Regier, T.; Paulsen, J.; Wright, G.; Coulthard, I.; Tan, K. H.; Sham, T. K. Blyth, R. I. R. *AIP Conf. Proc.* **2007**, *879,* 473–476.

[39] Liu, L. J.; Chen, J.; Sham, T. K. *J. Phys. Chem. C* **2010**, *114*, 21353-21359.

3.7 Supporting Information

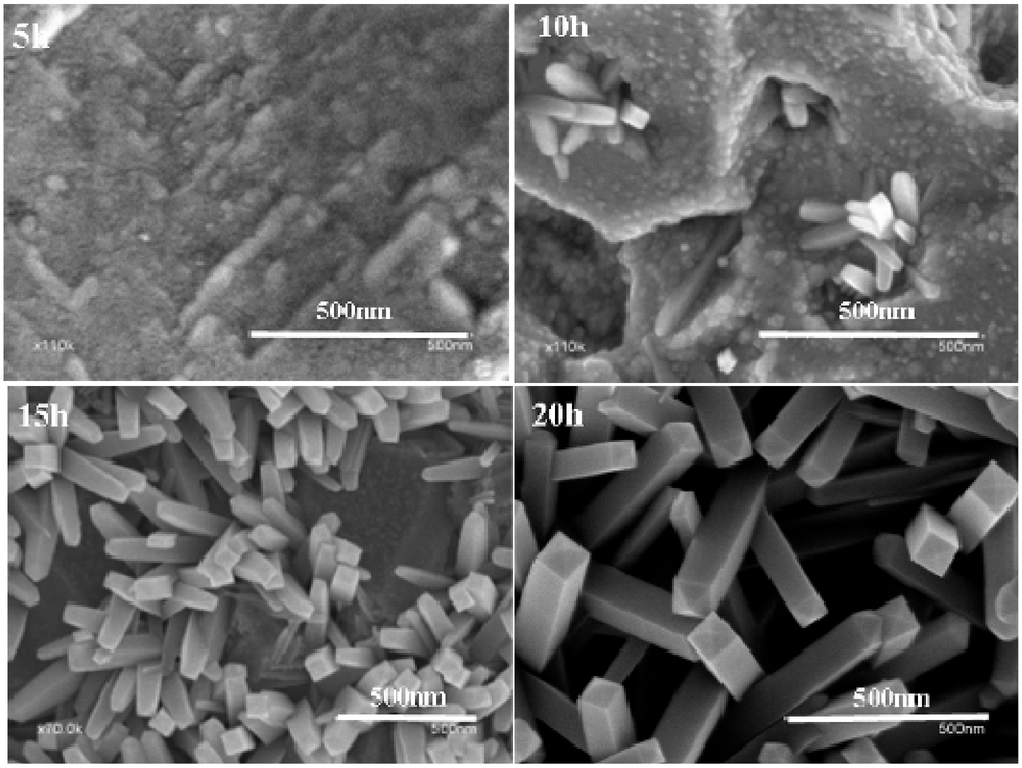

Figure SI 3.1 Morphology evolution of SnO_2 NWs on copper at different reaction time

Chapter 4

4 Defect-Rich Crystalline SnO_2 Immobilized on Graphene Nanosheets with Enhanced Cycle Performance for Li Ion Batteries

Although the electrochemical performances testing for pure SnO_2 nanostructures are greatly improved, the tread for capacity fading is inevitable as demonstrated from many reports. In another way, graphene has superior physical and chemical properties which is an ideal matrix for combination with nanosized tin-based materials, thus in this chapter we designed SnO_2 nanoparticle/Graphene system and evaluate its performances.

In this chapter, a one-step microwave-assisted hydrothermal method (MAHM) has been developed to synthesize SnO_2/graphene composites. It is shown that that fine SnO_2 nanoparticles with an average size of 3.5 nm can be homogeneously deposited on graphene nanosheets (GNSs) using this technique. The electronic structure as revealed from X-ray Absorption Near Edge Structure (XANES) shows that the SnO_2 nanoparticles are abundant in surface defects with oxygen vacancies which facilitate the immobilization of SnO_2 onto GNSs by electronic interaction. Carbon K edge XANES provide direct evidence of strong interaction between SnO_2 and GNSs. The SnO_2/graphene nanocomposites deliver a superior reversible capacity of 635 mAh g^{-1} after 100 cycles and display excellent rate performance.

KEYWORDS: Immobilization nanoparticles· SnO_2/graphene composites· X-ray absorption near-edge structures· Lithium ion batteries

Part of the content in this chapter has been published

D. Wang, X. Li, J. Wang, J. Yang, D. Geng, R. Li, M. Cai, T. K. Sham, X. Sun in *J Phys Chem C* **2012**, *116*, 22149.

4.1 Introduction

Lithium ion battery (LIB) is currently the dominant power source for portable electronic devices due to its high energy density, working voltage, electromotive force and light weight. Recent years have witnessed the intensive research effort that has been aimed at developing high capacity LIB electrodes with good stability for application in electrical/hybrid-electrical vehicles. Since the commercial graphite anode has a limited specific capacity of 372 mAh g^{-1}, much research attempts are focused on exploring graphite alternatives with high energy capacities. SnO_2 is considered one of the most promising substitutes because of its high lithium storage capability up to 782 mAh g^{-1}, more than twice as that of graphite [1-6]. However, the major drawback hampering its industrial application is the poor cycling performance which is caused by serious aggregation and considerable volume change upon cycling [7, 8].

One effective strategy commonly used to address these problems is to disperse SnO_2 nanocrystals on ductile carbonaceous support as a buffer matrix to maintain the electrode integrity during the charge/discharge process [9-11]. For example, improved battery performance has been achieved by loading SnO_2 on graphite or carbon nanotubes etc. [10, 12, 13]. Among all carbonaceous materials, graphene nanosheets (GNSs) has been regarded as a good matrix for SnO_2 anode since it has ultra-thin graphitic layers, excellent electronic conductivity, high surface areas (2600 m^2 g^{-1}), good mechanical properties and chemical stabilities [14-16]. Recent reports showed that hybrid GNSs-SnO_2 nanocomposites exhibited enhanced cycle performance [4, 17, 18]. Whereas, in order to facilitate the hybridization between SnO_2 and GNSs, additional reagents such as urea have to be applied in the solution, leading to complicated synthesis procedures and increased cost. In addition, it is often difficult to control the uniform deposition of metal oxide on GNSs since the whole GNSs are not homogeneously functionalized at theirs widespread surface [4, 18]. In situ chemical synthesis of SnO_2/graphene composites requires post thermal treatment, resulting in time consuming and complicated synthesis methodology [19]. “As previously reported by our group [17], we designed the SnO_2/graphene composites via atomic layer deposition, demonstrating this hybrid structure favors the increase of the electrochemical performance. Paek [4] et al. and

Zhang [20] et al. synthesized the SnO_2/graphene composites and found improved cycling performance compared with that of bare SnO_2; Yao [19] et al. and Lian [21] et al. prepared the SnO_2/graphene hybrids by an in situ chemical synthesis approach, high reversible specific capacity and excellent rate capability was achieved. Generally, enhanced performances are attributed to synergic effect of the hybrids. Despite the excellent electrochemical performances, up to now, little research has been focused on studying the electronic structure, chemical environment, chemical bonding and charge transfer between SnO_2 and GNSs behind that. Thus, investigation of how SnO_2 nanoparticles are immobilized or anchored on the GNSs is very relevant for the formation of resultant nanocomposites achieving desired performance.

Herein, we report a facile, simple and efficient microwave-assisted hydrothermal method (MWHM) to synthesize hybrid SnO_2/graphene nanocomposites without employing surfactants or templates (Figure 4.1), and then investigate the interaction between SnO_2 and GNSs using XANES. It is found that the rich surface defects of uniformly dispersed SnO_2 nanopariticles and the presence of oxygen based defects on the GNSs facilitate the immobilization onto GNSs, and such hybrid composites deliver a high reversible capacity of 635 mAh g^{-1} after 100 cycles and an excellent rate capability.

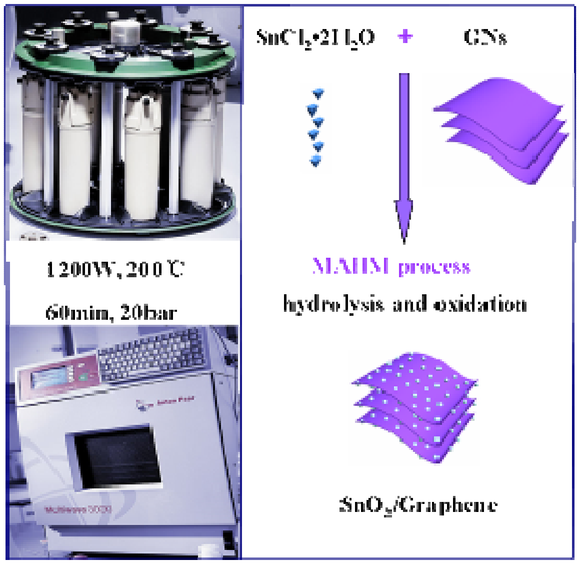

Figure 4.1 Illustration of (a) microwave-assisted hydrothermal system and (b) synthesis process of SnO_2/graphene nanocomposites.

4.2 Experimental Section

4.2.1 SnO_2/Graphene Synthesis

GNSs were synthesized using a modified Hummers method followed by the rapid heating of graphene oxide at 1050 ^oC for 30 s under Ar atmosphere [22]. SnO_2/graphene composites were synthesized by a rapid MWHM method. In a typical process, 22.5 mg $SnCl_2 \cdot 2H_2O$ was dissolved in 10 ml water. Then 8.25 mg of the as-prepared GNSs was added in the solution followed by vigorous ultrasonication for 2 h. The resulting black suspension was transferred and sealed in a high pressure Teflon vessel. These vessels were anchored to a rotor which was placed on a turntable in a microwave reaction system (Anton Paar Synthos 3000). The turntable was kept spun to ensure uniform heating during the reaction. The power was set at 1200 W with 8 minutes ramping time to reach 200 ^oC, and maintained at this temperature for 1 h before the system was cooled down to room temperature and the SnO_2/Graphene nanocomposites were collected. The pressure was below 20 bars throughout the synthesis. The as-synthesized product was first washed with ethanol and water several times to remove the Cl^- by centrifugation, and followed by vacuum drying in an oven at 80 ^oC overnight. Pure SnO_2 nanoparticles were prepared under the same parameters except the addition of GNSs. A schematic of the synthesis process is depicted in Figure 4.1.

4.2.2 Characterization

Powder X-ray diffraction (XRD, Rigaku RU-200BVH with a Co-Kα source (λ=1.7892 Å)) was used to analyze the phase composition of the as prepared SnO_2/graphene sample. Raman microspectroscopy (HORIBA Scientific LabRAM HR Raman spectrometer) was conducted under ambient condition with an incident laser beam at 532.03 nm. The SnO_2 contents (wt %) in the composites were determined by thermogravimetric analysis (TGA; Netzsch) with a heating rate of 10 ^oC min^{-1} in air from room temperature to 900 ^oC. Field emission scanning electron spectrometry (FE-SEM, Hitachi 4800S) coupled with energy dispersive spectroscopy (EDS), transmission electron microscope (TEM, Hitachi H-7000), and high resolution TEM (HRTEM, JEOL 2010 FEG microscope) were used to characterize the microscopic features. The XANES experiments on the Sn $M_{5,4}$, O K edge and C K edge were conducted on the undulator Spherical Grating Monochromator (SGM) beamline at the Canadian Light Source (CLS) located at the University of Saskatchewan in Saskatoon. XANES were recorded in total electron yield (TEY) using specimen current and X-ray fluorescence yield (FLY) using a Multi-Channel Plate [23].

4.2.3 Electrochemical Measurement

To evaluate the electrochemical performance of the composites, the samples were mixed with conductive carbon black and polyvinylidene fluoride in a weight ratio of 80:10:10 in N-methylpyrrolidinone (NMP) solvent. Then the slurry was uniformly cast on a copper foil (loading of SnO_2/Graphene is 0.67 mg/cm^2) and dried at 70 ^oC under vacuum overnight. The coin cells were assembled inside an argon-filled glove box using lithium metal foil as the counter electrode and the polypropylene as the separator. The electrolyte was 1M $LiPF_6$ dissolved in ethylene carbonate (EC) and dimethyl carbonate (DMC) solvent (1:1 volume ratio). The cells were tested on a computer controlled battery tester system (Arbin BT-2000). The profiles of galvanostatically charging and discharging curves were obtained at a voltage range of 0.01 to 3 V (vs. Li^+/Li) at a current density of 60 mA g^{-1}. Cyclic voltammetry (CV) measurements were performed on an electrochemical workstation (Potentiostat/Galvanostat/EIS (VMP3)) over the potential range of 0.01–3.0 V (vs. Li^+/Li) at a scanning rate of 0.1 mV s^{-1}. Electrochemical impedance spectroscopy (EIS) measurements were conducted by applying an AC voltage of 5 mV amplitude in the frequency range from 0.01 to 100 KHz at 0.7 V of the 10th discharge cycle.

4.3 Results and Discussion

Figure 4.1 presents the fabrication process of SnO_2/graphene composites. With this advanced MAHM technique, hybrid SnO_2/graphene nanocomposites were obtained within only one hour. Tin (II) chloride underwent rapid hydrolysis with the assistance of microwave heating and were transformed to $Sn(OH)_2$, which were then quickly oxidized to SnO_2 by the residue oxygen in the Teflon vessels at 200 ^oC.. Meanwhile, the fast reaction rate effectively inhibited possible aggregation of SnO_2 nanoparticles and the stacking of GNSs. A possible mechanism for the reaction was described in the following equations.

$$SnCl_2 + 2H_2O \xrightarrow{\text{hydrolysis}} Sn(OH)_2 + 2HCl \qquad (1)$$

$$2Sn(OH)_2 + O_2 \xrightarrow{\text{oxidation}} 2SnO_2 \ + 2H_2O \qquad (2)$$

The XRD patterns of GNSs and as-prepared SnO_2/graphene nanocomposite are illustrated in Figure 4.2a. All strong diffraction peaks in Figure 4.2a (top line) are consistent with tetragonal crystalline SnO_2 (JCPDS No. 41-1445) [4]. It is noted that there is no obvious GNSs patterns in the composites [21], due to the overlap of the diffraction peak for graphene (002) facet with that of (110) facet for SnO_2, and also the relatively weak intensity (bottom line) compared with SnO_2. The broad diffraction patterns indicate small particle size of the deposited SnO_2. Based on the (101) peak of SnO_2, the average crystal size is around 3.5 nm according to Scherrer’s equation.

The SnO_2/graphene composite was examined by Raman spectroscopy in comparison to GNSs. As shown in Figure 4.2b, the peaks at 1340 cm^{-1} and 1582 cm^{-1} are both observed, which stand for the D band and the G band, respectively [24,25]. It is noteworthy that the intensity ratio of I_D/I_G for the SnO_2/graphene composites is almost the same as GNSs, indicating no modification in the average size of the sp^2 graphitic domains in the composites. Thus SnO_2 nanocrystals did not change the pristine laminated structure of GNSs. For the SnO_2/graphene composites, it shows three visible Raman peaks at 472, 633, and 775 cm^{-1}, corresponding to the E_g, A_{1g}, and B_{2g} vibration modes of the rutile SnO_2 structure, respectively [26].

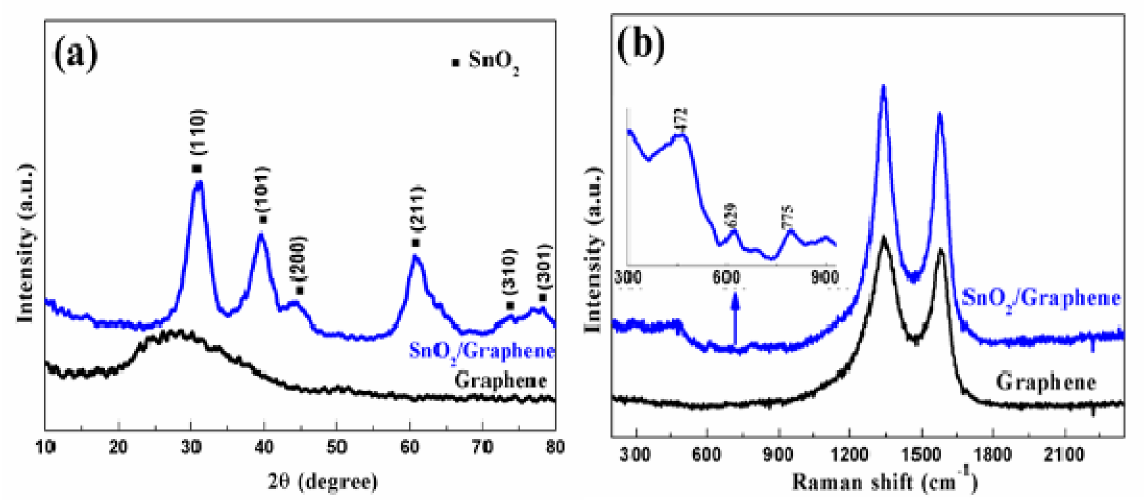

Figure 4.2 Characterization of graphene and as- prepared SnO$_2$/graphene nanocomposites: a) XRD spectra b) Raman spectra

The typical top view SEM image of GNSs is presented in Figure 4.3a. Obviously, the layered platelets composed of curled nanosheets are displayed, which are representative of GNSs. FE-SEM and TEM have been employed to unveil the morphology of the composites. It is also apparent from Figure 4.3b that the GNSs are uniformly covered by the ultra fine SnO$_2$ nanoparticles, which can be confirmed by TEM images (Figure 4.3c). Dark field TEM image of SnO$_2$/graphene composites (Figure SI 4.1) also reveals the homogeneous distribution of SnO$_2$ nanoparticles. A closer examination of the nanocomposites shown in Figure 4.3d confirms that the average size of highly dispersed SnO$_2$ nanoparticles is around 3.47 nm, close to the value calculated from the XRD pattern (3.50 nm); moreover, the HRTEM images displays two distinguishable images, linear strips of GNSs and spherical SnO$_2$ nanoparticles. The d-spacing of GNSs is estimated to be about 0.38 nm, which is much larger than that of the pristine graphite (0.34 nm), while the inter-planar distances of 0.34 and 0.24 nm can be identified as d (110) and d (200) of SnO$_2$ nanoparticles, respectively. According to the selected area electron diffraction (SAED) pattern (inset of Figure 4.3d), four distinct diffraction rings stand for the (110), (101), (200) and (210) crystalline planes of SnO$_2$, confirming the highly crystalline feature of SnO$_2$ nanoparticles. The crystalline feature for SnO$_2$ nanoparticle could also be clearly seen from the high angle annular dark field scanning transmission electron microscopy images (Figure SI 4.2). Such nanocomposites based on the 3D GNSs electronic conductive network have good electronic conductivity, and can better facilitate the immersion of electrolyte due to the considerable surface area. Also, it is worthy to mentioning that the widespread dispersed SnO_2 on GNSs could make full use of the GNSs as an excellent matrix to buffer the volume change of the Sn lattice during cycling. All these advantages in structure could contribute to improve the battery performance of SnO_2 anode for LIBs.

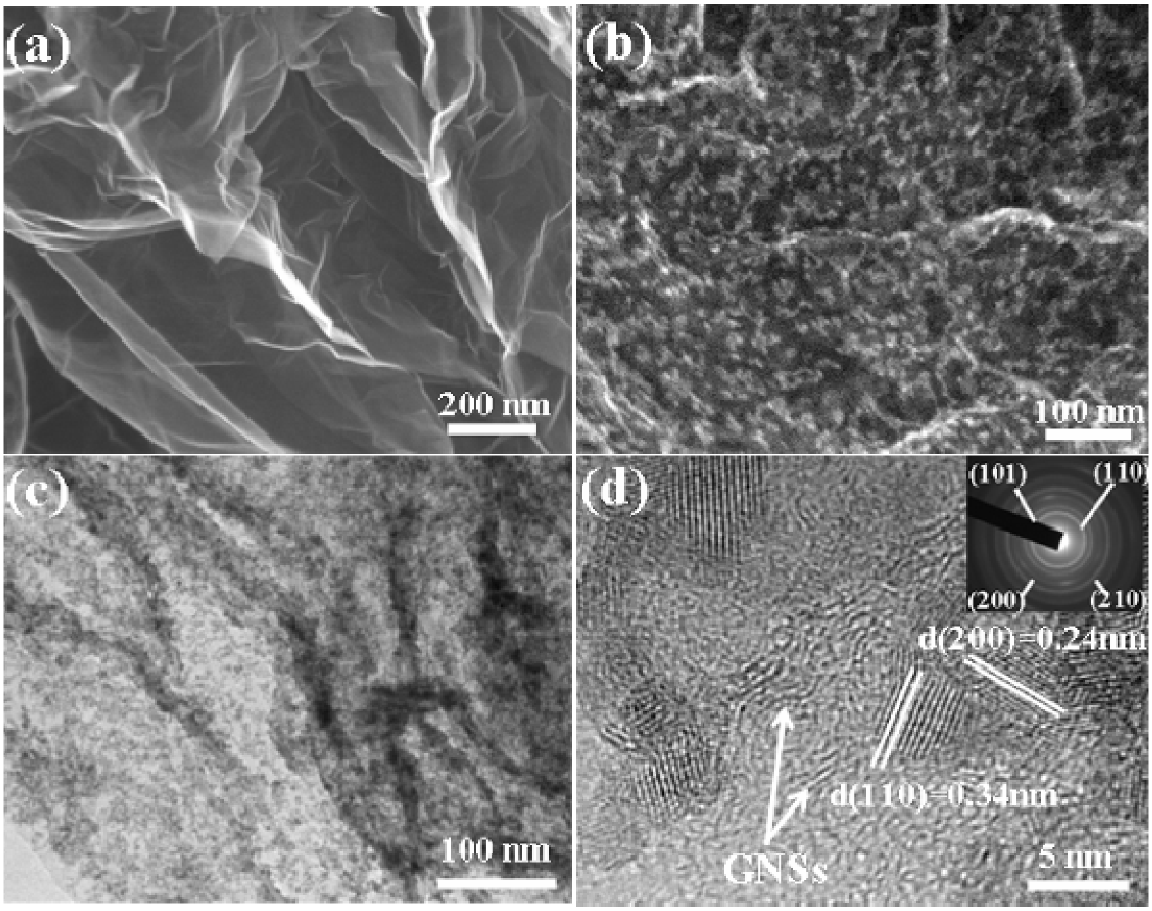

Figure 4.3 SEM images of (a) GNSs and (b) SnO_2/Graphene nanocomposites; (c) TEM image and (d) HRTEM image of SnO_2/Graphene nanocomposites. The inset in panel (d) is SAED patterns.

In order to define the SnO_2 contents (wt %) in the as-prepared SnO_2/graphene composite, thermal gravimetric analysis (TGA) was performed in the temperature range from room temperature to 900 ^{o}C in air. GNSs in the SnO_2/graphene nanocomposites are oxidized to CO_2 from 200 ^{o}C to 600 ^{o}C with a corresponding weight loss of 37% (as shown in Figure SI 4.3). Thus the content of SnO_2 in the nanocomposites is 63%. According to the amount of starting precursor $SnCl_2$ and GNSs, the designated weight percentage for SnO_2 in the composites is 64.5%. Thus, the conversion of the $SnCl_2$ is nearly 98%, illustrating high efficiency and controlled composition design of the microwave assisted hydrothermal system.

Exploring how SnO_2 nanoparticles are immobilized on the GNSs is very helpful to understand the hybrid structure for achieving the enhanced performance. Here, we investigated the unusual electronic properties of nanosized SnO_2 especially after its application to the hybrid structure with GNSs by XANES, which is very sensitive to the local chemical environment of the element.

Figure 4.4 shows the O K-edge and the Sn $M_{5,4}$ edge XANES spectra for SnO_2/graphene measured in Total Electron Yield (TEY) and Fluorescence Yield (FLY). These spectra track the unoccupied densities of states (DOS) of the atom of interest in the composite via dipole transitions. Thus the O K and Sn $M_{5,4}$ edge tracks the unoccupied DOS of O and Sn P character, respectively. In addition, TEY and FLY provides surface and bulk sensitivity. From the O K edge XANES (Figure 4.4a), the FLY spectrum tracks that of TEY, i.e. all exhibit positive edge jump with no noticeable broadening in the FLY. This observation indicates that the sample is sufficient thin comparing with the absorption cross-section at the O K-edge. It should be noted that for small edge jump relative to the pre-edge absorption, FLY often suffers thickness effect (self-absorption) resulting in noticeably broadening and even an inversion (see Sn $M_{5,4}$ edge discussion below). These spectral features arise from O 1s to 2p transition, probing the unoccupied densities of state of O 2p character in the conduction band. The Sn $M_{5,4}$ edge XANES (Figure 3b) corresponds to electron transitions from Sn 3d to the conduction band of Sn 5p character. Two sets of triplets peaks beginning at ~ 490 eV and 498 eV were observed, corresponding to $3d_{5/2}$ and $3d_{3/2}$ to $5p_{3/2}$ and $5p_{3/2,1/2}$ transitions, respectively. These are characteristic of rutile SnO_2 nanostructure features, in good agreement with previous results [27]. The Sn $M_{5,4}$ edge tracked by the two yields (TEY and FLY) are however dissimilar; in fact FLY is inverted due to self absorption. As noted above, inversion can occur in FLY in soft X-ray spectroscopy when the sample is thick relative to the penetration depth (often describe as the 1/e, or one-absorption length of the specimen) and the edge jump is very small relative to the absorption below the edge. A simple calculation using the X-ray calculator shows that for SnO_2, the Sn $M_{5,4}$ edge jump, $(\mu_{above} - \mu_{below}) / \mu_{below}$, is ~ 4% while the O K-edge jump is a factor of ~ 10.

Returning to the TEY spectrum of the Sn $M_{5,4}$ edge, we clearly see a pre-edge resonance at 488.1 eV just below the Sn M_5 edge, which is absent in bulk SnO_2. This peak has been previously attributed to surface or defects states caused by unsaturated coordination of surface Sn ions due to oxygen vacancies [28]. In the FLY spectrum which is bulk sensitive, a small “concave” (opposite of “bump”) also appeared at “488.1 eV”, demonstrating that the whole specimen containing SnO_2 nanoparticles is rich in surface or defects states due to their small size [29] and large surface to volume ratio. Such abundant surface states will likely facilitate charge redistribution and transport between SnO_2 and GNSs.

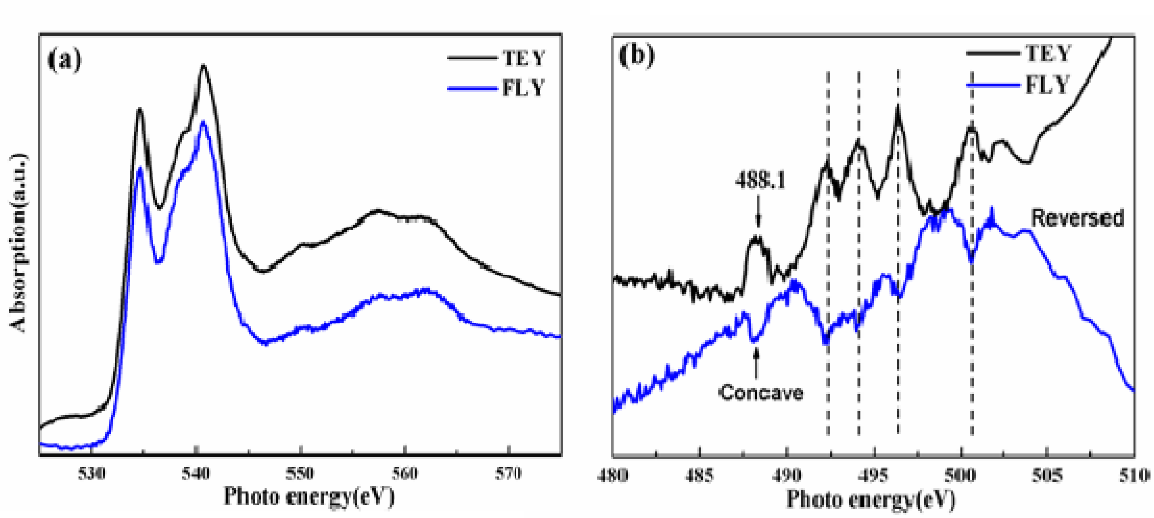

Figure 4.4 XANES region of the XAS spectra of the SnO_2/graphene composites: O K edge; (b) Sn $M_{5,4}$ edge, the FLY is inverted due to self absorption

In order to further clarify the interaction, carbon K-edge XANEs was also performed on SnO_2/graphene composites and compared with pure GNSs in TEY mode, as shown in Figure 4.5. Similar graphitic π* transition and σ* transition at 291.5 and 292.5 eV could also be tracked for SnO_2/graphene composites, indicating that graphene still keeps the graphitic framework intact after hybridization with SnO_2. The broad peak b centered at 288.3 eV reflects the resonance from carboxylic group, a chemical defect often found in graphitic systems such as nanotube and graphene [30]. More intriguingly, following interesting features unveiled the interaction between SnO_2 and GNSs: First, for peak a (π* transition which is proportional to unoccupied density of states), the intensity decreased after SnO_2 deposited on GNSs compared with pure GNSs, illustrating that n typed SnO_2 semiconductor donate electrons to 2p-derived π* states of GNSs. Second, SnO_2/graphene exhibits a more intense resonance for peak b compared with pure GNSs, the enhanced carboxylate bonding at 288.3 eV should be interpreted as interaction of SnO_2 with GNSs through chemical bonding. Third, as indicated in the inset spectrum, which shows the magnified spectrum of the red square region, it exhibits a slight energy shift of 0.15 eV to lower photon energy for composites compared with that of pure GNSs, consistent with the interpretation that carbon atoms of GNSs accept the electrons donated by SnO_2 nanopaticles. This further confirms that charge redistribution indeed takes place between SnO_2 and GNSs. It is conceivable that defect rich SnO_2 play an important role in immobilizing itself onto GNSs via electro static or electronic interaction to form a "Sn-OO-C" bond through the carboxylic functional group. This notion is in good agreement with recent work of SnO_2 nanoparticles on carbon nanotubes [30]. As a result, since SnO_2 is anchored onto GNSs intimately through spectroscopic evidence, enhanced electrochemical performance could be expected. A schematic for illustrating the chemical bonding and charge redistribution between nanoparticles and graphene is shown in Figure 4.5b.

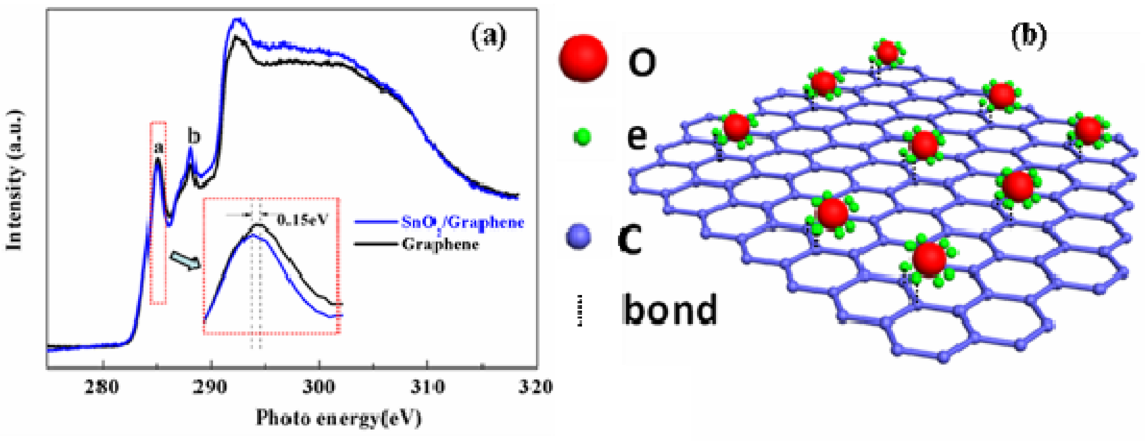

Figure 4.5 (a) Carbon K edge XANES spectra of the SnO_2/graphene composites and graphene. The inset indicates the energy shift (b) Schematic of the interaction between GNSs and nanoparticles

To evaluate the electrochemical reactivity of the SnO_2/graphene composites, cyclic voltammetry was performed, as shown in Figure 4.6a. In the first cycle, two obvious peaks appeared in the cathodic process, located around 0.8 and 0.12 V. The peak at around 0.8 V is attributed to the reduction of SnO_2 to Sn, the synchronous product of Li_2O (Eq. (1)) and the formation of solid electrolyte interface (SEI) layer [29]. The peak at 0.12 V occurs from the formation of a series Li_xSn alloys (Eq. (2)). For the anodic process, two oxidation peaks around 0.12 V and 0.57 V stand for the lithium extraction from the GNSs (Eq. (3)) and dealloying of the Li_xSn (Eq. (2)), respectively. It is interesting to note that one distinguished oxidation peak at 1.27 V shows up, demonstrating that Eq. (1) is partially reversible [31-34], resulting in the decomposition of Li_2O. Accordingly, the reduction peaks at 1.15 V for the second and third cycles are attributed to the formation of Li_2O again.[9]

$$SnO_2 + 4Li^+ + 4e \longrightarrow 2Li_2O + Sn \qquad (1)$$

$$Sn + xLi^+ + xe^- \longleftrightarrow Li_xSn \ (0 \leqslant x \leqslant 4.4) \qquad (2)$$

$$C(\text{graphene}) + xLi^+ + xe^- \longleftrightarrow Li_xC \qquad (3)$$

Figure 4.6b presents the charge and discharge profiles of the composites at a current density of 60 mA g^{-1} with a voltage range of 0.01 V ~ 3V. The initial small plateau in the potential range of 1.2 V to 0.8 V stands for classical conversion reaction between SnO_2 and Li^+, resulting in the formation of Sn and Li_2O in the first discharge process. This is in accordance with the cathodic peak around 0.8 V in the CV curves. The following long slope profiles of SnO_2/graphene nanocomposites indicated the formation of Li-Sn alloys and Li^+ intercalation into GNSs. The plateau (from 1.2 to 0.8 V) almost disappears at the second cycle, demonstrating that major Li_2O is formed in the first cycle. Because of this irreversible reaction as well as the SEI formed on the anodes [4], the discharge capacity dropped from 1688 mAh g^{-1} to 911 mAh g^{-1} in the first two cycles.

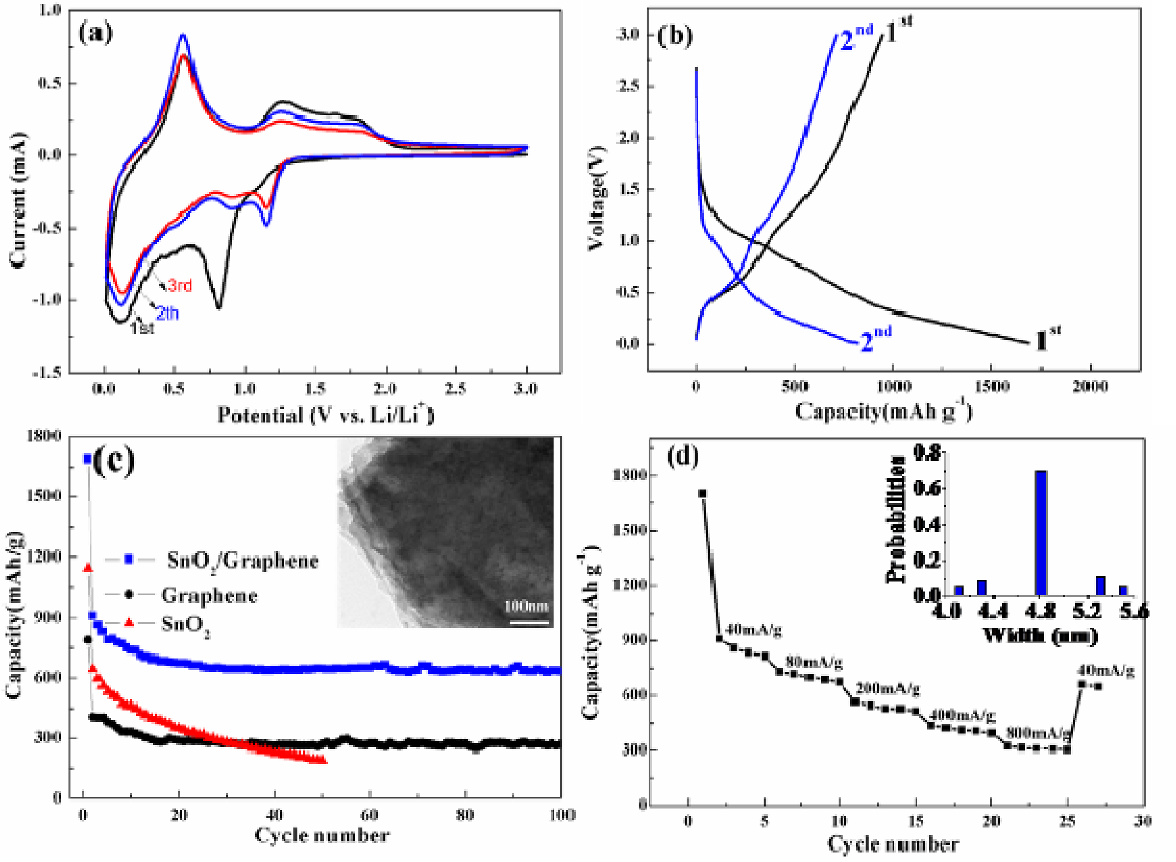

Figure 4.6 Electrochemical performance of SnO_2/graphene composites: (a) Cyclic Voltammetry (CV). (b) First two Charge-discharge profiles. (c) Cycle performance plots of bare graphene, SnO_2 and SnO_2/graphene composites at 60mA g^{-1}, inserted TEM image shows the morphology of nanocomposites electrodes after cycling. (d) Rate performance and inset shows size distribution of nanoparticles in composites after cycling.

Cyclic performance of SnO_2/Graphene nanocomposite is illustrated in Figure 4.6c in comparison with that of the pure GNSs anode. GNSs delivered a specific capacity of 784 mA h g^{-1} in the first discharge and exhibited an obvious fading at the second cycle, retaining only 270 mA h g^{-1} in the 100th cycle. As we mentioned in the introduction section, the SnO_2 anode with high capacity has an obvious disadvantage of the large volume change upon repeating cycling. As a result, the pure SnO_2 nanoparticles result in very low capacity retention that it can reach a reversible capacity of only 191 mA h g^{-1} in the 50th cycle. As for the composites, the initial reversible discharge capacity is 911 mA h g^{-1}. As the result of the anchoring of the SnO_2 nanoparticles on the matrix of GNSs in the nanocomposite, the cycle performance has been greatly improved and the capacity remains almost constant after the 15th cycle. At the 100th cycle, the discharge capacity still remains 635 mA h g^{-1}， which is about 70% retention of the reversible capacity. The coulombic efficiency of SnO_2/Graphene (as shown in Figure SI 4.4) at the first cycle is around 44% and then keeps increasing. It is over 95% after 12 cycles and maintains a high coulombic efficiency of more than 99% in further cycles. It is well known that SnO_2 anode suffers the huge volume change during the cycling, resulting in rapid capacity fading [4, 5]. Here, the minimized aggregation of GNSs due to the jamming of SnO_2 nanoparticles, spatially separating SnO_2 nanoparticles, hence 3D confinement of SnO_2 nanoparticles by GNSs are beneficial for achieving better cycling performance. Besides, the SnO_2 nanoparticles and the elastic GNSs in the hybrid SnO_2/graphene nanocomposites not only help release the stress formed during the lithium insertion process, but also decrease the pulverization. Clearly, the graphene as a good matrix can provide the important function in buffering volume change of SnO_2 anode, thereby enhancing its cycling stability.

The TEM image in the inset of Figure 4.6c shows the morphology of the nanocomposite electrode after 100 cycles at 60 mA g^{-1}. It reveals that the fine Sn nanoparticles remained highly dispersive in the GNSs matrix without any obvious volume change. The average size of nanopariticles is around 4.8 nm (the inset of Figure 4.6d), which is very close to that of initial particle size, indicating no obvious aggregation during cycling. This observation indicates that Sn nanopatciles are tightly pinned onto the GNSs and the detrimental agglomeration of nanoparticles was effectively alleviated to a large extent. More importantly, it is evident that dimensionally flexible GNSs can effectively accommodate the Sn volume change, and inhibits the pulverization of Sn, thus maintaining the integrity of the whole electrodes.

Figure 4.6d shows the rate capability of the nanocomposites from a current density of 40 up to 800 mA g^{-1}. The SnO_2/graphene nanocomposite displays an excellent rate capability. The SnO_2/graphene nanocomposite is still capable of delivering a substantial capacity of 717, 566 and 435 mA h g^{-1} at the high current densities of 80, 200 and 400 mA g^{-1}, respectively. Even when the highest current density of 800 mA g^{-1} was applied, the composites still exhibited a high reversible capacity of 330 mA h g^{-1}. It should be noted that when the current rate was reversed back to low current after 25 cycles, the specific discharge capacity of 711 mA h g^{-1} could be obtained, indicating that 73% of the initial reversible capacity (971 mA h g^{-1}) was recovered again. This result clearly demonstrates that the SnO_2/graphene nanocomposites could tolerate varied discharge current densities, which is a desirable characteristic for high power application. It thus appears that 3D GNSs would work as a highly conductive matrix when anchored by highly dispersed SnO_2 nanoparticles. Also, the ultrafine SnO_2 nanoparticles can shorten the transport path for both lithium ions and electrons thus realizing the high rate capability.

Figure 4.7 shows the electrochemical impedance spectroscopy for pure SnO_2 and SnO_2/GNSs electrodes, performed at 0.7 V at the 10th discharge cycle. A possible equivalent circuit is given in the inset of Figure 4.7 for interpretation. Re denotes electrolyte ohmic resistance, while Rsl is the resistance for Li^+ migration through the SEI film, C_{dl} and C_{sl} represents the double layer capacitance and passivation film capacitance, respectively. W is the finite length Warburg impedance and R_{ct} stands for the charge transfer resistance [31]. The values of R_e, R_{sl} and R_{ct} are obtained from the simulated data of EIS in Figure 4.7. It can be clearly seen that the diameter of the semicircle for SnO_2/GNSs is much smaller than that for pure SnO_2, indicating that the impedance value of SnO_2 nanoparticle is higher than SnO_2/GNSs nanocomposites. After simulation by the equivalent circuit, it is found that R_{ct} of SnO_2 and SnO_2/GNSs is 479.31 Ω and 51.93 Ω, respectively. The decreased resistance indicates the enhanced ionic conductivity in the composite, which is beneficial for Li^+ insertion/extraction into the anodes. By fine tuning the discharge and charge profiles, the SnO_2/graphene nanocomposites are expected to be promising candidates for high performance anode materials for LIBs.

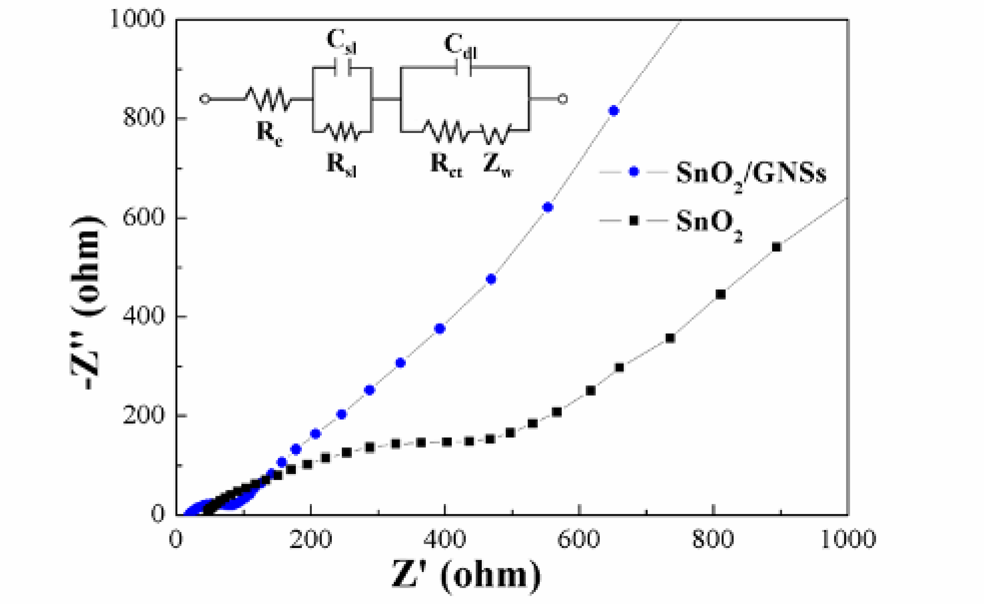

Figure 4.7 Electrochemical impedance spectra of (a) SnO_2 and (b) SnO_2/GNSs, inset: the equivalent circuit to fit the EIS.

4.4 Conclusions

In summary, 3D SnO_2/graphene nanocomposites were successfully synthesized by a rapid and facile MAHM method. Spatially separated SnO_2 nanoparticles were uniformly loaded on GNSs with content as high as 63 wt%. The electronic structure of the small rutile SnO_2 nanoparticles (~3.5 nm) have been investigated by XANES, showing that the SnO_2 nanoparticles dispersed on GNSs are abundant of surface and defects states, facilitating the immobilization of the SnO_2 onto GNSs. Carbon K edge XANEs features further identify strong interaction (e.g. chemical bonding, charge redistribution) between SnO_2 and GNSs. The resulting SnO_2/graphene composites exhibit a high reversible lithium storage capacity of 653 mA h g^{-1} in the 100th cycle at 60 mA g^{-1}. Furthermore, the nanocomposites can still maintain the discharge capacity as high as 313 mAh g^{-1} even cycled at high current density as high as 800 mA g^{-1}. Such outstanding performance demonstrates that the SnO_2/graphene nanocomposites systems reported here can be potential anodes for LIB in EV and HEV applications. Also, this work could open a new pathway for identifying interaction happened in nanocomposite electrodes for LIB by XANES.

4.5 Acknowledgements

This research was supported by Natural Sciences and Engineering Research Council of Canada (NSERC), General Motors of Canada, Canada Research Chair (CRC), Canada Foundation for Innovation (CFI), Ontario Innovation Trust (OIT) Program and University of Western Ontario. The Canadian Light Source is supported by CFI, NSERC, NRC, CHIR, and the University of Saskatchewan. The technical assistance of Tom Regier and David Chevrier of the Canadian Light Source is gratefully acknowledged.

4.6 References

[1] Cheng, B.; Russell, J. M.; Shi, W. S.; Zhang, L.; Samulski, E. T. *J. Am. Chem. Soc.* **2004**, *126*, 5972-5973.

[2] Dai, Z. R.; Pan, Z. W.; Wang, Z. L. *Adv. Funct.Mater.* **2003**, *13*, 9-24.

[3] Zhang, D. F.; Sun, L. D.; Jia, C. J.; Yan, Z. G.; You, L. P.; Yan, C. H. *J. Am. Chem. Soc.* **2005**, *127*, 13492-13493.

[4] Paek, S. M.; Yoo, E. J.; Honma, I. *Nano Lett.* **2009**, *9*, 72-75.

[5] Idota, Y.; Kubota, T.; Matsufuji, A.; Maekawa, Y.; Miyasaka, T. *Science* **1997**, *276*, 1395-1397.

[6] Lou, X. W.; Li, C. M.; Archer, L. A. *Adv. Mater.* **2009**, *21*, 2536-2539.

[7] Park, M. S.; Wang, G. X.; Kang, Y. M.; Wexler, D.; Dou, S. X.; Liu, H. K. *Angew. Chem., Int. Ed.* **2007**, *46*, 750-753.

[8] Liu, J.; Li, Y.; Huang, X.; Ding, R.; Hu, Y.; Jiang, J.; Liao, L. *J. Mater. Chem.* **2009**, *19*, 1859-1864.

[9] Han, S.; Jang, B.; Kim, T.; Oh, S. M.; Hyeon, T. *Adv. Funct. Mater.* **2005**, *15*, 1845-1850.

[10] Wen, Z.; Wang, Q.; Zhang, Q.; Li, J. *Adv. Funct. Mater.* **2007**, *17*, 2772-2778.

[11] Zhang, H. X.; Feng, C.; Zhai, Y. C.; Jiang, K. L.; Li, Q. Q.; Fan, S. S. *Adv. Mater.* **2009**, *21*, 2299-2304.

[12] Wang, Y.; Lee, J. Y. *J. Power Sources* **2005**, *144*, 220-225.

[13] Yuan, L.; Konstantinov, K.; Wang, G. X.; Liu, H. K.; Dou, S. X. *J. Power Sources* **2005**, *146*, 180-184.

[14] Novoselov, K. S.; Geim, A. K.; Morozov, S. V.; Jiang, D.; Zhang, Y.; Dubonons S. V.; Grigorieva, I. V.; Firsov, A. A. *Science* **2004**, *306*, 666-669.

[15] Novoselov, K. S.; Geim, A. K.; Morozov, S. V.; Jiang, D.; Katsnelson, M. I.; Grigorieva, I. V.; Dubonons, S. V.; Firsov, A. A. *Nature* **2005**,*438*, 197-200.

[16] Berger, C.; Song, Z. M.; Li, X. B.; Wu, X. S.; Brown, N.; Naud, C.; Mayou, D.; Li, T. B.; Hass, J.; Marchenkov, A. N.; et al. *Science* **2006,** *312,* 1191-1196.

[17] Li, X.; Meng, X.; Liu, J.; Geng, D.; Zhang, Y.; Banis, M.; Li, Y.; Li, R.; Sun, X.; Cai, M.; et al. *Adv. Funct. Mater.* **2012**, *22*, 1647-1654.

[18] Li, F. H.; Song, J. F.; Yang, H. F.; Gan, S. Y.; Zhang, Q. X.; Han, D. X.; Ivaska, A.; Niu, L. *Nanotechnology* **2009**, *20*, 455602.

[19] Yao, J.; Shen, X. P.; Wang, B.; Liu, H. K.; Wang, G. X. *Electrochem. Commun.* **2009**, *11*, 1849-1852.

[20] Zhang, M.; Lei, D. N.; Du, Z. F.; Yin, X. M.; Chen, L. B.; Li, Q. H.; Wang, Y. G.; Wang, T. H. *J. Mater. Chem.* **2011**, *21*, 1673-1676

[21] Lian, P. C.; Zhu, X. F.; Liang, S. Z.; Li, Z.; Yang, W. S.; Wang, H. H. *Electrochem. Acta* **2011**, *56*, 4532-4539

[22] Hummers, W. S.; Offeman, R. E. *J. Am. Chem. Soc.* **1958**, *80*, 1339.

[23] Regier, T.; Paulsen, J.; Wright, G.; Coulthard, I.; Tan, K.; Sham, T. K.; Blyth, R. I. R. *AIP Conf. Proc.* **2007**, *879,* 473-476.

[24] Tuinstra, F.; Koenig, J. L. *J. Chem. Phys.* **1970**, *53*, 1126-1130.

[25] Ferrari, A. C.; Robertson, J. *Phys. Rev. B* **2000**, *61*, 14095-14107.

[26] Peercy, P. S.; Morosin, B. *Phys. Rev. B* **1973**, *7*, 2779-2786.

[27] Zhou, X. T.; Heigl, F.; Murphy, M. W.; Regier, T.; Coulthard, I.; Blyth, R. I. R.; Sham, T. K. *Appl. Phys. Lett.* **2006**, *89*, 213109.

[28] Zhou, X. T.; Zhou, J. G.; Murphy, M. W.; Ko, J. Y. P.; Heigl, F.; Regier, T.; Blyth, R. I. R.; Sham, T. K. *J. Chem. Phys.* **2008**, *128*, 144703.

[29] Kucheyev, S. O.; Baumann, T. F.; Sterne, P. A.; Wang, Y. M.; Van Buuren, T.; Hamaza, A. V.; Terminello, L. J.; Willey, T. M. *Phys. Rev. B* **2005**, *72*, 035404.

[30] Zhou, J. G.; Wang, J.; Fang, H. T.; Sham, T. K. *J. Mater. Chem.* **2011**, *21*, 5944-5949.

[31] Lou, X. W.; Chen, J. S.; Chen, P.; Archer, L.A. *Chem. Mater*. **2009**, *21*, 2868-2874.

[32] Poizot, P.; Laruelle, S.; Grugeon, S.; Dupont, L.; Tarascon, J. M. *Nature* **2000**, *407*, 496-499.

[33] Gao, M.; Chen, X.; Pan, H.; Xiang, L.; Wu, F.; Liu, Y. *Electrochem. Acta* **2010**, *55*, 9067-9074.

[34] Titirici, M. M.; Hu, Y. S.; Demir-Cakan, R.; Maier, J.; Antonietti, M. *Chem. Mater.* **2008**, *20*, 1227-1229.

4.7 Supporting Information

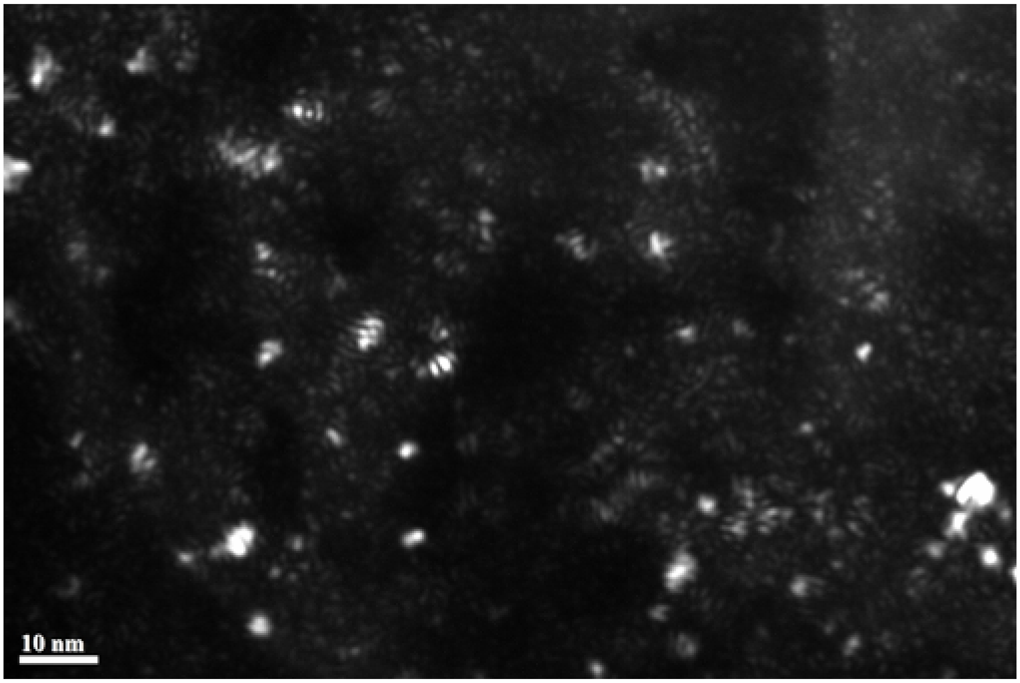

Figure SI 4.1 Dark field TEM image of SnO_2/graphene composites

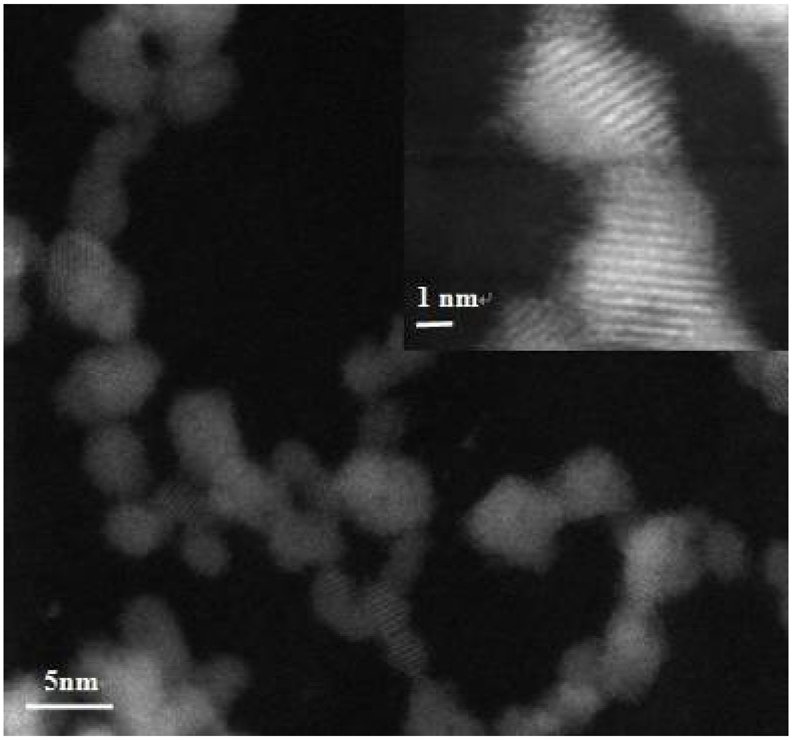

Figure SI 4.2 STEM HAADF images of SnO_2/graphene composites

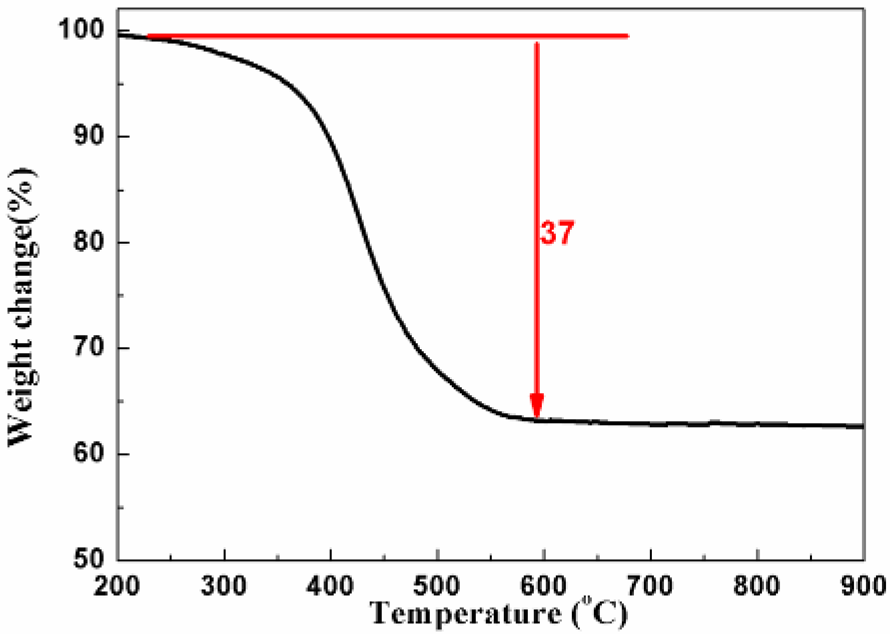

Figure SI 4.3 TGA curve of SnO_2/graphene composites.

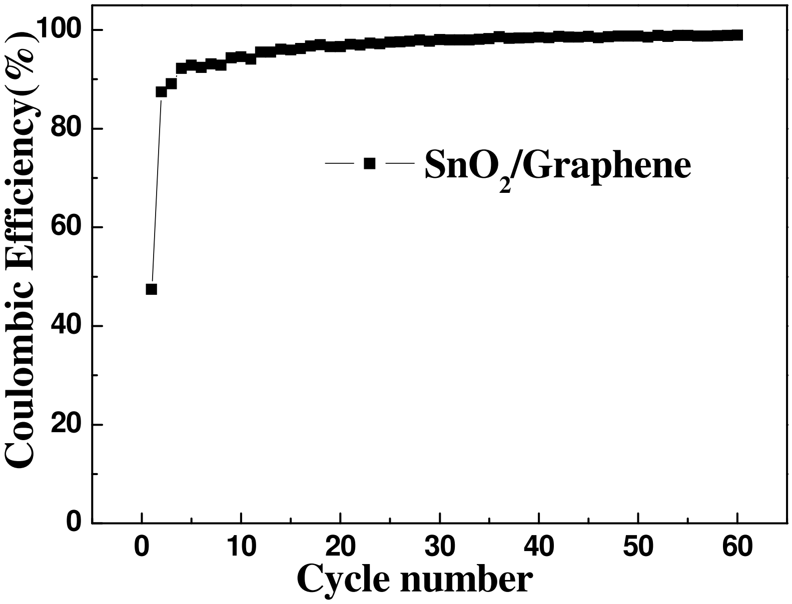

Figure SI 4.4 Coulombic efficiency of SnO_2/Graphene composites

Chapter 5

5 Layer by Layer Assembly of Sandwiched Graphene/SnO_2 Nanorod/Carbon Nanostructures with Ultrahigh Lithium Ion Storage Properties

Based on study in previous chapter on SnO_2 nanoparticles on graphene composites, it is found that the exposure of SnO_2 to electrolyte still exists which will cause irreversible capacity loss. Therefore, we aimed at developing sandwiched carbon coated SnO_2 naorod rooted on graphene composites to provide intact protection for SnO_2.

In this chapter, the sandwiched structures consisting of carbon coated SnO_2 nanorod grafted on garphene have been synthesized based on a seed assisted hydrothermal growth to form graphene supported SnO_2 nanorod, followed by a nanocarbon coating. As a potential anode for high power and energy applications, the hierarchical nanostructures exhibit greatly enhanced synergic effect with an extremely high lithium storage capability of up to 1419 mAh g^{-1} benefiting from the advanced structural features.

KEYWORDS: graphene, lithium ion batteries, XANES, sandwiched structure

---

Part of the content in this chapter has been published.

D. Wang, J. Yang, X. Li, D. Geng, R. Li, M. Cai, T.-K. Sham, X. Sun. *Energy Environ. Sci.,* **2013**, DOI:10.1039/C3EE40829A. (Back Cover page)

5.1 Introduction

Among various energy storage devices, lithium ion batteries (LIBs) have been intensely studied in recent years in connection with the continuously surging market demand for electric vehicles in terms of its high energy density, friendliness to the environment and acceptable high power density [1-3]. In order to store and transport energy more efficiently, a great deal of effort has been made on seeking and developing high performance LIBs, which mainly focuses on choice of electrodes and design of materials structure. Tin based anodes are regarded as attractive candidates considering its low charge/discharge potential and the high theoretical capacities [4, 5], for example, SnO_2 have specific capacity of about 780 mA h g^{-1} [6], which is more than twice that of commercialized graphite. However, similar to other high capacity anodes such as silicon [7, 8] and germanium [9, 10], the large volume changes (359%) between the fully alloyed and dealloyed states lead to pulverization and severe destruction of the electrode, resulting in fast fading of the capacity.

So far, two main mitigation strategies have been applied; one way is to exploit the structure-dependent properties of SnO_2 anodes [11]. Intensive studies have been carried out and a series of versatile SnO_2 nanostructures, such as nanoparticles [12, 13], nanowires [5], nanotubes [14], hollow nanospheres [6, 15], and nanocubes [16, 17], are found to be more sustainable to huge volume change during cycling. However, large-scale productions are hampered both in costly template [13, 18] or surfactant [17] and the requirement of retooling the current equipment. More importantly, the destruction of the desirable morphologies for electrodes could not be truly avoided especially at long cycles and high rate.

Another approach is to focus on fabricating hybrid nanostructures by embedding active tin-based materials into or immobilizing them onto soft and conductive matrix [19-24]. The highly flexible matrix could buffer the large volume expansion and contraction during cycling to keep the integrity of the whole electrodes intact. Recently, graphene based materials have received enormous attention due to its intriguing and desirable features such as large surface area (> 2630 m^2/g), excellent electronic conductivity, superior mechanical flexibility, and high theoretical capacity (784 mA h g^{-1}) [25, 26]. In our group, the graphene-based electrodes have been widely used in Li ion batteries and Li-Air batteries [27]. It is also believed that it will function as an appealing host to homogeneously anchor preferred target materials through its oxygen functionalized groups such as carbonyl (C=O) and cabonoxylic (C-OOH) bonds [27a, 28]. Lots of high performance electrode materials have been realized through combining active materials with graphene including Fe_3O_4/graphene [29], Co_3O_4/graphene [30], Ge/graphene [31], and Si/graphene [32].

Recently, the idea of designing hierarchical nanostructure for LIB has been implemented by several groups and has led to superior electrochemical performance [27a, 33-37]. Interestingly, in these hierarchical nanostructures, experimental capacity higher than theoretical capacity calculated according to a sum of contribution from each component is usually obtained and such phenomenon is often attributed to the enhanced synergetic effect benefiting from the unique hierarchical nanostructure. Recent results have proved the success and wide adaptability of this concept among various materials systems including SnO_2 nanoparticle [33] or SnO_2 nanosheets [34] on Graphene, SnO_2@C core-shell structures [35] or hierarchical Sn@C nanoparticles [36] on Graphene, carbon coated SnO_2 nanoparticle on CNTs [37] or Graphene [38], multilayered Sn-nanopillar arrays on graphene [39], carbon-coated a-Fe_2O_3 hollow nanohorns on the CNTs backbone with excellent electrochemical performances [40].

In this paper, we report a sandwiched hierarchical nanostructure composed of carbon coated SnO_2 nanorods grafted on the two dimensional (2D) surface of graphene (G/SnO_2 NR/C) based on the above mentioned idea. Starting from SnO_2 nanoparticle/Graphene (G/SnO_2 NP) composites obtained via microwave-assisted hydrothermal method, followed by seed-assisted tin oxide nanorod growth on graphene and subsequent carbon layer coating on top, the layer by layer assembled sandwiched G/SnO_2 NR/C were synthesized for the first time to the best of our knowledge. The 2D graphene network combined with the outmost carbon layer could provide protection to cushion the strain of SnO_2 nanorods interlayer, which prevents the electrically isolation of SnO_2 nanorods during the cycling. Meanwhile, due to the high electronic conductivity of graphene and outer carbon layer, the large surface area and nanoscale diffusion length, high rate capability is expected. As revealed by electrochemical evaluation, it displays ultrahigh lithium storage properties (1415 mAh g^{-1} at 150th cycle) and fast lithium insertion/de-insertion process (540 mAh g^{-1} at 3 C).

5.2 Experimental

5.2.1 Synthesis of Graphene, SnO_2 nanoparticle/Graphene and SnO_2 nanorod/Graphene

The detailed procedures for prepare graphene from graphene oxide and G/SnO_2 NP can be found in previous published paper [27a]. In a typical process of construction for G/SnO_2 NR hybrids, the as prepared 16 mg G/SnO_2 NP were ultrasonically dispersed into 20 mL stannate aqueous solution (0.5 mmol $SnCl_4$ and 8 mmol NaOH, Sigma-Aldrich.) vigorously for 30 minutes. Then the suspension was transferred into 50 mL high pressure Teflon-lined autoclave. The solution was subsequently heated to 200 ^{o}C and kept for 2h to facilitate the growth of SnO_2 nanorod. After rinsed with large amount of distilled water and ethanol to remove the sodium and choloride ions, the as-obtained G/SnO_2 NR hybrids were collected after final drying at 100 ^{o}C overnight for use in next step.

5.2.2 Synthesis of carbon coated SnO_2 nanorod Graphene

To obtain the G/SnO_2 NR/C hierarchical structures, 20 mg of the G/SnO_2 NR samples is dispersed in 40 mL of aqueous solution of glucose (60 mg). After thorough mixing by ultrasonication for 30 minutes, the suspension is transferred into a 50 mL Teflon-lined autoclave and kept at 200 ^{o}C for 18 h. The sandwiched G/SnO_2 NR/C hybrids were collected after filtration and dried at 80 ^{o}C overnight followed by annealing at 450 ^{o}C for 2 h under Ar atomosphere.

5.2.3 Characterization

Products were characterized by powder X-ray diffraction (XRD, Rigaku RU-200BVH with a Co-Kα source (λ=1.7892 Å)), raman microspectroscopy (HORIBA Scientific LabRAM HR Raman spectrometer) under ambient condition with an incident laser beam at 532.03 nm, thermogravimetric analysis (TGA; Netzsch), field-emission scanning electron spectrometry (FE-SEM, Hitachi 4800S) coupled with energy dispersive spectroscopy (EDS), transmission electron microscope (TEM, Hitachi H-7000), high resolution TEM (HRTEM, JEOL 2010 FEG microscope) and X-ray photoelectron spectroscopy (XPS, Kratos Axis Ultra Al at 14 kV). The XANES experiments on the Sn M edge, O K edge and C K edge for composites were conducted on the undulator Spherical Grating Monochromator (SGM) beamline at the Canadian Light Source (CLS) located at the University of Saskatchewan in Saskatoon.

5.2.4 Electrochemical Measurement

The working electrodes are composed of the testing materials (G/SnO_2 NR and G/SnO_2 NR/C), conductive carbon black and polyvinylidene fluoride (PVDF) in a weight ratio of 8:1:1. The coin cells (2032) were assembled using pure lithium metal foil as the counter electrode and the polypropylene as the separator inside an argon-filled glove box. The electrolyte applied was 1M $LiPF_6$ in a mixture of ethylene carbonate (EC) and dimethyl carbonate (DMC) solvent. The profiles of galvanostatically charging and discharging curves were collected on a computer controlled Arbin BT-2000 battery tester system at a cut-off voltage window of 0.01 to 3 V (vs. Li^+/Li). Electrochemical impedance spectroscopy (EIS) measurements were conducted on an electrochemical workstation (Potentiostat/Galvanostat/EIS (VMP3)) by applying an AC voltage of 5 mV amplitude in the frequency range from 0.01 to 100 KHz at 0.5 V of specified discharged cycles. The calculation of specific capacities for G/SnO_2 NR and G/SnO_2 NR/C is based on the weight of the composites.

5.3 Results and Discussion

Graphene was prepared by a modified Hummer's method [27, 41, 42] and G/SnO_2 NP composites were synthesized by a previously reported microwave-assisted hydrothermal method [27a]. For the synthesis of G/SnO_2 NR composites, the as-obtained G/SnO_2 NP composites was added into an aqueous solution of stannate in a Teflon vessel and then kept at 200 ^{o}C for 2 h. It is worth to mention that the on-top tiny SnO_2 nanoparticles (~3.5 nm) could act as seeds to facilitate the one dimensional growth and the formation of SnO_2 nanorods grafted on graphene, as demonstrated in Figure 5.1. G/SnO_2 NR/C composites were obtained by coating G/SnO_2 NR composites with a glucose derived carbon via a hydrothermal and continuously sintering process.

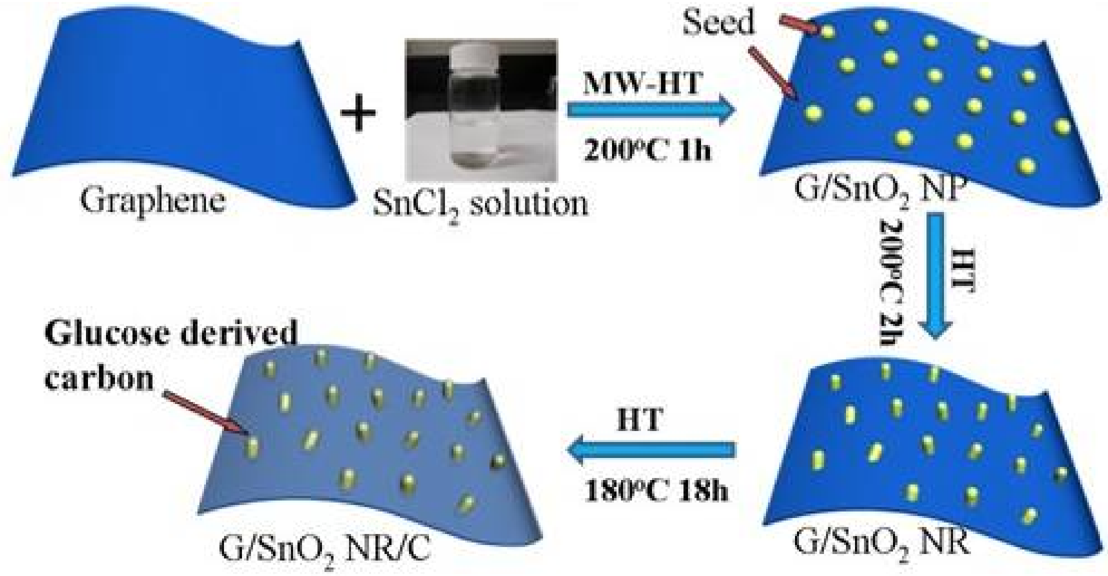

Figure 5.1 Illustration of the synthesis processes of G/SnO_2 NR/C nanocomposites: firstly, in-situ hydrolysis of Sn salts and immobilization of SnO_2 nanoparticles on graphene; secondly, SnO_2 nanoparticles seed-assisted hydrothermal process to get SnO_2 NR grafted on graphene; finally, nano-carbon coating on G/SnO_2 NR hierarchical structures by hydrothermal carbonization of glucose.

The morphologies and crystallographic structures of the hierarchical G/SnO_2 NR and G/SnO_2 NR/C nanocomposites were determined by electron microscope images and powder X-ray diffraction (XRD), as shown in Figure 5.2. XPS (X-ray photoelectron spectroscopy) data shown in Figure SI 5.1 clearly demonstrated that after thermal reduction, most oxygen groups are removed from Graphene oxide to form Graphene. The morphologies of pure graphene and G/SnO_2 NP can be found in previous reported results [27a], where small SnO_2 nanoparticels uniformly deposited on layered graphene. Figure 5.2a shows the scanning electron microscope (SEM) image of G/SnO_2 NR. It can be seen that dense SnO_2 NR arrays become rooted on the entire surface of graphene after hydrothermal treatment of the pre-deposited SnO_2 NP. It is worth noting that the very small and uniformly distributed SnO_2 NP [27a] in G/SnO_2 NP composites will function as a “seed” to induce the formation of SnO_2 NR and confine its growth direction, leading to the homogeneously decorated SnO_2 NR arrays on the 2D graphene surface. The highly crystalline SnO_2 NR possess a length of around 20–40 nm and a diameter of around 5-7 nm, as shown in Figure 5.2c. Figure 5.2b, d and e shows the morphologies of G/SnO_2 NR/C composites. After nano-carbon coating, the surface of the composites became smoother with an additional ultra thin outmost layer (as arrows pointed), indicating that the carbon layer has been successfully introduced on top of the G/SnO_2 NR hybrids, where SnO_2 NR are sandwiched between outmost carbon layer and graphene substrate to form a sandwiched hierarchical structure. A panoramic view in Figure 5.2e reveals that the 2D morphology is still well maintained. High resolution transmission electron microscope (HRTEM) image (Figure 5.2d) provides further evidence that the SnO_2 NRs are thoroughly covered by carbon with a thickness of 2-3 nm. The inset shows selected area electron diffraction (SAED) patterns representing facets of SnO_2 and a lattice spacing of 3.3 Å which corresponds to the (110) planes of rutile SnO_2, illustrating the high crystallinity of SnO_2 NR. Moreover, as unveiled by the elemental mapping spectra and energy dispersive X-ray (EDX) patterns of G/SnO_2 NR/C nanocomposites (Figure SI 5.2), the uniform distributions of C, O, Sn without other elements confirms the homogeneous distribution of highly purified SnO_2 rods in the hybrids.

To gain insight into the internal structure of the composites, an XRD experiment was carried out, as shown in Figure 5.2f. It can be seen that the XRD patterns for G/SnO_2 NR/C and G/SnO_2 NR composites are quite similar, and all intensive peaks match well with rutile SnO_2 (JCPDS No. 41-1445), illustrating that the crystal structure of SnO_2 remains intact after deposition of carbon layer. The broadening of the diffraction peaks is consistent with its nanostructure. Raman spectroscopy was further performed to examine the G/SnO_2 NR/C and G/SnO_2 NR composites (Figure SI 5.3a). The spectrum of graphene (G) was also given for comparison. It is clearly seen that all three samples exhibit intense peaks located at 1340 cm^{-1} and 1582 cm^{-1}, ascribed to D band and the G band, respectively [27, 43]. After deposition of SnO_2 NR, the intensity ratio of I_D/I_G is almost the same compared with that of pure graphene, indicating that SnO_2 NR has little effect on the graphitic domains of graphene and the laminated structure remains intact. Contrastively, the G/SnO_2 NR/C nanocomposites exhibit both a sharper G band and a higher I_G/I_D value, which should be attributed to the subsequently introduced carbon layer with good graphitic crystallinity. To quantify the contents of SnO_2 NR and carbon in the composites, thermogravimetric analysis (TGA) was carried out in air with a temperature range from room temperature to 750 ^{o}C, as shown in Figure SI 5.3b. The weight ratio of SnO_2 nanoparticle is calculated as 63.00% for G/SnO_2 NP in our previous report [27a], after seed-assisted hydrothermal process to obtain SnO_2 NR, the weight ratio of SnO_2 increased to 75.64%. With further carbon coating, the weight fraction of carbon in the hybrids increased from 24.36% (100%-75.64%) to 31.88% (100%-68.12%). All these results, combined with microscope images, demonstrate that hierarchically sandwiched G/SnO_2 NR/C composites have been successfully synthesized.

Desired electrochemical performance of electrodes is highly dependent on the choice of materials and the design of structures. In the sandwiched hierarchical G/SnO_2 NR/C composites, exploiting the electronic structure and chemical information (e.g. interaction, bonding and charge transfer) in-between each assembled layer is beneficial for further understanding of the improved electrochemical behavior. To investigate the local chemistry environment of the sandwiched hybrids and more importantly, to reveal the interaction and bonding between layers of the sandwich, x-ray absorption near edge structure spectroscopy (XANES), which is a chemical and elemental sensitive spectroscopic technique, was employed at specific edge of the materials.

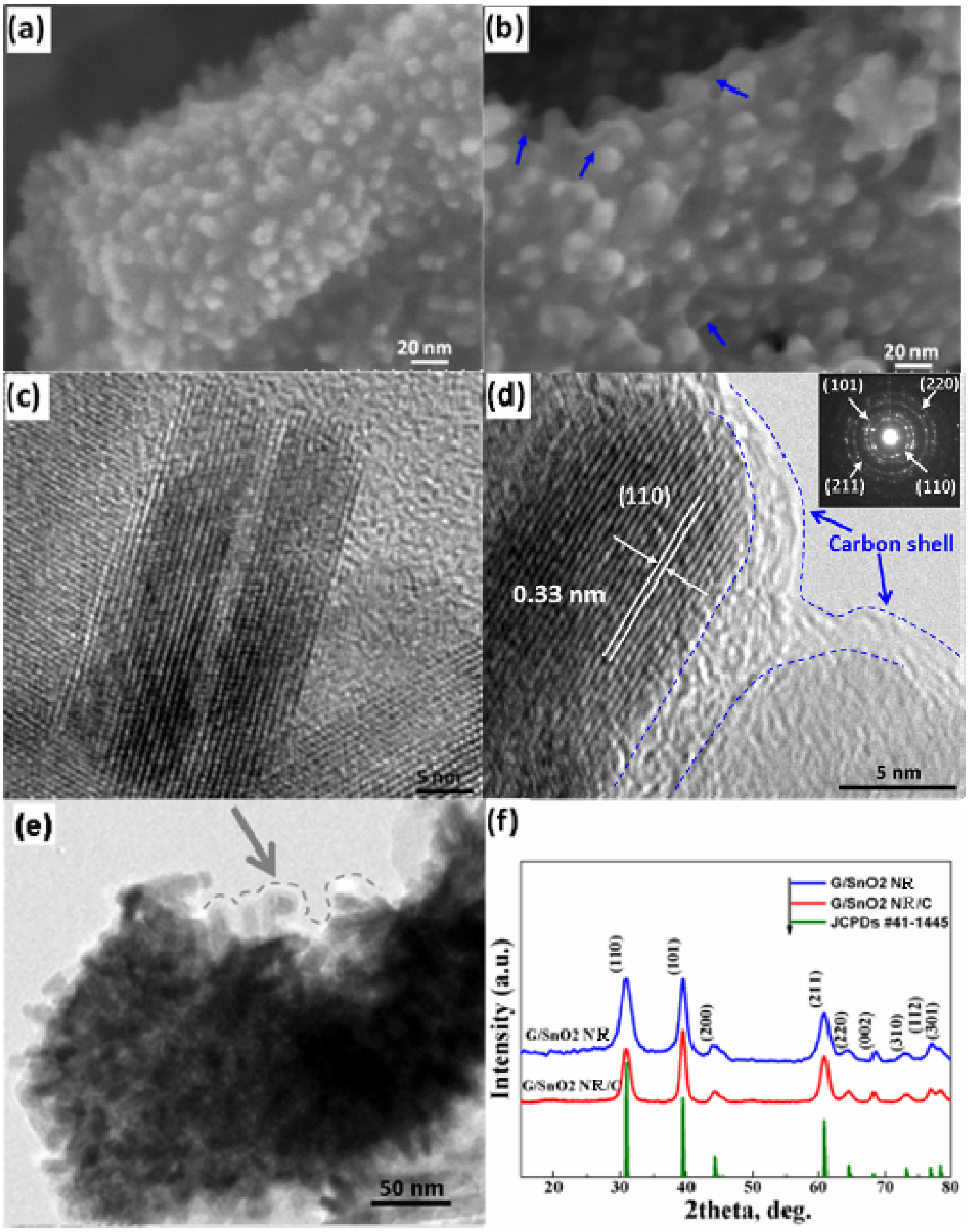

Figure 5.2 SEM image of G/SnO$_2$ NR nanocomposites (a) shows high density of SnO$_2$ NR on graphene and HRTEM image of G/SnO$_2$ NR hybrids (c) shows no obvious carbon layer; (b) SEM image and (d), (e) TEM images of G/SnO$_2$ NR/C nanocomposites, where arrows indicate the outmost carbon layer; (f) XRD patterns of G/SnO$_2$ NR and G/SnO$_2$ NR/C hybrids.

Figure 5.3a shows the carbon K edge XANES spectra for Graphene, G/SnO_2 NP, G/SnO_2 NR and G/SnO_2 NR/C composites. All spectra exhibit two main patterns located at ~285 eV and ~291 eV, which are attributed to graphitic π* and σ* transitions, respectively [27a, 44, 45]. The existence of these two transitions after deposition of SnO_2 NR followed by carbon coating indicates that the graphitic framework is kept intact and high electronic conductivity could be expected. Closer observation of the dotted rectangular region (magnified figure in the inset of Figure 5.3a) reveals that the spectra exhibits a gradual shift with some broadening toward the lower energy in the following order: graphene, G/SnO_2 NP, G/SnO_2 NR and G/SnO_2 NR/C hybrids. This observation indicates that after hybridization with SnO_2 nanorod, the carbon 2p-derived π* states in graphene or outmost carbon layer are accepting electrons from the n typed SnO_2 semiconductor, which is consistent with previously reported results [27a, 44, 45]. Another noticeable feature is the region between π* and σ* transitions, where the resonances arising here are ascribed to the oxygen containing functional groups, namely peak b at 288.2 eV to carbonyl (C=O) and peak c at 289.7 eV to carboxylic (-COOH). Obviously, after SnO_2 NR grafted on graphene, the transition at position c becomes distinct and stronger compared with that of pure graphene and G/SnO_2 NP. The emerging new peak illustrates that SnO_2 NR are also chemically bonded with surrounding carbon via carboxylic in G/SnO_2 NR and G/SnO_2 NR/C composites. The newly established bonding could also be tracked in the case of oxygen K-edge, as shown in Figure 5.3b. At position a, the appearance of the shoulder in the G/SnO_2 NR hybrids and much enhanced transition in G/SnO_2 NR/C composites further confirms that SnO_2 NR are firmly bonded with graphene and carbon layer through oxygen functionalized carboxylic group. All these observations, together with the charge transfer behavior at the π* states, provide direct spectroscopic evidence that chemical bonding via charge redistribution takes place between SnO_2 NR layer and the outmost carbon and graphene layers, which anchored SnO_2 interlayer intimately into a 2D carbon network. Thus, superior electrochemical performance could be expected, benefiting from the hierarchical nanocomposites structure and internal strong chemical bonding.

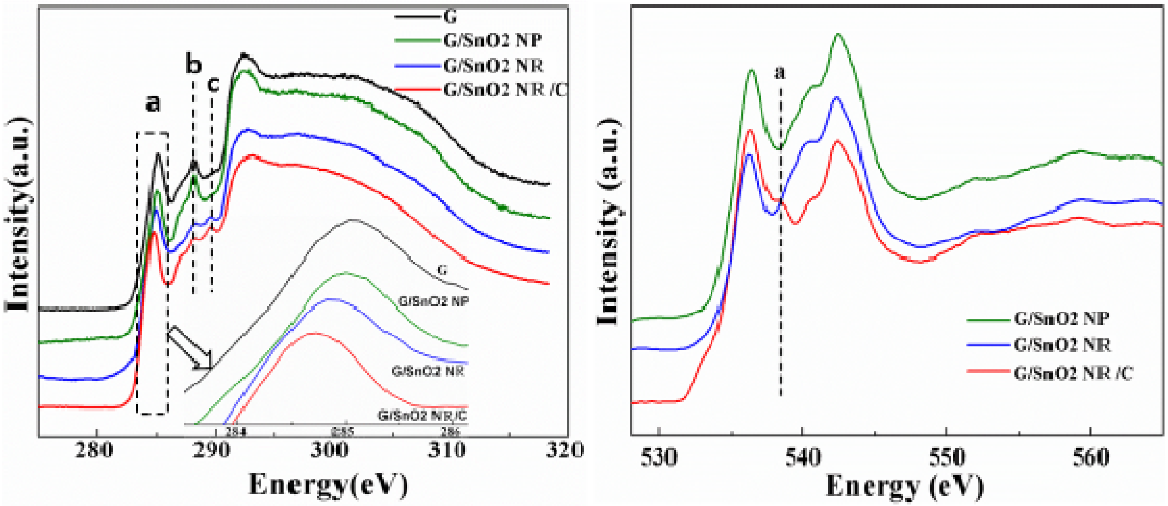

Figure 5.3 (a) C K edge XANES spectra of graphene, G/SnO$_2$ NP, G/SnO$_2$ NR and G/SnO$_2$ NR/C composites (the inset is the magnified region which shows gradually red shift of the π*); (b) O K edge XANES spectra of G/SnO$_2$ NP, G/SnO$_2$ NR and G/SnO$_2$ NR/C composites.

Intrigued by the structural features of G/SnO$_2$ NR/C hierarchical structures, we have evaluated their lithium storage properties for potential application as an anode material for LIBs. The charge/discharge profiles at typical cycles of G/SnO$_2$ NR/C at a current density of 100 mA g^{-1} with a voltage range of 0.01 V ~ 3V are shown in Figure 5.4a. The hybrids deliver a discharge and charge capacities of 1828 mA h g^{-1} and 1285 mA h g^{-1} respectively with an initial coulombic efficiency of 70% in the first cycle. The 30% irreversible capacity loss is attributed to the formation of Li$_2$O, inorganic solid electrolyte interface (SEI) film and electrolyte decomposition [19]. From the 10th cycle, the capacity becomes stable and the composites deliver a discharge capacity of 983 mA h g^{-1} up to 50th cycle. More interestingly, starting from the 50th cycle, the discharge capacity of G/SnO$_2$ NR/C hierarchical structures increases gradually to 1262 mA h g^{-1} in the 100th cycle and stabilizes to 1419 mA h g^{-1} in the 150th cycle, as shown in the inset of Figure 5.4a. To the best of our knowledge, such high electrochemical performance is rarely reported in literatures relating to graphene and other carbon-SnO$_2$ composites [19, 27a, 46]. Although behaviors of capacity increase have been reported in SnO$_2$ and other metal oxide systems, such great capacity increase of almost 440 mA h g^{-1} is not so common [19, 33, 46]. Figure 5.4b examined the galvanostatic cycle performances of G/SnO_2 NR and G/SnO_2 NR/C nanocomposites. It is found that at the same current density (0.1C), G/SnO_2 NR nanocomposites exhibit an initial discharge and charge capacity of 1870 and 1133 mAh g^{-1} respectively, with a coulombic efficiency of 60% and continuously decay of the lithium storage capability. At 50th cycle, it only preserves a discharge capacity of 389 mAh g^{-1}. In contrast, for the G/SnO_2 NR/C sandwiched system, the capacity becomes stable from the 10th cycle with higher coulombic efficiency of around 98% compared with that of G/SnO_2 NR (Figure SI 5.4). The inset further confirms the high and stable Coulombic efficiency for G/SnO_2 NR/C up to 350 cycles. The higher lithium storage properties and improved coulombic efficiency could only be attributed to the hierarchical sandwiched structure, which thoroughly sealed the SnO_2 NR inside from the morphology perspective and possessed strong internal chemical bonding between SnO_2 NR and carbon layer from the spectroscopic perspective. The intact and robust protection could prevent the interlayer SnO_2 NR from dropping off from the 2D networks during cycling, leading to improved cycling performance. Meanwhile, the outmost carbon layer could inhibit the direct contact between SnO_2 NR and electrolyte to reduce the amount of irreversible SEI, leading to high coulombic efficiency. More strikingly, the hierarchical structure could offer dramatically synergic effect and induce a continuous increase of capacity after 50 cycles. Similar capacity boosting is also observed for electrodes cycled at higher current density of 1C (1000 mA g^{-1}). As shown in Figure 5.4b, the discharge capacity of G/SnO_2 NR/C composite increases from the 100th cycle and stabilized at around 330th cycle with a increment value of 140 mA h g^{-1}, demonstrating that the results are convincing and the electrode has long cycle life.

Although the reasons for the capacity increase upon cycling are still unclear, the plausible explanations are generally ascribed to the following: As shown in the charge discharge profiles, by comparing discharge curves in 100th and 150th cycles with that in 50th cycle, it is found that part of contribution for capacity increase happens at low voltage (below 0.5 V). Lou and Maier et al. attributed such behavior to the reversibly formation and decomposition of organic polymeric/gel like film from the electrolyte, which could provide interfacial storage for excess lithium ions through a so-called “pseudo-capacitance-type behavior” [40, 47, 48]. It is reported that the contact area between the anodes and the electrolyte will also increase due to the inevitable pulverization of SnO_2 along with increasing cycles [18], resulting in a continuously formed film which provides extra lithium interfacial storage sites as demonstrated in different potential regions [40, 47, 48]. However, since the contribution of capacity increase from reversible film is usually limited in tin-based system and thus there should be other reasons accounting for high capacity increase (around 440 mA h g^{-1}). On the other hand, Lian et al. [33] and Yan et al. [49] claimed that such capacity increase is because of that the commonly regarded initial irreversible conversion reaction (Equation 1) is becoming partially reversible upon cycling.

$$SnO_2 + 4Li^+ + 4e^- \longrightarrow Sn + 2Li_2O \qquad (1)$$

To confirm this, the differential capacity versus voltage plots of G/SnO_2 NR/C composites in typical cycles are also given, as shown in figure SI 5.5. The initial cathodic process shows a sharp peak at 0.9 V corresponding to the conversion reaction of SnO_2 to Sn and the formation of Li_2O, while it is almost undetectable in the 2nd cycle, indicating the irreversible conversion process has been completed. However, the peak reappeared at the 100th and 150th cycles, indicating that the conversion reaction happens again and thus it is at least partially reversible. Moreover, in the anodic process, the gradually increased intensity of the peak around 1.3 V after 50th cycle further demonstrates the growing decomposition of Li_2O upon cycling [50], where it is prone to oxidize Sn back to SnO_2 in the charged states [49].

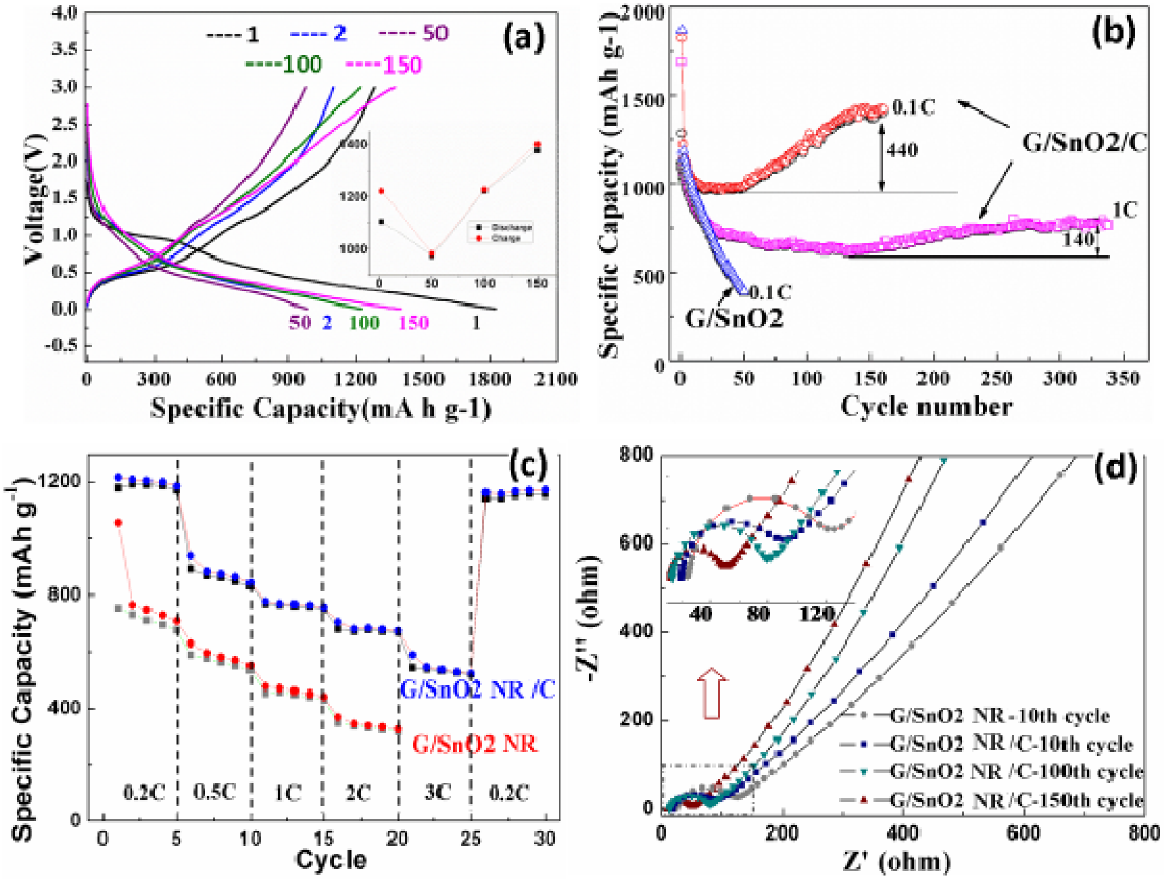

Figure 5.4 (a) Charge-discharge profiles of G/SnO$_2$ NR/C composites (inset shows the related charge-discharge capacities value versus cycle numbers); (b) Cycle performance plots of G/SnO$_2$ NR (0.1 C) and G/SnO$_2$ NR/C (0.1C and 1C) hybrids in the voltage window of 0.01-3.00 V; (c) Rate performances of G/SnO$_2$ NR and G/SnO$_2$ NR/C nanocomposites; (d) Nyquist plots of G/SnO$_2$ NR and G/SnO$_2$ NR/C nanocomposites at specified cycles, inset: the magnified curves show different diameters of semicircles. Note 1C= 1000 mA g^{-1}.

To check the evolution of morphology and structure of the electrodes after charge and discharge processes, HRTEM was further performed on cycled electrodes, as shown in Figure 5.5a-d. For G/SnO$_2$ NR hybrids, after 50 discharge/charge cycles, it is clearly seen that SnO$_2$ NR collapsed and pulverized into small particles after cycling. Large field of bare graphene without deposition of SnO$_2$ indicates that many exposed SnO$_2$ have detached from substrate. Figure 5.5b shows a small particle left on the edge of graphene and it has no obvious crystalline feature with a size around 6 nm. In contrast, after 350 discharge/charge cycles, G/SnO_2 NR/C nanocomposites still maintains its uniform distribution due to the intact protection of the sandwiched hierarchical structure, as shown in Figure 5.5c. More importantly, from the high magnification image in figure 5.5d, crystallized nanoparticles with a size of around 2 nm appeared (red circled region). The calculated inter-planar distance is 2.6 Å, which matches well with the (101) facet of SnO_2. The inset Fast Fourier Transform (FFT) electron diffraction pattern taken from the particles further demonstrates its good crystallinity. The direct observation of the SnO_2 in cycled electrodes further confirms that the conversion reaction of SnO_2 to Sn and Li_2O is reversible. Also, we performed the XANES at Sn M edge for the nanocomposites after cycles and compared with pure Sn and SnO_2 standards, as shown in Figure SI 5.6. It is found that the spectra for cycled G/SnO_2 NR/C nanocomposites and cycled G/SnO_2 NR nanocomposites exhibit distinct difference. Closer observation reveals that the spectrum for cycled G/SnO_2 NR nanocomposites tracks that of pure Sn, while spectrum of cycled G/SnO_2 NR/C nanocomposites tracks that of pure SnO_2. From the electrochemical curves, the morphologies and the spectra observed here, it is believed that the Sn particles generated from conversion reaction would become small and they are firmly anchored in carbonaceous layers during the cycling. With the outmost carbon and graphene protection, the Li_2O would be closely surrounded by the smaller and smaller Sn particles. On the other hand, it is well known that the required activation energy for oxidation and solid-state double decomposition reactions would be reduced with the decrease of particle size [48c]. In this case, when the Sn nanoparticles are small enough (e.g. 2 nm), the conversion reaction would become reversible as previously predicted by other groups [33, 51, 52]. It is worthy to note that the carbon layer could also prevent the loss of Li_2O from the hierarchical structure upon cycling, favoring its oxidation of Sn to SnO_2 [49]. While for G/SnO_2 NR nanocomposites, the exposed Sn and Li_2O would easily detach from graphene during cycling, leading to fast capacity fade. Figure 5.5e shows the schematic representation for G/SnO_2 NR and G/SnO_2 NR/C nanocomposites during cycling. Compared with G/SnO_2 NR nanocomposites where the exposed SnO_2 NR will break away from the graphene substrate and lose its activity, sandwiched G/SnO_2 NR/C nanocomposites exhibit higher cyclability due to the well protection benefiting from the hierarchical structure even at high current densities of 1C.

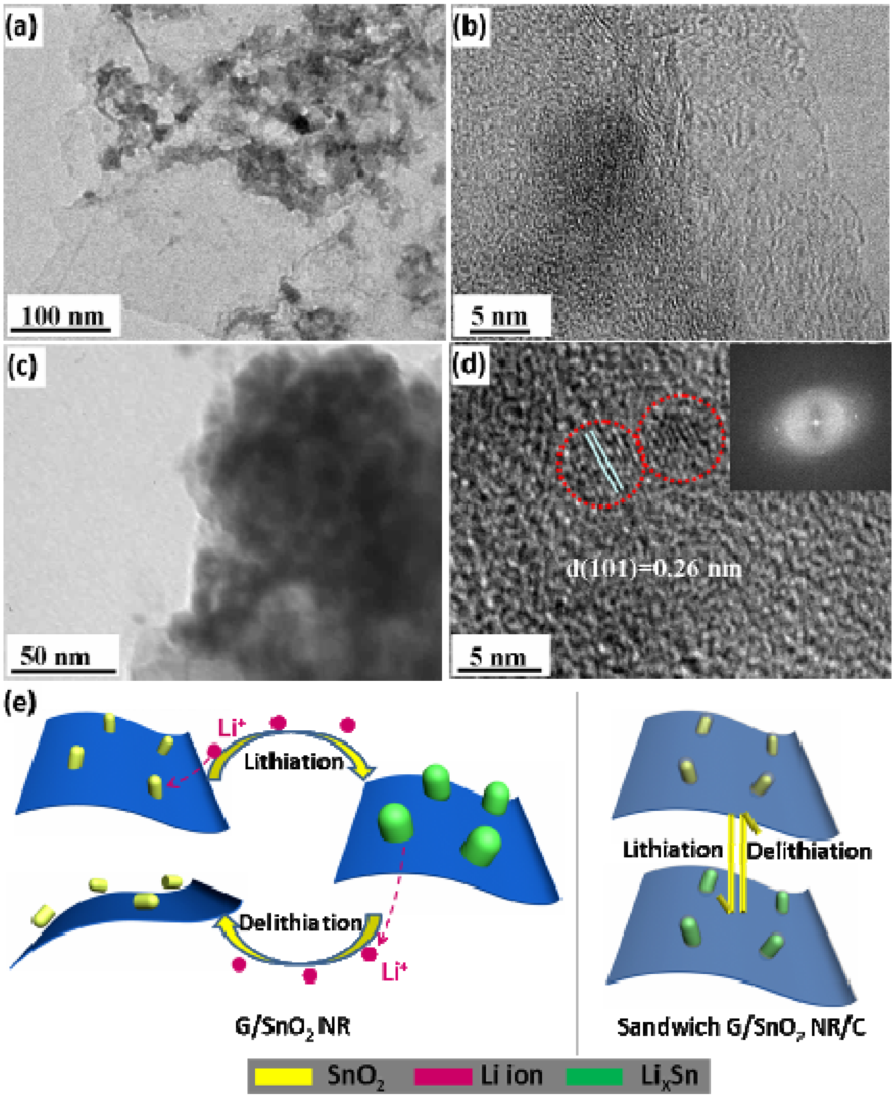

Figure 5.5 HRTEM images of nanocomposites after cycling: (a) and (b) G/SnO$_2$ NR after 50 cycles discharge/charge at 0.1C; (c) and (d) G/SnO$_2$ NR/C after 350 cycles discharge/charge at 1C, where the inset shows the Fast Fourier Transform (FFT) electron diffraction pattern taken from the red circled particles; (e) Schematic representation showing that sandwiched structure prevents isolation of SnO$_2$ NR during cycling.

After 160 discharge/charge cycles at 0.1C, the same cell for G/SnO$_2$ NR/C composites is further examined for high power applications, as shown in Figure 5.4c. Benefiting from the sandwiched hierarchical structure and robust chemical bonding between layers, the G/SnO_2 NR/C composites displays an excellent cycling response from a current density of 0.2C up to 3C(3000 mA g^{-1}). Remarkably, a high lithium storage capability of 540 mAh g^{-1} at 3C could still be obtained for the G/SnO_2 NR/C hybrids. More over, a constant capacity of around 1170 mAh g^{-1} can be restored when the current rate was reversed back to 0.2C. In contrast, freshly prepared G/SnO_2 NR half cell delivered only 350 mAh g^{-1} at 2C. Further more, AC impedance analysis for the half cell was carried out to elucidate the charge and contact resistance of G/SnO_2 NR and G/SnO_2 NR/C electrodes at selected cycle numbers, as plotted in Figure 5.4d. As evident from the drastically smaller diameter of the semicircle for G/SnO_2 NR/C in the 10th cycle compared with that for G/SnO_2 NR, the sandwiched hybrids shows much lower impedance than G/SnO_2 NR, benefiting from high conductive carbon coating. Further examinations of the plots at 100th and 150th cycles show even smaller semicircle for G/SnO_2 NR/C (clearly shown in the magnified curves), indicating the increased electron and lithium ion diffusion rate, which is resulted from the irreversible lithiated carbon shells [46] and shortened paths due to the reduced size of Sn nanoparticles upon cycling. Due to the reduced impedance and the facilitated transportation of electrons and lithium ions, G/SnO_2 NR/C composites exhibit both superior cycling and rate performances.

5.4 Conclusions

In summary, a sandwiched carbon coated SnO_2 NR grafted on graphene hierarchical structure has been successfully synthesized by a seed assisted hydrothermal growth of SnO_2 nanorod on graphene followed by glucose derived carbon coating. Benefiting from the advanced sandwiched hierarchical structure and the intimate chemical bonding between each layers, the nano-hybrids show drastically increased capacity due to the synergistic effect, which consequently leads to excellent electrochemical performances. The as-prepared G/SnO_2 NR/C nanocomposite exhibits an ultrahigh reversible specific capacity of 1419 mA h g^{-1} in the 150th cycle and high-rate capability at high current densities of 3000 mA g^{-1}. We believe that the synthesis concept could be easily extended to other electrode materials. Our system presented in this work offers significant implications on structural design for improving performances of electrodes in LIBs.

5.5 Acknowledgements

This research was supported by Natural Sciences and Engineering Research Council of Canada (NSERC), General Motors of Canada, Canada Research Chair (CRC), Canada Foundation for Innovation (CFI), Ontario Innovation Trust (OIT) Program. The Canadian Light Source is supported by CFI, NSERC, NRC, CHIR, and the University of Saskatchewan.

5.6 References

[1] P. G. Bruce, B. Scrosti and J. M. Tarascon, *Angew. Chem. Int. Ed.*, 2008, **47**, 2930–2946.

[2] J. M. Tarascon and M. Armand, *Nature*, 2001, **414**, 359–367.

[3] Y. Idota, T. Kubota, A. Matsufuji, Y. Maekawa and T. Miyasaka, *Science*, 1997, **276**, 1395-1397.

[4] D. Deng and J. Y. Lee, *Angew. Chem., Int. Ed.*, 2009, **48**, 1660-1663.

[5] M. S. Park, G. X. Wang, Y. M. Kang, D. Wexler, S. X. Dou and H. K. Liu, *Angew. Chem., Int. Ed.*, 2007, **119**, 764–767.

[6] X. W. Lou, C. M. Li and L. A. Archer, *Adv. Mater.*, 2009, **21**, 2536–2539.

[7] C. K. Chan, H. L. Peng, G. Liu, K. McIlwrath, X. F. Zhang, R. A. Huggins and Y. Cui. *Nat. Nanotechnol.*, 2008, **3**, 31–35.

[8] H. Kim and J. Cho, *Nano Lett.*, 2008, **8**, 3688–3691.

[9] M. G. Kim and J. Cho, *J. Electrochem. Soc.*, 2009, **156**, A277–A282.

[10] X. L. Wang, W. Q. Han, H. Chen, J. Bai, T. A. Tyson, X. Q. Yu, X. J. Wang and X. Q. Yang, *J. Am. Chem. Soc.*, 2011, **133**, 20692–20695.

[11] J. S. Chen and X. W. Lou, *Small*, 2013, **9**, DOI: 10.1002/smll.201202601.

[12] C. Kim, M. Noh, M. Choi, J. Cho and B. Park, *Chem. Mater.*, 2005, **17**, 3297–3301.

[13] H. J. Ahn, H. C. Choi, K. W. Park, S. B. Kim and Y. E. Sung, *J. Phys. Chem. B*, 2004, **108**, 9815–9820.

[14] Y. Wang, J. Y. Lee and H. C. Zeng, *Chem. Mater.*, 2005, **17**, 3899-3903.

[15] X. W. Lou, L. A. Archer and Z. Yang, *Adv. Mater.*, 2008, **20**, 3987–4019.

[16] Z. Wang, D. Luan, F. Boey and X. W. Lou, *J. Am. Chem. Soc.*, 2011, **133**, 4738–4741.

[17] R. Liu, S. Yang, F. Wang, X. Lu, Z. Yang and Bi Ding, *ACS Appl. Mater. Interfaces*. 2012, **4**, 1537−1542.

[18] H. Kim and J. Cho, *J. Mater. Chem.*, 2008, **18**, 771–775.

[19] X. Li, X. Meng, J. Liu, D. Geng, Y. Zhang, M. Banis, Y. Li, R. Li, X. Sun, M. Cai, and M. Verbrugge, *Adv. Funct. Mater.*, 2012, **22**, 1647-1654.

[20] X. Huang, X. Zhou, L. Zhou,K. Qian, Y. Wang, Z. Liu and C. Yu, *ChemPhysChem*, 2011, **12**, 278 – 281.

[21] G. X. Wang, J. H. Ahn, M. J. Lindsay, L. Sun, D. H. Bradhurst, S. X. Dou and H. K. Liu, *J. Power Sources*, 2001, **97**, 211–215.

[22] X. Y. Zhao, Z. H. Xia and D. G. Xia, *Electrochim. Acta*, 2010, **55**, 6004–6009.

[23] Y. Yu, Q. Yang, D. Teng, X. Yang and S. Ryu, *Electrochem. Commun.*, 2010, **12**, 1187–1190.

[24] Y. Wang, H. C. Zeng and J. Y. Lee, *Adv. Mater.*, 2006, **18**, 645–649.

[25] S. M. Paek, E. Yoo and I. Honma, *Nano Lett.*, 2009, **9**, 72 –75.

[26] H. Wang, L. Cui, Y. Yang, H. S. Casalongue, J. T. Robinson, Y. Liang, Y. Cui and H. Dai, *J. Am. Chem. Soc.*, 2010, **132**, 13978-13980.

[27] a) D. Wang, X. Li, J.Wang, J. Yang, D. Geng, M.Cai, R. Li, T. K. Sham and X. Sun, *J. Phys. Chem. C*, 2012, **116**, 22149–22156; b) X. Li, D. Geng, Y. Zhang, X. Meng, R. Li and X. Sun, *Electrochem. Commun.*, 2011, **13**, 822-825; c) J. Yang, J. Wang, D. Wang, X. Li, D. Geng, G. Liang, M. Gauthier, R. Li, X. Sun, *J. Power Sources*, 2012, **208**, 340-344; d) J. Yang, J. Wang, Y. Tang, D. Wang, X. Li, Y. Hu, R. Li, G. Liang, T.-K. Sham, X. Sun, *Energy Environ. Sci.*, 2013, DOI: 10.1039/C3EE24163G; e) Y. Hu, X. Li, J. Wang, R. Li, X. Sun, *J Power Sources*, 2013, **237**, 41-46; f) Y. Li, J. Wang, X. Li, D. Geng, R. Li, X. Sun, Superior Energy Capacity of Graphene Nanosheets for Nonaqueous Lithium-Oxygen Battery. *Chem. Commun.* 2011, **47**, 9438-9440; g) Y. Li, J. Wang, X. Li, D. Geng, M. Banis, R. Li, X. Sun, *Electrochem. Commun.* 2012, **18**, 12-15.

[28] a) J. Zhou, J. Wang, L. Zuin, T. Regier, Y. Hu, H. Wang, Y. Liang, J. Maley, R. Sammynaiken and H. Dai, *Phys. Chem. Chem. Phys.*, 2012,**14**, 9578-9581; b) J. Zhou, H. Fang, J. M. Maley, J. Y. P. Ko, M. Murphy, Y. Chu, R. Sammynaiken and T. K. Sham, *J. Phys. Chem. C*, 2009, **113**, 6114–6117.

[29] G. Zhou, D. W. Wang, F. Li, L. L. Zhang, N. Li, Z. S. Wu, L. Wen,G. Q. Lu, H. M. Cheng, *Chem. Mater.*, 2010, **22**, 5306-5313.

[30] S. Q. Chen and Y. Wang, *J. Mater. Chem.*, 2010, **20**, 9735–9739.

[31] J. Cheng and J. Du, *Cryst. Eng. Comm.*, 2012, **14**, 397-400.

[32] J. K. Lee, K. B. Smith, C. M. Hayner and H. H. Kung, *Chem. Commun.*, 2010, **46**, 2025–2027.

[33] P. Lian, X. Zhu, S. Liang, Z. Li, W. Yang and H. Wang, *Electrochim. Acta*, 2011, **56**, 4532–4539.

[34] S. Ding, D. Luan, F. Boey, J. S. Chen and X. W. Lou, *Chem. Commun.*, 2011, **47**, 7155-7157.

[35] Z. Y. Wang, Z. C. Wang, S. Madhavi and X. W. Lou, *J. Mater. Chem.*, 2012, **22**, 2526–2531.

[36] Y. Q. Zou and Y. Wang, ACS Nano, 2011, **5**, 8108-8114.

[37] S. Ding, J. S. Chen and X. W. Lou, *Chem-Asian J.*, 2011, **6**, 2278 – 2281.

[38] J. Cheng, H. Xin, H. Zheng and B. Wang, *J. Power Sources.*, 2013, **232**, 152-158.

[39] L. Ji, Z. Tan, T. Kuykendall, E. J. An, Y. Fu, V. Battaglia and Y. Zhang, *Energy Environ. Sci.*, 2011, **4**, 3611-3616.

[40] Z. Wang, D. Luan, S. Madhavi, Y. Hu and X. W. Lou, *Energy Environ. Sci.*, 2012, **5**, 5252-5256.

[41] W. S. Hummers and R. E. Offeman, *J. Am. Chem. Soc.*, 1958, **80**, 1339-

[42] D. Geng, Y. Chen, Y. Chen, Y. Li, R. Li, X. Sun, S. Ye and S. Knights. *Energy Environ. Sci.*, 2011, **4**, 760-764.

[43] F. Tuinstra and J. L. Koenig, *J. Chem. Phys.* 1970, **53**, 1126-1130.

[44] J. Zhou, J. Wang, H. Fang and T. K. Sham, *J. Mater. Chem.*, 2011, **21**, 5944–5949.

[45] J. Zhou, J. Wang, H. Fang, C. Wu, J. N. Cutler and T. K. Sham, *Chem. Commun.*, 2010, **46**, 2778–2780.

[46] Y. Su, S. Li, D. Wu, F. Zhang, H. Liang, P. Gao, C. Cheng and X. Feng, *ACS Nano*, 2012, **6**, 8349–8356.

[47] J. Jamnik and J. Maier, *Phys. Chem. Chem. Phys.*, 2003, **5**, 5215-5220.

[48] a) P. Poizot, S. Laruelle, S. Grugeon, L. Dupont and J-M. Tarascon, *Nature*, 2000, **407**, 496-499; b) S. Laruelle, S. Grugeon, P. Poizot, M. Dollé, L. Dupont and J-M. Tarascon, J. Electrochem. Soc., 2002, 149, A627–A634; c) P. L. Taberna, S. Mitra, P. Poizot, P. Simon and J. M. Tarascon, *Nat. Mater.*, 2006, **5**, 567-573.

[49] Y. Yu, C. Chen and Y. Shi, *Adv. Mater.*, 2007, **19**, 993–997.

[50] I. A. Courtney and J. R. Dahn, *J. Electrochem. Soc.*, 1997, **144**, 2943-2948.

[51] R. Demir-Cakan, Y. S. Hu, M. Antonietti, J. Maier and M. M. Titirici, *Chem. Mater.*, 2008, **20**, 1227-1229.

[52] S. Han, B. Jang, T. Kim, S. M. Oh and T. Hyeon, *Adv. Funct. Mater.*, 2005, **15**, 1845-1850.

Broader context

High power/energy density lithium-ion batteries (LIBs) are regarded as a promising energy system for widespread application of electric vehicles and hybrid electric vehicles, which have a large amount of market value in facing the environmental pollution and the depletion of fossil fuels. Exploiting high performance and safe electrodes is crucial for acceleration the practical use since current graphite based anode is approaching the limit and it couldn't satisfy the urgent demand. In this communication, we designed a novel sandwiched hierarchical structure composed by graphene substrate, intermediate SnO_2 nanorod arrays and the outmost carbon layer. Based on the advantages of intrinsic structure and the strong chemical bonding between each layers, the sandwiched hybrids exhibit ultrahigh lithium storage as well as excellent rate performances when evaluated as an anode material for LIBs.

5.7 Supporting Information

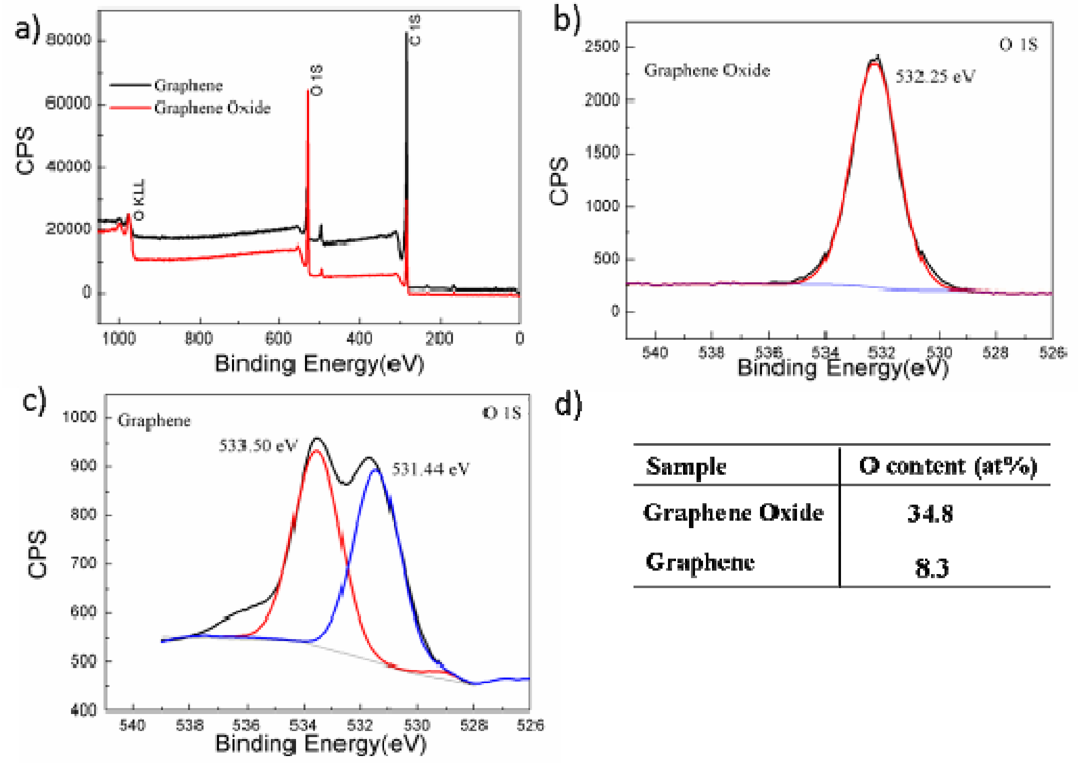

Sample	O content (at%)
Graphene Oxide	34.8
Graphene	8.3

Figure SI 5.1 XPS patterns of Graphene Oxide and Graphene sample: a) survey; b) O 1S of Graphene Oxide; c) O1S of Graphene; d) O content summary.

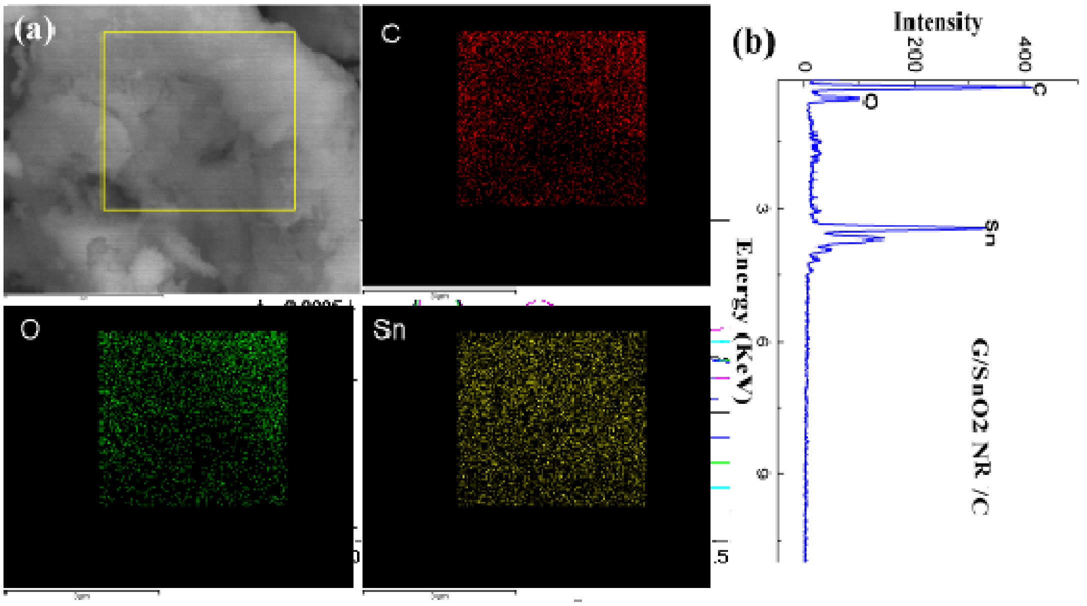

Figure SI 5.2 (a) Elemental mapping spectra and (b) energy dispersive X-ray (EDX) patterns of G/SnO$_2$ NR/C nanocomposites.

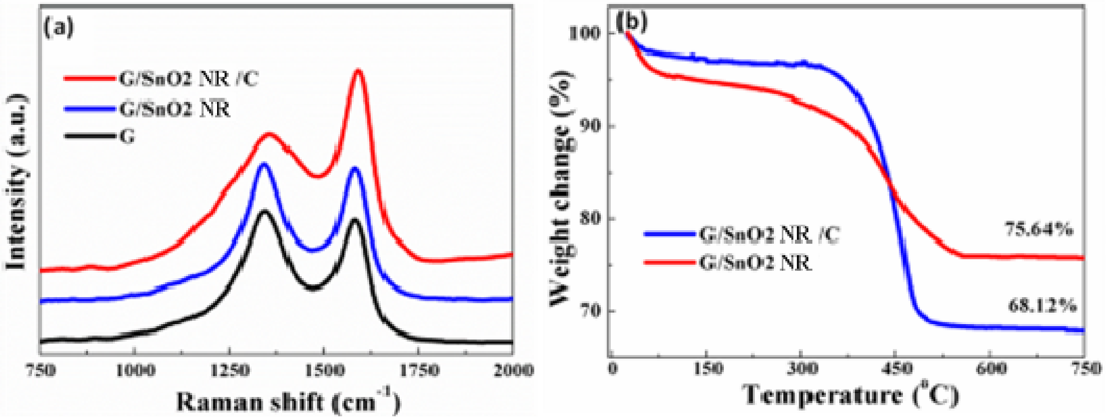

Figure SI 5.3 Characterization of G/SnO$_2$ NR and G/SnO$_2$ NR/C nanocomposites: (a) Raman spectra; (b) TGA curves.

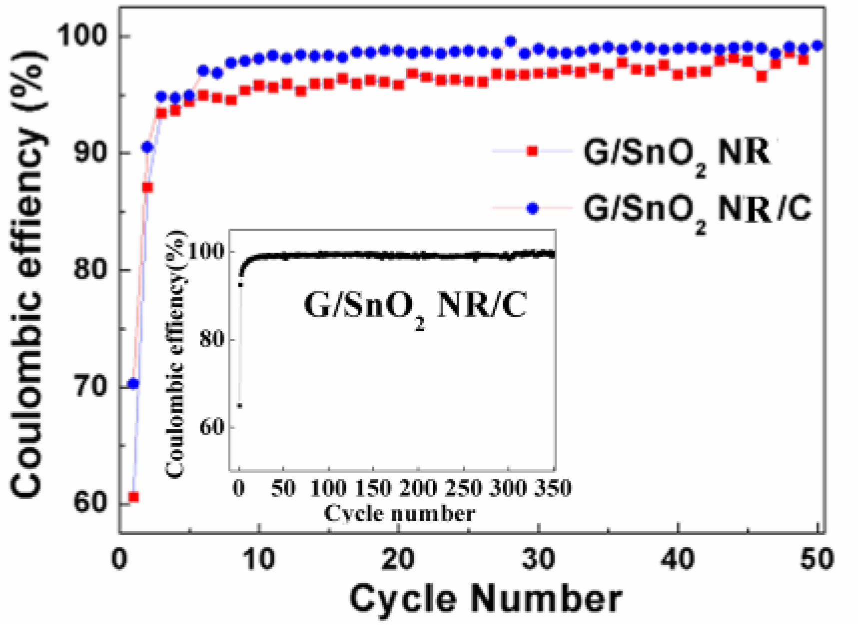

Figure SI 5.4 A comparison of Coulombic efficiency of G/SnO$_2$ NR and G/SnO$_2$ NR/C in the first 50 cycles at 0.1C (inset shows the Coulombic efficiency of G/SnO$_2$ NR/C at 1C for 350 cycles).

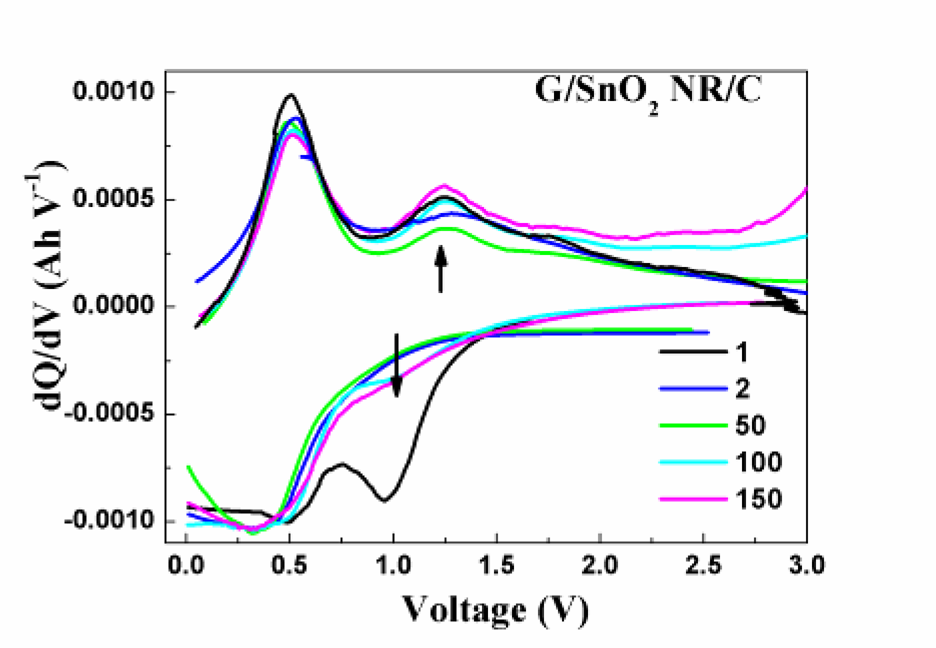

Figure SI 5.5 The differential capacity versus voltage plots of G/SnO$_2$ NR/C sandwiched composites at selected cycle numbers.

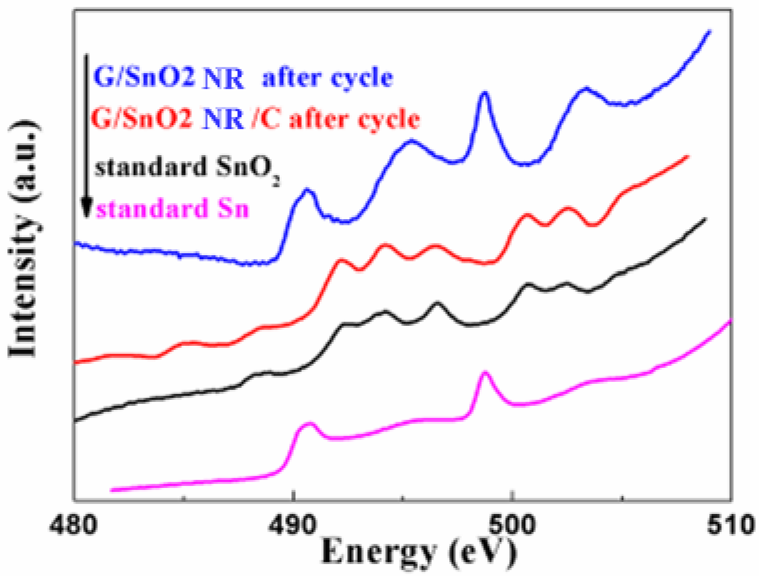

Figure SI 5.6 Sn M edge XANES spectra of standard Sn, SnO_2 and nanocomposites after cycling.

Chapter 6

6 Hierarchical nanostructured core–shell Sn@C nanoparticles embedded in graphene nanosheets: spectroscopic view and their application in lithium ion batteries

In last chapter, a success model of sandwiched graphene/SnO_2 nanorod/carbon composites has been designed. For Sn anodes, it presents even higher capacity than SnO_2. Designing hierarchical tin-based anodes also have great potential as promising candidates for LIB. Therefore, we tried to design hierarchical Sn-C composites using facile and scalable CVD route.

In this chapter, the hierarchical carbon encapsulated tin (Sn@C) embedded graphene nanosheets (GNs) composites (Sn@C-GNs) have been successfully fabricated via a simple and scalable one-step chemical vapor deposition (CVD) procedure. The GNs supported Sn@C core-shell structure consists a crystalline tin core, which is thoroughly covered by a carbon shell and more interestingly, extra voids are present between the carbon shell and the tin core. Synchrotron spectroscopy confirms that the metallic tin core is free of oxidation and the existence of charge redistribution transfer from tin to the carbonaceous materials of the shell, facilitating their intimate contact by chemical bonding and resultant lattice variation. The hybrid electrodes of this material exhibit a highly stable and reversible capacity together with an excellent rate capability, which benefits from the improved electrochemical properties of tin provided by the protective carbon matrix, voids and the flexible GNs matrix.

KEYWORDS: graphene, lithium ion batteries, Sn-C, X-ray absorption near edge structure, core shell structure

---

Note: Part of the content in this chapter has been published.

D. Wang, X. Li, J. Yang, J. Wang, D. Geng, R. Li, M. Cai, T.-K. Sham, X. Sun in Phys Chem Chem Phys, 2013, 15, 3535.

6.1 Introduction

With increasing demand on lithium ion batteries both in scientific and industrial fields, greater efforts have been devoted recently to fabricating functional nanocomposites , enabling the synergic effect of the individual unique properties of different components in the composite [1, 2]. In general, constructing such novel architecture can lead to higher energy density and cyclic durability [3-5]. Tin based materials have attracted considerable attention as anode candidate owing to their high theoretical capacity (about 994 mA h g^{-1}) [6], competitive cost, and easy to process. Nevertheless, there are critical problems hindering the practical implementation of this material, including the associated pulverization and capacity fading originated from a drastic volume change (over 250%) during the lithium insertion–extraction electrochemical process [7, 8].

Currently, two substantial avenues are applied collectively to circumvent these problems focusing on (i) tuning the morphologies of Sn into nanostructure and (ii) exploiting ideal matrixes confining the volume change by the so-called “cushion effect” [3-5]. As a result, many designs of tin-based nanocomposites are driven by the possibility of combining its high lithium storage properties with enhanced stability [9-12]. Nanosized carbon additives, for example graphene, are considered as a promising supplementary and appeals a great deal of effort due to its intriguing features such as large surface area (more than 2630 m^2 g^{-1}), high electronic conductivity, superior mechanical flexibility, and high theoretical capacity (786 mA h g^{-1}) [13-17]. Because graphene can effectively buffer the volume change during cycling, applying graphene as a matrix to incorporate metal or metal oxide for nanoarchitectured composites could result electrodes with superior durability. Various hybrids including Co_3O_4/graphene [18], Fe_2O_3/graphene [19], Sn/graphene [20] and SnO_2/graphene [21-23] etc. have been synthesized and demonstrated enhanced electrochemistry performance compared with bare metal or metal oxides. Meanwhile, the design of core-shelled nanostuctures also achieved improved electrochemical performances such as SnO_2@C [24, 25] and Sn@C [26, 27] nanostructured systems. Wang et. al have successfully synthesized nanocomposite based on core-shelled Sn@C nanowire and SnSb@C nanoparticles hybriding with graphene [26, 27]. The nanocomposites exhibited radically improved lithium storage capabilities and rate performance. However, the procedures are complicated involving multiple steps; in addition toxic reagents such as $NaBH_4$ and post heat treatment are required, which results in high cost and fussy parameters. More importantly, there is no fundamental study of the interaction between tin and carbon behind the electrochemical performance.

X-ray absorption near-edge structure (XANES) spectroscopy, which tracks the modulation of the X-ray absorption coefficient above an absorption edge of a core level of an element in a chemical environment, has proven to be a powerful technique in unveiling the chemical structure and bonding between metal oxides and carbon nanotubes, such as SnO_2/CNTs [28] and RuO_2/CNTs [29] etc. Nevertheless, for hierarchical core-shelled Sn@C nanocomposites, little has been reported on the interaction between the Sn and carbonaceous materials by XANES, which is crucial for understanding the mechanism behind the improved electrochemical performances. Here, we present a facile and scalable one-step CVD method to synthesize Sn@C-GNs composites. The hierarchical Sn@C core-shelled nanostructures were anchored on GNs uniformly and densely with the crystalline Sn core and the carbon shell intact. XANES at relevant edges unveil the intimate correlation between metallic tin and surrounded carbonaceous materials, which immobilizes Sn into carbon shell or GNs and compresses the lattice of Sn atoms. It is shown that the hybrid composite exhibits both high reversible lithium storage properties and an excellent rate capability benefiting from the synergic effect of each component in the composite.

6.2 Experimental

6.2.1 Sn@C-GNs synthesis

GNs were prepared applying a modified Hummers method to get graphene oxide first, and then performing the rapid heating of graphene oxide at 1050 ^{o}C at Ar atmosphere. In a typical process of synthesizing Sn@C-GNs composites, the as prepared 80 mg GNs and 400 mg SnO_2 (325mesh, Aldrich) were ultrasonically dispersed into 40 mL ethanol solution for 30 min first. Then the suspension were filtered and dried at 80 ^{o}C overnight to collect SnO_2/GNs composites. The as-obtained SnO_2/GNs were put in a tube furnace and heat treated at 800 ^{o}C for 30min at 200 sccm gas mixtures (10% ethylene and 90%

argon) atmosphere to realize the in-situ formation of Sn@C-GNs composites. After cooling to room temperature with pure Ar, Sn@C-GNs nanostructure was obtained. For Sn@C composites, the procedures are the same except the addition of GNs.

6.2.2 Characterization

The as-obtained products are characterized by powder X-ray diffraction (XRD, Rigaku RU-200BVH with a Co-Kα source (λ=1.7892 Å)), field emission scanning electron spectrometry (FE-SEM, Hitachi 4800S) coupled with energy dispersive spectroscopy (EDS), transmission electron microscope (TEM, Hitachi H-7000), and high resolution TEM (HRTEM, JEOL 2010 FEG microscope) and raman microspectroscopy (HORIBA Scientific LabRAM HR Raman spectrometer) with incident laser beam at wavelength of 532.03 nm under ambient condition. The carbon contents (wt %) were calculated by thermogravimetric analysis (TGA; Netzsch) in air from room temperature to 700 ^{o}C. The XANES experiments on the Sn L_3 and C Kedge were conducted on the undulator Soft X-ray Microcharacterization Beamline (SXRMB) and Spherical Grating Monochromator (SGM) beamline at the Canadian Light Source (CLS) located at the University of Saskatchewan in Saskatoon, which were recorded in total electron yield (TEY) using specimen current and X-ray fluorescence yield (FLY) using a Multi-Channel Plate. Sn M edge spectra and extended X-ray absorption fine structure (EXAFS) data were obtained from the X-ray Science Division (XSD) partnered with the Pacific Northwest Consortium (PNC) at Sector 20 of Advanced Photon Source, which were recorded in transmission mode.

6.2.3 Electrochemical Measurement

The as-prepared samples were mixed with conductive carbon black and polyvinylidene fluoride in a weight ratio of 8:1:1 in N-methylpyrrolidinone (NMP) solvent. After working electrodes were dried at 80 ^{o}C under vacuum overnight, the coin cells were assembled using lithium metal foil as the counter electrode and the polypropylene as the separator inside an argon-filled glove box. The electrolyte was 1M $LiPF_6$ in ethylene carbonate (EC) and dimethyl carbonate (DMC) solvent (1:1 volume ratio). The profiles of galvanostatically charging and discharging curves were obtained on a computer controlled battery tester system (Arbin BT-2000) at a voltage range of 0.01 to 3 V (vs. Li^+/Li) with a current density of 75 mA g^{-1}. Cyclic voltammetry (CV) measurements were performed on an electrochemical workstation (Potentiostat/Galvanostat/EIS (VMP3)) at a scanning rate of 0.1 mV s^{-1}.

6.3 Results and Discussion

The Sn@C-GNs composites are synthesized by a fast, simple and scalable one-step CVD procedure. The following description is consistent with the observation reported in subsequent sections. First, ethylene reduces SnO_2 supported on GNs to metallic Sn nanoparticles, and then carbon, originating from the decomposition of ethylene, forms a shell at the surface of Sn nanoparticles (carbon has low solubility in tin during CVD process). It should be noted that the Sn nanoparticles discussed here are in liquid state at 800 ^{o}C and thus accompanying possible coalescence in between separated nanoparticles could take place, leading to the increase of particle size. It is worth to mention that the anchoring of tin oxide nanoparticles on GNs greatly avoids the merge. In another way, once the carbon shell is formed, it can serve as a geometrical separator and thus the aggregation of Sn nanoparticles can be effectively inhibited. In the subsequent cooling process, the Sn droplet will transforms into solid Sn nanoparticles, accompanied with volume shrinkage, resulting void space at the interface of Sn core and carbon shell. During the entire fabrication process, the GNs remains as a stable substrate for *in-situ* nanocomposites formation. The growth process of Sn@C-GNs hierarchical nanostructure is illustrated in Figure 6.1.

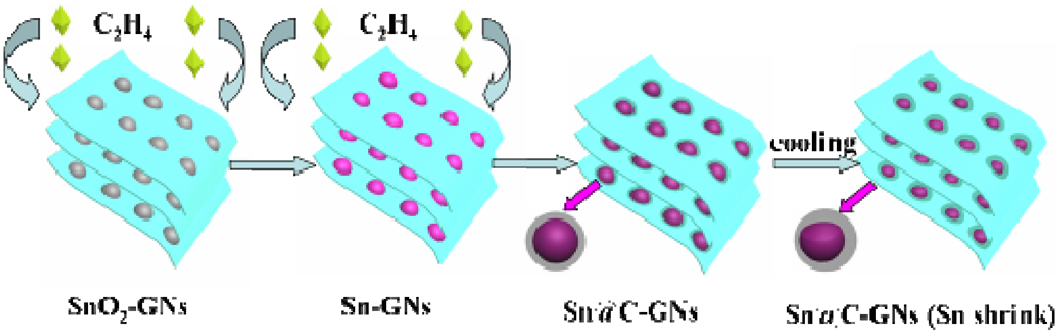

Figure 6.1 Schematic sketch for the Sn@C-GNs composites growth procedures.

Figure 6.2 shows the X-ray diffraction (XRD) patterns of Sn@C, Sn@C-GNs nanocomposites and GNs. Only one broad peak centered at 28.4° was detected in GNs, which is attributed to the (002) facet. For Sn@C and Sn@C-GNs hybrids, all strong peaks match well with the β-Sn nanocrystals (PDF: 89-2761). It is noted that Sn@C-GNs nanocomposites exhibit broader diffraction patterns compared with that of Sn@C composites, indicating smaller tin particle size. Based on the (200) peak, the average crystal size of tin particles in Sn@C-GNs nanostructures is around 75.6 nm according to Scherrer's equation. Moreover, there are no obvious peaks indexed for carbonaceous materials such as GNs or carbon shell due to their low crystallinity. It should also be noted that no SnO_2 characteristic peaks were identified, indicating that the original SnO_2 was completely reduced to Sn by the ethylene at 800 °C.

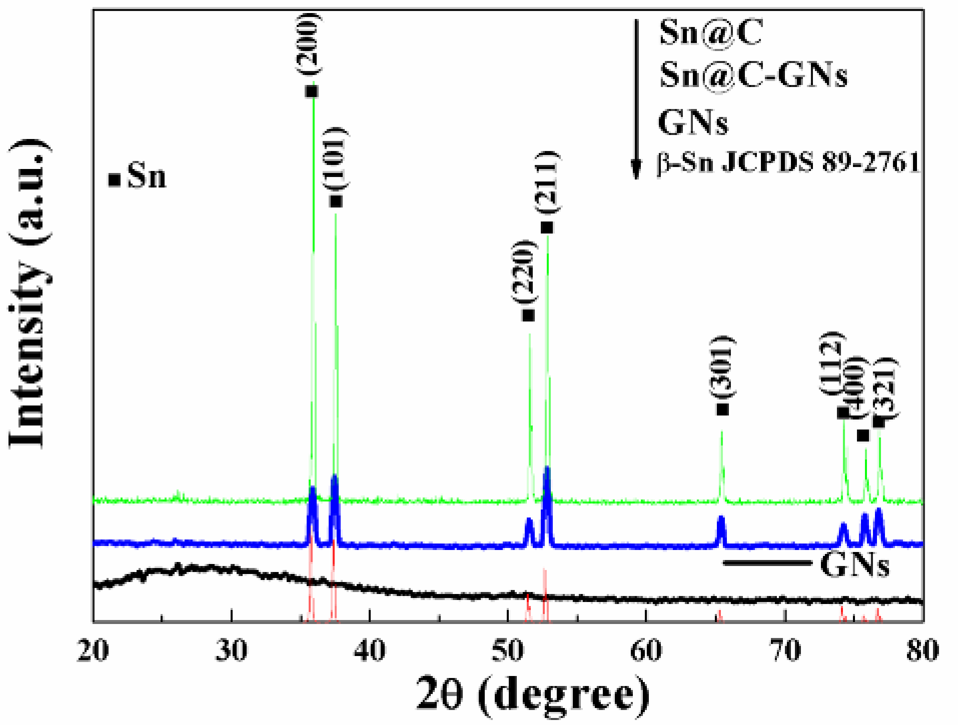

Figure 6.2 XRD patterns of GNs, Sn@C and Sn@C-GNs composites.

Figure SI 6.1 shows the typical scanning electron microscopy (SEM) and transmission electron microscope (TEM) image of GNs. It can be seen that GNs is composed of layered platelets with a curved structure. The ripped nanosheets exhibit high transparence for electrons under SEM and TEM, due to its ultrathin layer. The morphology of Sn@C nanocomposite is shown in Figure 6.3a. Sn nanoparticles exhibit a non-uniform size distribution from 50 nm up to 2 μm combined a carbon shell with a thickness around 10 nm. In contrast, figure 6.3b confirmed that the morphologies of Sn@C-GNs are indeed GNs supported core-shell structure. It can be seen that the Sn@C nanostructure distributed densely on GNs with a more uniform size compared with that of Sn@C nanostructures without GNs. Interestingly, from low magnification SEM images (inset of figure 6.3b), the layered morphologies could still be easily observed, indicating that GNs served as stable support for deposition of Sn@C composites. Meanwhile, deposited Sn@C nanostructures effectively spatially inhibit the assembly of GNs. Figure 6.3c and d shows the TEM image of Sn@C-GNs nanostructure. With GNs, the supported Sn@C nanostructure exhibits a uniform thickness of the outer carbon shell around 50 nm and a diameter of the inner Sn core between 60 nm to 100 nm. Compared with Sn@C without GNs, the significantly improved uniformity of Sn@C-GNs is due to the spatial separation of Sn nanoparticles and immobilization by GNs, preventing coalescence between Sn nanoparticles and resultant irregular increase of particle size. Also, SnO_2 are widespread and well dispersed onto GNs, the two dimensional open system facilitates the diffusion of ethylene gas, introducing more sites for reaction between SnO_2 and ethylene due to a large surface to volume ratio, accelerating the reaction rate of ethylene with SnO_2. As a result, the formation of carbon shell is faster, which could effectively prevent the liquid tin droplet from further agglomeration. The outside carbon shell could also help to buffer the volume change of Sn anodes during cycling, thus improving its cycle life [9]. For Sn@C without GNs, the partial agglomeration of Sn nanoparticles is inevitable due to the lack of separation and immobilization impacts provided by GNs, as illustrated in the inset of figure 6.3a, the size of some Sn particles increases up to 2 μm. Meanwhile, it has thinner carbon shell (around 10 nm) compared with that of Sn@C-GNs synthesized under the same reaction conditions (e.g. time, temperature and flow rate of carrier gas), which could be attributed to a relatively slower deposition rate of carbon caused by limited reaction sites. Intriguingly, close observation of the Sn@C-GNs system reveals voids between Sn core and carbon shell, as indicated by black arrows in figure 6.3e. This is due to the contraction of Sn nanoparicles, that is, the liquid Sn obtained at high temperature (800 ^{o}C) would solidify with shrinkage of volum when the temperature is below the melting point of Sn metal (231.93 ^{o}C) during the cooling process. Thus, the encapsulation of Sn by the carbon shell must have taken place at high temperature. It is noted that the voids produced here can offer extra space to relieve the stress and mitigate other adverse effect accompanied with expansion/contraction of Sn anodes during the lithium alloying and dealloying processes, combining the core-shell structure and the flexible graphene matrix, therefore improved electrochemical performances are expected.

To further clarify the structure and crystallinity of the Sn core and the carbon shell, high resolution TEM images taken from two areas highlighted with red rectangular region as “e” and “f” in figure 6.3, are shown in figure 6.3e and 6.3f, respectively. Figure 6.3e shows the lattice image of the exposed tin core from a broken Sn@C-GNs nanostructure, the lattice fringe with a measured inter-planar distance of 0.301 nm matches well with {200} Sn set of planes, indicating that the inner core is pure metallic Sn. Figure 6.3f shows the lattice image of the carbon shell taken at the exterior shell of an intact Sn@C nanoparticles. It is found that the carbon layers are composed of staggered and shortened graphene sheets with a calculated lattice fringe of 0.355 nm, which is slightly larger than the standard graphitized carbon (0.335 nm). The swollen carbon layers could offer more room to facilitate lithium diffusion. The crystalline Sn and low crystallized carbon shell are further proved from the selected area electron diffraction (SAED) patterns from diffraction dots (tin) and weak ring (carbon), as shown in figure 6.3g. Energy dispersive spectroscopy (EDS) patterns of Sn@C-GNs nanocomposites (figure 6.3h) also illustrate that only Sn and C are detected in the composites, indicating all SnO_2 have been totally reduced to Sn, which is in good agreement with the XRD results. Based on these desirable structures- the flexible GNs, the outside carbon shell, the well spatially separated Sn@C nanostructures and the voids between the Sn@C nanostructures, the hierarchical Sn@C-GNs nanocomposites are anticipated to show excellent battery performances.

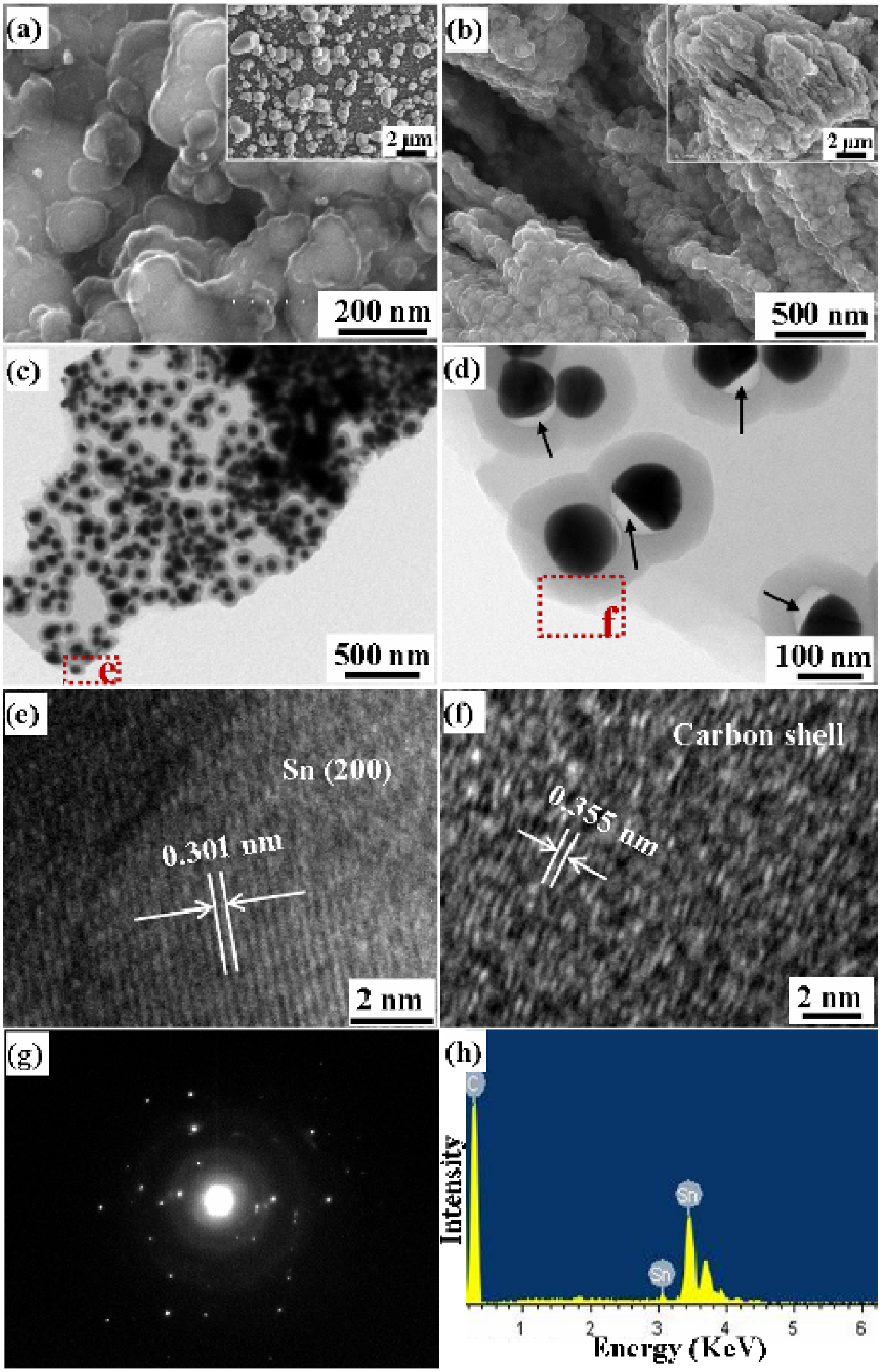

Figure 6.3 SEM images of (a) Sn@C composites and (b) Sn@C-GNs nanocomposites (insets show the relevant low magnification images); (c), (d) TEM images and (e), (f)

HRTEM images of Sn@C-GNs nanocomposites at red rectangular region e (tin core) and f (carbon shell); (g) SAED patterns and (h) EDS patterns of Sn@C-GNs nanocomposites.

The Sn@C and Sn@C-GNs nanostructures were further investigated by Raman spectroscopy compared with pure GNs. As illustrated in figure SI 6.2a, the peaks located at 1340 cm^{-1} and 1582 cm^{-1} are clearly tracked for all three samples, which can be ascribed to D band and G band, respectively [5]. The I_D/I_G values calculated for Sn@C, Sn@C-GNs and GNs were 0.97, 0.98, and 1.13, respectively. The intensity ratio of I_D/I_G for Sn@C and Sn@C-GNs are similar, indicating the layered carbon shells in Sn@C-GNs composites mainly contributes to the Raman signal and the partially disordered crystal structure as demonstrated in HRTEM images. The composites also exhibit a lower value of I_D/I_G compared with that of pure GNs, indicating its bigger size of the in-plane sp^2 domains and improved graphitic crystallinity. As a result, good conductivity could be expected for the core-shelled hybrids. Thermal gravimetric analysis (TGA) was also carried out in air to quantify the carbon and tin content in the Sn@C and Sn@C-GNs composites, as shown in figure SI 6.3b. Carbon was oxidized to CO_2 from 200 ^oC to 650 ^oC with a corresponding weight loss of 11.35% for Sn@C composites and 22.04% for Sn@C-GNs. TGA data of pure Sn was also given for comparison and clarification, where Sn shows a trace of increase of weight due to slight oxidation. Therefore, neglect the oxidation effect of tin (only around 1% in the temperature zone), the tin contents in Sn@C and Sn@C-GNs are calculated as 88.65% (100%-11.35%) and 77.96% (100%-22.04%), respectively.

The study of the electronic structure of each component in the composite and the interaction between Sn core with carbon shell or GNs are crucial for understanding and optimizing the synergic effect in hierarchical Sn@C-GNs composites employed as anodes for LIB. XANES is a spectroscopic technique which probes the local structure and bonding of an element of interest. By probing the unoccupied electronic states of the absorbing atom with a tunable synchrotron light source across an absorption edge, one can probe the local chemical environment and occupation (densities of states) of defect states as well as the conduction band. The interaction between Sn and carbonaceous could be unveiled by performing the XANES scans at the Sn L_3 (2p–5s, 5d) and C K (1s–2p) edge, studying the change of electronic structure and local chemistry environment.

Figure 6.4a shows the total electron yield (TEY) spectrum of Sn@C-GNs at Sn L_3 edge. The spectra for SnO_2 and Sn nanopariticle were also given for comparison. It can be seen that the surface sensitive TEY spectra of Sn@C-GNs are similar to Sn nanoparticles while obviously different from that of SnO_2 nanoparticles. For SnO_2 nanoparticles, it exhibits obvious electron transition from Sn 2p orbitals into unoccupied states with hybrid s and d character; the sharp peaks indicate localized electronic states, while for Sn and Sn@C-GNs, the resonance is less intense and broader, indicating a transition to the free electron like conduction band above the Fermi level [30, 31]. The excitation peak for Sn@C-GNs shows that the Sn nanoparticles in Sn@C-GNs composites are metallic. Besides, the more quenched and broader two pre-edge peaks “a” and “b” compared with pure SnO_2 nanopariticles also indicate the free electron like valence characteristics of Sn in Sn@C-GNs composites. Spectra presented here indicate that Sn nanoparticles are well protected from oxidation by the carbon shell in hierarchical composites, which is reasonable since Sn@C-GNs composites are synthesized by a reductive CVD process.

To further investigate the interaction between Sn with carbonaceous materials, carbon K-edge XANES was also performed on Sn@C-GNs composites and compared with pure graphene in both TEY and X-ray fluorescence yield (FLY) modes, as shown in figure 6.4b, 6.4c and 6.4d. For GNs, characteristic peaks of the graphitic structure can be easily tracked at 285.1 eV for π^* transition and at 291.5 and 292.5 eV for σ^* transition [32]. The broad peak at 288.3 eV indicates the existence of a carboxylic group. In contrast, the Sn@C-GNs exhibit the similar resonance for σ^* transition and carboxylic group while a relative low resonance for π^* transition and in TEY spectrum. It should be noted that in Sn@C-GNs, two kinds of carbon from GNs and partially crystallized carbon shell both contribute to the electron transition from carbon 1s to previously unoccupied electronic states. The π^* states have the same symmetry of and are related to perpendicular orientation of the molecular orbital (axis) of the π^* orbital in benzene or graphite. Combining the HRTEM image of the carbon shell, which also shows the layered graphene-like structure, its XANES is expected to be similar to GNs except lower absorption intensity at 1s to C-C π* orbital transition. This is reasonable since the shell is near spherical and will exhibit little polarization dependence. Considering the partially crystallized carbon is composed of staggered and shortened carbon basal planes, the irregular orientation at the perpendicular direction of the π* orbital could cause low probability to π* excitation. Figure 6.4c shows the magnified spectrum of the red square region in figure 3b, it is clearly observed that for Sn@C-GNs composites, the TEY spectrum exhibits a slight energy shift of 0.15 eV to lower excitation energy compared with that of pure GNs, illustrating that carbon atoms accept the electrons donated by Sn nanopaticles. The shift of energy is consistent with the notion that Sn-C shell interaction via charge redistribution indeed takes place between Sn nanopaticles and carbonaceous materials, favoring the immobilization of Sn onto surrounded carbon atoms. Such charge transfer from Sn to C 2p-derived π* states in graphene or carbon shell could also result a reduced π* transition intensity (proportional to unoccupied density of states, pending no countervailing symmetry arguments). Turning to the FLY spectrum (Figure 6.4d), which is bulk sensitive and the features are broadened due to the saturation effects (the fluorescence photon is reabsorbed by the sample); despite the broadening, the decreased intensity for Sn@C-GNs compared with pure GNs at π* states were also observed. It should be noted that the peak intensity at 288.3 eV also decreases, this may indicate that the decrease of carboxylic groups after the reductive CVD with ethylene. From these results, charge transfer and chemical bonding between Sn and carbonaceous materials in Sn@C-GNs composites are clearly evident.

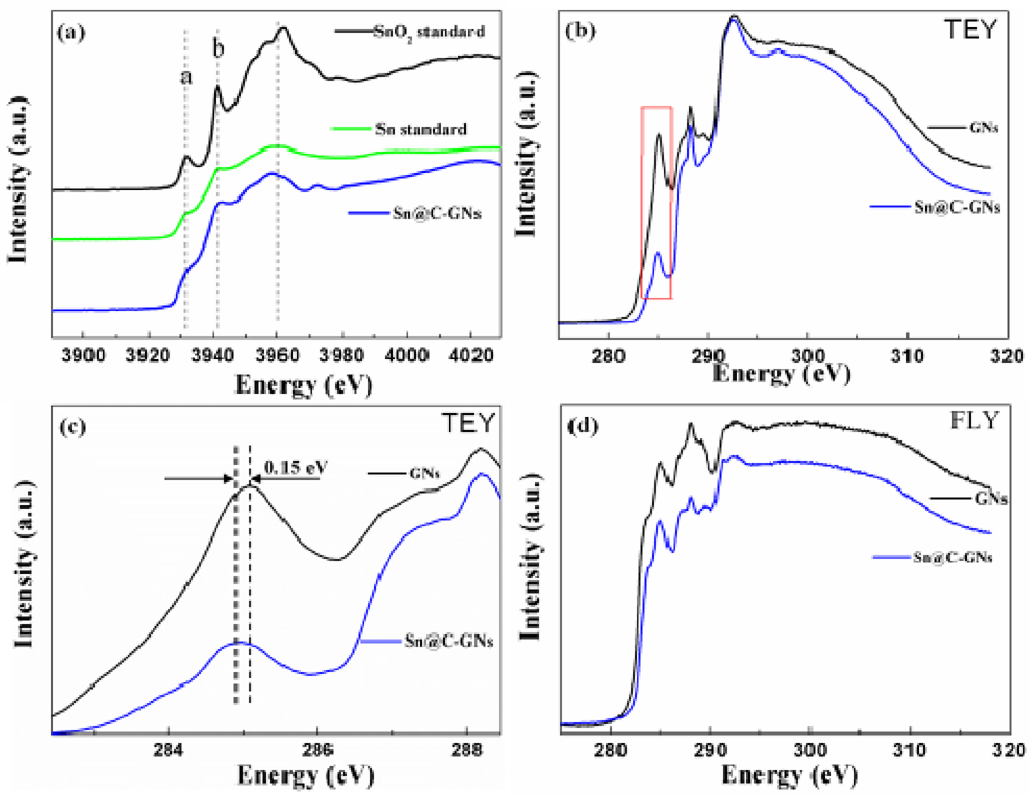

Figure 6.4 (a) TEY spectrum of Sn L$_3$ edge for Sn@C-GNs, Sn and SnO$_2$ nanoparticles. Carbon K-edge XANEs for Sn@C-GNs and GNs: (b) TEY spectrum, (c) Magnified TEY spectrum and (d) FLY spectrum.

Figure 6.5a shows the Sn K edge spectrum for Sn@C-GNs, Sn foil and SnO$_2$ nanoparticles. It can be seen that all three samples shows a high-energy K edge centered around 29.2 keV. SnO$_2$ nanoparticles exhibit a broad edge jump at around 29210 eV while Sn@C-GNs composites and Sn show a similar edge jump centered at 29206 eV. The high energy resonance for SnO$_2$ should be attributed to the higher Sn (IV) ions. For Sn@C-GNs, Figure 6.5b shows Fourier transform magnitudes of Sn K edge extended X-ray absorption fine structure (EXAFS) spectrum for Sn@C-GNs, in comparison with those of reference Sn foil and SnO$_2$ materials. Tin oxides show typical FT peaks of Sn-O bonding at 1.45 Å for Sn^{4+}-O and a Sn-O-Sn bonding above 3 Å, while Sn metal gives a FT peak of Sn-Sn metallic bonding at about 2.9 Å. For Sn@C-GNs, there are FT peaks of Sn-Sn metallic bonding at about 2.57 Å and Sn-C bonding in the surface region at 1.7 Å [32]. The peak feature without the peak [Sn-O-Sn] means Sn are well protected by carbon shell from oxidation. As a result, the as-prepared Sn metallic state can be supported by help of carbon shell. More intriguingly, the decreased Sn-Sn bonding length (2.57 Å) in the Sn@C-GNs composites compared with that of standard tin foil (2.9 Å) indicates that Sn lattice is compressed by the surrounded carbon atoms, in combination with the electrons transfer and appearance of Sn-C bond, the spectrum features indicate the intimate contact (chemical bonding and lattice compression) at molecular scale between Sn core and surrounded carbon atoms. A scheme diagram reflecting the bonds variation and charge redistribution is illustrated in figure 6.5c.

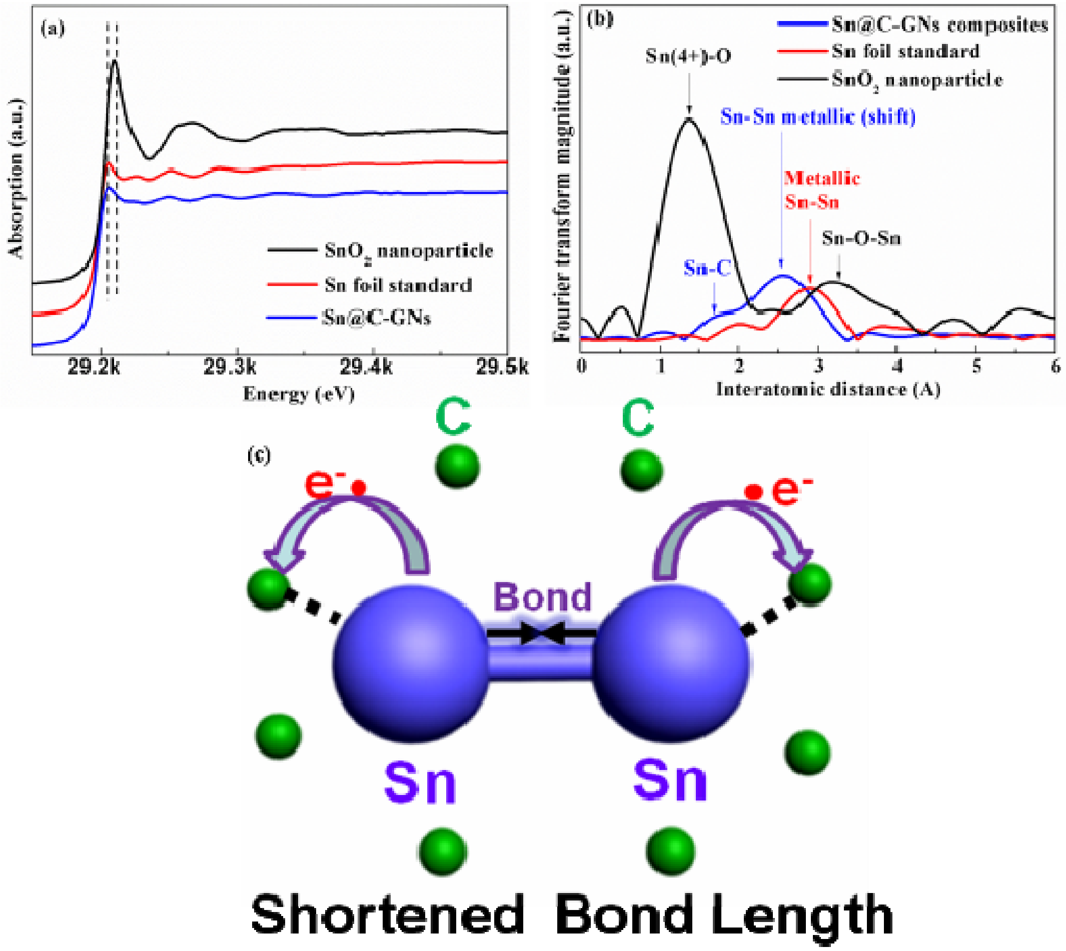

Figure 6.5 (a) XANES spectrum of Sn K edge and (b) Fourier-transformed (FT) magnitudes of Sn K edge k^3-weighted EXAFS spectra for Sn@C-GNs, SnO_2 nanoparticles and Sn foil. (c) The schematic representation of chemical bonding and lattice compression in Sn@C-GNs composites.

The cyclic voltammetry plots of the Sn@C-GNs composites are shown in Figure 6.6a. For the first cathodic scan, the peaks positioned at 0.65 V and 0.35 V are referred to the alloying process of lithium into tin forming LixSn [18], while the peak at 0 V are referred to the intercalation of lithium into carbon shell and graphene forming LiC_6. Turn to the anodic process, the weak and broad oxidation peak at ~0.12 V stands for the lithium extraction from the carbon or GNS. A series of peaks between 0.4 and 0.8 V are assigned to the de-alloying reaction of Li_xSn [21]. It is seen that the plots of the second and third scans are almost overlapped, indicating that good electrochemical reversibility of lithium storage in the Sn@C-GNs composites starts from the second cycle. In contrast, CV curves for Sn@C without GNs are shown in Figure SI 6.3. The continuous decreased current intensity along with cycles demonstrates its poor stability. Figure 5b presents the first two charge and discharge profiles of the composites at a current density of 75 mA g^{-1} with a voltage range of 0.01 V ~ 3V. The initial discharge curve exhibits a long slope starting from around 0.9 V to 0 V accompanying two small plateaus located at 0.65 V and 0.35 V, which can be assigned to the alloying of lithium with tin and interaction of lithium into carbon or graphene reactions. This observation is in good agreement with the CV curves shown above. Further, the nanocomposites clearly deliver a high initial discharge capacity of 1069 mA h g^{-1}. Due most probably to the solid electrolyte interface formation on low crystallized carbon, the capacity fades to 750 mAh g^{-1} for the second discharge cycle [21-23].

To evaluate the lifetime of Sn@C-GNs composites electrodes during cycling, galvanostatic long term cycles measurement was carried out, as shown in figure 5c. For comparison, Sn@C composites without GNs and pure GNs were also performed at the same current density of 75 mA g^{-1} with a voltage range of 0.01 V-3 V. As we previously reported [33, 34], GNs achieve a high discharge capacity of 788 mA h g^{-1} initially followed by an obvious fading in the following cycles, maintaining only 270 mA h g^{-1} in the 100th cycle. For the Sn@C composites without GNs, however, the discharge capacity also decreases despite the high specific capacity of 1036 mA h g^{-1} at the initial cycle, and only delivers a lithium storage capability of 188 mA h g^{-1} at the 100th cycle. The poor cycle performance of Sn@C composites without GNs indicates that the outer carbon shell could not effectively buffer the volume change of the wider size distribution of the inner

Sn core and prevent resultant pulverization of electrodes. In contrast, after hybridizing with GNs, the Sn@C-GNs exhibits both excellent cycle stability and high specific capacity. The initial discharge capacity could reach as high as 1069 mA h g^{-1}. More importantly, after 100 cycles, the discharge capacity still remains at 566 mA h g^{-1}, which is more than two and three times of that for bare GNs and Sn@C without GNs composites. We propose that the prolonged lifetime is due to (1) better confinement of the thick carbon shell in the composite with GNs compared with that in Sn@C composites without GNs; (2) improved mechanical properties provided by the flexible and robust GNs support and the outer carbon shell, (3) the well spatially separated Sn@C nanoparticles with uniform size, (4) the minimized aggregation of GNs due to jamming of Sn@C nanoparticles, and (5) the extra voids between Sn core and carbon shell. Considering the state-of- the-art of anodes such as commercial graphite, which is 372 mA h g^{-1}, the hierarchical composite demonstrates its superiority as a potential alternative anode. The Sn@C-GNs nanocomposite also exhibits excellent rate capability compared with Sn@C composites, as illustrated in Figure 5d. It can be seen that the composite still delivers a discharge capacity of 286 mA h g^{-1} when the current density was increased stepwise up to 3750 mA g^{-1}. More intriguingly, it is worthily noting that once the current rate is reversed back to 75 mA g^{-1}, a stable discharge capacity of 560 mA h g^{-1} returns, which is comparable to that of the same cell cycled galvostatically (566 mA h g^{-1} at the 100th cycle). This observation indicates that the Sn@C-GNs nanocomposite can endure varying discharge rate while keeping high energy densities in the meantime, which is more than welcome especially for practical applications in EVs. To our knowledge, the obtained electrochemical performance of hierarchical nanostructured Sn@C-GNs composites is comparable or even superior to the literature reported Sn based and other core shelled Sn@C nanocomposites [9, 20, 26, 35-37]. Combining the excellent electrical conductivity of GNs and carbon shell, the hierarchical morphology of Sn@C-GNs, which facilitates electrolyte immersion, and the intimate contact between Sn nanoparticles and carbonaceous materials, fast electrons and lithium ions exchange rate can be realized.

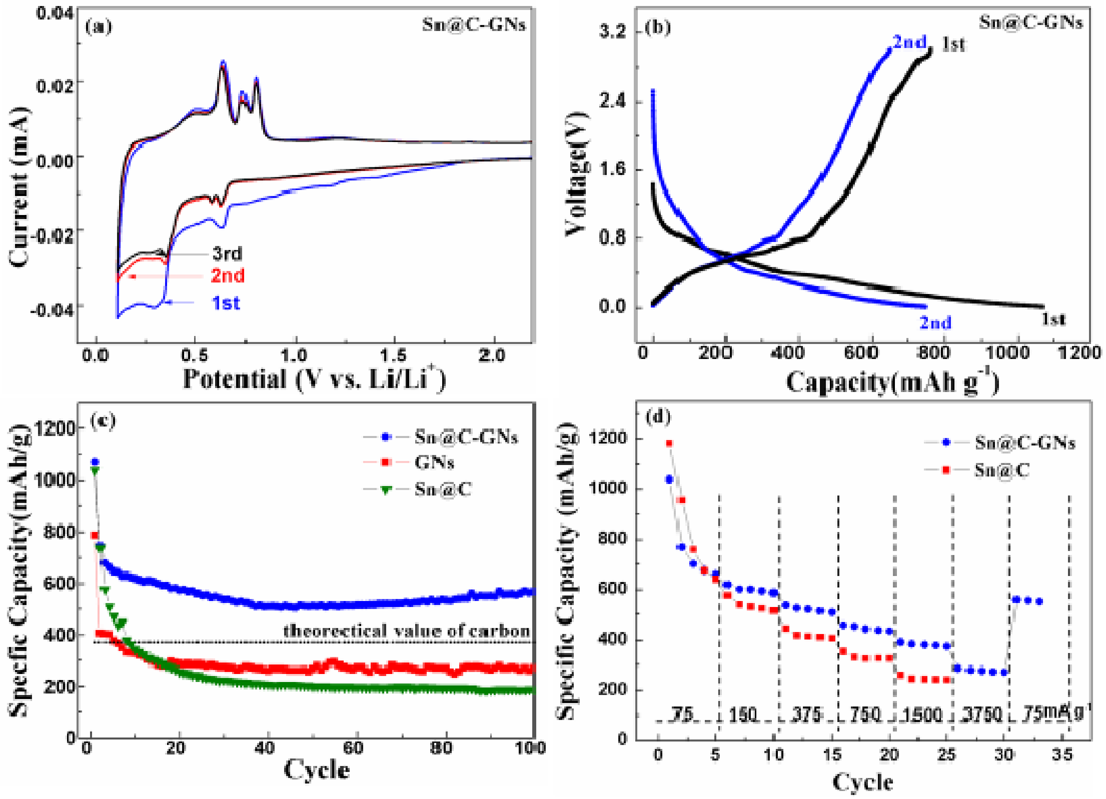

Figure 6.6 (a) Cyclic voltammogram (CV) and (b) First two Charge-discharge profiles of Sn@C-GNs composites (c) Cycle performance plots of bare graphene, Sn@C composites and Sn@C-GNs nanocomposites at 75 mA g^{-1}. (d) Rate performance of Sn@C-GNs and Sn@C composites.

To investigate the improved electrochemical performance of the hierarchical nanostructure, TEM were performed to examine the morphology variation of Sn@C with and without GNs nanocomposites electrodes after 100 cycles. For Sn@C without GNs electrodes, many exposed big Sn particles can be found after 100 cycles and the carbon shell fractures and falls apart from the Sn core, indicating that carbon shell could not maintain the volume change of Sn, which leads to the poor cycling. In contrast, for Sn@C-GNs, it reveals that the Sn nanoparticles were still embedded in the carbon shell and GNs matrix without any obvious volume change (Figure SI 6.4). It is demonstrated that core-shelled Sn@C are well kept and pinned onto the GNs during the cycling. The result that Sn nanoparticles in the hierarchical composite showed less agglomeration and size variation should be ascribed to the well protection of outer carbon shell and GNs, which effectively accommodate the strain and stress arising from the volume change of tin and avoid the detachment of active materials from the current collector during cycling. As a result, enhanced cyclic stability and rate capability was achieved. Thus, the Sn@C-GNs nanocomposites can be potential anodes applied in high performance LIBs.

6.4 Conclusions

Sn@C-GNs composite has been successfully synthesized by an effective one-step CVD strategy. The core-shell nanostructured Sn@C composites embedded in GNs exhibit high lithium storage capacities compared with pure GNs and Sn@C composites without GNs due to the flexible carbon shell, the encapsulated voids between Sn core and carbon shell caused by Sn shrinkage, and GNs, which can buffer the huge Sn core volume change during cycling. The Sn@C-GNS also demonstrates excellent rate performance combining the hierarchical structure of Sn@C-GNs and the high electrical conductivity provided by the GNs and carbon shell. XANES and EXAFS study at the Sn K, M, L_3 edge and the C K-edge clearly demonstrates that chemical bonding, charge transfer and lattice variation take place between Sn and carbonaceous materials, which anchors the Sn nanoparticles into the carbon shell and GNs firmly and facilitates fast charge transfer rate between Sn and carbonaceous materials. All these observations demonstrate that the hierarchical Sn@C-GNs can act as an alternative anode for EVs and HEVs applications and synchrotron spectroscopy glean a more complete understanding of the mechanism behind the improved performances.

6.5 Acknowledgements

This research was supported by Natural Sciences and Engineering Research Council of Canada (NSERC), General Motors of Canada, Canada Research Chair (CRC), Canada Foundation for Innovation (CFI), Ontario Innovation Trust (OIT) Program, X-ray Science Division (XSD)/Pacific Northwest Consortium (PNC) at Sector 20 of Advanced Photon Source and University of Western Ontario. The Canadian Light Source is supported by CFI, NSERC, NRC, CHIR, and the University of Saskatchewan.

6.6 References

[1] A. S. Aricó, P. Bruce, B. Scrosati, J. M. Tarascon and W. V. Schalkwijk, *Nat. Mater.*, 2005, **4**, 366-377.

[2] R. Bashyam and P. Zelenay, *Nature*, 2006, **443**, 63-66.

[3] S. M. Paek, E. J. Yoo and I. Honma, *Nano Lett.*, **2009**, **9**, 72-75.

[4] X. W. Lou, C. M. Li and L. A. Archer, *Adv. Mater.*, 2009, **21**, 2536-2539.

[5] J. Yang, J. Wang, D. Wang, X. Li, D. Geng, G. Liang, M. Gauthier, R. Li and X. Sun. *J. Power Sources*, 2012, **208**, 340-344.

[6] Y. Idota, T. Kubota, A. Matsufuji, Y. Maekawa and T. Miyasaka, *Science*, 1997, ***276***, 1395-1397.

[7] D. Larcher, S. Beattie, M. Morcrette, K. Edstroem, J. C. Jumas and J. M. Tarascon, *J. Mater. Chem.*, 2007, **17**, 3759-3772.

[8] I. A. Courtney and J. R. Dahn, *J. Electrochem. Soc.*, 1997, **144**, 2943-2948.

[9] D. Deng and J. Y. Lee, *Angew. Chem. Int. Ed.*, 2009, **48**, 1660-1663.

[10] J. Hassoun, G. Derrien, S. Panero and B. Scrosati, *Adv. Mater.*, 2008, **20**, 3169-3175.

[11] G. Derrien, J. Hassoun, S. Panero and B. Scrosati, *Adv. Mater.*, 2007, **19**, 2336-2340.

[12] K. T. Lee, Y. S. Jung and S. M. Oh, *J. Am. Chem. Soc.*, 2003, **125**, 5652-5653.

[13] G. X. Wang, X. P. Shen, J. Yao and J. Park, *Carbon*, 2009, **47**, 2049-2053.

[14] K. S. Novoselov, A. K. Geim, S. V. Morozov, D. Jiang, Y. Zhang, S. V. Dubonons, I. V. Grigorieva and A. A. Firsov, *Science*, 2004, **306**, 666-669.

[15] K. S. Novoselov, A. K. Geim, S. V. Morozov, D. Jiang, M. I. Katsnelson, I. V. Grigorieva, S. V. Dubonons and A. A. Firsov, *Nature*, 2005, **438**, 197-200.

[16] C. Berger, Z. M. Song, X. B. Li, X. S. Wu, N. Brown, C. Naud, D. Mayou, T. B. Li, J. Hass, A. N. Marchenkov, E. H. Conrad, P. N. First and W. A. de Heer, *Science*, 2006, **312**, 1191-1196.

[17] S. Stankovich, D. A. Dikin, G. H. B. Dommett, K. M. Kohlhaas, E. J. Zimney, E. A. Stach, R. D. Piner, S. T. Nguyen and R. S. Ruoff, *Nature*, 2006, **442**, 282-286.

[18] Z. S. Wu, W. C. Ren, L. Wen, L. B. Gao, J. P. Zhao, Z. P. Chen, G. M. Zhou, F. Li, and H. M. Cheng, *ACS Nano*, 2010, **4**, 3187–3194.

[19] G. M. Zhou, D. W. Wang, F. Li, L. L. Zhang, N. Li, Z. S. Wu, L. Wen, G. Q. Lu, and H. M. Cheng. *Chem. Mater.*, 2010, **22**, 5306-5313.

[20] G. Wang, B. Wang, X. Wang, J. Park, S. Dou, H. Ahn, and K. Kim, *J. Mater. Chem.,* 2009, **19**, 8378-8384.

[21] X. F. Li, X. B. Meng, J. Liu, D. S. Geng, Y. Zhang, M. N. Banis, Y. L. Li, J. L. Yang, R. Y. Li, X. L. Sun, M. Cai and M. W. Verbrugge, *Adv. Funct. Mater.*, 2012, **22**, 1647-1654.

[22] J. Yao, X. P. Shen, B. Wang, H. K. Liu and G. X. Wang, *Electrochem. Commun.*, 2009, **11**, 1849-1852.

[23] S. Ding, D. Luan, F. Boey, J. Chen, X. W. Lou. *Chem. Commun.*, 2011, **47**, 7155-7157.

[24] J. S. Chen, Y. L. Cheah, Y. T. Chen, N. Jayaprakash, S. Madhavi, Y. H. Yang, X. W. Lou. . *J. Phys. Chem. C*, 2009, **113**, 20504–20508.

[25] X. W. Lou, J. S. Chen, P. Chen, L. A. Archer. *Chemistry of Materials*, 2009, **21**, 2868-2874.

[26] S. Q. Chen, P. Chen, M. H. Wu, D. Y. Pan and Y. Wang, *Electrochem. Commun.*, 2010, **12**, 1302-1306.

[27] Y. Q. Zou and Y. Wang, *ACS Nano*, 2011, **5**, 8108-8114.

[28] J. G. Zhou, H. T. Fang, J. M. Maley, J. Y. P. Ko, M. Murphy, Y. Chu, R. Sammynaiken and T. K. Sham, *J. Phys Chem. C*, 2009, **113**, 6114-6117.

[29] J. G. Zhou, H. T. Fang, Y. F. Hu, T. K. Sham, C. X. Wu, M. Liu and F. Li. *J. Phys. Chem. C*, 2009, **113**, 10747-10750.

[30] T. K. Sham, *Phys. Rev. B*, 1985, **31**, 1888-1902.

[31] T. K. Sham, *International Journal of Nanotechnology*, 2008, **5**, 1194-1246.

[32] M. Noh, Y. Kim, M. G. Kim,H. Lee,H. Kim,Y. Kwon, Y. Lee and J. Cho, *Chem. Mater.*, 2005, **17**, 3320-3324.

[33] X. F. Li, D. S. Geng, Y. Zhang, X. B. Meng, R. Y. Li and X. L. Sun, *Electrochem. Commun.*, 2011, **13**, 822-825.

[34] D. Wang, X. Li, J. Wang, J. Yang, D. Geng, R. Li, M. Cai, T. K. Sham and X. Sun. *J. Phys. Chem. C*, 2012, **116**, 22149–22156.

[35] K. Hsu, C. Liu, P. Chen, C. Lee and H. Chiu. *J. Mater. Chem.,* 2012, **22**, 21533-21539.

[36] B. Luo, B. Wang, M. Liang, J. Ning, X. Li and L. Zhi. *Adv. Mater.*, 2012, **24**, 1405–1409.

[37] H. Liu, R. Hu, M. Zeng, J. Liu and M. Zhu. *J. Mater. Chem.*, 2012, **22**, 8022-8028.

6.7 Supporting Information

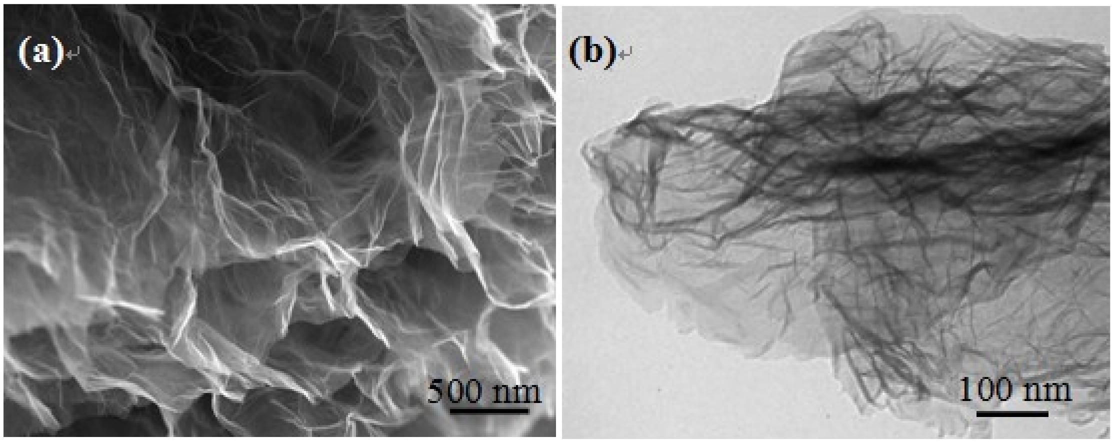

Figure SI 6.1 SEM image (a) and TEM image (b) of GNs.

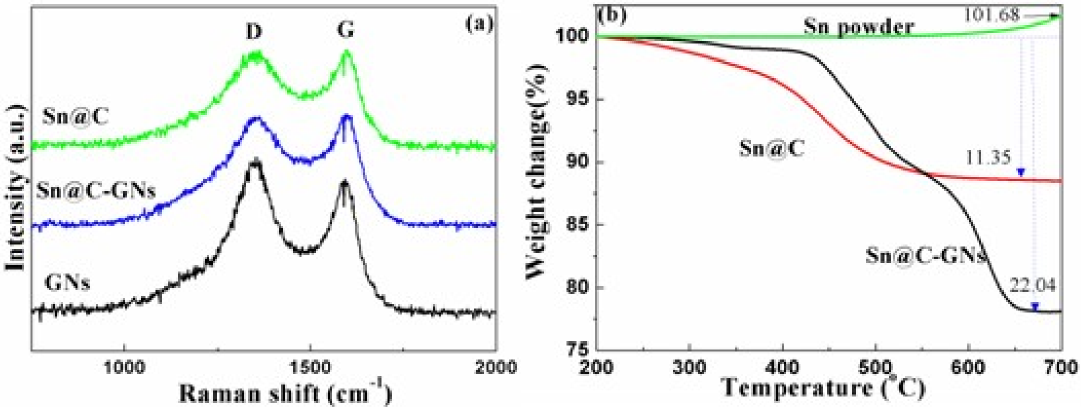

Figure SI 6.2 (a) Raman spectra of Sn powder, Sn@C and Sn@C-GNs; (b) TGA curves of Sn@C, Sn@C-GNs and GNs.

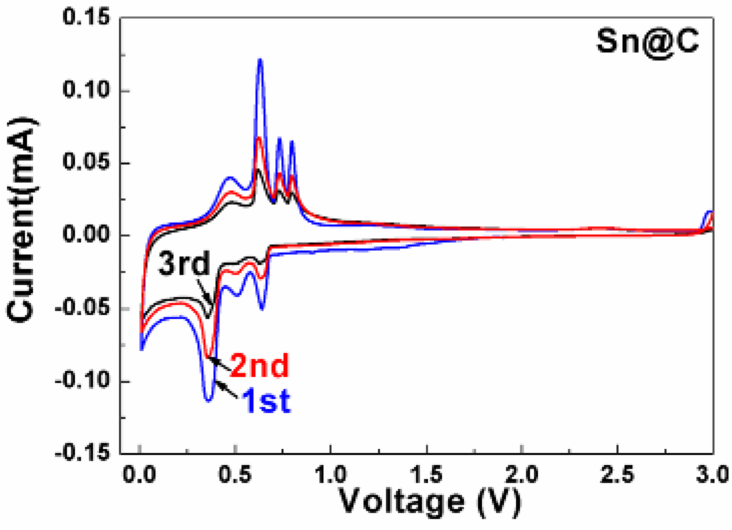

Figure SI 6.3 Cyclic voltammogram (CV) of Sn@C composites.

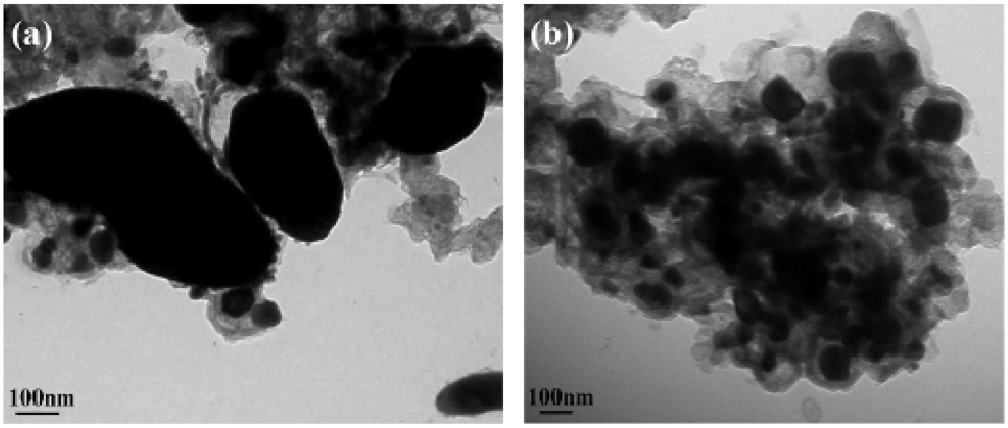

Figure SI 6.4 TEM image of Sn@C (a) and Sn@C-GNs (b) after 100 cycles.

Chapter 7

7 Engineering of co-axial carbon sheath tin core nanowires with chemical vapor deposition and its improved lithium storage capability

Hierarchical nanostuctured core-shell Sn@C embedded graphene composites have been demonstrated as promising high performance anodes in chapter 6. Based on this, designing Sn@C nanostructures on copper and stainless steel (SS) foils which are low cost current collectors for LIB is more welcome for practical application. Further, exploiting nanowire structure has been demonstrated as an effective way to alleviate the issues related to tin-based anodes. Thus, we aim to design and grow Sn@C nanowires on copper and SS.

In this chapter, co-axial carbon sheath tin core nanowires have been prepared using a simple one-step chemical vapor deposition (CVD) route. The obtained nanowires have a carbon shell with Sn and Sn alloys core. Scanning transmission X-ray microscopy (STXM) spectra characterize the electronic structure of a single nanowire for Sn@C on copper substrate, illustrating the carbon nature as well as the metallic Cu in CuSn alloys. Both two composites deliver high and stable lithium storage capabilities, benefiting from the flexible carbon shell and one dimensional structure.

KEYWORDS: core-shell structure, lithium ion batteries, Sn-C, scanning transmission X-ray microscopy, nanowire

---

Note: A version of this paper is in preparation.

7.1 Introduction

The emerging demand for application of lithium ion batteries in electric vehicles and hybrid electric vehicles requires the advance in developing high energy densities electrodes [1-3]. The current commercialized graphite have limited capacities of 372 mA h g^{-1} based on the formation of LiC_6, which could satisfy the need for large-scale power tools [4]. Tin based anode is promising candidate due to the high theoretical capacities based on alloying/dealloying mechanism. However, the accompanying serious volume variation (359%) during battery running will lead to electrode pulverization and loss of electronic contact between the active materials and the current collector, leading to poor cycling performances, thus impeding the practical applications [5-9].

Three avenues are generally applied to solve the issue in tin based anodes: fabricating nanostructured tin anodes to provide free space to absorb the extra volume expansion during alloying processes [10]; introducing other inert metals to form tin based alloys and then mitigate the stress and strain [11-12]; constructing tin embedded flexible matrix (usually carbon) to buffer the volume alternations [13-15]. A combination of these strategies mentioned above has been demonstrated successful and high capacity with superior durability Sn anodes is achieved including hierarchical SnO_2/C [16], SnO_2/graphene [5, 17] and core-shelled FeSn@C nanowries [18]. Our groups have already proposed the core-shelled Sn@C nanostuctures on graphene previously and the composites exhibit high cyclic and rate performances [6].

Recently, scanning transmission X-ray microscopy (STXM) is demonstrated as a powerful tool based on the high brilliant third generation light source. It probes the electronic structure through X-ray absorption near edge structures (XANES) while simultaneously characterizes the microscopy with a spatial resolution of 30 nm. It is especially useful for identifying chemical states in nanostuctures such as nitrogen doped carbon nanotubes, RuO_2/CNT and different thickness graphene [19-21].

In this paper, Sn@C core-shell nanowires are synthesized on copper and SS substrates, which are common current collector for LIB. Heteroatom from substrates will be incorporated into tin to form alloys with carbon shell outside. STXM are performed to provide a chemical mapping for single core-shelled nanowire. The obtained composites exhibit improved cyclic and rate performances.

7.2 Experimental

7.2.1 Synthesis of Sn@C-Cu and Sn@C-SS composites

In a typical process of fabrication for Sn@C on SS and copper, 80 mg SnO_2 nanoparticles (325 mesh, Aldrich) were vigorously ultrasonicated in 20 mL ethanol for 2 h. Metal Substrates (copper or stainless steel, 9/16 inch in diameter) were cleaned by acetone and ethanol for several times, and then pressed under 6000 LBs for 3 minutes to get a flat surface. Then the suspension obtained in the first step are dropped slowly onto the surface of substrates and dried under 80 ^{o}C in the oven for 5 minutes. The dropping and drying steps are repeated several times until the surfaces of the substrates are totally covered. The as-obtained SnO_2 deposited substrates were transferred to a furnace and annealed at 800 ^{o}C for 1h in gas mixtures with ethylene concentration of 10% (in volume) in Ar and then the Sn@C nanowires are then obtained on SS and Cu and they are denoted as Sn@C-SS and Sn@C-Cu.

7.2.2 Characterization

The as-prepared samples are characterized by X-ray diffraction (XRD, Rigaku RU-200BVH with a Co-Kα source (λ=1.7892 Å)), scanning electron spectrometry (FE-SEM, Hitachi 4800S) operated at 5 kV, energy dispersive spectroscopy (EDS), transmission electron microscope (TEM, Hitachi H-7000), and high resolution TEM (HRTEM, JEOL 2010 FEG microscope). STXM measurement was performed at the SM beamline of Canadian Light Source (CLS) using zone plate optics with a 30 nm spatial resolution of this zone plate. Images are collected at photon energy in the range of carbon K edge to Cu L_3 edge and analyzed using aXis2000 software package [22].

7.2.3 Electrochemical Measurement

The active nanowires (peeled from the substrates) were mixed with carbon black and polyvinylidene fluoride in a weight ratio of 8:1:1 in N-methylpyrrolidinone (NMP) solvent. After thorough grinding, the slurry were spread on copper foil and cut into round disk after overnight drying. The coin cells were assembled inside an argon-filled glove box with lithium metal foil as counter electrode and the polypropylene as the separator. The electrolyte is composed of ethylene carbonate (EC) and dimethyl carbonate (DMC) solvent (1:1 volume ratio) with 1M $LiPF_6$. The charging and discharging profiles curves and rate performances were obtained on a computer controlled battery tester system (Arbin BT-2000) at a voltage range of 0.01 to 3 V (vs. Li^+/Li) with at various current densities. Cyclic voltammetry (CV) data were collectedon an electrochemical workstation (Potentiostat/Galvanostat/EIS (VMP3)) at a scanning rate of 0.1 mV s^{-1}.

7.3 Results and Discussion

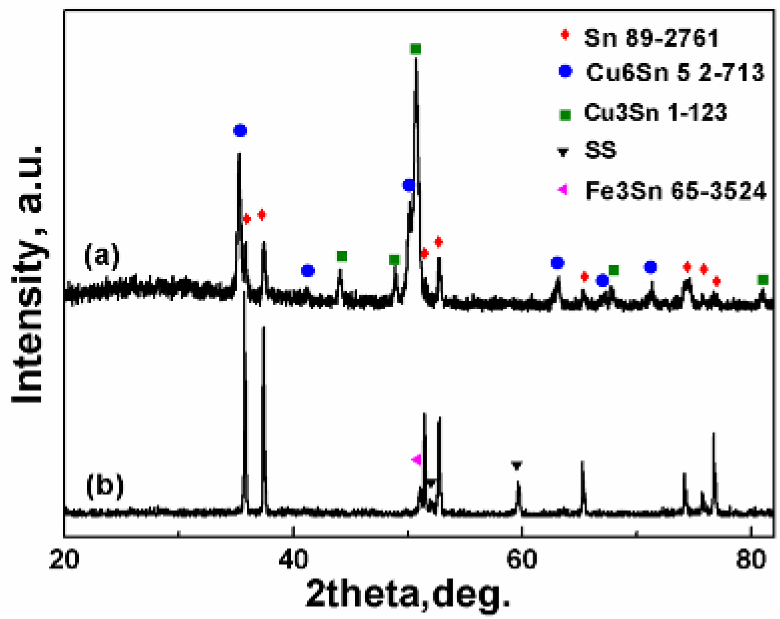

Figure 7.1 XRD patterns of (a) Sn@C-Cu and (b) Sn@C-SS composites.

The XRD patterns of Sn@C core-shell nanowires on two different substrates for the optimized samples are shown in Figure 7.1. It can be seen that both samples exhibit intensive diffraction peaks in the diffractogram, indicating high crystallinity structures are obtained. No peaks indexed to SnO_2 can be observed, illustrating the SnO_2 precursors have been fully reduced. Further identification reveals the existence of CuSn alloys and FeSn alloys where the heteroatom comes from the substrate copper and stainless steel. Sn@C-Cu shows various CuSn alloys includes coexistence of Cu_6Sn and Cu_3Sn with Sn, while Sn@C-SS possesses low intensity of diffraction peaks for Fe_3Sn alloys which may be due to low activity of Fe than Cu during CVD process. Moreover, no carbon peaks could be identified, demonstrating the low crystallinity feature of carbon shell. The crystalline metalic Sn peaks in the two composites could be indexed to beta Sn (JCPDS card No. 04-0673), similar to our previous work on graphene substrates, the EDX spectra shown in Figure SI7.1 for Sn@C-Cu and Sn@C-SS illustrate the existence of copper in the final products of Sn@C-Cu while iron is hard to be detected in the Sn@C-SS which may be due to the low content of Sn-Fe alloys.

The morphologies of Sn@C-Cu and Sn@C-SS are unveiled using SEM and TEM, as shown in Figure 7.2. Obviously, the one dimensional core-shell structures are observed in both composites with uniform distribution. For Sn@C-Cu as shown in Figure 7.2a and 7.2c, the core has a diameter around 80-100 nm and the shell of carbon is around 80 nm. While for Sn@C-SS, it is around 50 nm for core and 100 nm for shell respectively. A low magnification SEM image shown in Figure SI7.2 illustrates the dense and uniform Sn@C nanowire arrays on the surface of SS. Further comparison of TEM images of as-obtained carbon shells in two substrates, it can be seen that the carbon for the Sn@C-Cu is rough while for that of Sn@C-SS, it is much smoother. Noting that the reaction parameters are the same for two substrates, the smaller diameter for core and thicker shell for carbon in Sn@C-SS should be attributed to substrates. Previous synthesis of CNTs in our group has demonstrated that Fe in SS could catalyze the decomposition of ethylene, forming nanotube while the catalytic activity for copper is not obvious. Thus, it is believed that carbon decomposition rate is higher for SS substrate, generating a thicker coating on core-shell structure. As revealed in XRD, the Fe element in the Fe-Sn alloy could also facilitate the formation of carbon. To check the crystallinity of the carbon, HRTEM are further performed, as shown in Figure 7.3. Figure 7.3a and 7.3b exhibit the HRTEM image of the carbon from Sn@C-Cu and Sn@C-SS, respectively. The crystal structures for carbon are obviously different in these two composites. No lattice fringe can be identified for Sn@C-Cu, indicating amorphous feature. For Sn@C-SS, discontinuous lattice fringe shows up, after calculation, it is around 0.37 nm and 0.38 nm, slighter large than that of crystallized graphite of (002) facets of 0.33 nm, the swollen carbon shows a disordered structure. SAD patterns further confirms the improved crystallization degree for carbon in Sn@C-SS, where it shows narrow diffraction rings than dispersed and broad rings in Sn@C-Cu. The diffraction dots are originated from the tin core.

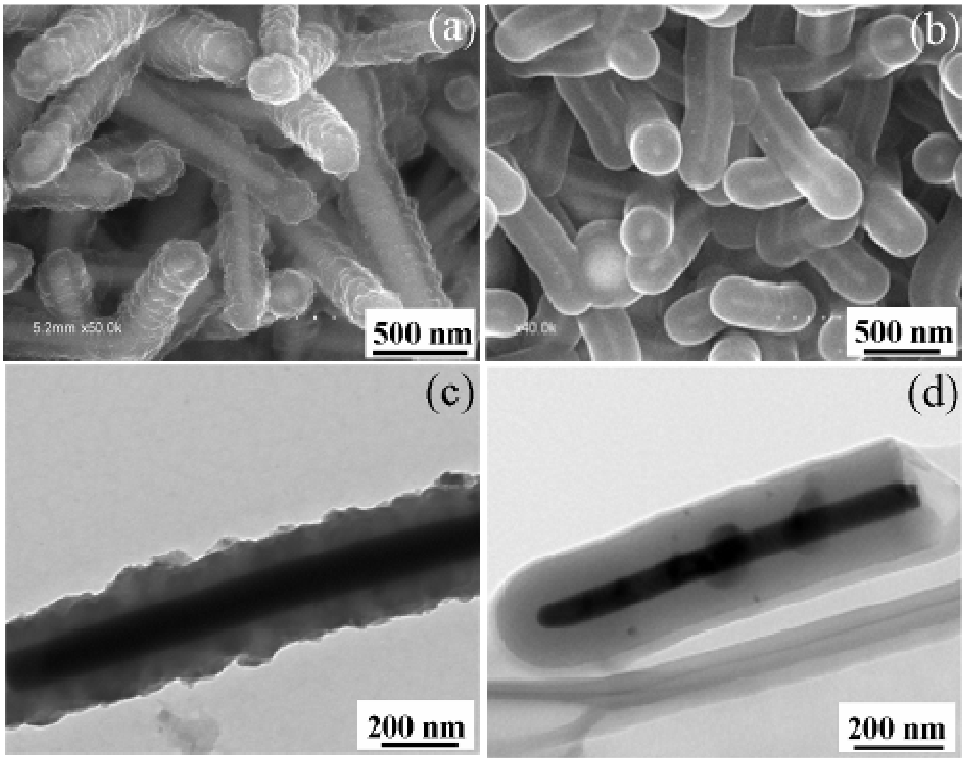

Figure 7.2 SEM images of (a) Sn@C-Cu and (b) Sn@C-SS nanocomposites; (c) TEM images of (c) Sn@C-Cu and (d) Sn@C-SS nanocomposites;

It is believed that iron from SS substrate could not only act as catalyst to facilitate the deposition rate of ethylene, but also improve the nature of deposited carbon to obtain a better crystallinity than that on copper. For Sn@C-Cu, we further performed other reaction time and temperature and investigated their effects on morphologies of the final products. Figure SI7.3 shows the SEM images of Sn@C-Cu obtained at different reaction conditions. It can be seen that prolonging reaction time to 1h, the nanowire structure will collapsed into 2 to 3 microparticles, with a carbon shell around 500 nm and a core up to several micros (Figure SI7.3a and SI7.3b). Reducing the reaction time to 15 minutes, it can be seen that the carbon thickness is greatly reduced to 25 nm while the Sn core have multiple morphologies including nanowires and isolated nanoparticles, the diameters are in the range from 20 nm to 200 nm, as shown in Figure SI7.3c and SI7.3d. It is concluded that reaction time has significant impact on morphologies, where the carbon thickness are proportional to reaction time, while 30 min is the optimized time at 800 ^oC to obtain nanowire morphologies. The reaction temperature effect is further conducted, as shown in Figure SI7.3e and SI7.3f. The obtained products exhibit a microsized core-shell structure. Increasing reaction temperature will increase the decomposition rate of carbon, leading to thicker carbon coating up to 250 nm. The thicker coating of carbon may inhibit the formation of nanowire, leading to agglomerated big particles in the core. It should be noted that carbon shell obtained at increasing temperature of 850 ^oC has smooth surface, illustrating better crystallinity due to higher temperature.

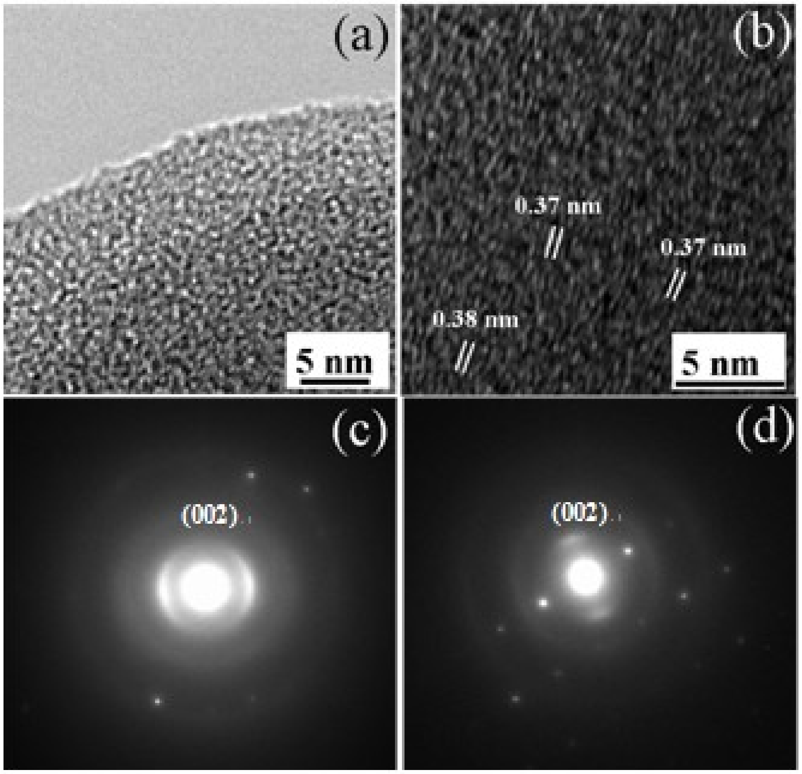

Figure 7.3 HRTEM images of the carbon shell from (a) Sn@C-Cu and (b) Sn@C-SS nanocomposites; SAED patterns of (c) Sn@C-Cu and (d) Sn@C-SS nanocomposites.

The STXM image of Sn@C-Cu nanowires recorded at the 292 eV is shown in Figure 7.4d. The core-shelled nanostrucures can be identified easily which matched well with the SEM and TEM results. The average of the stacked images from Figure 7.4c reveals the similar size of the core and shell to that of electron microscopy. The red square region is picked and chemical maps are obtained in this region. It is clearly identified from the chemical mapping results from Figure 7.4a and 7.4b that the core is composed of carbon (green color) and the shell has the copper element (red color), while carbon and copper could not be found in other regions.

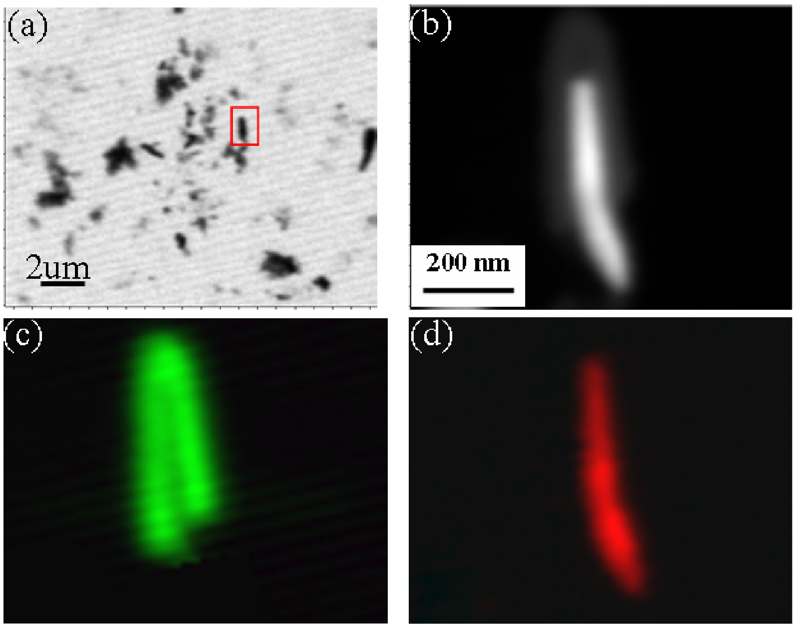

Figure 7.4 STXM chemical maps of Sn@C-Cu: (a) Composite map at 292 eV, the red square region shows the picked region of interest; (b) Composite map for relevant components from the average of the stacked images; (c) chemical map of carbon; (d) chemical map of Cu from the Cu-Sn alloys.

Compared with EDX results, STXM mapping has further capability to identify the chemical states of the carbon and copper elements. Figure 7.5 exhibited the XANES spectrum collected at the core and shell regions. Carbon K edge XANES exhibit a π* transition at 285.2 eV and σ* transition at 292.1 eV, which are characteristic of the sp^2 carbon structure. For the copper L_3 edge XANES, a pre-edge peak at about 931 eV is attributed to the electron transitions from 2p to 3d states. The transitions at 934.8 eV and 940.6 eV are characteristic features of metallic copper, indicating the Cu (0) feature in the core. STXM spectrum provides local electronic structure of single Sn@C-Cu nanowire.

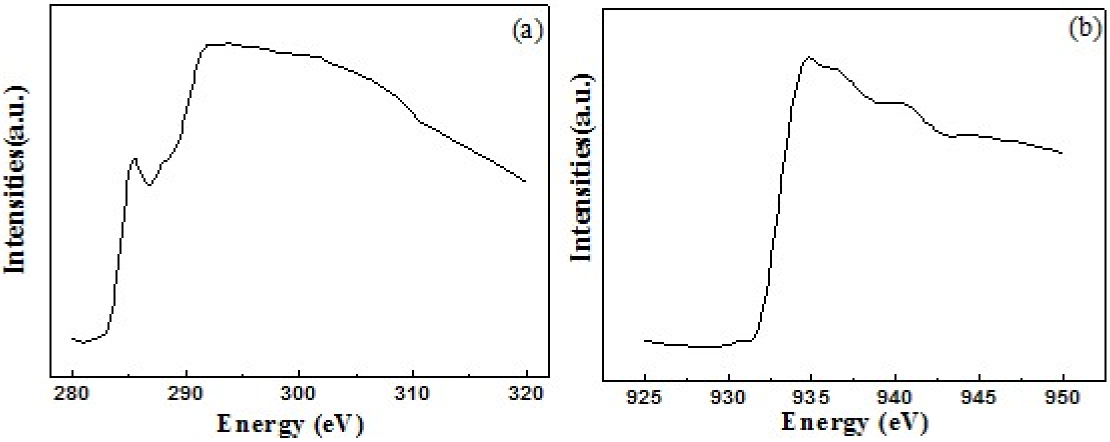

Figure 7.5 Transmission XANES of the core and the shell regions of a single nanowire (in Figure 7.4) at (a) carbon K-edge and (b) copper L_3-edge recorded in TEY mode.

Figure 7.6a and 7.6b shows the first charge-discharge profiles of the Sn@C-Cu and Sn@C-SS products performed at a current density of 50 mA g^{-1} with voltage window of 0.01 V to3 V. In the first discharge profile, both two composites exhibited a long slope in the range of 0.9 V to 0 V and no obvious plateau could be tracked, representing the alloying process of lithium with tin and intercalation process of lithium into carbon. For Sn@C-SS, it delivers an initial capacity of 724 mA h g^{-1}g, slighter larger than that of Sn@C-Cu, which is 689 mA h g^{-1} However, the initial coulombic efficiency for Sn@C-SS is 68%, lower than that of Sn@C-Cu, which is 77%. Both two composites shows decreased charge and discharge capacities in the second cycle, due to the irreversible SEI formation. Turn to the CV curves in Figure 7.6c and 7.6d, a groups of peaks aroused at between 0.5 and 0.7 V in cathodic scan and 0.4 and 0.8 V in the anodic scan are assigned to the alloying/de-alloying reaction of Li_xSn. The peaks around 0 V is attributed to the intercalation of lithium into carbon, which agreed well with the charge-discharge profiles.

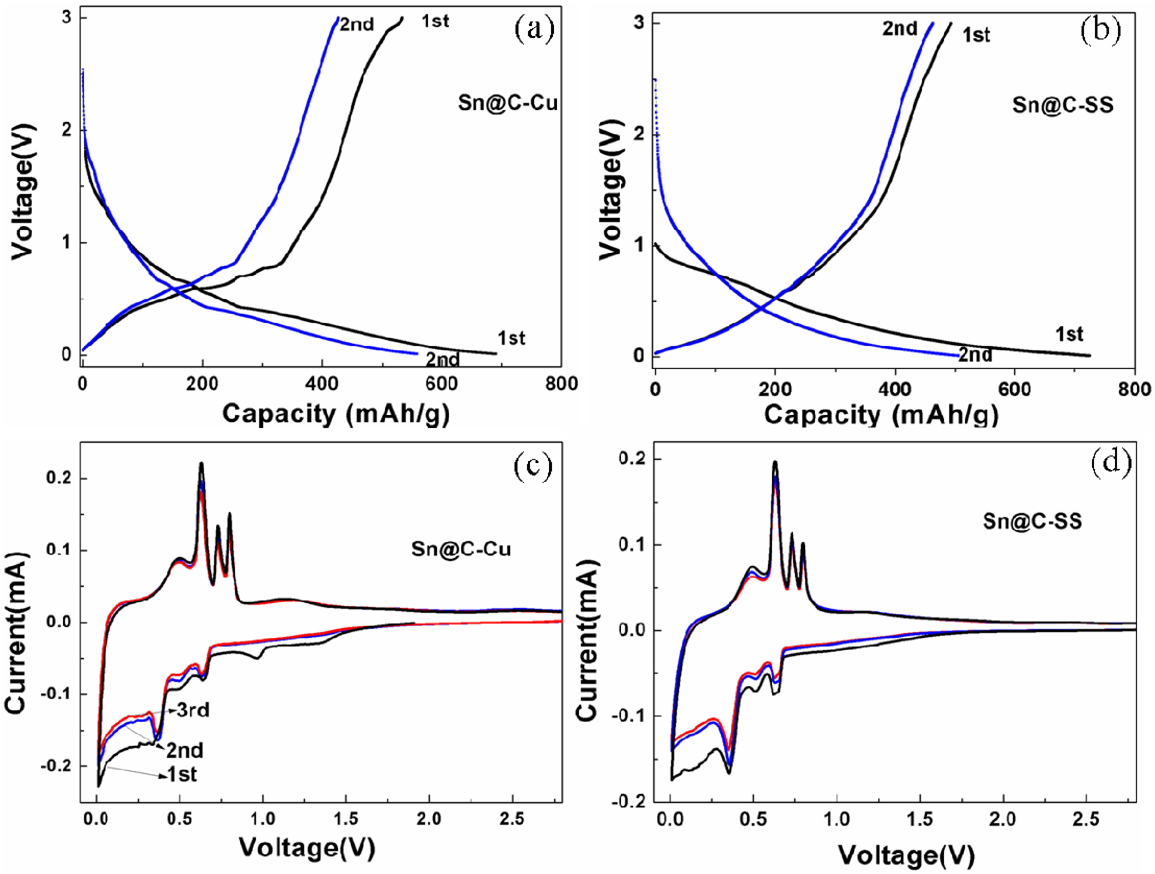

Figure 7.6 First two Charge-discharge profiles of (a) Sn@C-Cu and (b) Sn@C-SS nanocomposites; Cyclic Voltammetry of (c) Sn@C-Cu and (d) Sn@C-SS nanocomposites;.

The cycle performances and rate performances of the two composites are conducted and the results are shown in Figure 7.7. Pure nanosized Sn anodes are also tested for comparison. It can be seen that for Sn@C-SS, it delivers an initial discharge capacity of 724 mA h g^{-1}, after 80 cycles, the capacity maintains at 489 mA h g^{-1}. For Sn@C-Cu, the initial discharge capacity is 689 mA h g^{-1}, maintaining 374 mA h g^{-1} in the 80th cycle. The higher capacity in Sn@C-SS should be attributed to the low amount of FeSn content in the Sn core, while Sn@C-Cu has large amount of Cu-Sn alloys as shown in XRD patterns. The inert Cu would decrease the whole capacity in the composites. Obviously, compared with the no-carbon coated pure Sn electrodes, the capacity fade quickly, leaving a capacity of only 60 mA h g^{-1}at the 50th cycle due to the large volume variation upon cycling. The stable cycling behavior in composites of Sn@C-Cu and Sn@C-SS should be attributed to the flexible carbon shell, which absorbs the stress and strain from the tin and maintains the integrity of the whole electrodes. Thus, the cycling behaviors are quite stable since the fifth cycle. The rate capabilities for these two composites are further evaluated, as shown in Figure 7.7b, both two composites exhibit good electrochemical performance at various current densities, benefiting from the core-shelled nanostructure and good conductivity. Sn@C-SS exhibit high lithium storage capability due to low amount of Sn alloys.

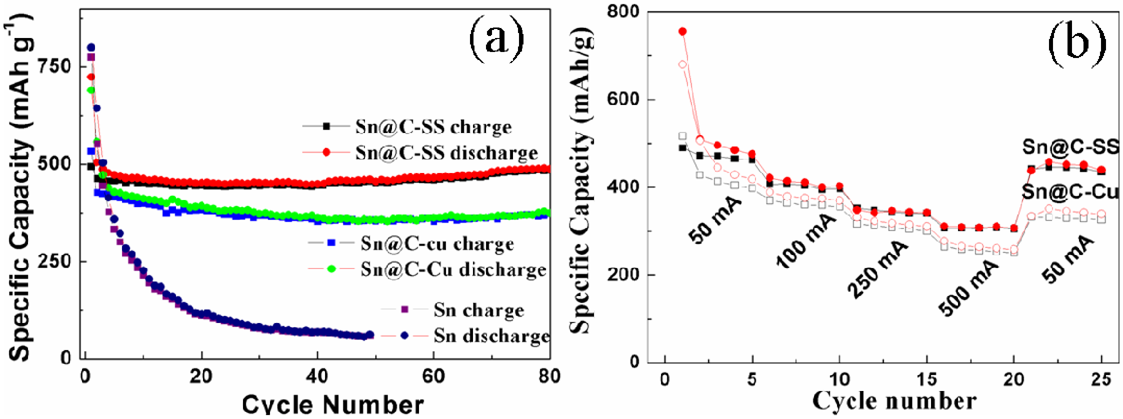

Figure 7.7 (a) Cycle performance plots of bare Sn, Sn@C-Cu and Sn@C-SS composites at 50 mA g^{-1}; (b) Rate performances of Sn@C-Cu and Sn@C-SS composites.

Figure 7.8 shows the TEM images of the composites after 80 cycles, for Sn@C-Cu in Figure 7.8a, the amorphous carbon fractured due to lithium intercalation, while carbon in Sn@C-SS still maintains its original morphology due to better crystallization. More interestingly, after 80 cycle, the core are still well embedded in carbon matrix without big size alternation, indicating the well protection from the carbon shell and thus stable cycling performances are achieved in both samples.

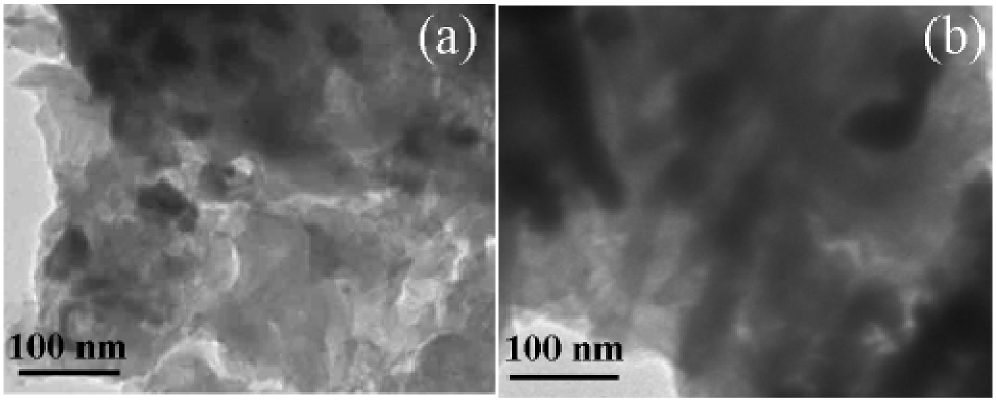

Figure 7.8 TEM images of (a) Sn@C-Cu and (b) Sn@C-SS composites after cycling.

Figure 7.9 shows the electrochemical impedance spectroscopy for Sn@C-Cu and Sn@C-SS electrodes, performed at 0.7 V at the 10th discharge cycle. The diameter of the semicircle for Sn@C-SS is smaller than that for Sn@C-Cu, indicating that the impedance value is smaller and the high lithium ion transportation rate. The amorphous carbon in Sn@C-Cu may impede the lithium transportation and have lower electronic conductivity. The EIS results indicate that Sn@C-SS have higher electronic conductivity and charge transfer rate, thus higher rate capability is achieved than that of Sn@C-Cu.

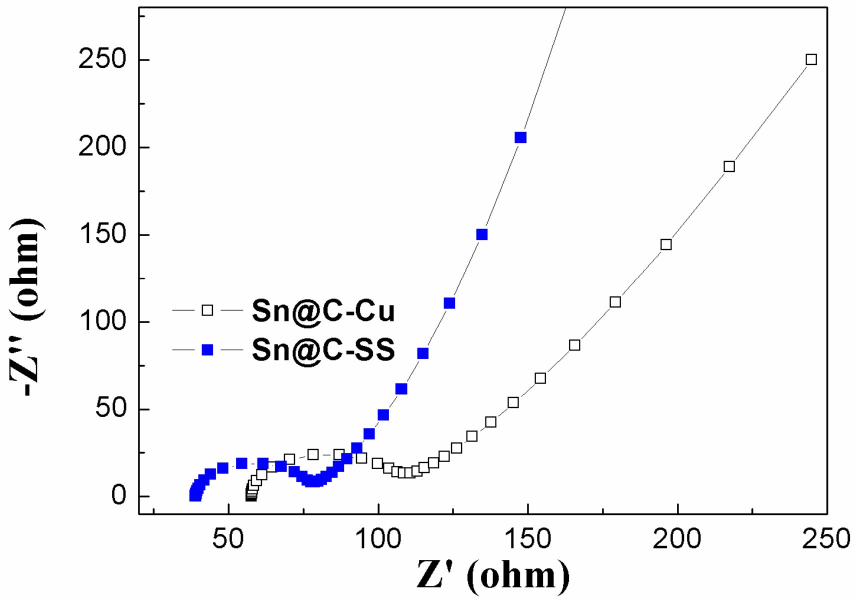

Figure 7.9 Electrochemical impedance spectra (EIS) of Sn@C-Cu and Sn@C-SS nanocomposites

7.4 Conclusions

In summary, two different carbon sheath tin core nanowires are obtained on copper and stainless steel substrates successfully using a facile CVD route. Sn@C-Cu has higher amount of Cu-Sn alloys in core and amorphous carbon shell, while Sn@C-SS exhibits higher quality of carbon. Synchrotron STXM results illustrate the metallic Cu and carbon nature. Both Sn@C-Cu and Sn@C-SS core-shell nanowires exhibit stable lithium storage capabilities. The higher cyclic and rate capability of Sn@C-SS comes from the improved carbon crystallinity and low amount of tin alloys.

7.5 Acknowledgements

Authors would like to give acknowledgements to Natural Sciences and Engineering Research Council of Canada (NSERC), General Motors of Canada, Canada Research Chair (CRC), Canada Foundation for Innovation (CFI), Ontario Innovation Trust (OIT) Program. The Canadian Light Source is supported by CFI, NSERC, NRC, CHIR, and the University of Saskatchewan. The SM beamline is specialy thanked.

7.6 References

[1] A. S. Aricó, P. Bruce, B. Scrosati, J. M. Tarascon and W. V. Schalkwijk, *Nat. Mater.*, 2005, **4**, 366.

[2] M. Armand and J. M. Tarascon, *Nature*, 2008, **451**, 652.

[3] J. M. Tarascon and M. Armand, *Nature*, 2001, **414**, 359.

[4] D. Y. Pan, S. Wang, B. Zhao, M. H. Wu, H. J. Zhang, Y. Wang and Z. Jiao, *Chem. Mater.*, 2009, **21**, 3136.

[5] D. Wang, X. Li, J. Wang, J. Yang, D. Geng, R. Li, M. Cai, T. K. Sham and X. Sun, *J. Phys. Chem. C*, 2012, **116,** 22149.

[6] D. Wang, X. Li, J. Yang, J. Wang, D. Geng, R. Li, M. Cai, T. K. Sham and X. Sun, *Phys. Chem. Chem. Phys.*, 2013, **15**, 3535.

[7] Y. Idota, T. Kubota, A. Matsufuji, Y. Maekawa and T. Miyasaka, *Science*, 1997, **276**, 1395.

[8] D. Larcher, S. Beattie, M. Morcrette, K. Edstroem, J. C. Jumas and J. M. Tarascon, *J. Mater. Chem.*, 2007, **17**, 3759.

[9] I. A. Courtney and J. R. Dahn, *J. Electrochem. Soc.*, 1997, **144**, 2943.

[10] C. S. Wang, A. J. Appleby and F. E. Little, *J. Power Sources*, 2001, **9**3, 174.

[11] P. P. Ferguson, A. D. W. Todd and J. R. Dahn, *Electrochem. Commun.*, 2008, **10**, 25.

[12] S. H. Lee, M. Mathews, H. Toghiani, D. O. Wipf and C. U. Pittman, *Chem. Mater.*, 2009, **21**, 2306.

[13] X. Li, X. Meng, J. Liu, D. Geng, Y. Zhang, M. Banis, Y. Li, R. Li, X. Sun, M. Cai, and M. Verbrugge, *Adv. Funct. Mater.*, 2012, **22**, 1647.

[14] X. Huang, X. Zhou, L. Zhou,K. Qian, Y. Wang, Z. Liu and C. Yu, *ChemPhysChem*, 2011, **12**, 278.

[15] G. X. Wang, J. H. Ahn, M. J. Lindsay, L. Sun, D. H. Bradhurst, S. X. Dou and H. K. Liu, *J. Power Sources.*, 2001, **97**, 211.

[16] Z. Y. Wang, Z. C. Wang, S. Madhavi and X. W. Lou, *J. Mater. Chem.*, 2012, **22**, 2526.

[17] P. Lian, X. Zhu, S. Liang, Z. Li, W. Yang and H. Wang, *Electrochimica Acta*, 2011, **56**, 4532.

[18] X. Li, Y. Zhong, M. Cai, M. P. Balogh, D. Wang, Y. Zhang, R. Li and X. Sun. *Electrochim. Acta*, 2013, **89**, 387.

[19] J. G. Zhou, J. Wang, H. T. Fang; C. X. Wu, J. N. Cutler and T. K. Sham, *Chem. Commun.*, 2010, **46**, 2778.

[20] J. G. Zhou, J. Wang, C. L. Sun, J. M. Maley, R. Sammynaiken, T. K. Sham and W. F. Pong. *J. Mater. Chem.*, 2011, **21**, 14622.

[21] J. Zhou, J. Wang, H. Liu, M. N. Banis, X. Sun and T. K. Sham. *J. Phys. Chem. Lett.*, 2010, **1**, 1709.

[22] http://unicorn.mcmaster.ca.proxy2.lib.uwo.ca/aXis2000.html.

7.7 Supporting information

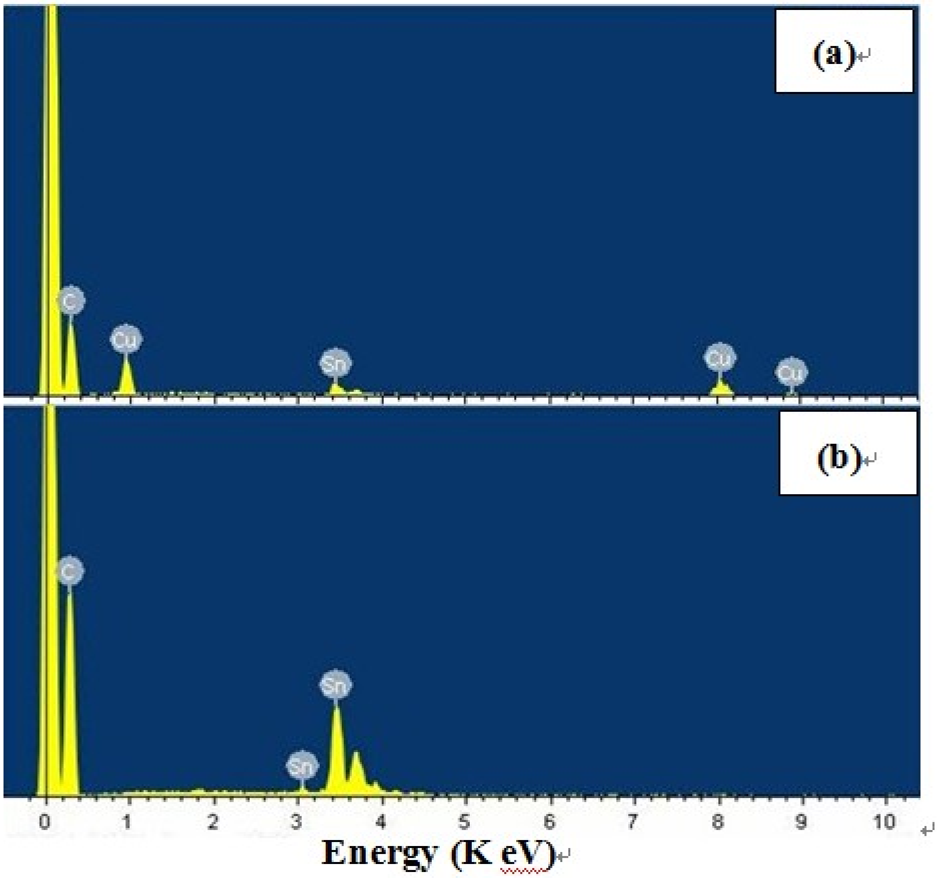

Figure SI 7.1 EDX spectrum of (a) Sn@C-Cu and (b) Sn@C-SS.

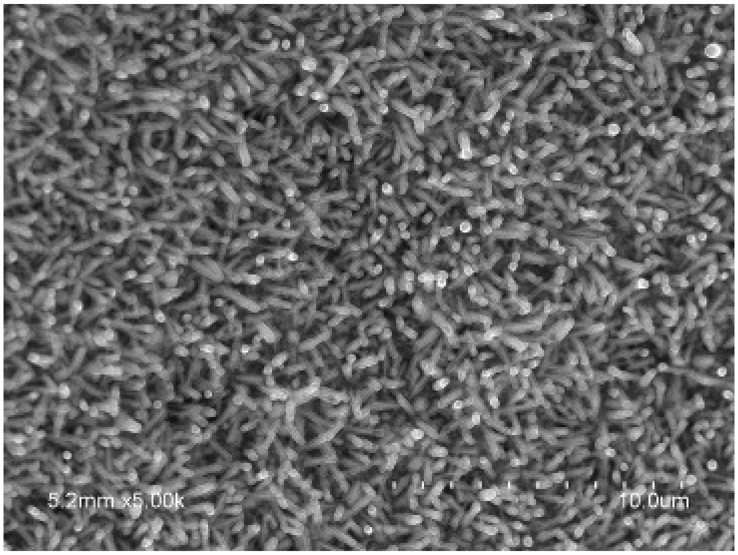

Figure SI 7.2 SEM image of synthesized Sn@C-SS.

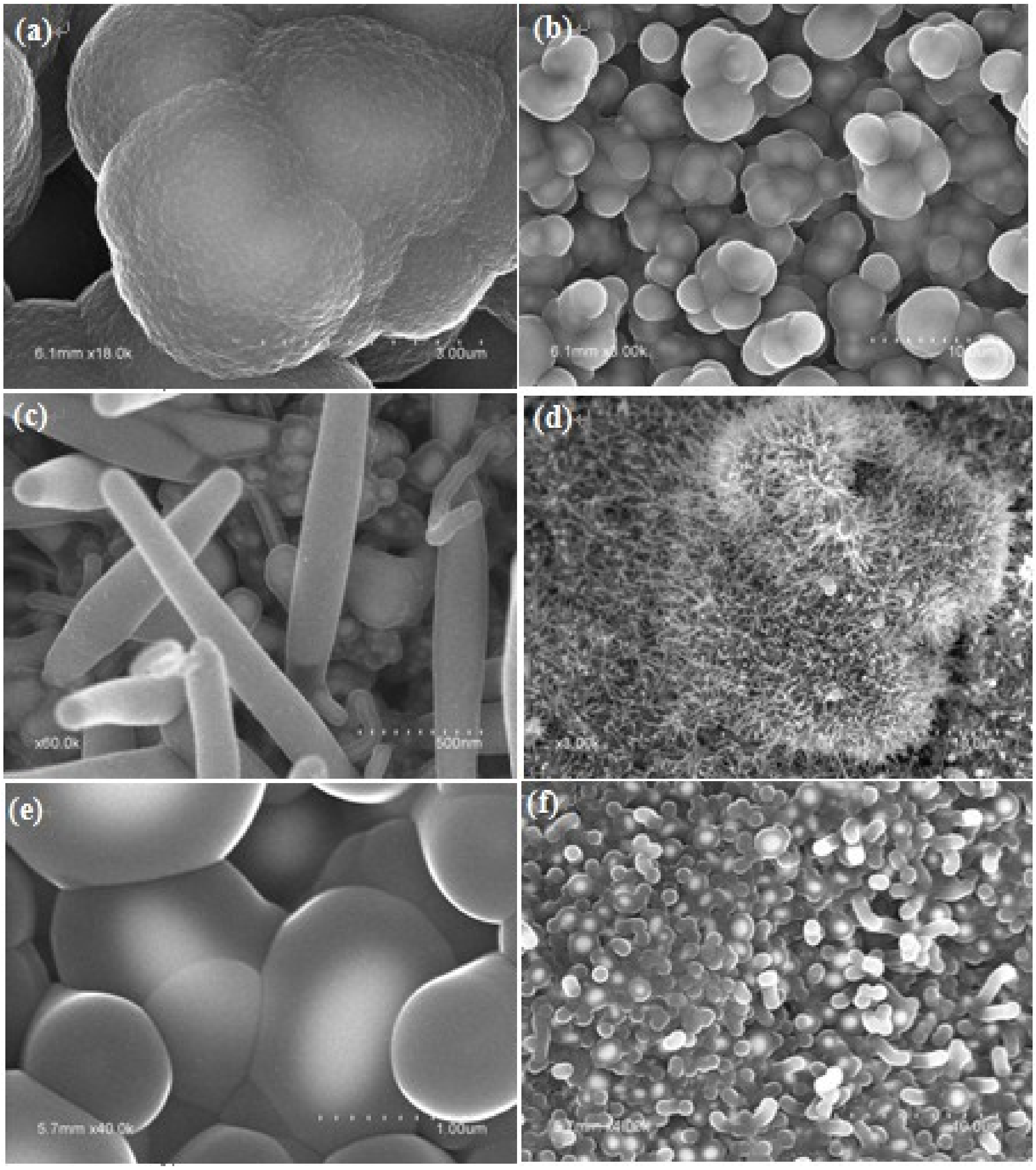

Figure SI 7.3 SEM images of synthesized Sn@C-Cu with different parameters: (a, b) 800°C 2h; (c, d) 800 °C 15 min; (e, f) 850 °C 30min

Chapter 8

8 Aluminum Oxide Surface Coating on Various Sized Tin Dioxide Anodes with Enhanced Electrochemical Performances

Except for carbon coating on tin-based nanomaterials such as Sn and SnO2 discussed above, other coatings such as metal and metal oxide coatings are also interesting. Atomic layer deposition is a unique coating technique for depositing ultrathin and uniform coatings used in LIB field. Therefore, we presented a case study on utilizing ALD technique to deposit Al_2O_3 on SnO_2 electrodes to see its effect on electrochemical performances of tin-based anodes.

In this chapter, a systematic study thickness effect of Al_2O_3 coating on electrochemical performances of various sized SnO_2 electrodes has been studied in this paper. It is found that the different volume changes on various sized SnO_2 electrodes can be controlled by the optimized thickness of Al_2O_3 coating layers with a range from less than 1 nm up to 3 nm deposited by ALD, which have significantly impact on the electrochemical behavior of the composites. The well defined and optimized Al_2O_3 layer could not only relieve mechanical degradation and improve cycling stability, but also form an artificial SEI layer to prevent the chemical reaction between SnO_2 and the electrolyte, leading to improved electrochemical performances compared with bare SnO_2 electrodes.

KEYWORDS: atomic layer deposition, tin dioxide, surface coating, lithium ion batteries

---

Note: A version of this chapter will be submitted after get the permission from GM.

8.1 Introduction

With the eager demands for alternative energy source to replace the conventional fossil fuels, lithium ion batteries (LIBs) have been widely studied these years and are regarded as one of the most promising candidates [1, 2]. More and more interests in LIBs are focusing on enhancing the lithium storage capability to satisfy the need for large-scale applications such as electrical grids, hybrid electrical vehicles and full electrical vehicles [3,4]. The state of art LIBs has limited capabilities including safety concerns, high price and low energy densities. Such issues could be overcome by exploiting new types of electrode materials and attempting various electrode composites [5-8].

Many researches have been concentrated on tin-based anodes originating from its attractive features including large reserves, environmental friendliness, low operating potential level and high lithium storage capabilities, which are more than twice of that of commercialized graphite (e.g. 784 mAh g^{-1} for SnO_2, 992 mAh g^{-1} for Sn) [7, 9]. However, starting from the work of Idota [10], more than a decade of efforts are devoted to struggling for improved cycling stability that is highly deteriorated by volume variation (>300%), accompanying serious pulverization of electrodes, undesired accumulation of thick solid electrolyte interface (SEI) and falling off of Sn based materials. Among plentiful approaches aiming at the challenges, designing nanostructured tin-based composites are regarded as one of the most effective strategies. A variety of composites including SnO_2/graphene [7, 11], Sn/graphene [12, 13], $SnO_2/Co_3O_4/C$ [14], SnO_2/SiC/graphene nanocomposites [15] have been proposed and improved long life cycling and rate performances have been obtained. However, nanostructured electrodes have high amount of SEI due to the large contact area with electrolyte, resulting low initial coulombic efficiency. Also, the mechanical and chemical degradation of SEI will cause vicious circle, resulting depletion of electrolyte and waste of electrodes.

Surface modification of electrodes especially surface coating on active materials has been proved as an effective route to stabilize the SEI layer. More over, it could mechanically maintain the integration of the whole electrode. A desired coating layer should be ionic conductive to facilitate the charge transfer, while mechanically and electrochemically stable to continuously prohibit the contact between electrolyte and electrodes. Meanwhile, the coating layer should be controlled in a limited amount to maximize the whole capacity of the composites. Recently, atomic layer deposition (ALD) technique has attracted great interest as a novel tool and approach for application in LIBs because of its excellent controllability which could realize conformal coating in the scope of atomic layers [16]. Enhanced electrochemical performance was achieved using ALD coating for cathode electrodes such as $LiCoO_2$ [17-20], $LiNi_{1/3}Mn_{1/3}Co_{1/3}O_2$ [21-23] and $LiMn_2O_4$ [24, 25]. Dillon demonstrated the success of MoO_3 electrodes with Al_2O_3 coating [26]. Xiao [27] et al. and Huang [28] et al. reported the multifunctional effect of Al_2O_3 on Si thin film and patterned Si electrodes with improved current efficiency. Jung et al. found that a whole battery (separator, cathode and anode) with Al_2O_3 coating could endure extremely severe condition such as high voltage over 4.5 V [29]. However, no publication has been focused on ALD coating on popular SnO_2 based anodes to our best knowledge. Herein, a systematic study of Al_2O_3 coating thickness effect on electrochemical behaviors of SnO_2 electrodes has been proposed. To set up a simple but detailed model, three sized pure SnO_2 electrodes was chosen as references and compared with Al_2O_3coated electrodes. The well defined and optimized Al_2O_3 coating could mitigate mechanical and chemical degradation of SEI layer and electrodes, leading to improved electrochemical behavior compared with pure SnO_2 electrodes.

8.2 Experimental

8.2.1 Synthesis of SnO_2 nanoparticles

In a typical process of SnO_2 nanoparticles, 2 mmol $SnCl_4$ was dissolved in 10 mL aqueous solution and vigorously stirred for 30 minutes to obtain clear solution. Then the transparent solution was transferred into 20 mL high pressure microwave- assisted Teflon-lined autoclave (Anton Paar Synthos 3000). The solution was subsequently heated to 120 ^{o}C and kept for 20 minutes. After cooling to room temperature, the obtained samples are rinsed with large amount of distilled water and ethanol. Then the as-obtained products were collected after final drying at 100 ^{o}C overnight for use in next step. To get three different sized SnO_2 nanoparticles, the products are annealed in tube furnace at different temperatures for 2h (400 °C for SnO_2-A, 600 °C for SnO_2-B and 925 °C for SnO_2-C respectively).

8.2.2 Synthesis of ALD-Al_2O_3 coated SnO_2 electrodes

The working electrodes are composed of the SnO_2 nanomaterials (SnO_2-A, SnO_2-B or SnO_2-C), conductive carbon black and polyvinylidene fluoride (PVDF) in a weight ratio of 8:1:1. The slurry obtained with N-methylpyrrolidinone (NMP) solvent was uniformly cast on a copper foil and dried at 70 °C under vacuum overnight. The as-prepared electrodes are ready for ALD coating without further treatment.

ALD-Al_2O_3 was coated directly on SnO_2 electrodes in an ALD reactor (Savannah 100, Cambridge Nanotechnology Inc., USA) using Trimethylaluminum (TMA) as Al precursor and H_2O as the oxidizer. The deposition temperature was set as 100 °C. Different ALD cycles (2, 5 and 20 cycles) were designed to get different coating layer thickness. The coated electrodes were applied for lithium ion battery testing without further treatment.

8.2.3 Characterization

Products were characterized by X-ray diffraction (XRD, Rigaku RU-200BVH with a Co-Kα source (λ=1.7892 Å)), field-emission scanning electron spectrometry (FE-SEM, Hitachi 4800S), transmission electron microscope (TEM, Hitachi H-7000), high-resolution transmission electron microscope (HRTEM, JEOL 2010 FEG microscope), dispersive spectroscopy (EDS). The X-ray absorption near edge structure (XANES) experiments on the Al K edge were conducted on the undulator Spherical Grating Monochromator (SGM) beamline at the Canadian Light Source (CLS) located at the University of Saskatchewan in Saskatoon. Sn K edge XANES and extended X-ray absorption fine structure (EXAFS) data were obtained from the X-ray Science Division (XSD)/Pacific Northwest Consortium (PNC) at Sector 20 of Advanced Photon Source located in Argonne national laboratory, which were recorded in fluorescence mode.

8.2.4 Electrochemical Measurement

The electrochemical experiments were conducted applying two electrode coin cells (2032) assembled using pure lithium metal sheets as the counter electrode and the polypropylene film as the separator inside an argon-filled glove box ($O_2 < 1$ ppm). The electrolyte was 1.0 M $LiPF_6$ in a mixture of ethylene carbonate (EC) and dimethyl carbonate (DMC) solvent (1:1 in volume). The profiles of galvanostatically charging and discharging curves were collected on a computer controlled Arbin BT-2000 battery tester system at a cut-off voltage window of 0.01 to 3 V (vs. Li^+/Li). Cyclic voltammetry (CV) measurements were conducted on an electrochemical workstation (Potentiostat/Galvanostat/EIS (VMP3)) at a scanning rate of 0.1 mV s^{-1} in an voltage range of 0.01–3.0 V (vs. Li^+/Li).

8.3 Results and Discussion

The SnO_2 nanoparticles are synthesized by microwave-assisted hydrothermal method through hydrolysis of $SnCl_4$ in aqueous solution at 120 ^oC for 20 min followed by annealing at selected temperature in air for 2h. For distinction, the samples are denoted as SnO_2-A (annealed at 400 ^oC), SnO_2-B (annealed at 600 ^oC) and SnO_2-C (annealed at 900 ^oC). Then ALD coating of Al_2O_3 were directly applied on the electrodes composed by SnO_2 nanomaterials. In order to obtain different thickness for Al_2O_3 layers, 2 cycle, 5 cycle and 20 cycle ALD are selected using $Al(CH_3)_3$ and water as precursors at 100 ^oC. The Al_2O_3 coated electrodes thus obtained were without further treatment and are henceforth denoted as x-SnO_2-A, x-SnO_2-B and x-SnO_2-C (x=2, 5, 20 for specified 2, 5 and 20 ALD cycles, respectively).

Figure 8.1a compares the XRD patterns of different sized SnO_2 with and without Al_2O_3 coating, where all strong spectra matched well with rutile SnO_2 (JCPDS No: 41-1445), indicating crystallized SnO_2 are successfully synthesized without detectable impurities. Further examination shows that XRD spectra of SnO_2-C is stronger and sharper than that of SnO_2-B and SnO_2-A, illustrating higher crystallinity due to higher temperature annealing. Also, the peaks for SnO_2-C are narrower than that of SnO_2-B and SnO_2-A, indicating that the grain size is bigger. Based on calculation using Scherrer's equation from the strongest peak, an average size of 4.1 nm, 8.8 nm and 25.8 nm are obtained for SnO_2-A, SnO_2-B and SnO_2-C respectively. It should be mentioned that for Al_2O_3 coated SnO_2 samples, no peaks for Al_2O_3 phase was observed which is due to its amorphous feature taking into consideration that the ALD deposited Al_2O_3 was obtained at 100 ^{o}C. Figure SI 8.1a displays the electron dispersive x-ray (EDX) spectrum of 20-SnO_2-C. The appearance of Al signals conclusively illustrates that Al element is successfully introduced into SnO_2 composites. To identify the chemical states of Al, X-ray absorption near edge structure (XANES) was conducted at Al K edge for the 20-SnO_2-C electrodes. As depicted in Figure 8.1b, the Al K edge spectrum is similar to that of the standard α-Al_2O_3, elucidating the formation of Al_2O_3 after ALD process. Compared with standard Al_2O_3 which exhibits two resolved peaks centered at 1567 and 1571 eV, the spectrum for 20-SnO_2-C is broadened with only one broad peak located at 1570 eV, confirming its highly disordered amorphous state. Thus the XANES results confirm that amorphous Al_2O_3 are successfully coated on SnO_2 particles.

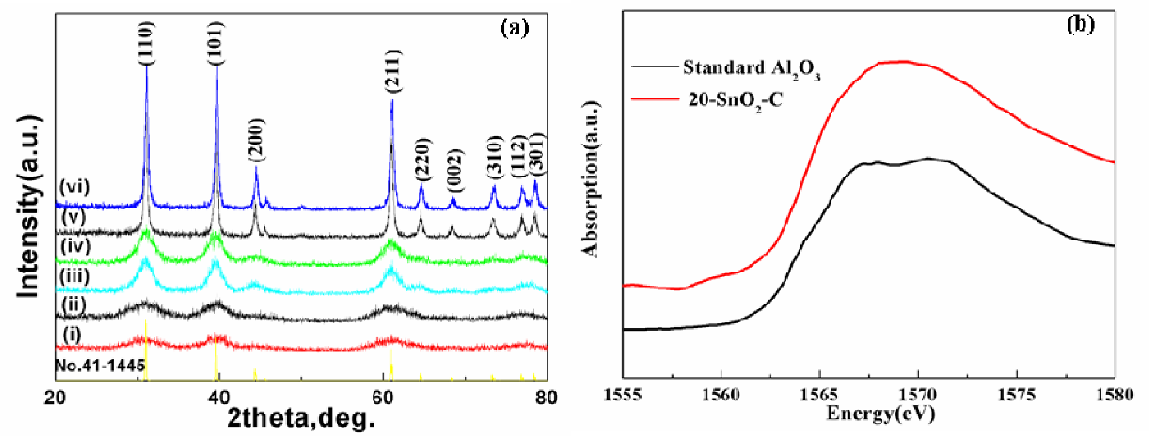

Figure 8.1 (a) XRD spectrum of different sized SnO_2: (i) SnO_2-A; (ii) 20-SnO_2-A; (iii) SnO_2-B; (iv) 20-SnO_2-B; (v) SnO_2-C; (vi) 20-SnO_2-C; (b) Al K edge XANES of 20-SnO_2-C and standard Al_2O_3.

The morphologies of three sized SnO_2 and the Al_2O_3 coating layer were examined using TEM, as shown in Figure 8.2. Three different sized SnO_2 nanoparicles with average diameters of 3 nm, 10 nm and 25 nm are unambiguously shown in Figure 8.2a, 8.2b and 8.2c respectively. Figure SI 8.1b to SI 8.1d depict the SEM images of the different sized SnO_2, where spherical nanoparticles exhibit uniform size distribution. Higher temperature annealing will facilitate the growth rate of crystallite, leading to bigger particle size. Meanwhile, all particles present high crystallinity with clean surface, as convinced from the clear lattice fringes of the HRTEM images. The morphologies of 2-SnO_2-C, 5-SnO_2-C and 20-SnO_2-C composites are shown in Figure 8.2d, 8.2e and 8.2f. For 2-SnO_2-C, the Al_2O_3 coating layer is hard to be tracked because of the too thin thickness taking into account of only 2 ALD cycle. Staring from 5 cycle, it is evident that conformal Al_2O_3 layer are successfully coated on the surface of SnO_2 particles, which presents distinct contrast under electro spectroscopy compared to that of the crystallized SnO_2. With the increase of ALD cycle from 5 to 20 cycle, the thickness of Al_2O_3 layer increased from ~0.8 nm to ~3.1 nm, illustrating that the thickness of Al_2O_3 could be precisely tuned upon specified ALD cycles. The Al_2O_3 shell displays no crystalline features in both samples, which is consistent with the XANES result. Uniform Al_2O_3 coating layer with similar thickness could also be found for 20-SnO_2-A and 20-SnO_2-B electrodes, as revealed in Figure SI 8.2. EDX mapping (Figure SI 8.3) of 20-SnO_2-A further confirms the homogeneous distribution of Al element, the carbon signal come from the conductive carbon black during preparation of electrodes. Al_2O_3 could be homogeneously deposited on different sized SnO_2 electrodes using ALD technique, which is critical for optimal electrochemical behavior.

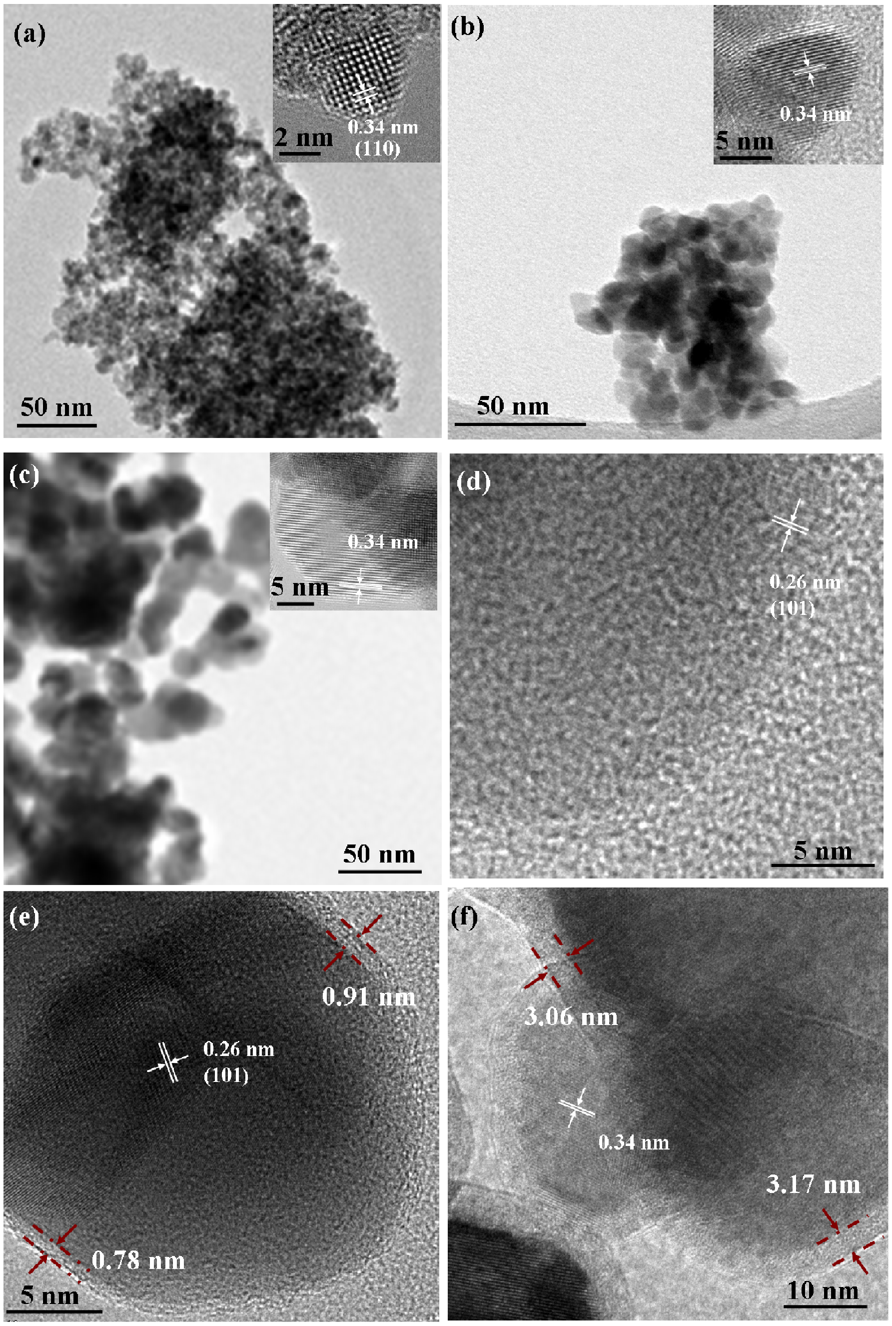

Figure 8.2 TEM images of SnO_2 (inset show HRTEM images of single particles) and Al_2O_3 coated SnO_2 samples: (a) SnO_2-A;(b) SnO_2-B; (c) SnO_2-C; (d) 2-SnO_2-C; (e) 5-SnO_2-C; (f) 20-SnO_2-C.

Electrochemical performances of the obtained Al_2O_3 coated electrodes and bare electrodes particles are compared in Figure 8.3. Cyclic performances are undertaken at a voltage window of 0.01 to 3 V with a current density of 50 mA g^{-1}. The rate performances are conducted at various current densities of 50 up to 1000 mA g^{-1} and then reverse back to 50 mA g^{-1}. As presented in Figure 8.3a and 8.3b, for SnO_2-A, it delivers an initial discharge capacity of 1951 mA h g^{-1} and stabilized from 20th cycle, remaining 530 mAh g^{-1} in the 60th cycle. It should be noted that since the particle size is small enough (3 nm) and below the critical size [30]. The stress and strain caused by volume change is not serious and thus a stable discharge and charge capacity was obtained. For the Al_2O_3 coated samples with various coating cycles, all samples still exhibit stable cycling performance, but their specific capacities are obviously different. The 2-SnO_2-A and 5-SnO_2-A exhibit increased capacities of 883 mA h g^{-1} and 612 mA h g^{-1} respectively at 60th cycle, while the 20 cycle coated sample maintains a decreased capacity of 420 mA h g^{-1}. Noting the Al_2O_3 layer is thin but conformal coated on SnO_2 for SnO_2-A and 5-SnO_2-A, the coated Al_2O_3 could effectively inhibit the direct contact between SnO_2 and electrolyte, reducing the amount of SEI which is unstable and easily mechanically degraded, leading to increased capacities. For 20-SnO_2-A, the coating thickness is comparable to the size of SnO_2 particles as depicted in Figure SI 8.2a. Since bare electrodes already display steady cyclic performance, thicker Al_2O_3 coating layer could only result in lower capacity in the view of whole electrodes. The 2 cycle ALD coating is demonstrated as the optimal coating layer for SnO_2-A. A comparison of first two charge-discharge profiles of bare SnO_2-A and 2-SnO_2-A shows similar plateaus of two electrodes, indicating that the Al_2O_3 layer have no effect on potential plateaus of SnO_2, as presented in Figure SI 8.4. The initial plateau located in between 1.2 V to 0.8 V is conversion reaction between SnO_2 and Li^+ and the formation of Sn and Li_2O [7]. The following long slope profiles stands for the formation of Li-Sn alloys. For bare SnO_2-B, it exhibits poorer cyclic performance compared with SnO_2-A due to the increased size and accompanied high expansion/contraction rate, as illustrated in Figure 8.3c. At 60th cycle, the capacity drops to only 220 mA h g^{-1}. For the ALD-coated SnO_2-B electrodes, they all exhibit improved lithium storage capabilities. As depicted in Figure 8.3d, at the 60th cycle, the 2-SnO_2-B, 5-SnO_2-B and 20-SnO_2-B show capacities of 456, 512 and 388 mA h g^{-1} respectively. The cyclic stabilities follow the order: 20-SnO_2-B > 5-SnO_2-B >2-SnO_2-B. Noting that for SnO_2-B, only 2 cycle ALD coating layer (less than 0.2 nm empirically) coating couldn't radically buffer the volume changing of SnO_2-B during cycling very well. Thus the 2-SnO_2-B shows poorer cyclic performance compared with 5-SnO_2-B and 20-SnO_2-B. Similar phenomenon could also be tracked for the rate performances of different ALD coated electrodes, where the 2-SnO_2-B also exhibits fast decay of performances under high rate. Contrastively, for 5-SnO_2-B and 20-SnO_2-B composites, the coating layer could not only prevent the large amount formation of SEI, but more importantly, it can effectively absorb the strain and stress brought by SnO_2, providing a cushion effect. For 10 nm sized SnO_2-B, the 5 cycle ALD coating is regarded as the optimal coating. Turn to the biggest sized SnO_2-C shown in Figure 8.3e, the SnO_2-C electrode shows the poorest cyclic performance among all three bare electrodes, preserving only a capacity of 123 mA h g^{-1} at 60th cycle due to its largest volume variation. For the coated samples shown in Figure 8.3f, it is clearly that the Al_2O_3 coating can significantly improve the stabilities for all three specified ALD cycles. For SnO_2-C, it is demonstrated that the 20-SnO_2-C exhibits the best cyclic stability, presenting a capacity of 535 mA h g^{-1} at the 60th cycle, which is four times higher than pure SnO_2-C. For 5-SnO_2-C and 2-SnO_2-C, the tendency for capacity declination is inevitable, leaving capacities of 446 and 365 mA h g^{-1} respectively at the 60th cycle. The poorer cyclic capabilities of them compared with that of 20-SnO_2-C indicate that the coating layer of 5 and/or 2 cycle ALD are not robust enough to endure the expansion/contraction for SnO_2-C in prolonged cycles. Similarly, rate performance profiles further confirmed the increased stabilities for ALD coated samples due to the protection from outside Al_2O_3 layer. Figure SI 8.5 present the first three cyclic voltammetry (CV) curves of SnO_2-C and 20-SnO_2-C. The shape for CV curves of coated electrodes is quite similar to that of pure SnO_2-C electrode, indicating that coating layer has no effect on the reaction mechanism of SnO_2 to lithium. The reduction peak at 0.78 V can be attributed to Li insertion into the SnO_2, accompanied by phase transformation SnO_2 to Sn and Li_2O [7, 30]. The second pronounced reduction peak at around 0.25 V can be ascribed to the alloy of lithium with Sn to form Li_xSn. For the anodic scan, the peak located around of 0.52 V is attributed to the dealloying of the Li_xSn. It can be seen that for the 20-SnO_2-C sample, the oxidation peaks at 0.53 V decreased less than that of pure SnO_2-C electrode, indicating the improved stability by the coating layers. Xiao [27] et al. also reported that the Al_2O_3 could react with lithium ions and electrolyte to form an artificial solid electrolyte interface layer, improving the ionic conductivity that is favorable for high rate performance and enhanced current efficiency. As shown in Figure SI 8.6, compared with no coated raw samples, all Al_2O_3 coated samples exhibit improved current efficiency especially in the first ten cycles, benefiting from the Al_2O_3 layer which forms an artificial ionic conductive SEI layer and prevents the mechanical and electrochemical degradation of the electrodes. The thickest coating exhibits the best Coulombic efficiency due to its most robust framework and highly ionic conductive channels.

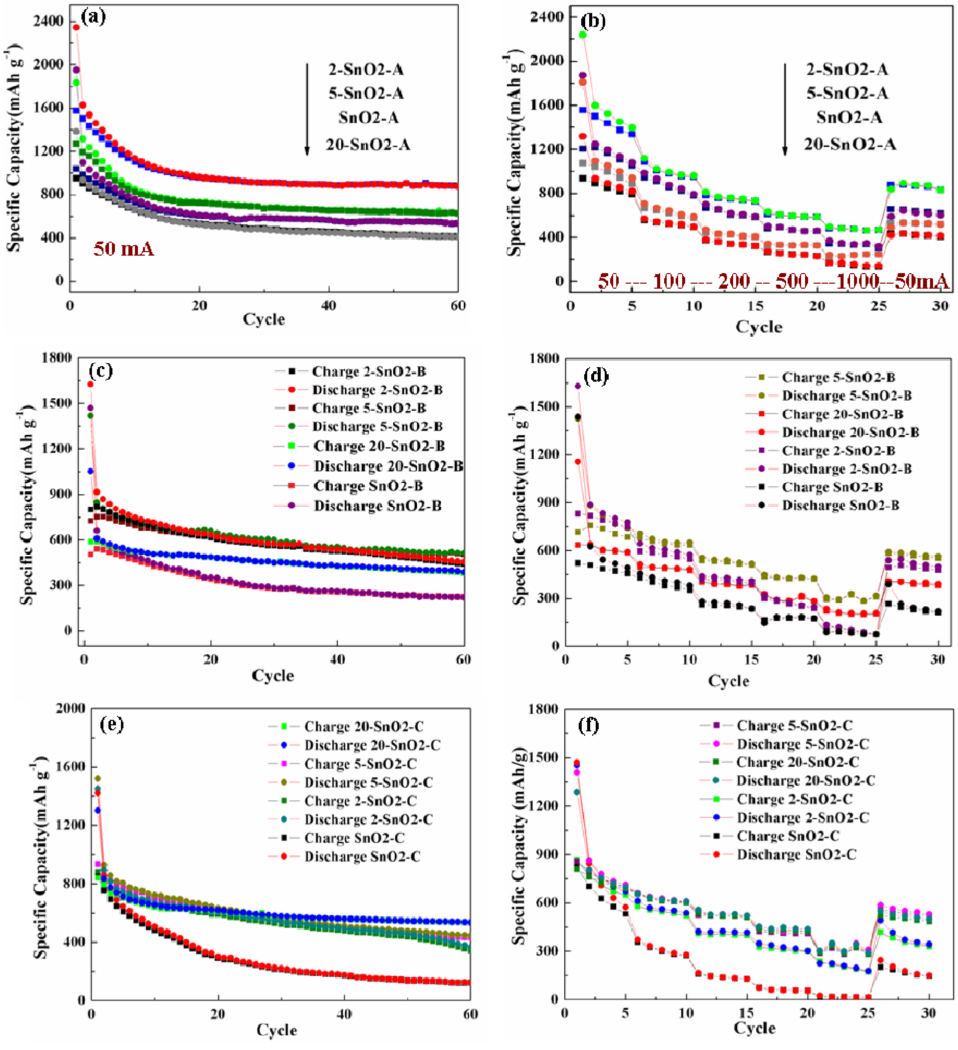

Figure 8.3 (a, c, e) Cycling performances (at 50 mA/g) and (b, d, f) rate performances (at 50 mA/g to 1000 mA/g) of Al_2O_3 coated and no coated SnO_2 samples: (a, b) SnO_2-A series; (c, d) SnO_2-B series; (e, f) SnO_2-C series

In order to examine the morphology evolution of SnO_2 particles after cycling, HRTEM was further performed, as shown in Figure 8.4. For pure SnO_2-A electrode in Figure 8.4a, it reveals that lots of blurry SEI film can be tracked as arrows pointed. Some crystallites can also be found, however, the size of the particles became irregular due to the pulverization and they tend to aggregate to form bigger sized particles (as demonstrated in circles). It is believed the pulverization of SnO_2 will produce new fresh surface, upon contact with electrolyte, leading to more and more amount of SEI and waste of active materials. Conversely, after cycling, the 2-SnO_2-A electrode still maintains its original morphology without obvious change of size as depicted in Figure 8.4b. A careful examination illustrates that a thin layer appeared in the outside of the nanoparticles, which is hardly found for the original 2-SnO_2-A particles before cycling. The thin layer emerged here should be ascribed to the artificial SEI layer formed by reaction of Al_2O_3 with electrolyte or lithium ions [27]. Such artificial SEI layer is ionic conductive and could mitigate the pulverization of the SnO_2 core, inhibiting the formation of undesired SEI between SnO_2 and electrolyte, resulting in excellent electrochemical behavior. For bare SnO_2-C electrode after cycling, SnO_2 particles pulverized into small particles without crystalline features, as shown in Figure 8.4c. Also, thick SEI film accumulated at the surface of small particle (as arrow indicated) through reaction of electrolyte with continuously emerged fresh surface of SnO_2-C due to its pulverization. The unstable and not uniform covered SEI film could deteriorates the cycling performances of electrodes. In contrast, for cycled 20-SnO_2-C electrodes shown in Figure 8.4d, the spherical particle are still well maintained under the protection of the outside shell which expands a little bit compared with that before cycling. The swollen shell may be caused by reaction of lithium ions or electrolyte with Al_2O_3 to form an ionic conductive SEI layer. More importantly, the SnO_2 core without pulverization elucidated that the highly stable artificial SEI layer could effectively buffer the stress and strain upon cycling. The elemental mapping was further performed on 20-SnO_2-C electrode after 60 cycles, as shown in Figure SI 8.7 The distribution of Al is still homogeneous in the electrode after cycling along with the F signal, illustrating that artificial SEI is tightly attached to the inside core and the integrity of the electrode is well maintained. Figure 8.4e shows the schematic representation for ALD coated and bare SnO_2 electrodes during cycling, where the coating layer could form an artificial SEI layer to effectively inhibit the detrimental reaction between SnO_2 and electrolyte. As a result, improved cycling performance and rate performances were obtained for optimal ALD coated electrodes.

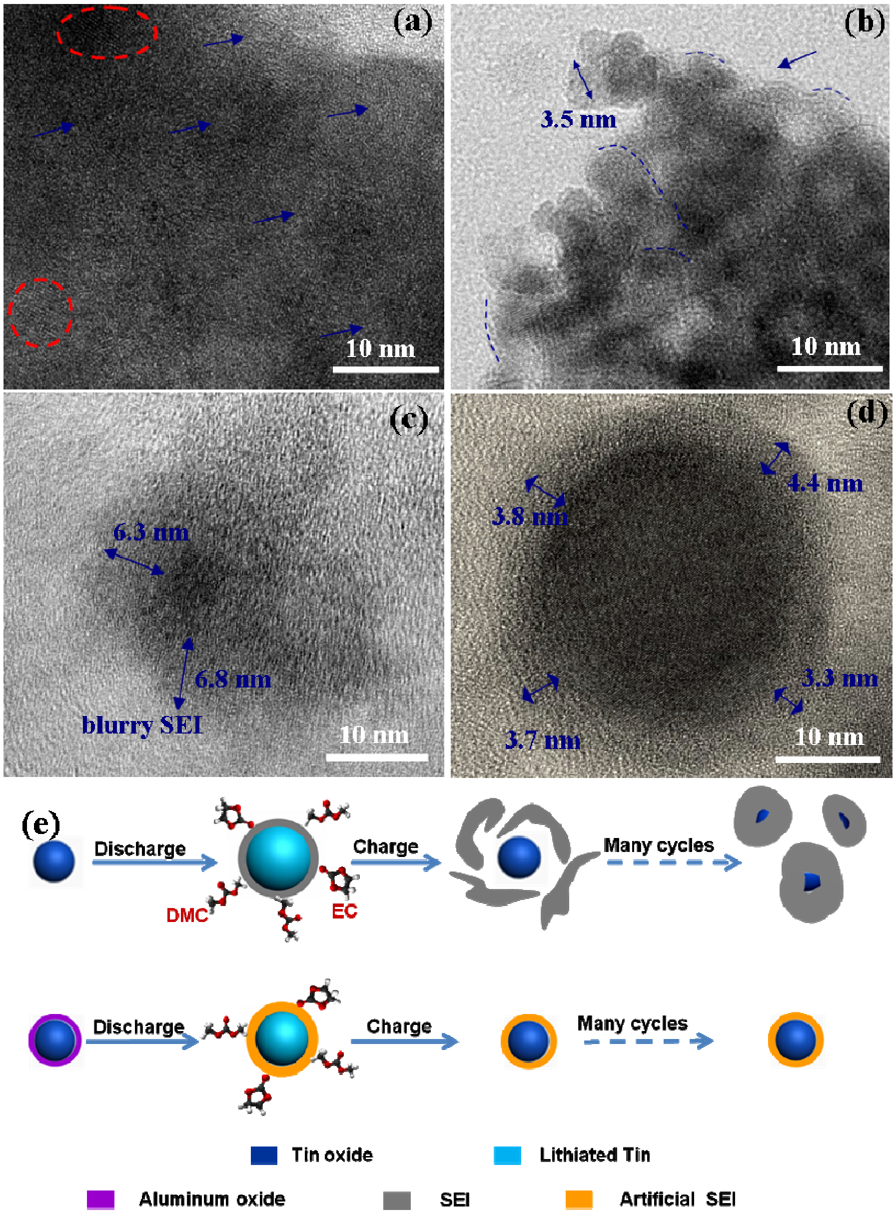

Figure 8.4 TEM images of (a) SnO_2-A and (b) 2-SnO_2-A after 60 cycles at 50 mA g-1. (c) SnO_2-C and (d) 20-SnO_2-C after 60 cycles at 50 mA g-1. (e) Schematic representation showing that SEI formation on pure SnO_2 and Al_2O_3 coated SnO_2 upon cycling.

XANES is a powerful tool to characterize the chemical environment and electronic structure of the targets. To unveil the local chemistry environment variation of the electrodes behind their different electrochemical performances, Sn K edge XANES on the 2cycle ALD coated and no coated SnO_2-A electrodes before and after cycling were performed. As shown in Figure 8.5, it can be seen that the spectrum of 2-SnO_2-A overlapped well with that of pure SnO_2-A, illustrating that the deposition of Al_2O_3 did not affect the local symmetry and chemical states of SnO_2. For SnO_2-A electrodes after 60 cycles, its spectrum became more broadening with slight shift towards lower energy, indicating a more disordered feature with reduced valence states. More intriguingly, for 2-SnO_2-A after cycling, the line shape is identical to that of the 2-SnO_2-A, illustrating that the outside Al_2O_3 coating could effectively protects the integrity and crystallinity of the core SnO_2. Figure 8.5b shows Fourier transform of the Sn K edge Extended X-ray Absorption Fine Structure (EXAFS) spectra k3χ(k). All four samples exhibit similar spectra except their magnitude which is a function of coordination number and Debye-Waller factor, a measure of mean square displacement of the interatomic distance between the absorbing atom and the scatterrer. It is found that the magnitude decreases a little bit after coating of Al_2O_3, indicating that the outside Al_2O_3 shell may affect the ordered arrangement of the SnO_2 particles at the interface. For bare SnO_2-A after cycling, the magnitude decreases considerably, demonstrating an increase of the disorder inside the crystallite and a decrease of the crystallite size which is in accordance with the HRTEM results. While for 2-SnO_2-A after cycling, the decrease of magnitudes is not significant, elucidating that both the crystallinity and size of crystallites are well kept by the Al_2O_3 layer. Thus the XANES and EXAFS data provide direct spectroscopic evidence that the coating layer helps maintain the size and structure of the electrodes, resulting in improved electrochemical behaviors and electrodes integrity.

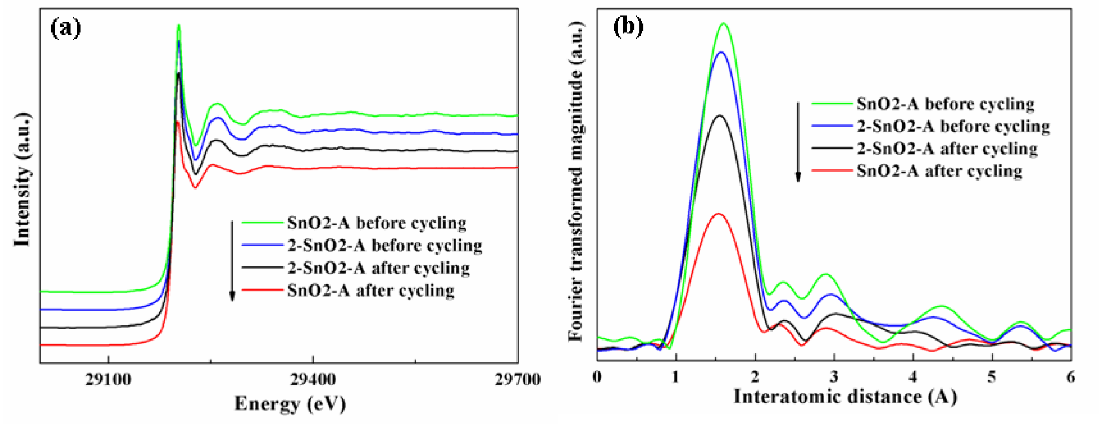

Figure 8.5 (a) XANES spectrum of Sn K edge and (b) Fourier-transformed (FT) magnitudes of Sn K edge k^3-weighted EXAFS (Extended X-ray absorption fine structure) spectra for 2 cycle ALD coated and bare SnO_2 electrodes before and after cycling.

8.4 Conclusions

In summary, controlled Al_2O_3 layer have been successfully coated on different sized SnO_2 particles using ALD technique. As convinced by the HRTEM results and synchrotron radiation spectrum, the well defined and optimized Al_2O_3 coating layer could maintain the integrity of electrodes by suppressing the volume change to increase the cyclic performances. It could also function as artificial ionic conductive SEI layer and inhibit the direct contact between SnO_2 with the electrolyte to increase the rate capability and the Couloumbic efficiency. This work opens a path way for study connection between coating layer and inside active electrodes and will inspire future application of ALD technique on electrodes for lithium ion batteries.

8.5 Acknowledgements

This research was supported by Natural Sciences and Engineering Research Council of Canada (NSERC), General Motors of Canada, Canada Research Chair (CRC), Canada Foundation for Innovation (CFI), Ontario Innovation Trust (OIT) Program. The Canadian Light Source is supported by CFI, NSERC, NRC, CHIR, and the University of Saskatchewan.

8.6 References

[1] A. K. Padhi, K. S. Nanjundaswamy and J. B. Goodenough, *J. Electrochem. Soc.*, 1997, **144**, 1188-1194.

[2] L. X. Yuan, Z. H. Wang, W. X. Zhang, X. L. Hu, J. T. Chen, Y. H. Huang and J. B. Goodenough, *Energ. Environ. Sci.*, 2011, **4**, 269-284.

[3] L. F. Shen, E. Uchaker, X. G. Zhang and G. Z. Cao, *Adv. Mater*, 2012, **24**, 6502-6506.

[4] L. Wang, X. M. He, W. T. Sun, J. L. Wang, Y. D. Li and S. S. Fan, *Nano Lett.*, 2012, **12**, 5632-5636.

[5] J. L. Yang, J. J. Wang, D. N. Wang, X. F. Li, D. S. Geng, G. X. Liang, M. Gauthier, R. Y. Li and X. L. Sun, *J. Power Sources*, 2012, **208**, 340-344.

[6] M. Ben Yahia, F. Lemoigno, G. Rousse, F. Boucher, J. M. Tarascon and M. L. Doublet, *Energ. Environ. Sci*, 2012, **5**, 9584-9594.

[7] D. N. Wang, X. F. Li, J. J. Wang, J. L. Yang, D. S. Geng, R. Y. Li, M. Cai, T. K. Sham and X. L. Sun, *J. Phys. Chem. C*, 2012, **116**, 22149-22156.

[8] Z. Y. Wang, D. Y. Luan, S. Madhavi, Y. Hu and X. W. Lou, *Energ. Environ. Sci.*, 2012, **5**, 5252-5256.

[9] D. Wang, X. Li, J. Yang, J. Wang, D. Geng, R. Li, M. Cai, T. K. Sham and X. Sun, *Phys. Chem. Chem. Phys.*, 2013, **15**, 3535-3542.

[10] Y. Idota, T. Kubota, A. Matsufuji, Y. Maekawa and T. Miyasaka, *Science*, 1997, **276**, 1395-1397.

[11] S. M. Paek, E. Yoo and I. Honma, *Nano Lett.*, 2009, **9**, 72-75.

[12] B. Luo, B. Wang, X. L. Li, Y. Y. Jia, M. H. Liang and L. J. Zhi, *Adv. Mater.*, 2012, **24**, 5525-5525.

[13] L. W. Ji, Z. K. Tan, T. Kuykendall, E. J. An, Y. B. Fu, V. Battaglia and Y. G. Zhang, *Energ. Environ. Sci.*, 2011, **4**, 3611-3616.

[14] Y. Qi, H. Zhang, N. Du, C. X. Zhai and D. R. Yang, *Rsc. Adv.*, 2012, **2**, 9511-9516.

[15] Z. X. Chen, M. Zhou, Y. L. Cao, X. P. Ai, H. X. Yang and J. Liu, *Adv. Energ. Mater.*, 2012, **2**, 95-102.

[16] X. B. Meng, X. Q. Yang and X. L. Sun, *Adv. Mater.*, 2012, **24**, 3589-3615.

[17] J. T. Lee, F. M. Wang, C. S. Cheng, C. C. Li and C. H. Lin, *Electrochim. Acta.*, 2010, **55**, 4002-4006.

[18] I. D. Scott, Y. S. Jung, A. S. Cavanagh, Y. F. An, A. C. Dillon, S. M. George and S. H. Lee, *Nano Lett.*, 2011, **11**, 414-418.

[19] H. M. Cheng, F. M. Wang, J. P. Chu, R. Santhanam, J. Rick and S. C. Lo, *J. Phys. Chem. C*, 2012, **116**, 7629-7637.

[20] Y. S. Jung, P. Lu, A. S. Cavanagh, C. Ban, G. H. Kim, S. H. Lee, S. M. George, S. J. Harris and A. C. Dillon, *Adv. Energ. Mater.*, 2013, **3**, 213-219.

[21] Y. S. Jung, A. S. Cavanagh, Y. F. Yan, S. M. George and A. Manthiram, *J. Electrochem. Soc.*, 2011, **158**, A1298-A1302.

[22] L. A. Riley, S. Van Ana, A. S. Cavanagh, Y. F. Yan, S. M. George, P. Liu, A. C. Dillon and S. H. Lee, *J. Power Sources*, 2011, **196**, 3317-3324.

[23] M. Bettge, Y. Li, B. Sankaran, N. D. Rago, T. Spila, R. T. Haasch, I. Petrov and D. P. Abraham, *J. Power Sources*, 2013, **233**, 346-357.

[24] D. S. Guan, J. A. Jeevarajan and Y. Wang, *Nanoscale*, 2011, **3**, 1465-1469.

[25] X. Luan, D. Guan and Y. Wang, *J. Nanosci. Nanotechnol.*, 2012, **12**, 7113-7120.

[26] L. A. Riley, A. S. Cavanagh, S. M. George, Y. S. Jung, Y. F. Yan, S. H. Lee and A. C. Dillon, *Chem. Phys. Chem.*, 2010, **11**, 2124-2130.

[27] X. C. Xiao, P. Lu and D. Ahn, *Adv. Mater.*, 2011, **23**, 3911-3915.

[28] Y. He, X. Q. Yu, Y. H. Wang, H. Li and X. J. Huang, *Adv. Mater.*, 2011, **23**, 4938-4941.

[29] Y. S. Jung, A. S. Cavanagh, L. Gedvilas, N. E. Widjonarko, I. D. Scott, S. H. Lee, G. H. Kim, S. M. George and A. C. Dillon, *Adv. Energ. Mater.*, 2012, **2**, 1022-1027.

[30] C. Kim, M. Noh, M. Choi, J. Cho and B. Park, *Chem. Mater.*, 2005, **17**, 3297-3301.

8.7 Supporting Information

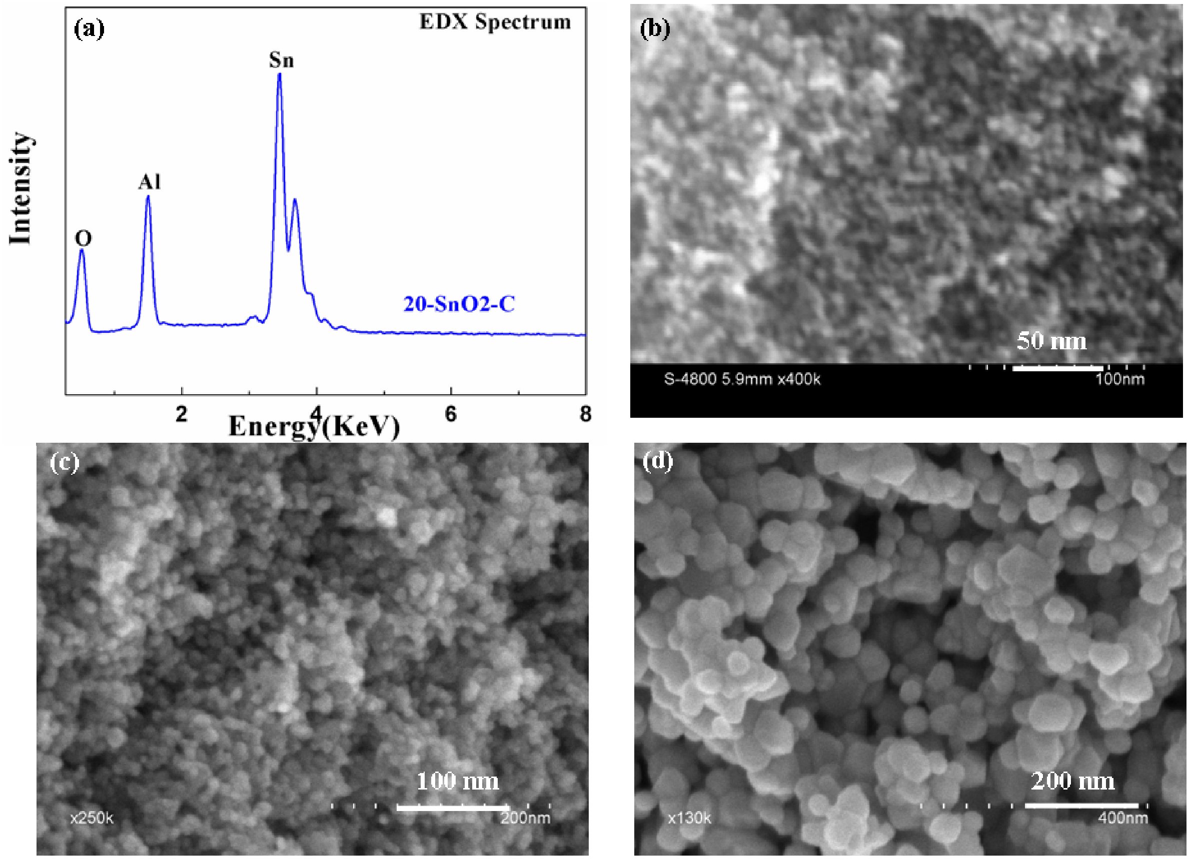

Figure SI 8.1 (a) EDX spectrum of 20-SnO_2-C and SEM images of (b) SnO_2-A, (c) SnO_2-B and (d) SnO_2-C.

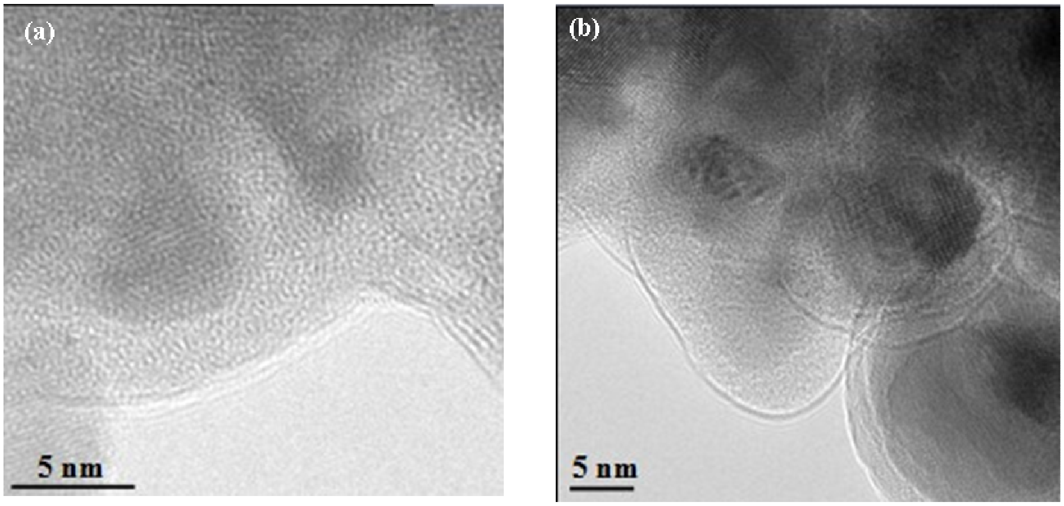

Figure SI 8.2 TEM images of (a) 20-SnO$_2$-A and (b) 20-SnO$_2$-B.

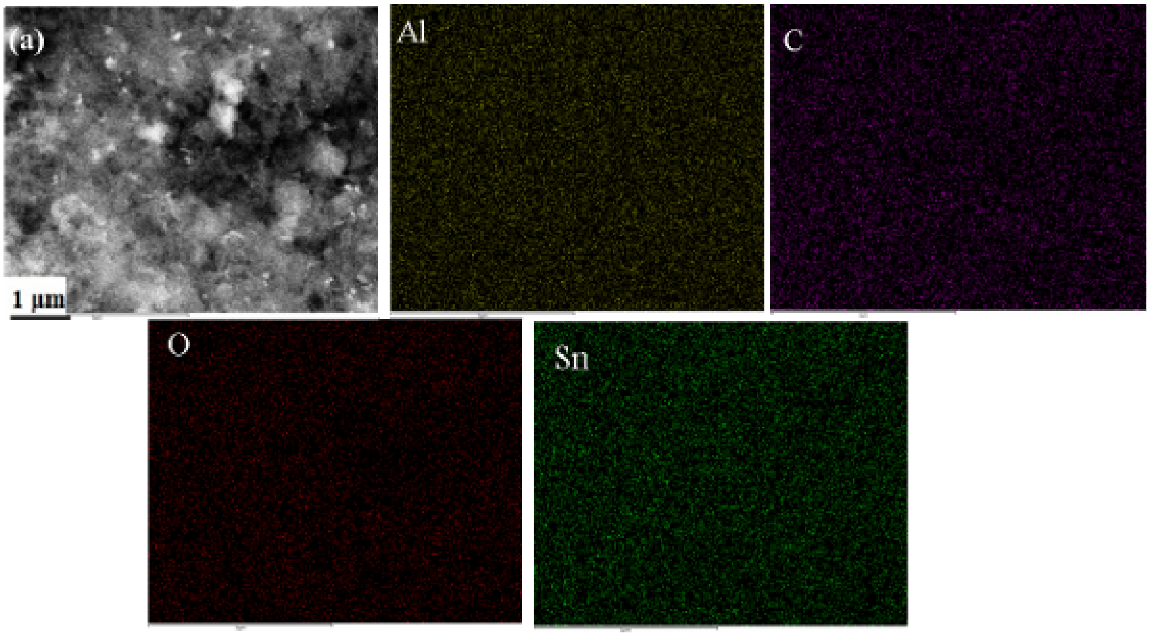

Figure SI 8.3 Elemental mapping spectra of 20-SnO$_2$-A.

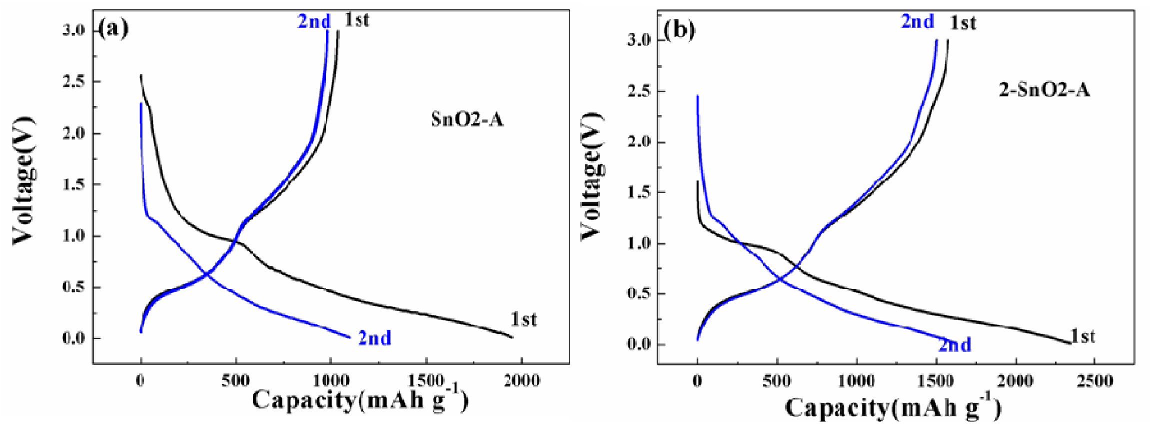

Figure SI 8.4 Charge-discharge profiles of (a) SnO_2-A and (b) 2-SnO_2-A electrodes.

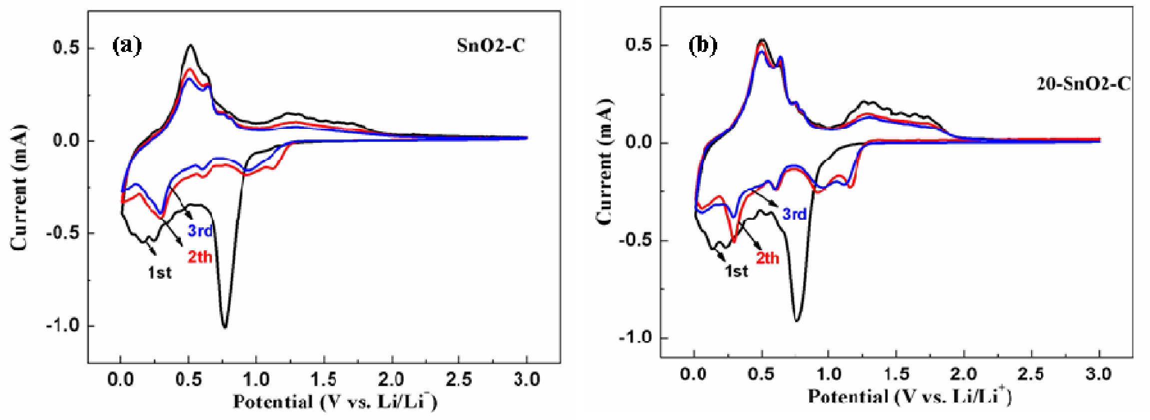

Figure SI 8.5 Cyclic Voltammetry (CV) of (a) SnO_2-C and (b) 20-SnO_2-C electrodes.

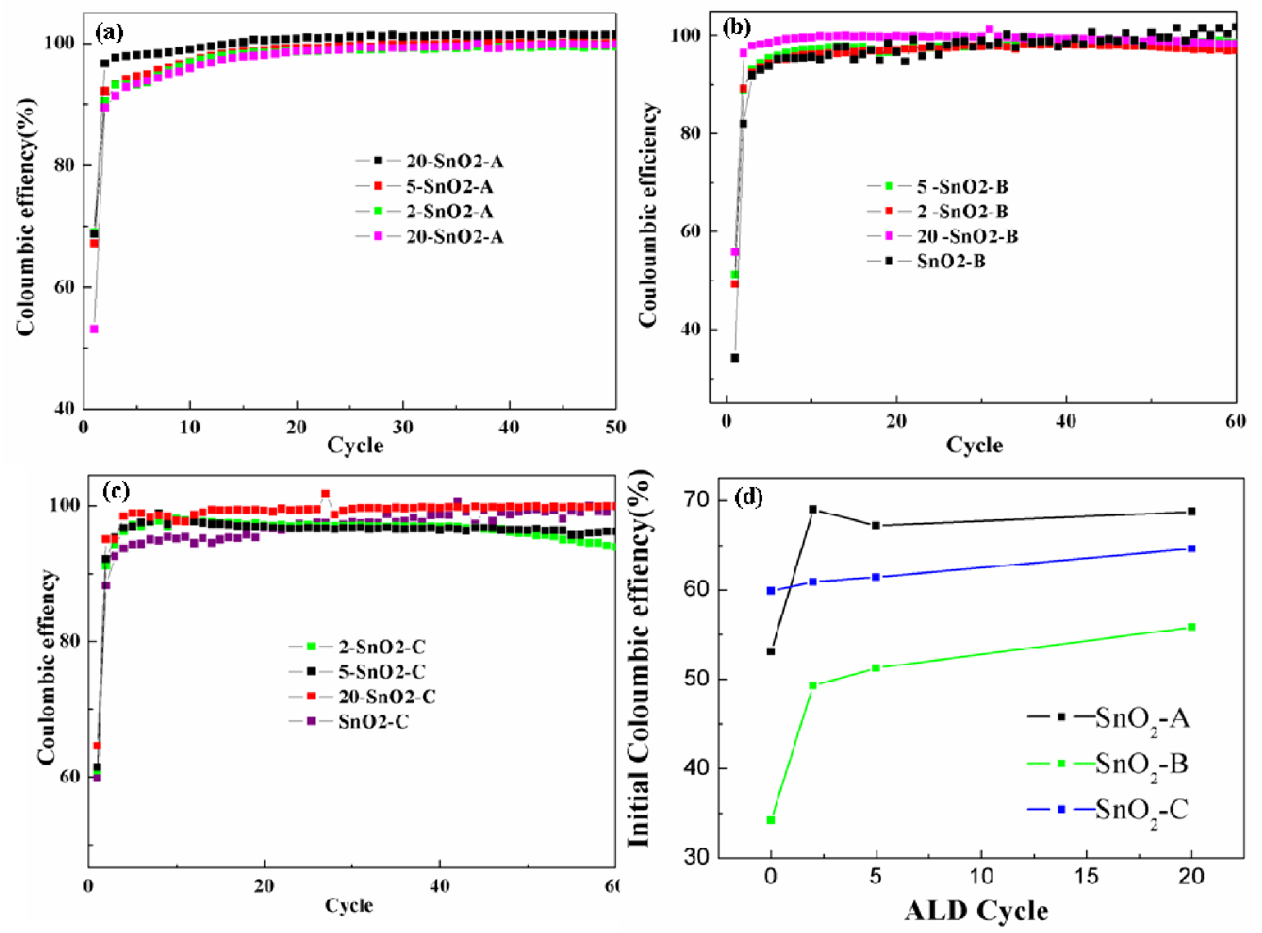

Figure SI 8.6 Coulombic efficiency of SnO_2 and ALD coated SnO_2. (a) SnO_2-A series; (b) SnO_2-B series; (c) SnO_2-C series. (d) Initial couloumbic efficiency of coated and non-coated electrodes.

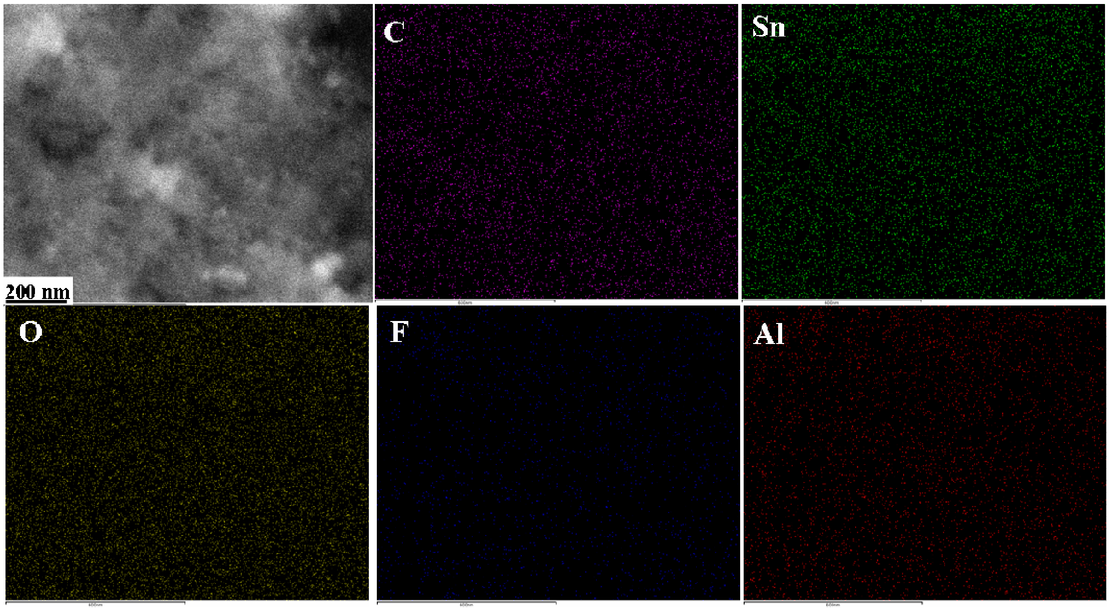

Figure SI 8.7 Elemental mapping spectra of 20-SnO_2-C after cycling.

Chapter 9

9 Conclusions and Future Perspectives

9.1 Conclusions

Lithium ion batteries are clean and recyclable energy systems which are expected not only to power hand-held electronic devices, but also to electrify the vehicles thus realizing the replacement of the combustion engine. The current state LIB still could not compete with fossil fuels powered equipments in terms of energy densities, cost, safety and other factors. Since the performance of a battery system highly relies on the electrodes, accordingly, extensive research has been focused on the exploitation of attractive replacements with higher capacities than the current graphitic carbon anodes to circumvent the low energy density issue.

Tin-based anodes are regarded as promising candidates due to their high theoretical capacities which are generally more than twice of that of graphite. However, the large lithium driven volume variation during cycling makes tin-based systems suffer from serious capacity decay, hampering its practical applications. Extensive efforts have been conducted to overcome this issue. The development of hierarchical nanostructures combined with the flexible matrix which function as buffer is one of most effective route to achieve high performance tin-based anodes.

The main focuses for the thesis are developing hierarchical nanostructured tin-based anodes and carbonaceous composites for advanced anodes with high cyclic and lithium storage capabilities. Moreover, synchrotron based X-ray absorption technique are employed as a powerful tool to unveil and understanding the relation between materials structures and electrochemical performances through the study the local electronic structures.

Firstly, we conducted the research on one dimensional SnO_2 NW. Vertically aligned SnO_2 NWs arrays were obtained on stainless steel (SS) and copper substrates via a facile hydrothermal route. The SnO_2 NWs were rooted on the substrates with an octahedral tip.

A time dependant-morphology evolution study was conducted to unveil the growth mechanism, from initial nuclei gradually to SnO_2 NW arrays. XEOL data show that both SnO_2 samples exhibit yellow-green luminescence, originating from the intrinsic surface states. The unique near IR luminescence for SnO_2 NW on SS is attributed to high density of surface or defect states, which is monitored by the resonance at Sn $M_{5,4}$-edge XANES.

Secondly, hierarchical 3D SnO_2/graphene nanocomposites are prepared using a rapid and facile microwave assisted hydrothermal method. The homogeneously distributed SnO_2 nanoparticles thus obtained are quite small (~3.5 nm), which are abundant of surface and defect states as revealed from Sn $M_{5,4}$ edge XANES. Carbon K edge XANES further confirm the charge transfer (electron donation) from SnO_2 to carbon as well as strong chemical bonding of "Sn-OO-C" through surface/defect states. The resultant SnO_2/graphene composites exhibit a high and stable reversible lithium storage capacity of 653 mA h g^{-1} in the first 100th cycle at 60 mA g^{-1}. Furthermore, the nanocomposite shows high rate capabilities: It can still maintain the discharge capacity as high as 313 mA h g^{-1} even cycled at high current density as high as 800 mA g^{-1}. This work could open a new pathway for identifying interaction happened in nanocomposite electrodes for LIB by XANES.

Thirdly, we describe a sandwiched carbon coated SnO_2 nanowire/graphene hierarchical structure which was successfully synthesized by a layer by layer formation process (seed assisted hydrothermal growth of SnO_2 nanorod on graphene followed by glucose derived carbon coating). The carbon layer coating and the graphene matrix could efficiently provide a "cushion effect" to hold the integrity of the electrodes and the high electron transportation channels. More over, XANES spectra demonstrate chemical bonding between each layer through carboxylic groups and electrons are continuously transferred from SnO_2 to carbon. More importantly, Sn M edge data reveal the different phase transformation in carbon coated and un-coated SnO_2 nanowire/graphene after cycling, where the re-formation of SnO_2 in sandwiched systems are confirmed. As a result, these nano-hybrids show drastically increased capacity due to the synergistic effect: it exhibits an ultrahigh reversible specific capacity of 1419 mA h g^{-1} in the 150th cycle and a high-rate capability at high current densities up to 3000 mA g^{-1}. The concept of hierarchical model could be easily extended to other electrode materials. It will have significant implications on structural design for improving performances of electrodes in LIBs.

Fourthly, applying chemical vapor deposition method, Sn@C-GNs has been obtained. The core-shell nanostructured Sn@C composites embedded in GNs have extra voids due to the shrinkage of Sn upon cooling. XANES and EXAFS study at the Sn K, M, L_3 edge and the C K-edge clearly demonstrates that chemical bonding, charge transfer (electrons transferred from Sn to carbon) and lattice variation (Sn-Sn bond are compressed by the surrounded carbon atoms) take place between Sn and carbonaceous materials, which anchors the Sn nanoparticles into the carbon shell and graphene matrix firmly and induces fast charge transfer rate. Also, benefitting from the core-shelled structure, where flexibile carbon shell and graphene sheet substrate could buffer the volume variation, the core-shell nanostructured Sn@C composites embedded in GNs delivers a high lithium storage capacities of 566 mAh g^{-1} at the 100th cycle. The hierarchical structure could be a promising anode for electrical vehicle applications.

Fifthly, carbon sheath/tin core nanowires are obtained on metallic SS and copper substrates using chemical vapor deposition method. Cu and Fe will be introduced to Sn to form alloys as convinced from XRD. More importantly, the scanning transmission X-ray microscopy (STXM) are performed on a single nanowire to chemical mapping the electronic structure with XANES information, where core of metallic copper, Sn and amorphous carbon shell are mapped with a resolution of ~30 nm, the composites obtained using SS substrate shows lower amount of tin alloys and higher crystalline carbon than that of copper, leading to improved lithium storage capabilities and rate capabilities. The synthesis route could be easily applied to other core-shelled metal/carbon system and STXM demonstrates its superiority in locally chemical mapping low dimensional nanomateirals.

Lastly, in addition to the carbon coating strategy, we further applied ALD techniques to modify the surface of SnO_2 nanoparticles with three different particle sizes. The Al_2O_3 layer with controlled thickness from less than 1 nm to 3 nm is realized. Al K edge XANES shows the amorphous nature of Al_2O_3. For 3 nm sized SnO_2 composed electrodes, 2 cycle ALD coating have the best cyclic and rate capabilities in comparison with the un-coated and other cycles coated samples. For the 10 nm and 25 nm sized SnO_2 nanoparticle electrodes, 5 cycle and 20 cycle ALD coating are proved the best, respectively. Sn K-edge EXAFS of the electrodes after cycling demonstrate the pulverization and amorphorization are alleviated for coated electrodes. HRTEM results show that the optimized Al_2O_3 coating layer can protect active materials by suppressing the volume change to increase the cyclic performances. Further, the Al_2O_3 layer would act as artificial ionic conductive SEI layer and inhibit the direct contact between SnO_2 with the electrolyte to increase the rate capability and the coulombic efficiency. This work inspires future application of ALD technique on coating electrodes for improving electrochemical performance of lithium ion batteries.

The major contributions of the thesis are summarized below:

With the objectives to enhance the electrochemical performances of current-state lithium ion batteries in mind, various tin-based nanostructures have been designed and developed including nanowires, nanoparticles, core-shell structure, sandwiched structures. The synchrotron based X-ray absorption spectra have been used to unveil the electronic structures in these systems. Moreover, these hierarchical nanostructures exhibit 2-5 times better lithium storage capabilities and rate capabilities than conventional systems. The authors believe that all these studies will have profound impact on boosting commercialization of high performances anodes for lithium ion battery applications and the combination of conventional with synchrotron technique will further progress.

9.2 Future Work

The thesis presents a series of successful design on nanostructures and carbonaceous composites in one way. However, other approaches are still worthy to try in the following aspects:

1) To address the issue of cycling behavior of tin based anodes, incorporation of other electrochemically active or inactive matrix elements (metals), for example Ca, Cu, Co, Al, Ti and Ni, is regarded as an effective approach [1-4]. The concept of introducing heteroatoms has the following advantages: enhancing the electronic conductivity of

the composites; the buffering or absorbing the volume changes and leading to improved cycling process; other elements may help catalyze the lithium alloying/dealloying process and facilitate the lithium transportation kinetics. In combination with synchrotron based technique, which is highly elemental and chemically site sensitive, the phase composition, element distribution, chemical states and reaction mechanism upon cycling can be identified and studied in details.

2) Besides involving other elements, exploitation of relation between crystal structure and long-term cycling stability is also meaningful. Many papers have reported the choice of optimized starting crystal structure and facets would have significant impact on electrochemical performances. It is demonstrated, for example, SnO_6 octahedral would exhibit higher and more stable lithium reaction behavior than SnO_4 tetrahedral [5-7]. It is more drastic considering the structure destruction based on the SnO_x reaction in the first lithium alloying process, where the SnO_x are reduced to form Sn. The current explanation is that the local structure of the tin thus formed is highly dependent on the structure of the staring materials. However, more experimental and theoretical evidences are needed to have a clear and convincible statement.

3) The case study of surface modification using ALD technique on SnO_2 electrodes indicates that ALD has great potential on improving performances of tin based anodes. In the future, applying ALD technique to realize various surface coating such as TiO_2, ZrO_2 as well as fabrication of tin-based anodes could be a promising direction to further enhance the performance of current electrodes system and develop new battery constructer such as thin film battery and 3D all-solid-state microbatteries [8] based on the success of solid electrolyte.

4) For the combination of conventional characterization capabilities with SR technique, designing an electrochemical cell with battery stations while in-situ allowing SR X-ray beam [9] to penetrate and generating spectrum during cycling is an ideal way to study the lithiation/delithiation mechanism. Moreover, with the development of SR tomography such as STXM technique, it is reasonable to believe that fruitful advance in the field will be pushed forward.

9.3 References

[1] Amatucci, G. G.; Blyr, A.; Sigala, C.; Alfonse, P.; Tarascon, J. M. Solid State Ionics, 1997, 104, 13.

[2] Huggins, R. A. J. Power Sources, 1999, 81, 13.

[3] Besenhard, J. O.; Wachtler, M.; Winter, M.; Andreaus, R.; Rom, I.; Sitte, W. J. Power Sources, 1999, 81, 268.

[4] Zhang, W. J. J. Power Sources, 2011, 196, 877.

[5] Tarascon, J. M.; Guyomard, D. Electrochim. Acta, 1993, 38, 1221.

[6] Tirado, J. L. Mater. Sci. Eng. R, 2003, 40, 103.

[7] Chen, J. S.; Archer, L. A.; Lou, X. W. J. Mater. Chem., 2011, 21, 9912.

[8] Meng, X. B.; Yang, X. Q.; Sun, X. L. Adv. Mater. 2012, 24, 3589.

[9] Nedoseykina, T.; Kim, M. G.; Park, S. A.; Kim, H. S.; Kim, S. B.; Cho, J.; Lee, Y. Electrochim. Acta, 2010, 55, 8876.

Appendices

Appendix A Copyright release from ACS Publications

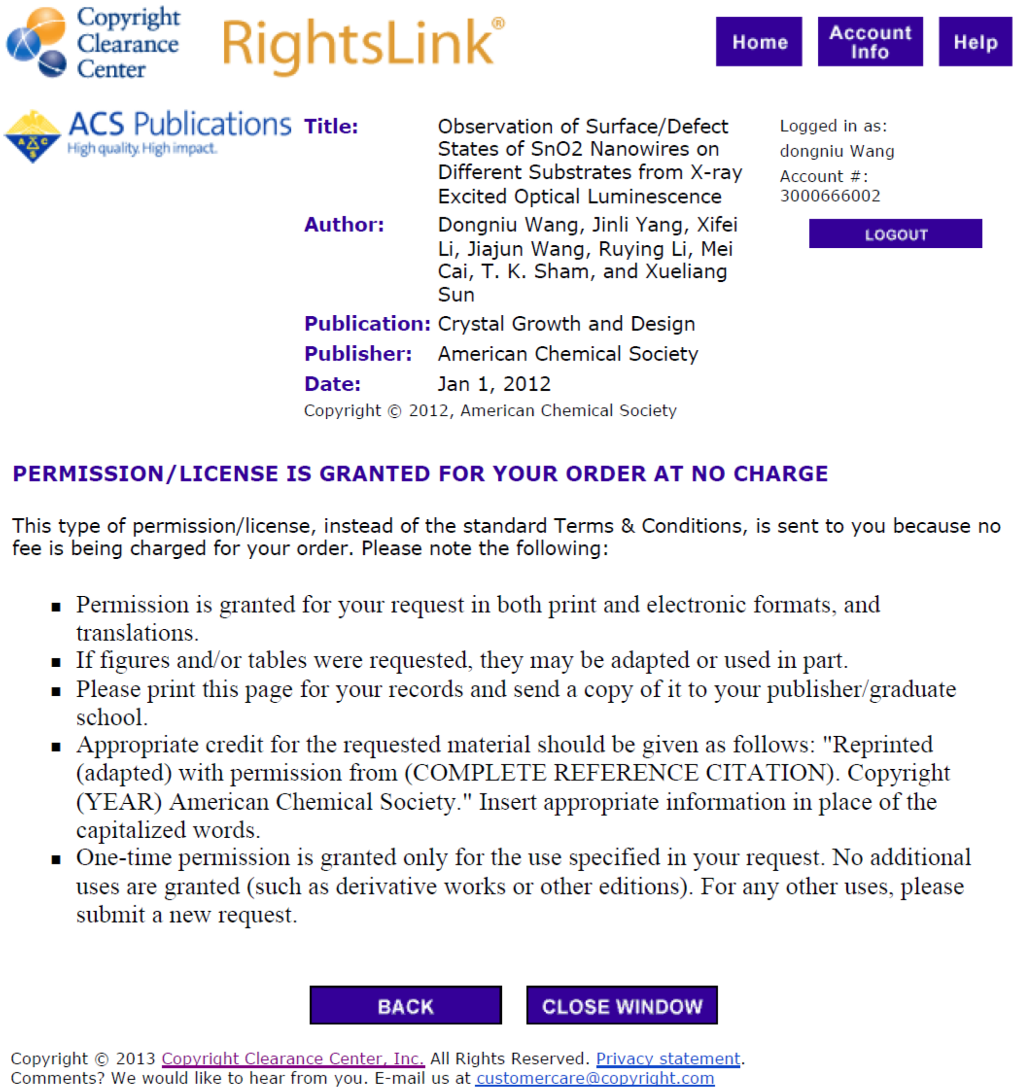

Title: Observation of Surface/Defect States of SnO2 Nanowires on Different Substrates from X-ray Excited Optical Luminescence

Author: Dongniu Wang, Jinli Yang, Xifei Li, Jiajun Wang, Ruying Li, Mei Cai, T. K. Sham, and Xueliang Sun

Publication: Crystal Growth and Design

Publisher: American Chemical Society

Date: Jan 1, 2012

Copyright © 2012, American Chemical Society

Logged in as:
dongniu Wang
Account #:
3000666002

PERMISSION/LICENSE IS GRANTED FOR YOUR ORDER AT NO CHARGE

This type of permission/license, instead of the standard Terms & Conditions, is sent to you because no fee is being charged for your order. Please note the following:

- Permission is granted for your request in both print and electronic formats, and translations.
- If figures and/or tables were requested, they may be adapted or used in part.
- Please print this page for your records and send a copy of it to your publisher/graduate school.
- Appropriate credit for the requested material should be given as follows: "Reprinted (adapted) with permission from (COMPLETE REFERENCE CITATION). Copyright (YEAR) American Chemical Society." Insert appropriate information in place of the capitalized words.
- One-time permission is granted only for the use specified in your request. No additional uses are granted (such as derivative works or other editions). For any other uses, please submit a new request.

Copyright © 2013 Copyright Clearance Center, Inc. All Rights Reserved. Privacy statement.
Comments? We would like to hear from you. E-mail us at customercare@copyright.com

Appendix B Copyright release from ACS Publications

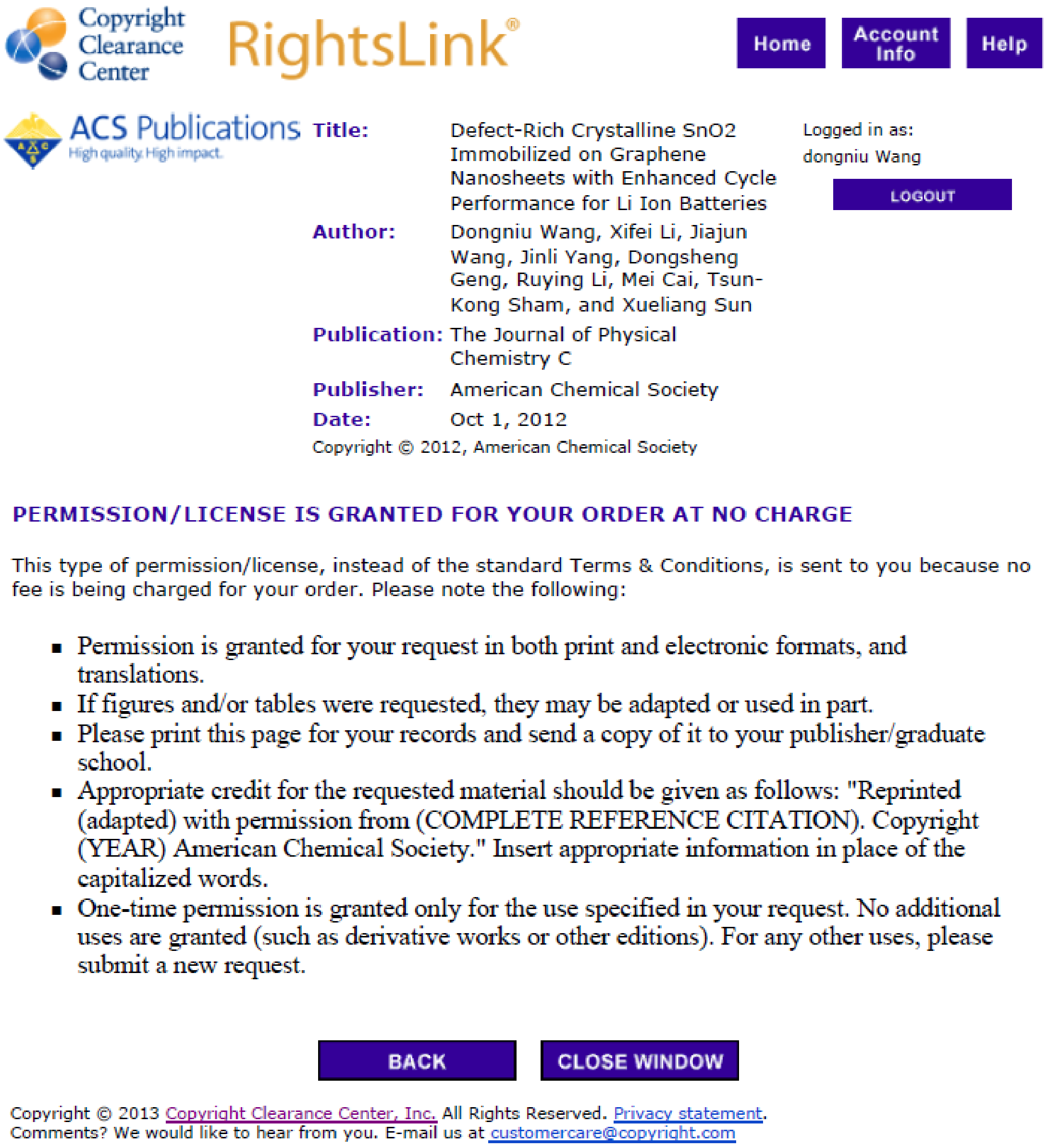

Title:	Defect-Rich Crystalline SnO2 Immobilized on Graphene Nanosheets with Enhanced Cycle Performance for Li Ion Batteries
Author:	Dongniu Wang, Xifei Li, Jiajun Wang, Jinli Yang, Dongsheng Geng, Ruying Li, Mei Cai, Tsun-Kong Sham, and Xueliang Sun
Publication:	The Journal of Physical Chemistry C
Publisher:	American Chemical Society
Date:	Oct 1, 2012

Logged in as:
dongniu Wang

PERMISSION/LICENSE IS GRANTED FOR YOUR ORDER AT NO CHARGE

This type of permission/license, instead of the standard Terms & Conditions, is sent to you because no fee is being charged for your order. Please note the following:

- Permission is granted for your request in both print and electronic formats, and translations.
- If figures and/or tables were requested, they may be adapted or used in part.
- Please print this page for your records and send a copy of it to your publisher/graduate school.
- Appropriate credit for the requested material should be given as follows: "Reprinted (adapted) with permission from (COMPLETE REFERENCE CITATION). Copyright (YEAR) American Chemical Society." Insert appropriate information in place of the capitalized words.
- One-time permission is granted only for the use specified in your request. No additional uses are granted (such as derivative works or other editions). For any other uses, please submit a new request.

Appendix C Permission from Royal Society of Chemistry (RSC) for published article

Published article: Hierarchical nanostructured core-shell Sn@C nanoparticles embedded in graphene nanosheets: spectroscopic view and their application in lithium ion batteries.

Phys Chem Chem Phys. 2013, 15, 3535-3542. link: http://pubs.rsc.org/en/content/articlelanding/2013/CP/c3cp44172e

Published article: Layer by layer assembly of sandwiched Graphene/SnO_2 Nanorod/Carbon nanostructures with ultrahigh lithium ion storage properties.

Energy Environ. Sci., 2013, DOI: 10.1039/C3EE40829A. link: http://pubs.rsc.org/en/content/articlelanding/2013/EE/C3EE40829A

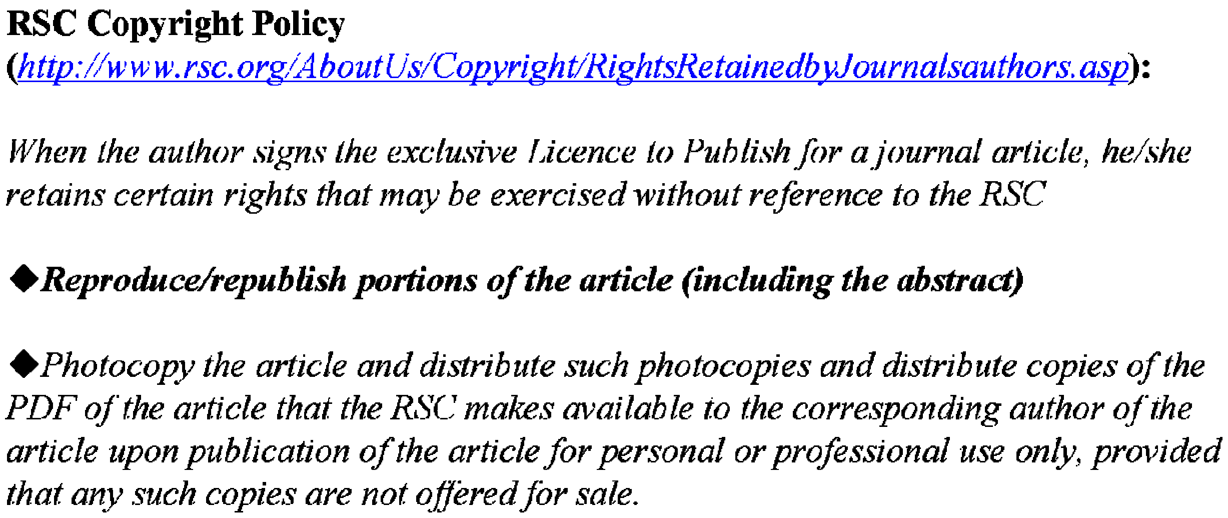

RSC Copyright Policy (*http://www.rsc.org/AboutUs/Copyright/RightsRetainedbyJournalsauthors.asp*):

When the author signs the exclusive Licence to Publish for a journal article, he/she retains certain rights that may be exercised without reference to the RSC

◆***Reproduce/republish portions of the article (including the abstract)***

◆*Photocopy the article and distribute such photocopies and distribute copies of the PDF of the article that the RSC makes available to the corresponding author of the article upon publication of the article for personal or professional use only, provided that any such copies are not offered for sale.*

Reproduced by permission of The Royal Society of Chemistry

Curriculum Vitae

Name:	Dongniu Wang
Post-secondary Education and Degrees:	Harbin Institute of Technology Harbin, Heilongjiang, China 2003-2007 B.Sc.
	Harbin Institute of Technology Harbin, Heilongjiang, China 2007-2009 M.A.
	Western University London, Ontario, Canada 2009-2013 Ph.D.
Related Work Experience	Teaching Assistant and Research Assistant Western University, London， Ontario, Canada 2009-2013

Publications:

1. **D. Wang**, X. Li, J. Wang, J. Yang, D. Geng, R. Li, M. Cai, T.-K. Sham, X. Sun, *Defect-Rich Crystalline SnO_2 Immobilized on Graphene Nanosheets with Enhanced Cycle Performance.* **J. Phys. Chem. C**, 116 (2012) 22149-22156.

2. **D. Wang**, J. Yang, X. Li, J. Wang, R. Li, M. Cai, T. K. Sham, X. Sun. *Observation of Surface/Defect States of SnO_2 Nanowires on Different Substrates from X-ray Excited Optical Luminescence.* **Cryst. Growth Des.** 12 (2012) 397-402.

3. **D. Wang**, X. Li, J. Yang, J. Wang, D. Geng, M. Cai, R. Li, T. K. Sham, X.Sun. *Hierarchical Nanostructured Core-Shelled Sn@C Nanoparticles Embedded in Graphene Nanosheetes: Spectroscopic View and Its Application for Lithium Ion batteries.* **Phys. Chem. Chem. Phys.**, 15 (2013) 3535-3542.

4. **D. Wang**, J. Yang, X. Li, D. Geng, R. Li, M. Cai, T.-K. Sham, X. Sun. *Layer by Layer Assembly of Sandwiched Graphene/SnO_2 Nanorod/Carbon Nanostructures with Ultrahigh Lithium Ion Storage Properties.* **Energy Environ. Sci.** (2013) DOI:

10.1039/C3EE40829A.

5. **D. Wang**, J. Yang, T. K. Sham, X. Sun. *Alumina Coated Tin Oxide Anodes with Enhanced Stabilities by Atomic Layer Deposition.* (2013) to be Submitted.

6. **D. Wang**, J. Yang, T. K. Sham, X. Sun. *Engineering of co-axial carbon sheath tin core nanowires with chemical vapor deposition and its improved lithium storage capability.* (2013) to be Submitted.

7. S. Yang, **D. Wang**, G. Liang, Y. Yiu, J. Wang, L. Liu, X. Sun, T.-K. Sham, *Soft X-ray XANES Studies of Various Phases Related to $LiFePO_4$ Based Cathode Materials.* **Energy Environ. Sci.** 5 (2012) 7007-7016.

8. J. Yang, J. Wang, Y. Tang, **D. Wang**, X. Li, Y. Hu, R. Li, G. Liang, T.-K. Sham, X. Sun, *Impact of Stacked Graphene and Unfolded Graphene on the Morphology of $LiFePO_4$ as a Superior Cathode Material for Rechargeable Lithium Batteries.* **Energy Environ. Sci.** 6 (2013) 1521-1528.

9. Y. Tang, Z. Wang, **D. Wang**, J. Yang, B. Xiao, G. Liang, R. Li, X. Sun, T.-K. Sham, *Soft X-ray Absorption Spectroscopy Evidence of $LiMPO_4$ (M=Fe, Mn) Aging in Ambient Atmosphere.* (2013) Submitted.

10. J. Yang, J. Wang, Y. Tang, **D. Wang**, B. Xiao, X. Li, R. Li, G. Liang,T.-K. Sham, X. Sun, *In-situ Self-catalyzed Formation of Core-shell $LiFePO_4$@CNTs Nanowire for Ultra-high Rate Performance Lithium-ion Batteries.* **J. Mater. Chem. A** 1 (2013) 7306-7311.

11. J. Yang, J. Wang, X. Li, **D. Wang**, J. Liu, G. Liang, M. Gauthier, Y. Li, R. Li, X. Sun, *Hierarchically Porous $LiFePO_4$/Nitrogen-doped Carbon Nanotube Composite for Lithium Ion Batteries Cathodes.* **J. Mater. Chem.** 22(2012) 7537-7543.

12. X. Li, Y. Zhong, M. Cai, M. P. Balogh, **D. Wang**, Y. Zhang, R. Li, X. Sun, *Tin-Alloy Heterostructures Encapsulated in Amorphous Carbon Nanotubes as Hybrid Anodes in Rechargeable Lithium Ion Batteries.* **Electrochim. Acta** 89 (2013) 387-393.

13. Y. Li, J. Wang, X. Li, D. Geng, M. N. Banis, Y. Tang, **D. Wang**, R. Li, T.-K. Sham, X. Sun, *Discharge Product Morphology and Increased Charge Performance of Lithium-oxygen Batteries with Graphene Nanosheet Electrodes: The Effect of Sulphur Doping*. **J. Mater. Chem.** 22 (2012) 20170-20174.

14. X. Li, J. Liu, Y, Zhang, Y. Li, H. Liu, X. Meng, J. Yang, D. Geng, **D. Wang**, R. Li, X. Sun, *High Concentration Nitrogen Doped Carbon Nanotube Anodes with Superior Li^+ Storage Performance for Lithium Rechargeable Battery Application.* **J. Power Sources** 197 (2012) 238-245.

15. J. Yang, J. Wang, **D. Wang**, X. Li, D. Geng, G. Liang, M. Gauthier, R. Li, X. Sun, *3D Porous $LiFePO_4$-graphene Hybrid Electrodes with Enhanced Performance for Li-ion Batteries.* **J. Power Sources** 208 (2012) 340-344.

16. J. Liu, X. Li, J. Yang, D. Geng, Y. Li, **D. Wang**, R. Li, X. Sun, *Microwave-assisted Hydrothermal Synthesis of Nanostructured Spinel $Li_4Ti_5O_{12}$ as Anode Materials for Lithium Ion Batteries.* **Electrochim. Acta** 63 (2012) 100-104.

Conferences:

1. D. Wang, X. Li, J. Yang, D. Geng, R. Li, M. Cai, T.-K. Sham, X. Sun. " Hierarchical Core-Shelled Sn@C and SnO_2@C Nanostructures embedded in Graphene Nanosheetes as Anodes for Lithium Ion Batteries" 223rd ECS meeting. Toronto, Ontario, May 12-16, 2013.

2. D. Wang, X. Li, J. Wang, J. Yang, D. Geng, R. Li, T.-K. Sham, X. Sun, "Controlled Synthesis of SnO_2 Nanostructures by Hydrothermal Method as Anodes of LIB". International Meeting on Lithium Batteries (IMLB-2010). Montreal, Quebec, June 27-July 3. 2010

3. D. Wang, X. Li, J. Wang, J. Yang, D. Geng, R. Li, M. Cai, T.-K. Sham, X. Sun, "Sn and SnO_2 based Graphene Nanocomposites with Enhanced Performances as Anodes for LIB". 24th Canadian Materials Science Conference. London, Ontario, June 5-8. 2012.

4. D. Wang, X. Li, J. Wang, J. Yang, D. Geng, R. Li, M. Cai, T.-K. Sham, X. Sun, " Sn based Carbonaceous Nanocomposites as Anode Materials for Lithium-ion Batteries”. 3rd Annual Nano Ontario conferences., Waterloo, Ontario, October 11-12. 2012.

5. Y. M. Yiu, S. L. Yang, **D. Wang,** X. Sun, T.-K. Sham. “Ab-initio Calculation of the XANES of Lithium Phosphates and $LiFePO_4$”. The 15th Intenational Conference on X-ray Absorption Fine Structure. Beijing, China. July 22-28, 2012.

6. D. Wang, X. Li, J. Wang, J. Yang, D. Geng, R. Li, T.-K. Sham, X. Sun. “Controlled Synthesis of SnO_2 Nanostructures by Hydrothermal Method as Anodes of LIB.” ECS Canadian Section Fall Symposium. London, Ontario, September 18. 2010.